Automation of an Atomic Force Microscope for nanomechanical analysis in cell populations

Sergio Proa Coronado

Université Fédérale
Toulouse Midi-Pyrénées

THÈSE

En vue de l'obtention du

DOCTORAT DE L'UNIVERSITÉ DE TOULOUSE

Délivré par l'Université Toulouse 3 - Paul Sabatier

Cotutelle internationale : Instituto Politecnico Nacional

Présentée et soutenue par

Sergio PROA CORONADO

Le 27 février 2020

Automatisation des mesures AFM pour des applications en biologie

Ecole doctorale : **SDM - SCIENCES DE LA MATIERE - Toulouse**

Spécialité : **Nanophysique**

Unité de recherche :
LAAS - Laboratoire d'Analyse et d'Architecture des Systèmes

Thèse dirigée par
Etienne DAGUE et Adrián Martínez-Rivas

Jury

M. Vincent DUPRES, Rapporteur
M. Sid LABDI, Rapporteur
Mme Laurence RESSIER, Examinatrice
M. Childérick SÉVERAC, Examinateur
M. Juan Vicente MÉNDEZ Méndez, Examinateur
M. Hugo MARTÍNEZ Gutiérrez, Examinateur
M. Etienne DAGUE, Directeur de thèse
M. Adrian MARTINEZ Rivas, Co-directeur de thèse

Instituto Politécnico Nacional

ESCUELA NACIONAL DE CIENCIAS BIOLÓGICAS

SECCIÓN DE ESTUDIOS DE POSGRADO E INVESTIGACIÓN

“Automatización de un Microscopio de Fuerza Atómica para el análisis nanomecánico en poblaciones celulares”

TESIS

Que como uno de los requisitos para obtener el grado de

Doctor en Nanociencias y Micro-nanotecnologías

Cotutela internacional: Université Toulouse 3 – Paul Sabatier

Presenta

M. EN C.I.C. Sergio Proa Coronado

Directores de tesis:

Dr. Adrián Martínez Rivas

Dr. Etienne Dague

Jurado:

Dr. Hugo Martínez Gutiérrez

Dr. Juan Vicente Méndez Méndez

Dr. Adrián Martínez Rivas

Dr. Etienne Dague

Dr. Childérick Séverac

Mexico, CDMX, Enero 2020

Table of Contents

List of Figures

Acknowledgments

This thesis work is dedicated to my family, my parents Juan Proa and Belén Coronado, who have given me strength and support in my decision to pursue a doctorate. To my sisters Cintia Proa and María Magdalena Proa, because they had believed in me even when I did not, and they have pushed me to keep going and not to give up during this journey.

To my thesis advisors, Dr. Adrián Martínez and Dr. Etienne Dague, who have placed their trust in me and supported me in the realization of this work, your guidance has been fundamental to my doctoral training, and I hope I have not exhausted your patience during the time we have been working together. To Dr. Childérick Séverac, thanks to him and his challenges, I was able to overcome my limits and gain confidence in myself, also because his ideas were fundamental to the development of this thesis. I would also like to thank the members of my tutorial committee, Dr. Juan Vicente Méndez Méndez, and Dr. Hugo Martínez Gutiérrez because their advice and guidance helped me to conclude this work.

To my old friends, Pablo, Yunuen, Rada, Lechuga, Edgar, Irving, Jorge, Alberto, Nancy, Gerardo, Mauricio, Leonel, César, Víctor, and Germán. To my new friends, Juan Carlos, Sayuri, and Paulina, each one of you have contributed to make me a better person, that and your presence helped me to be able to do this thesis work. To my friends Rodrigo and Diana, because they supported me in one of the darkest and most stressful moments of my life, and it is thanks to you that I was able to undertake this journey.

To the Escuela Nainloca de Ciencias Biológicas of the Instituto Politécnico Nacional, for giving me the opportunity to grow personally and professionally. To the Laboratory of Analysis and Architecture of Systems (LAAS) in France, specially to the ELIA team for allowing me to prove myself abroad, helping me in my work, and for receiving me in such a warm way that made me miss my homeland a little less during my stay. Also, to Dr. Marie Véronique Le Lann and Digaly Tcholna for their work applying machine learning algorithms to our data.

To the Conacyt (CVU 515300), for having made me a scholarship holder and for supporting me financially for this thesis work.

Abstract

In recent years mechanical phenotype of cells (such as adhesion, elasticity, stiffness), also known as mechanical properties, has been proved to be a valid identifier to distinguish healthy cells from diseased cells. Researchers around the world have related the mechanical phenotype to cancer, cardiovascular, and blood-related diseases, among others. Atomic force microscopy (AFM) is the most used technique to measure mechanical properties, and it makes it possible to obtain the properties at the nanoscale. However, AFM manipulation requires high technical skills, and initially, it was not designed for biological samples. However, the capability to analyze samples in air or liquid in recent years makes it more appealing for the living area. However, using the current AFMs, it is not straightforward to analyze a high number of cells or cell population and then it is difficult to obtain statistical results. This doctoral thesis aims at solving the problem of low throughput, an automated methodology is proposed to do it. This methodology is based on the combination of two techniques, cell arrays, and AFM automation. The mechanical measurements are done automatically by executing a developed Jython script, and the cells are immobilized in known positions proposing here a number of conducted measurements compared with was found in the literature.

Firstly, Immobilization is done for the microbes in microfabricated PDMS stamps and the mammalian cells in commercial cell arrays (BIOSOFT and CYTOO). The immobilization is done, in the case of the microbes, using convective/capillary assembly technique reaching ~85 % filling rate. And for the mammalian cells, the technique used attached the cell to a surface previously functionalized. Next, the AFM was modified to perform the measurements automatically. The automation was made by developing a Jython written script and executed directly in a commercial BioAFM (JPK Germany). The script is versatile, and it has been adapted, or it can be adapted to several sample configurations. The script performs a small number of indentations (9 or 16) on the sample, acquiring force curves from different regions of the cells and at the same time, reducing the time spent on each cell.

The results demonstrated that increasing the number of cells impacts the number of measurements done to the cells, and it is still possible to obtain results comparable to the results reported in the literature. For the first time, the stiffness analysis on ~900 yeast cells (*C. albicans*) is reported, and it is evident the presence of two subpopulations. We compared native yeast cells with caspofungin treated yeast cells. The results were obtained in 4 h with 9 indentations per cell. For the HeLa cells, the comparison was made between native HeLa cells and fixed HeLa cells; and ~80 cells were analyzed in 30 minutes. In both cases (mammalian and yeast cells), a shift between the native and treated cells was observed, this shift agrees with the literature and proves that is possible to reduce the number of indentations done to the cells if the number of analyzed cells is high. Thanks to the massive amount of data collected, it was possible to use Machine learning, and the preliminary results show that it is possible to distinguish between native and treated cells. The differentiation was made entering the descriptors: stiffness, adhesion, and work of adhesion to the machine learning algorithm.

This work contributes to achieving a statistical significance, which is one of the main drawbacks of AFM mechanical analysis and can be considered as one of the first steps to have a diagnostic tool from the atomic force microscope.

Resumen

En años recientes el fenotipo mecánico de las células (tales como adhesión, elasticidad, rigidez), también conocido como propiedades mecánicas, ha demostrado ser un método de identificación válido para poder distinguir entre células sanas y células enfermas. Investigadores alrededor del mundo han establecido una relación entre el fenotipo mecánico y enfermedades como el cáncer, enfermedades cardiovasculares, enfermedades de la sangre, entre otras. La microscopía de fuerza atómica (AFM por sus siglas en inglés) es una de las técnicas mas utilizada para obtener propiedades mecánicas, mediante esta herramienta es posible obtener las propiedades mecánicas a nanoescala. Sin embargo, la manipulación del AFM requiere un alto grado de habilidades técnicas y en un inicio no fue diseñado para analizar muestras biológicas. No obstante, sus capacidades para analizar muestras tanto en liquido como en aire, en años recientes le han vuelto mas atractivo para el área biológica. Sin embargo, en su estado actual no es posible analizar un gran numero de células. Esto dificulta la validación de resultados ya que no es fácil obtener relevancia estadística. Esta tesis doctoral se enfoca en resolver el problema del bajo rendimiento y para conseguirlo proponemos una metodología automatizada. Dicha metodología está basada en la combinación de dos técnicas, arreglos celulares y automatización del AFM. Las mediciones mecánicas son realizadas automáticamente al ejecutar un script desarrollado en este trabajo de tesis, y las células fueron inmovilizadas en posiciones conocidas con la ayuda de los arreglos celulares.

El primer paso de la metodología es la inmovilización de las células. La inmovilización en el caso de los microbios se realiza en estampas de PDMS microfabricadas y para las células de mamíferos la inmovilización se realizó en arreglos celulares comerciales (BIOSOFT y CYTOO). La técnica utilizada para inmovilizar los microbios fue el montaje convectivo/capilar, alcanzando una tasa de llenado de ~85%. Y para las células de mamíferos la técnica utilizada fue la funcionalización de la superficie. El siguiente paso fue la modificación del AFM para realizar las mediciones de manera automática. La automatización fue desarrollada mediante el lenguaje Jython y ejecutado en un BioAFM comercial. El script es versátil y ha sido adaptado, o puede ser adaptado, a múltiples configuraciones. El script hace que la punta realice un número pequeño de identaciones (9 o 16) en la muestra, adquiriendo curvas de fuerza de diferentes regiones de las células y al mismo tiempo, reduce el tiempo invertido en medir las propiedades mecánicas de cada célula.

Los resultados demuestran que incrementar el número de células impacta en el número de mediciones hechas a las células, y es posible obtener resultados equiparables a los reportados en la literatura. Por primera vez el análisis de rigidez de ~900 células de levadura (*C. albicans*) es reportado y la presencia de subpoblaciones puede observarse. Comparamos células nativas de levadura con células tratadas con caspofungin. Los resultados fueron obtenidos en 4 h con 9 identaciones por célula. Para el caso de las células HeLa, la comparación fue realizada entre células HeLa nativas y células HeLa fijadas; y ~80 células fueron analizadas en 30 min. En ambos casos (tanto células de mamíferos como nativas), un corrimiento entre las células nativas y tratadas puede verse, este corrimiento concuerda con lo reportado en la literatura y demuestra que es posible reducir el número de identaciones hechas a las células si el número de células es alto. Gracias a la cantidad masiva de datos recolectados fue posible utilizar aprendizaje automático y los resultados preliminares demuestran que es posible distinguir entre células nativas y células tratadas. La

diferenciación fue hecha utilizando los descriptores: rigidez, adhesión y el trabajo de adhesión. Este trabajo contribuye a sobrepasar una de las principales limitaciones del análisis mecánico en el AFM, la relevancia estadística, y puede ser considerado como uno de los primeros pasos para obtener una herramienta de diagnostico a partir del microscopio de fuerza atómica.

Introduction

Atomic force microscopy (AFM) is a widely used technique around the globe. It consists of a sharp tip mounted on a flexible cantilever, and this cantilever is attached to a piezoelectric ceramic that moves on x, y, and z positions. A laser beam reflects on the back of the cantilever to a four-quadrant photodiode, so as the tip scans the surface, it obtains topographical images based on the position of the laser in the photodiode[1]. However, AFM not only captures images, but it also allows mechanical studies by performing force spectroscopy. The results of this analysis are known as force curves (force vs. distance plots), of which it is possible to obtain mechanical properties, such as Young modulus, stiffness, adhesion.

Label-free biomarkers, otherwise, do not need chemical reactions to be detected because they are based on the biophysical properties of the target molecules, and usually, the sensing is based on mechanical, electrical, or optical signals[2]. Mechanical properties (also known as the mechanical phenotype) are considered as label-free biomarkers. In the case of cancer Lekka et al.[3] and Cross et al.[4] founded a decrease in the Young modulus by one order of magnitude when comparing cancer cells against healthy cells. Omidvar[5], Bastatas[6], and Smolyakov et al.[7] reported increased adhesion in cancer cells, which contributes to invasion. Not only the mechanical properties have been used to differentiate diseased cells from healthy ones, in the field of microbiology mechanical properties have been used to analyze the response of *Streptococcus pyogenes* to rokitamicyn[8] or to analyze the elongation of *Pseudomonas aeruginosa* cells under ticarcillin antibiotic[9]. In mammalian cells, AFM is not a favored technique; other techniques are more appealing because they can analyze faster. Techniques such as magnetic twisting cytometry[10], optical tweezers[11], particle tracking microrheology[12], parallel plate rheometry[13], cell monolayer rheometry[14], and optical stretching[15].

The focus of this thesis work is modifying the way AFM performs mechanical measurements, and increasing the number of samples analyzed. In the literature, some attempts have been made to increase the number of samples analyzed with an AFM For example, Wang et.al.[16] developed an automated system that uses image processing to identify Raji cell locations so the AFM tip can identify the position of the cells and move exactly above the cells to take measurements. The location and measurement of the cells are done within 3 s per cell. However, their system had some requirements: the algorithm recognizes only round shape cells (which is usually the sign of dying cells), this confines the system only to a specific cell geometry.

Moreover, the substrate had to be completely flat, and the agglomeration of cells was to be avoided because the system did not withdraw the tip from the sample. Finally, the authors did not report the number of cells analyzed per hour; they reported only a test with 4 cells per scanning area.

In another effort to increase the AFM measurements on tissues Roy et.al[17] developed a system that used image processing to align the AFM probe automatically with a tissue of interest, they were able to obtain in an area of 80 μm x 150 μm up to 480 force curves in ~80 min. Another approach was reported by Favre et.al.[18], they developed an array of cantilevers that are controlled by one AFM, all working at the same time to acquire images from different regions of a sample. However, to apply this technology to a cell population, the cantilever arrays should be fabricated with the same dimensions as the cell arrays.

Recently Antoine Dujardin et.al.[19] reported an automated procedure that allows an AFM to obtain biomechanical analysis on prokaryotes. A python script was implemented in a Dimension Fast Scan-Bio AFM (Bruker, Santa Barbara, CA, USA). However, this process takes considerable time to realign the photodetector and perform the engagement step. They report the analysis of 501 areas in 8 h 35 min. The system was tested with fixed *Yersinia pseudotuberculosis* and living *Mycobacterium bovis* BCG bacteria. Finally, a force volume image was performed to identify the bioelements in each well. This image was used to determine the bacteria positions (based on their height) and then enclosed images (2x2 µm2 area) of supposedly only the cells were performed. The reported images are height and Peak Force-error signals discarding the option to perform a mechanical analysis on the analyzed bacteria.

In this thesis work, the objective was to develop an automated methodology based on cell array immobilization and commercial AFM technology, capable of increasing the number of samples analyzed by force spectroscopy with an AFM in a short period of time, which can give statistical significance to AFM results. Because we believe that AFM automation reduces the time consumed when a sample is analyzed, leading to an increase in the number of samples studied, permitting, for example, cell population analysis. Also, showing that if the number of samples increases drastically, the number of performed mechanical measurements becomes irrelevant. We used two types of cells to test our hypothesis, *Candida albicans*, and HeLa cells. The results expected for microbial cells (*C. albicans*) are ~1000 cells in 4h and ~100 mammalian cells (HeLa) in 2h. The first step of our methodology is the immobilization of cells, and the second is to execute a script on a commercial AFM to perform indentations (9 – 16) automatically on different regions of the samples. Reducing the number of nanoindentations on the sample (from hundreds to a few tens) is possible to accelerate the speed of the process, and then the number of samples can be increased.

Finally, the massive data obtained with the methodology presented here allowed us to implement machine learning (ML) algorithms to the data. The ML analysis demonstrate that it was not possible to differentiate native from treated cells considering only one mechanical property. However, with the data of three mechanical properties (adhesion, stiffness, and work of adhesion) it is possible to discern between cells with a ~86% of confidence.

This document summarizes our work and present for the first time the evidence on heterogeneity on a cell population and also proves that increasing the number of cells to almost thousand derives in less significance related to the number of measurements taken per cell. The résumé detaille chapter summarizes the most important results of our work. The methods of micropatterning chapter is a summary of one of the papers published in this thesis work. The state of the art chapter presents the works reported on the literature about cell immobilization and AFM automation, the presentation of this information is to compare what has been already reported in the area of this thesis work. In the materials and methods chapter, the methodologies used for cell array fabrication and cell immobilization are presented. Also, the algorithms developed to automate the mechanical measurements in the AFM are listed, and the parameters used to develop the experiments are presented. The Results and discussion chapter, presents all the results obtained from this work are presented, microbial, mammalian, and a proposal to adopt the methodology to material science and glycan arrays is presented. Finally, in the conclusion and future work chapter we present the main conclusions obtained from this doctoral thesis and also, proposals for future work, aiming to obtain a tool capable of be used in diagnosis.

References

(1) Formosa, C.; Dague, E. Imaging Living Yeast Cells and Quantifying Their Biophysical Properties by Atomic Force Microscopy. In *Advanced Microscopy in Mycology*; Dahms, T. E. S., Czymmek, K. J., Eds.; Fungal Biology; Springer International Publishing: Cham, 2015; pp 125–141. https://doi.org/10.1007/978-3-319-22437-4_7.

(2) Syahir, A.; Usui, K.; Tomizaki, K.; Kajikawa, K.; Mihara, H. Label and Label-Free Detection Techniques for Protein Microarrays. *Microarrays* **2015**, *4* (2), 228–244. https://doi.org/10.3390/microarrays4020228.

(3) Lekka, M.; Laidler, P.; Gil, D.; Lekki, J.; Stachura, Z.; Hrynkiewicz, A. Z. Elasticity of Normal and Cancerous Human Bladder Cells Studied by Scanning Force Microscopy. *Eur. Biophys. J.* **1999**, *28* (4), 312–316. https://doi.org/10.1007/s002490050213.

(4) Cross, S. E.; Jin, Y.-S.; Rao, J.; Gimzewski, J. K. Nanomechanical Analysis of Cells from Cancer Patients. *Nat. Nanotechnol.* **2007**, *2* (12), 780–783. https://doi.org/10.1038/nnano.2007.388.

(5) Omidvar, R.; Tafazzoli-shadpour, M.; Shokrgozar, M. A.; Rostami, M. Atomic Force Microscope-Based Single Cell Force Spectroscopy of Breast Cancer Cell Lines: An Approach for Evaluating Cellular Invasion. *J. Biomech.* **2014**, *47* (13), 3373–3379. https://doi.org/10.1016/j.jbiomech.2014.08.002.

(6) Bastatas, L.; Martinez-Marin, D.; Matthews, J.; Hashem, J.; Lee, Y. J.; Sennoune, S.; Filleur, S.; Martinez-Zaguilan, R.; Park, S. AFM Nano-Mechanics and Calcium Dynamics of Prostate Cancer Cells with Distinct Metastatic Potential. *Biochim. Biophys. Acta BBA - Gen. Subj.* **2012**, *1820* (7), 1111–1120. https://doi.org/10.1016/j.bbagen.2012.02.006.

(7) Smolyakov, G.; Thiebot, B.; Campillo, C.; Labdi, S.; Severac, C.; Pelta, J.; Dague, É. Elasticity, Adhesion, and Tether Extrusion on Breast Cancer Cells Provide a Signature of Their Invasive Potential. *ACS Appl. Mater. Interfaces* **2016**, *8* (41), 27426–27431. https://doi.org/10.1021/acsami.6b07698.

(8) Braga, P. C.; Ricci, D. Differences in the Susceptibility of Streptococcus Pyogenes to Rokitamycin and Erythromycin A Revealed by Morphostructural Atomic Force Microscopy. *J. Antimicrob. Chemother.* **2002**, *50* (4), 457–460. https://doi.org/10.1093/jac/dkf180.

(9) Formosa, C.; Grare, M.; Duval, R. E.; Dague, E. Nanoscale Effects of Antibiotics on P. Aeruginosa. *Nanomedicine Nanotechnol. Biol. Med.* **2012**, *8* (1), 12–16. https://doi.org/10.1016/j.nano.2011.09.009.

(10) Wang, N.; Butler, J. P.; Ingber, D. E. Mechanotransduction across the Cell Surface and through the Cytoskeleton. *Science* **1993**, *260* (5111), 1124–1127. https://doi.org/10.1126/science.7684161.

(11) Svoboda, K.; Block, S. M. Biological Applications of Optical Forces. *Annu. Rev. Biophys. Biomol. Struct.* **1994**, *23* (1), 247–285. https://doi.org/10.1146/annurev.bb.23.060194.001335.

(12) Wirtz, D. Particle-Tracking Microrheology of Living Cells: Principles and Applications. *Annu. Rev. Biophys.* **2009**, *38* (1), 301–326. https://doi.org/10.1146/annurev.biophys.050708.133724.

(13) Thoumine, O.; Ott, A. Time Scale Dependent Viscoelastic and Contractile Regimes in Fibroblasts Probed by Microplate Manipulation. *J. Cell Sci.* **1997**, *110* (17), 2109–2116.

(14) Fernández, P.; Heymann, L.; Ott, A.; Aksel, N.; Pullarkat, P. A. Shear Rheology of a Cell Monolayer. *New J. Phys.* **2007**, *9* (11), 419–419. https://doi.org/10.1088/1367-2630/9/11/419.

(15) Guck, J.; Ananthakrishnan, R.; Mahmood, H.; Moon, T. J.; Cunningham, C. C.; Käs, J. The Optical Stretcher: A Novel Laser Tool to Micromanipulate Cells. *Biophys. J.* **2001**, *81* (2), 767–784. https://doi.org/10.1016/S0006-3495(01)75740-2.

(16) Wang, Z.; Liu, L.; Wang, Y.; Xi, N.; Dong, Z.; Li, M.; Yuan, S. A Fully Automated System for Measuring Cellular Mechanical Properties. *J. Lab. Autom.* **2012**, *17* (6), 443–448. https://doi.org/10.1177/2211068212460236.
(17) Roy, R.; Chen, W.; Cong, L.; Goodell, L. A.; Foran, D. J.; Desai, J. P. A Semi-Automated Positioning System for Contact-Mode Atomic Force Microscopy (AFM). *IEEE Trans. Autom. Sci. Eng.* **2013**, *10* (2), 462–465. https://doi.org/10.1109/TASE.2012.2226154.
(18) Favre, M.; Polesel-Maris, J.; Overstolz, T.; Niedermann, P.; Dasen, S.; Gruener, G.; Ischer, R.; Vettiger, P.; Liley, M.; Heinzelmann, H.; et al. Parallel AFM Imaging and Force Spectroscopy Using Two-Dimensional Probe Arrays for Applications in Cell Biology. *J. Mol. Recognit.* **2011**, *24* (3), 446–452. https://doi.org/10.1002/jmr.1119.
(19) Dujardin, A.; Wolf, P. D.; Lafont, F.; Dupres, V. Automated Multi-Sample Acquisition and Analysis Using Atomic Force Microscopy for Biomedical Applications. *PLOS ONE* **2019**, *14* (3), e0213853. https://doi.org/10.1371/journal.pone.0213853.

Résumé détaillé

Introduction et motivations

Ces dernières années, le phénotype mécanique des cellules (comme l'adhésion, l'élasticité, la rigidité), également connu sous le nom de propriétés mécaniques, s'est avéré être un identificateur valide pour distinguer les cellules saines des cellules malades. Des chercheurs du monde entier ont établi un lien entre le phénotype mécanique et le cancer, les maladies cardiovasculaires et les maladies liées au sang, entre autres. La microscopie à force atomique (AFM) est la technique la plus utilisée pour mesurer les propriétés mécaniques et permet d'obtenir les propriétés à l'échelle nanométrique. Cependant, la manipulation de l'AFM nécessite des compétences techniques élevées, et au départ, elle n'a pas été conçue pour les échantillons biologiques. Cependant, la capacité d'analyser des échantillons dans l'air ou dans les liquides au cours des dernières années la rend plus attrayante pour l'espace de vie. Mais, dans son état actuel, il n'est pas possible d'analyser un grand nombre de cellules. Cette thèse de doctorat vise à résoudre le problème du faible débit, et une méthodologie automatisée est proposée pour le faire. Cette méthodologie est basée sur la combinaison de deux techniques, les réseaux de cellules et l'automatisation AFM. Les mesures mécaniques se font automatiquement en exécutant un script développé dans ce travail de thèse, et les cellules sont immobilisées dans des positions connues grâce aux réseaux de cellules. La méthodologie commence par l'immobilisation des cellules. L'immobilisation se fait pour les microbes dans les timbres PDMS microfabriqués et les cellules de mammifères dans les réseaux cellulaires commerciaux (BIOSOFT et CYTOO). L'immobilisation se fait, dans le cas des microbes, à l'aide d'une technique d'assemblage convectif/capillaire atteignant un taux de remplissage de ~85 %. Et pour les cellules de mammifères, elles étaient attachées à une surface préalablement fonctionnalisée. Ensuite, l'AFM a été modifié pour effectuer les mesures automatiquement. L'automatisation a été réalisée en développant un script écrit en Jython et exécuté directement dans un BioAFM commercial. Le script effectue un petit nombre d'empreintes (9 ou 16) sur l'échantillon, en acquérant des courbes de force provenant de différentes régions des cellules et en réduisant en même temps le temps passé sur chaque cellule. Les résultats démontrent que l'augmentation du nombre de cellules a un impact sur le nombre de mesures effectuées sur les cellules, et il est toujours possible d'obtenir des résultats comparables aux résultats rapportés dans la littérature. Pour la première fois, l'analyse de rigidité sur ~900 cellules de levure (C. albicans) en 4 h est rapportée et l'on observe la présence de sous-populations. Nous avons comparé des cellules indigènes à des cellules de C. albicans traitées à la caspofongine. Pour les cellules HeLa, la comparaison a été faite entre les cellules HeLa natives et les cellules HeLa fixes, et environ 80 cellules ont été analysées en 30 minutes. Dans les deux cas (cellules de mammifères et de levures), on a observé un décalage entre les cellules indigènes et les cellules traitées, ce décalage correspond à la littérature et prouve qu'il est possible de réduire le nombre d'indentations faites sur les cellules. Grâce à l'énorme quantité de données recueillies, il a été possible d'utiliser l'apprentissage automatique, et les résultats préliminaires montrent qu'il est possible de distinguer les cellules indigènes des cellules traitées. La différenciation s'est faite en entrant les descripteurs : rigidité, adhérence, et travail d'adhésion à

l'algorithme d'apprentissage machine. Ce travail contribue à l'obtention d'une signification statistique, qui est l'un des principaux inconvénients de l'analyse mécanique AFM et peut être considéré comme l'une des premières étapes pour réaliser un outil de diagnostic au microscope à force atomique.

Contexte

Origines de la microscopie à force atomique.

La microscopie à force atomique (AFM) est une technique largement utilisée dans le monde entier. Cette technique est basée sur la microscopie à effet tunnel à balayage (STM). Présentée pour la première fois par Binning et Rohrer en 1982[1] la STM utilise une pointe métallique fixée à l'extrémité d'un cantilever. La pointe s'approche de la surface, et en utilisant un courant tunnel, elle balaie la surface (le courant tunnel est maintenu constant grâce à un contrôle de rétroaction). C'est une technique capable d'obtenir des images topographiques et d'atteindre une résolution atomique. La STM peut être réalisée dans des environnements d'air, de liquide ou de vide[2]. Cependant, le STM a besoin d'échantillons conducteurs, ce qui rend la technique non adaptée aux échantillons biologiques. Une façon de surmonter cette limitation est de revêtir l'échantillon d'une couche conductrice, mais, cela rend moins pertinent pour les expériences biologiques.
L'AFM est capable d'atteindre une résolution atomique dans certaines conditions. L'AFM peut surmonter les limites de la résolution optique et, par rapport à la microscopie électronique, elle n'a pas besoin que l'échantillon soit conducteur[3]. L'AFM est constitué d'une pointe acérée montée sur un cantilever flexible, ce cantilever est fixé à une céramique piézoélectrique (figure 1) qui se déplace sur les positions x, y et z. Un faisceau laser tombe sur l'arrière du cantilever, et il est réfléchi vers une photodiode à quatre quadrants, de sorte que lorsque la pointe balaie la surface, elle obtient des images topographiques basées sur la position du laser dans la photodiode[4]. Cependant, l'AFM ne se contente pas de capturer des images, mais il permet également de réaliser des études mécaniques en effectuant une spectroscopie de force. Les résultats de cette analyse sont connus sous le nom de courbes de force (graphiques de force en fonction de la distance). Il est possible d'extraire des courbes de force, par exemple, les valeurs du module de Young, la rigidité, l'adhérence.

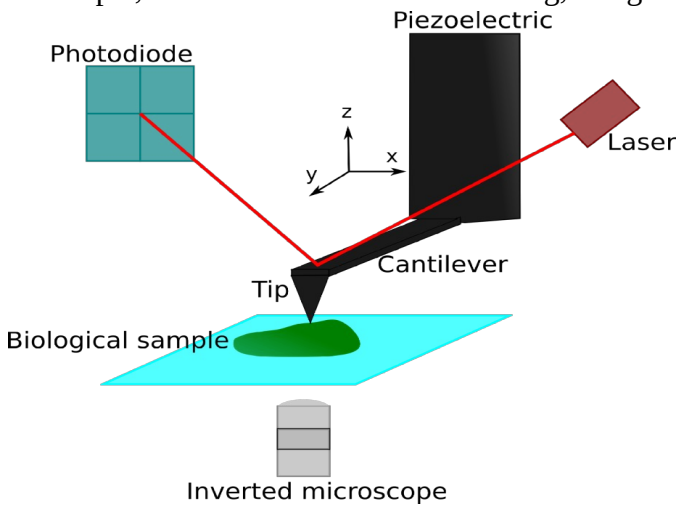

Figure 1. Schéma du principe de l'AFM.

Ce travail utilise la technique AFM car c'est l'une des méthodes les plus connues pour obtenir des propriétés mécaniques, cette technique ne nécessite pratiquement aucune préparation des échantillons et il n'est pas nécessaire d'introduire des modifications chimiques sur les échantillons. Les étapes suivantes reprennent la procédure standard pour obtenir des courbes de force à partir d'un AFM : la première étape est l'étalonnage du cantilever, puis l'échantillon est placé sur la platine du microscope et une image topographique peut être acquise pour déterminer la position des cellules, la pointe est déplacée vers la région centrale de chaque cellule. L'AFM réalise des empreintes à différents endroits de la cellule, et des courbes de force sont obtenues et enregistrées. Enfin, lorsque toutes les cellules ont été mesurées, la platine est déplacée et de nouvelles cellules sont introduites dans le champ de vision de l'AFM.
Un AFM peut fonctionner selon différents modes : contact, sans contact et contact intermittent (principalement utilisé pour l'imagerie) selon l'échantillon. Différents modes peuvent être sélectionnés pour obtenir les résultats souhaités.
En mode contact, la sonde est en permanence en contact avec l'échantillon ; un système de rétroaction en boucle fermée permet de lever ou d'abaisser la pointe (ou l'échantillon) pour maintenir une déflexion constante sur le cantilever. L'optimisation se fait à l'aide de deux paramètres, le gain proportionnel fixe l'amplitude, et le gain intégral fixe la réponse temporelle de l'action corrective. Le mode sans contact utilise des forces à longue portée pour l'imagerie de la surface. Le cantilever oscille près de sa fréquence de résonance, et l'image est générée par le décalage de la fréquence du cantilever basé sur l'interaction pointe/échantillon. Enfin, le contact intermittent (aussi appelé mode de frappe) fait également osciller le cantilever à sa fréquence de résonance avec une amplitude plus élevée ; la topologie de la surface est mesurée comme en mode de contact tout en maintenant un amortissement constant de l'oscillation du cantilever. Les avantages de ce dernier mode sont la réduction des forces (verticales et latérales) et des interactions adhésives, de sorte qu'il permet d'imager des échantillons mous ou des molécules qui ne sont pas fermement fixées à la surface.
Un nouveau mode a été ajouté dernièrement aux AFMs[3]. Ce mode mesure les courbes de force en fonction de la distance dans chaque pixel. Selon le fabricant de l'AFM, ce mode reçoit des noms différents, par exemple, mode de saut, imagerie quantitative (QI) ou mode de force de pointe. Ce mode peut être considéré comme une extension de la spectroscopie de force AFM (en gardant à l'esprit que la spectroscopie de force n'est pas un mode d'imagerie) car, sur chaque pixel, il applique une force précisément contrôlée (~100 pN) permettant d'obtenir une image topographique avec des informations mécaniques quantitatives.
Depuis le début, l'AFM a été considérée comme une technique cruciale pouvant être impliquée dans différentes études, et la biologie est l'un des domaines dans lesquels cette technique peut contribuer. L'une des contributions essentielles de l'AFM au domaine du vivant a été l'imagerie de la dynamique de la croissance des cristaux de virus, obtenue par Malkin et al.[5] Un autre exemple est l'utilisation de la spectroscopie de force à une seule molécule appliquée au dépliage de la titine, la protéine sarcomérique géante du muscle strié[6]. L'article fait état d'un tracé en dents de scie caractéristique pour les molécules de titane individuelles plus grosses. Tao et al.[7] a utilisé l'AFM pour extraire les propriétés mécaniques de l'os à une échelle non explorée à l'époque.
Les contributions de l'AFM à la biologie ont contribué au développement de la région et de la technique elle-même. Par exemple, Meister A. et al.[8] a publié un système de distribution de liquide (FluidFM) basé sur des cantilevers creux capables de distribuer des molécules solubles ou d'extraire

des composants spécifiques de la cellule. Enfin, Ando T. et al.[9] a signalé en 2001 le premier AFM à grande vitesse utilisé pour imager les molécules de myosine V se déplaçant sur le mica.
Le travail présenté ici est également une modification de la AFM. Il découle de la nécessité d'analyser un grand nombre d'échantillons en peu de temps.

Un nouveau biomarqueur (phénotype mécanique)

Les biomarqueurs sans marqueurs, n'ont pas besoin de réactions chimiques pour être détectés car ils sont basés sur les propriétés biophysiques des molécules cibles, et habituellement, les principes de biodétection sont des signaux mécaniques, électriques ou optiques[10]. Les propriétés mécaniques (aussi connues sous le nom de phénotype mécanique) sont considérées comme des biomarqueurs sans étiquette. Elles ont été utilisées ; par exemple, dans le cas du cancer, Lekka et al.[11] et Cross et al.[12] a fondé une diminution du module de Young d'un ordre de grandeur en comparant les cellules cancéreuses aux cellules saines. Omidvar[13], Bastatas[14], et Smolyakov et al.[15] a signalé une augmentation de l'adhérence dans les cellules cancéreuses, ce qui contribue à l'invasion. Cependant, le cancer n'est pas la seule maladie qui a été associée à des changements dans les propriétés mécaniques des cellules. La rigidité des érythrocytes a été liée au diabète sucré, aux maladies coronariennes[16], Déficit en G6PD, et sphérocytose héréditaire[17]. Dans le domaine des maladies cardiovasculaires, les propriétés mécaniques des cardiomyocytes ont été étudiées par Benech et al.[18] et ils ont rapporté une augmentation de la rigidité des cardiomyocytes vivants de souris diabétiques. Dague et al.[19] a également constaté un déplacement mitochondrial sur les cardiomyocytes de souris atteintes d'insuffisance cardiaque et une augmentation générale de la rigidité de la surface des cardiomyocytes.
Non seulement les propriétés mécaniques ont été utilisées pour différencier les cellules malades des cellules saines, mais dans le domaine de la microbiologie, les propriétés mécaniques ont été utilisées pour analyser la réponse de Streptococcus pyogenes à la rokitamicine[20]. Et pour analyser l'élongation des cellules de Pseudomonas aeruginosa sous antibiotique ticarcilline[21] parmi beaucoup d'autres exemples.
Comme l'AFM est couramment utilisée pour analyser des cellules individuelles, le nombre d'échantillons étudiés avec elle est faible. L'extraction des propriétés mécaniques des cellules de mammifères est réalisée à l'aide d'autres techniques développées. Ces techniques sont capables d'analyser un nombre important de cellules dans un temps relativement court, ce qui bat les capacités de l'AFM, et sont décrites ici.

Techniques pour extraire les propriétés mécaniques des cellules de mammifères.

Cytométrie par torsion magnétique (MTC)

Sur cette technique (figure 2), des microbilles ferromagnétiques sphériques sont liées à la surface des cellules par des ligands récepteurs spécifiques puis un fort champ magnétique externe est appliqué pour aligner les moments magnétiques de toutes les billes à la surface. Après avoir appliqué un champ magnétique faible perpendiculairement au premier champ pour tordre les billes (contrainte de cisaillement contrôlée), on mesure la rotation moyenne des billes avec un magnétomètre classique. Avec le MTC, il est possible de mesurer la rotation des billes qui se traduit

par la contrainte sur le cytosquelette[22]. Néanmoins, cette technique présente quelques inconvénients, tels que, les couples appliqués ne sont pas constants dans le temps[23], ou le fait qu'il applique des forces plus faibles que l'AFM et aussi, la rotation du bourrelet magnétique génère un déplacement x, y et z et pour déterminer une déformation z il est nécessaire de prendre plusieurs balayages z ce qui signifie appliquer des forces pour beaucoup plus de cycles[24].

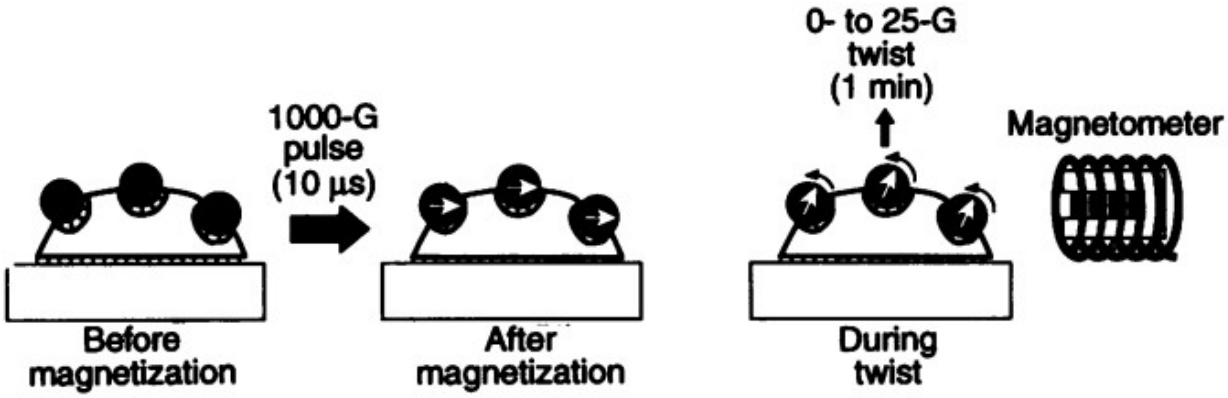

Figure 2. Principe de la cytométrie à torsion magnétique. Les microbilles sont liées à la surface de la cellule et un champ magnétique puissant est appliqué pour orienter le moment magnétique des billes, puis un champ magnétique de torsion plus faible orienté à 90° par rapport au champ plus fort est appliqué et la rotation moyenne des billes (déformation angulaire) est mesurée à l'aide d'un magnétomètre. L'image a été prise de[22].

Pincettes optiques (OT)

Cette technique utilise la force du gradient, qui est proportionnelle au gradient spatial de l'intensité lumineuse. La force du gradient provient des dipôles électriques fluctuants qui sont induits lorsque la lumière traverse des objets transparents[25,26]. La procédure pour mesurer la rigidité sur des échantillons biologiques, par exemple, consiste à pousser une microsphère dans la cellule et à mesurer la force exercée sur la microsphère par la cellule[27]. Les pinces optiques fonctionnent avec des forces allant de un à 100 pN, et une caractéristique importante à considérer est que la force d'attraction due à la réfraction de la lumière à la surface doit être suffisante pour surmonter toute autre force agissant pour pousser les objets. De plus, les pinces optiques ont besoin d'objectifs de microscope avec des ouvertures numériques (NAs) plus élevées, et comme la limite de la taille focale impose une limite supérieure à la force de gradient, il est nécessaire d'utiliser des forces plus fortes pour piéger les objets à l'échelle nanométrique ; cela signifie que le laser doit être de très haute puissance[28].

Microrhéologie du suivi des particules (PTM)

Dans cette approche, des billes (<1 μm de diamètre) sont injectées directement à l'intérieur du cytoplasme des cellules. Les billes se dispersent plus rapidement dans le cytoplasme, et à l'aide d'un microscope à fluorescence, les mouvements des billes sont enregistrés. Ces mouvements sont analysés en termes de viscosité et d'élasticité. La figure 3 illustre le processus général de la PTM[29,30].

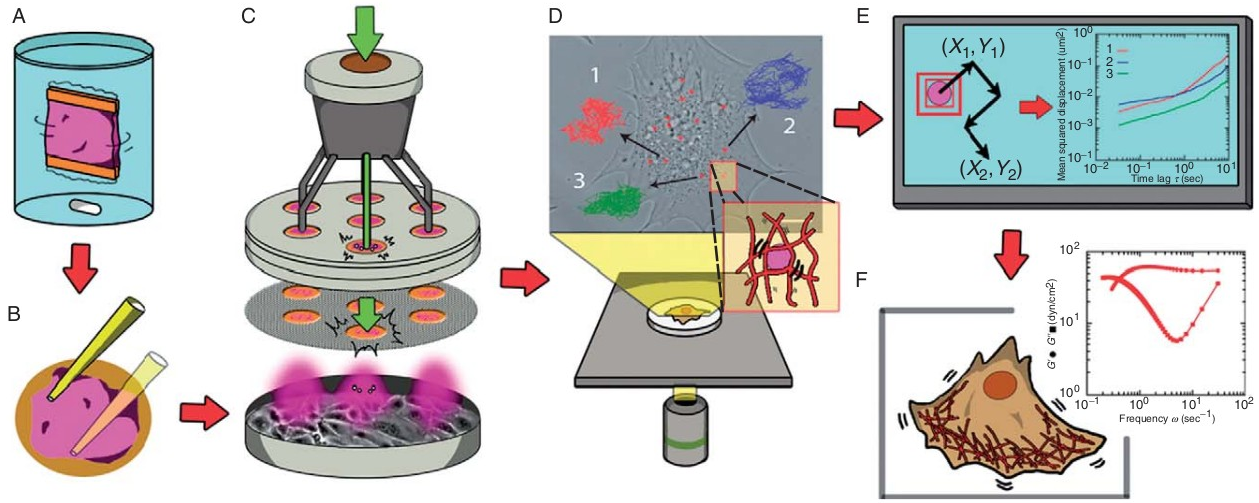

Figure 3. Microrhéologie de suivi de particules. A) Nanoparticules préparées par dialyse. B) Nanoparticules dialysées déposées sur un microsupport. C) Injection balistique des nanoparticules dans le cytoplasme. D) La microscopie fluorescente à fort grossissement permet de suivre les trajectoires des particules incorporées à l'intérieur de la cellule. E) Les particules suivies par la mesure du déplacement centroïde pondéré sont converties en déplacements carrés moyens. F) Les déplacements carrés moyens sont transformés en modules viscoélastiques dépendant de la fréquence, ce qui donne des informations sur la déformabilité locale et la viscoélasticité de la cellule. L'image a été prise de[30].

Idéalement, toute technique d'imagerie pourrait imager, localiser et suivre les petites particules au fil du temps et la technique est capable d'agir comme un rhéomètre ; toutefois, l'imagerie est généralement limitée aux configurations de nanoscanner à grand champ[31]. On a signalé que le PTM avait des limites lorsqu'il était appliqué à des matériaux complexes[32]. De plus, la technique a des limites liées à la propriété liquide visqueuse ou solide élastique des matériaux analysés[29,31].

Rhéométrie à plaques parallèles

Cette technique utilise, comme son nom l'indique, deux plaques parallèles, l'une rigide et adhésive, et l'autre souple, qui sert à mesurer la force appliquée aux cellules. Les cellules sont déposées sur les plaques rigides, puis les cellules sont placées contre une microplaque souple non adhésive ou adhésive (plaque adhésive pour les mesures de traction et de perturbation sinusoïdale et non adhésive pour l'analyse de la compression)[33]. La figure 4 montre le principe de fonctionnement de cette méthode ; le déplacement fin dans l'axe des y de la plaque rigide est contrôlé par ordinateur. Les deux microplaques sont reliées à des micromanipulateurs connectés sur les côtés opposés d'une platine de microscope inversée. Pour l'analyse, la comparaison des données est faite entre la forme initiale de la cellule et après l'application de la déformation. De plus, la déflexion de la microplaque flexible est utilisée ; avec ces deux paramètres, l'indice de forme est calculé.

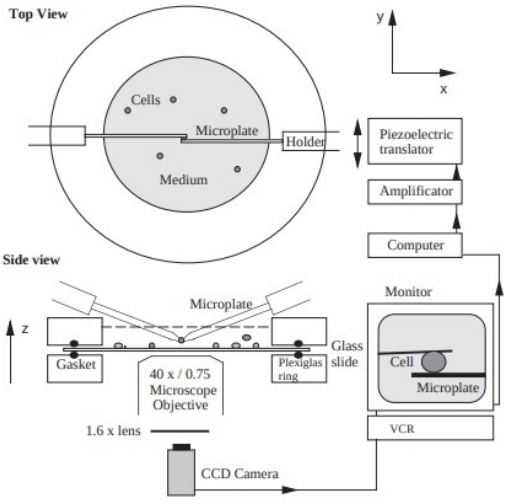

Figure 4. Rhéométrie à plaques parallèles. Les cellules sont suspendues sur le milieu à l'intérieur d'une chambre de manipulation, les cellules sont déposées sur la plaque rigide par gravité. La durée du test est de 35 à 75 minutes. L'image a été prise de[33].

Les erreurs dans les mesures de la technique de rhéométrie à plaques parallèles proviennent de différentes sources comme le manque de parallélisme des plaques, les effets de chauffage visqueux, les incertitudes sur la taille de l'interstice, le sous-remplissage de l'échantillon, la défaillance des bords et la migration radiale[34]. Tous ces effets affectent grandement les résultats obtenus avec cette technique.

Rhéologie de la monocouche cellulaire (CMR)

Cette technique a d'abord adapté un rhéomètre commun pour réaliser des études d'écoulement et de déformation sur les échantillons (figure 5). Les mesures sont effectuées sur une monocouche de cellules déposées entre deux disques de verre parallèles. La plaque supérieure est fixée à la tête de mesure du rhéomètre et la plaque inférieure à une base, cette plaque possède une sortie permettant de changer le milieu des cellules et d'injecter des agents biochimiques sans perturber les cellules. Lorsqu'une force a appliqué les modifications aux cellules, celles-ci sont suivies au microscope et à la caméra CCD, ce qui permet de mesurer les différences entre les images. Le CMR permet l'analyse de plusieurs cellules en même temps (106 cellules). L'étape cruciale de cette technique est d'obtenir un parallélisme entre les plaques. Après le dépôt, les cellules sont laissées au repos pendant environ une heure avant de commencer toute mesure. Une grande variété de techniques de sondage peut être réalisée (variation oscillatoire de fréquence ou d'amplitude, contrainte ou déformation contrôlée, expériences de rampe et déformations de grande amplitude)[35].

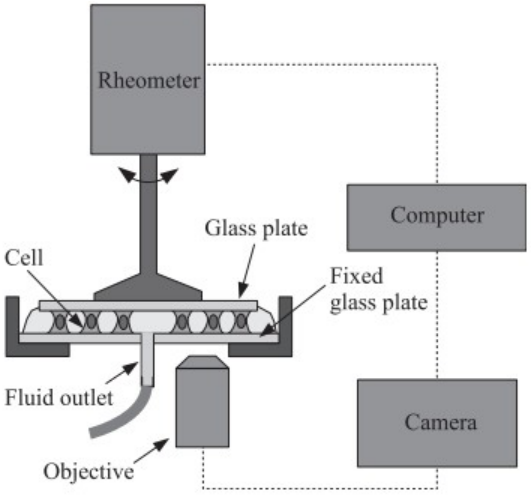

Figure 5. Principe de rhéologie de la monocouche cellulaire. L'image a été prise de[35].

La figure 5 montre que cette technique utilise un rhéomètre et, de ce fait, elle présente les inconvénients de la rhéométrie à plaques parallèles, tels que : effets de chauffage visqueux, incertitudes dans l'espace, manque de parallélisme dans les plaques et sous-remplissage de l'échantillon[34].

Étirement optique (OS)

Dans cette technique, les cellules sont déformées par deux faisceaux laser opposés non focalisés, car les forces de surface sont additives et les cellules s'étendent donc dans l'axe des faisceaux[36]. La figure 6 montre un schéma du brancard optique ; le faisceau laser est divisé en deux par un séparateur de faisceau couplé à des fibres optiques. Sur un microscope inversé, un système microfluidique est monté, les cellules passent par un canal microfluidique, et chaque fois qu'une cellule est piégée et déformée, le flux est arrêté. Cette méthode permet une analyse en série d'un grand nombre de cellules[36,37].

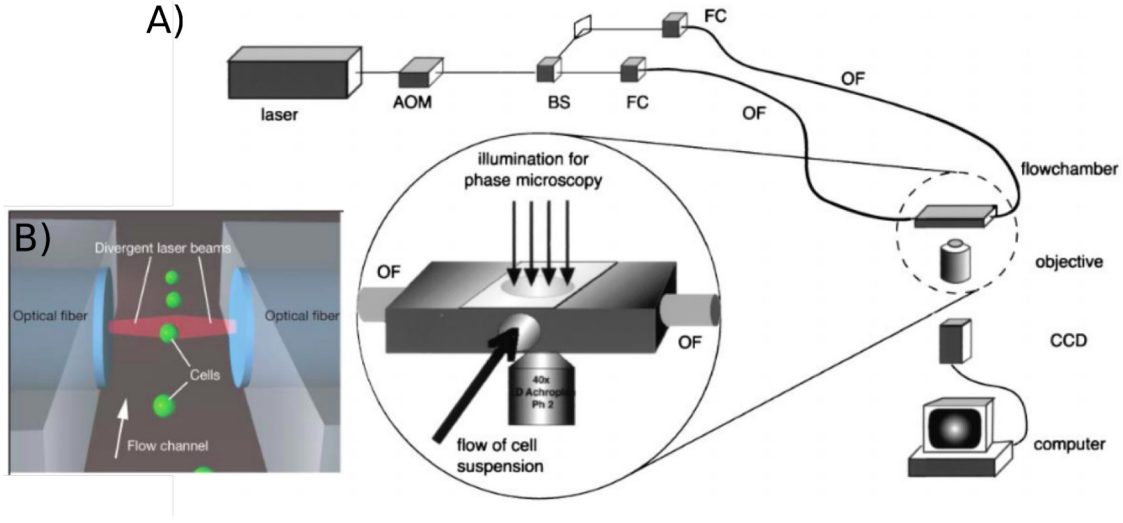

Figure 6. Schéma d'étirage optique. A) Mise en place d'un brancard optique, l'intensité du laser est contrôlée par un modulateur acousto-optique (AOM), il est ensuite divisé en deux par un séparateur de faisceau (BS), couplé à des fibres optiques (OF) en utilisant des coupleurs de fibres (FC). Les images capturées par une caméra CCD sont traitées par un ordinateur. B) Détail de la chambre d'écoulement utilisée pour aligner les extrémités des fibres et pour faire passer la cellule dans le microcanal où les cellules sont piégées et déformées. A a été pris de[36] *et B a été pris de*[31].

Actuellement, la principale limitation de la technique du brancard optique est son débit, environ une cellule par 10 s et aussi, la possibilité de réaliser sur une même cellule des analyses avec des fonctionnalités différentes[38].
Toutes les techniques présentées ont une chose en commun, elles mesurent toutes indirectement les propriétés mécaniques des cellules en utilisant le traitement d'image. Le développement d'une méthodologie qui permet à l'AFM d'atteindre un haut débit comme les techniques mentionnées précédemment pourrait donner un feedback important d'une technique capable de détecter et de mesurer directement les propriétés mécaniques des cellules de mammifères. Cependant, le développement n'est pas une tâche facile, car l'émulation du sens du toucher exige plus que la mesure elle-même, elle exige aussi une façon différente d'analyser les données.

AFM Automation

L'AFM a été développée comme un outil de recherche, ce qui implique que pour la faire fonctionner, des compétences techniques sont nécessaires. De plus, il n'est pas possible d'analyser des centaines d'échantillons en peu de temps (<1 cellule/10 min)[39], ce qui limite la signification statistique, et cela découle d'une possibilité moindre de l'utiliser pour le diagnostic. Certains travaux signalés ont été essayés pour résoudre ou surmonter le nombre limité d'échantillons qui sont analysés par un AFM conventionnel. Par exemple, Wang et.al[40] a signalé un système automatisé pour analyser les cellules de Raji. Le système identifie les cellules et leur emplacement en utilisant la reconnaissance d'images. L'identification, la localisation et la mesure des cellules se fait en 3 s par cellule. Cependant, le système a besoin de cellules de forme ronde pour être reconnu (c'est généralement le signe de cellules mourantes), de plus, le substrat de la cellule doit être complètement plat et l'agglomération des cellules doit être évitée car le système ne retire pas la pointe de l'échantillon. Finalement, les auteurs rapportent seulement un test avec 4 cellules par zone de balayage.
Roy et.al[41] a fait état d'une méthodologie différente pour l'analyse des tissus. Ils ont développé un système qui aligne automatiquement la sonde AFM avec un tissu d'intérêt en utilisant le traitement d'image, ils ont pu obtenir dans une zone de 80 µm x 150 µm jusqu'à 480 courbes de force en ~80 min. Une autre approche rapportée par Favre et.al[42] montre un AFM contrôlant un ensemble de cantilevers, l'objectif de leur mise en place est d'acquérir en même temps plusieurs images (ou d'autres études) de différentes régions de l'échantillon. Cependant, le système n'a pas été testé avec des échantillons biologiques et pour le mettre en œuvre sur une population cellulaire, les matrices en porte-à-faux doivent être fabriquées en fonction des dimensions des matrices cellulaires.
Un autre exemple qui utilise le parallélisme des GFA, a été rapporté par Sadeghian et.al[43], leur système a miniaturisé 44 AFM dans une zone de 450 mm (zone de type wafer). Les AFM miniaturisés sont capables d'effectuer des analyses individuelles sur l'échantillon. L'essai du système a été effectué en imitant des nanoparticules d'or colloïdal (10 nm de diamètre) déposées sur du mica. Le système améliore le temps passé dans l'analyse de l'échantillon. Cependant, la localisation des régions d'intérêt est faite manuellement et pour adapter cette méthodologie à la population de cellules, les matrices de cellules doivent être fabriquées pour correspondre aux positions des AFM.
Les œuvres listées ne considèrent pas l'apport automatique de nouvelles cellules dans le champ de vision, c'est une caractéristique importante à considérer car elle consomme beaucoup de temps.

Antoine Dujardin et.al[44] ont rapporté une procédure automatisée similaire à la méthodologie présentée dans ce travail de thèse, ils ont utilisé un AFM pour obtenir des images sur les procaryotes. Ils ont utilisé un script python implémenté dans un AFM Dimension Fast Scan-Bio (Bruker, Santa Barbara, CA, USA) pour aller automatiquement de cellule en cellule et en obtenir des images. Leur système commence par faire une image du volume de force pour identifier les bioéléments dans chaque puits. Cette image a été utilisée pour déterminer les positions des bactéries (en fonction de leur hauteur), puis des images fermées (2x2 µm2 de surface) de supposées cellules seulement ont été réalisées. Cependant, ce processus prend un temps considérable pour réaligner le photodétecteur et effectuer l'engagement. Le système a été testé avec des bactéries fixes *Yersinia pseudotuberculosis* et vivantes *Mycobacterium bovis* BCG et ils rapportent l'analyse de 501 zones en 8 h 35 min. Enfin, les images rapportées sont des signaux d'erreur de hauteur et de force de crête qui écartent la possibilité d'effectuer une analyse mécanique sur les bactéries analysées.
Mon travail de thèse de doctorat a été consacré au développement d'une méthodologie automatisée originale, précédemment soumise comme brevet[45] pour mesurer les propriétés mécaniques des cellules. La méthodologie combine un algorithme de copyright développé[46] exécuté comme un script sur les AFM commerciales avec une stratégie intelligente d'immobilisation des cellules. Le script déplace automatiquement la pointe de cellule en cellule pour enregistrer les courbes de force de chaque cellule d'une population cellulaire. Les cellules sont immobilisées à des endroits connus dans des micropuits d'un tampon PDMS microfabriqué[47] ou en utilisant des réseaux de cellules de mammifères prédéfinis (BIOSOFT®, CYTOO®). Une fois que la pointe a balayé toutes les cellules de la zone de balayage, une étape motrice se déplace automatiquement et amène un nouveau réseau de cellules dans la zone de balayage pour relancer la méthodologie.
Le système a été testé sur des eucaryotes *C. albicans* parce qu'ils sont connus comme des levures pathogènes opportunistes, ce qui représente l'une des principales infections nosocomiales, et aussi sur des cellules HeLa largement étudiées dans le monde entier. Nous avons décidé de comparer des cellules de *C. albicans* natives avec des cellules de *C. albicans* traitées à la caspofongine. La caspofungine est un antifongique de dernière génération de la classe des échinocandines, connu pour modifier les propriétés mécaniques de la paroi cellulaire de la levure[48]. Dans notre test, la méthodologie automatisée prend un temps moyen de 12 secondes pour réaliser 9 nanoindentations par cellule et par micropuits, ce qui donne un grand nombre de courbes de force qui se situent entre 8 000 et 9 000 en 4 h, fournissant une méthode pour des mesures à haut débit d'une population de cellules. Ce processus automatisé peut être considéré comme la première étape d'un futur outil de diagnostic viable[45]. Grâce à ce développement, nous présentons pour la première fois les propriétés mécaniques d'une population cellulaire (800-900 cellules) mesurées par l'AFM, en soulignant que les propriétés mécaniques au sein de la population cellulaire ne sont pas homogènes et peuvent expliquer les résultats contradictoires de la littérature. Pour les cellules HeLa, une preuve de concept est présentée (en utilisant des cellules vivantes contre des cellules HeLa fixes). Environ 80 cellules HeLa ont été analysées en 30 minutes. La preuve de concept permet de réaliser le potentiel de la méthodologie, appliquée aux expériences sur les populations de cellules de mammifères.

Justification, hypothèse

L'AFM est l'une des techniques les plus utilisées pour obtenir les propriétés mécaniques des cellules. Cependant, elle a été conçue comme un outil de recherche confiné aux laboratoires

universitaires. C'est dans le milieu universitaire que des chercheurs comme Cross et al.[12] ont signalé l'utilisation de propriétés nanomécaniques pour identifier les cellules cancéreuses. L'une des principales limites qui empêchent l'utilisation de l'AFM pour le diagnostic est le nombre limité d'échantillons qui peuvent être analysés. En statistique, des formules comme Cochran[49] ou Yamane[50] aident à déterminer une taille d'échantillon statistiquement significative. Cependant, il est nécessaire d'avoir accès à l'écart-type de la population ou à la taille de la population. Certains documents que l'on peut trouver dans la littérature[48,51] rapportent certaines valeurs basées sur une taille d'échantillon minimale (<10 cellules), ce qui les rend peu fiables en ce qui concerne la signification statistique de la population. Ce travail vise à changer la façon dont l'AFM analyse les cellules, afin qu'il soit possible d'évaluer les populations cellulaires et d'obtenir une signification statistique. De plus, ce travail donne la possibilité de tester et d'améliorer les technologies actuelles de réseaux de cellules (réseaux de cellules de mammifères microfabriquées), d'immobilisation et de GFA en adaptant des étapes spécifiques à ces technologies pour l'analyse d'échantillons massifs.

Hypothèse

La première hypothèse de ce travail de thèse est que l'automatisation du déplacement entre les cellules, peut rendre le processus plus rapide et permet d'analyser beaucoup plus de cellules.
La seconde hypothèse est que seules quelques mesures (courbes de force) par cellules sont nécessaires pour décrire correctement le comportement général de la cellule.
Ces deux hypothèses nous poussent à remettre en question le paradigme habituel des mesures de l'AFM en biologie. Habituellement, quelques cellules sont analysées et des milliers de courbes de force sont enregistrées, par cellule. Ces informations sont précieuses à l'échelle d'une cellule mais ne donnent aucune information à l'échelle de la population. Une question très fréquente des biologistes est la fiabilité statistique des résultats, dans le contexte d'une population hétérogène.
Le nouveau paradigme qui découle de notre hypothèse est donc d'analyser des centaines de cellules, et de n'effectuer que quelques mesures sur chaque cellule.

Objectifs

Généralités

L'objectif principal est de développer un AFM automatisé pour augmenter le nombre de cellules analysées en peu de temps. Ce développement est basé sur une stratégie intelligente d'immobilisation des cellules et sur l'utilisation d'un AFM commercial. De plus, l'énorme quantité de données (courbes de force) va être analysée avec de nouvelles techniques comme l'apprentissage automatique. La quantité de données générées pourrait nous donner une signification statistique.

Spécifique

Pour atteindre l'objectif général, j'ai dû fixer plusieurs objectifs secondaires qui sont énumérés ci-dessous :

- Atteindre un taux de remplissage élevé et reproductible (supérieur à 80 %), des timbres PDMS
- Développer un script pour permettre l'acquisition automatisée des mesures de force AFM.
- Atteindre un nombre élevé (~1000) de cellules analysées dans un court laps de temps (~4 h).

- Effectuer différents essais avec un nombre différent de mesures mécaniques (9, 16) par cellule pour déterminer si une différence appréciable peut être observée dans l'analyse statistique.
- Comparer les propriétés mécaniques rapportées des cellules de levure et de mammifères à celles obtenues avec cette méthodologie.
- Comparer et analyser deux technologies de matrices de mammifères (BIOSOFT et CYTOO) pour déterminer la viabilité à employer dans la méthodologie développée dans ce travail de thèse.

Résultats

Comme la méthodologie présentée dans ce travail peut être appliquée à une variété d'échantillons, les résultats ont été classés en trois catégories : C. albicans, cellules HeLa et Glycan et résultats des réseaux de matériel. De plus, cette méthodologie nous permet d'obtenir un nombre élevé de courbes de force par expérience, ce qui permet d'interagir avec de grandes données et ensuite d'apprendre par machine.

Candida albicans

Réseaux de cellules et immobilisation

Les C. albicans ont été immobilisés sur des timbres PDMS préfabriqués ; le dessin des timbres est illustré à la figure 7. Les micropuits ont été conçus en plusieurs dimensions (allant de 1,5 µm x 1,5 µm à 6 µm x 6 µm) ; chaque dimension couvre une surface de 1 mm x 1 mm carré (L sur la figure 7). Cependant, des résultats optimaux ont été obtenus avec des puits de 4,5 µm. La profondeur des puits était de ~4 µm. Les détails de la fabrication des tampons PDMS, l'immobilisation des cellules et les détails des algorithmes (tels que la taille des régions d'indentation, la recherche des micropuits et le mouvement à travers le tampon PDMS) sont présentés au chapitre 3 Matériaux et méthodes.

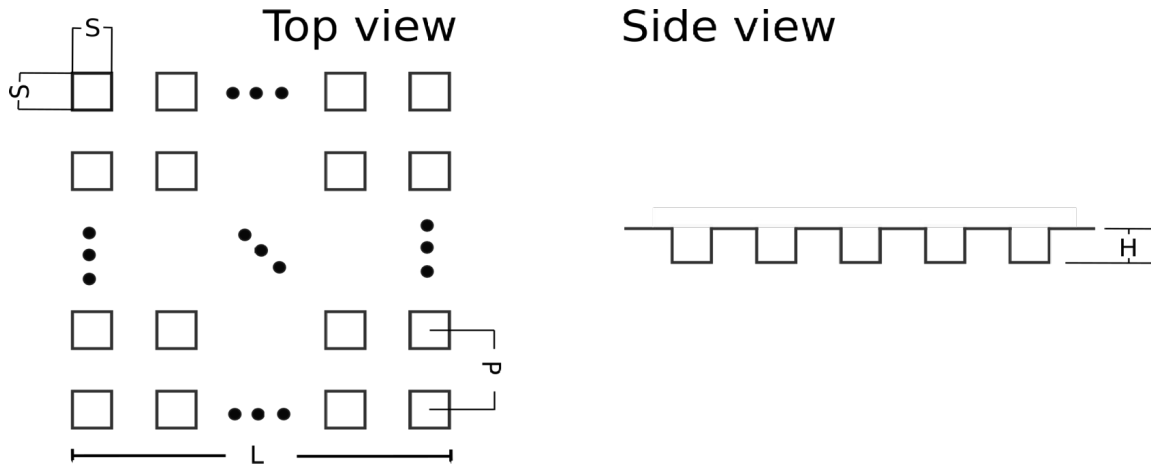

Figure 7. Conception des timbres PDMS. Chaque carré représente un puits microfabriqué S = 4,5 µm, la distance entre les puits est P = 9 µm - 10 µm. L = 1mm est la longueur totale couverte par les micropuits et H est la hauteur des micropuits qui est de ~4 µm.

L'immobilisation des cellules de C. albicans a été effectuée conformément aux travaux publiés par Formosa et al.[47] avec quelques modifications, en bref, une fois que le PDMS a été retiré du moule maître, une gouttelette du surnageant est déposée sur le tampon PDMS (suffisamment pour couvrir la surface) pendant environ 40 minutes, puis elle est remplacée par une gouttelette de la culture cellulaire et laissée au repos pendant 15 minutes, enfin par assemblage convectif/capillaire manuel les cellules sont traînées dans les puits. La figure 8 compare un tampon vide avec un tampon rempli de cellules, avec les modifications de la procédure originale rapportées sur le même papier, nous avons obtenu un taux de remplissage de 85 %, de façon répétitive.

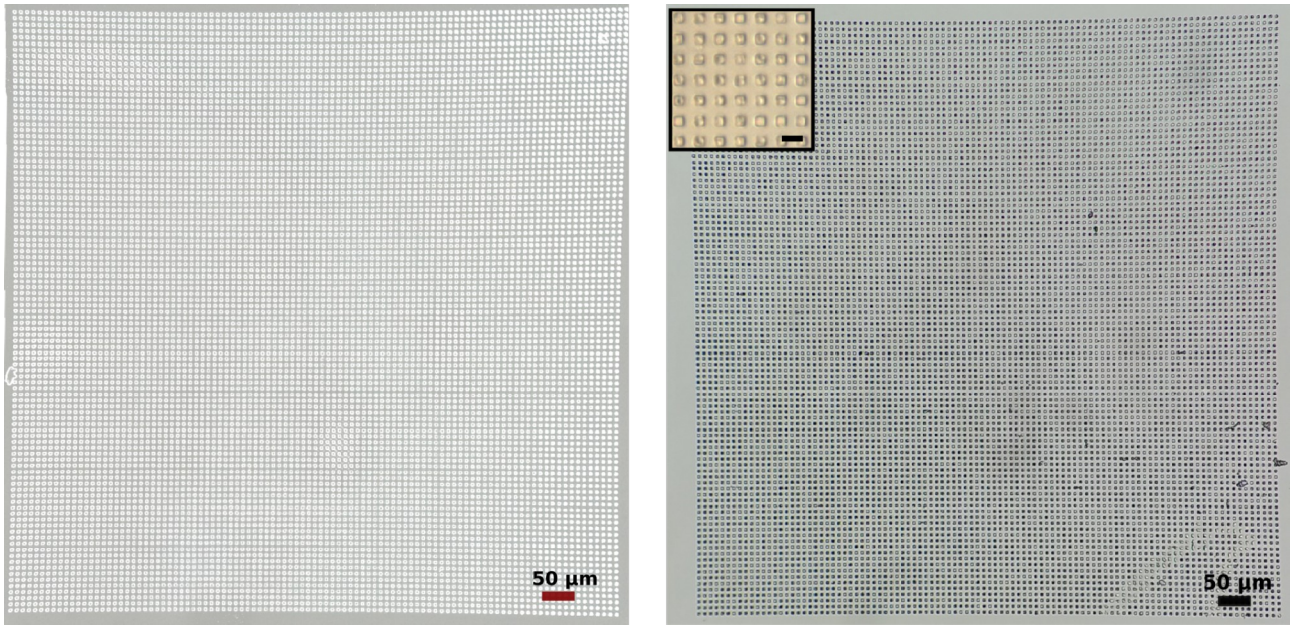

Figure 8. Images optiques des timbres PDMS. La gauche montre un timbre PDMS vide tandis que la droite montre le timbre PDMS après la technique d'assemblage convectif/capillaire. Inlet montre une image enregistrée avec la caméra optique de l'AFM (la barre d'échelle est de 10 µm). La surface couverte par les motifs est de 1mm x 1 mm. Taux de remplissage ~85 %.

Exécution de l'algorithme

La figure 9 montre les images optiques capturées à des moments précis de l'exécution du script. La description de l'algorithme est présentée au chapitre 3 Matériels et méthodes. Elle illustre la segmentation de l'échantillon en différentes zones de balayage (9A et 9B) effectuée pour maximiser le nombre de cellules analysées. Une fois la pointe positionnée sur un micropuits, 9 ou 16 indentations sont réalisées (9D). 9 et 16 indentations par puits ont été essayées pour garantir des mesures sur différentes parties de la cellule. Les mesures sont effectuées sur chaque micropuits (9C) à l'intérieur de la zone de balayage. Chaque fois que la pointe se déplace d'un micropuits à l'autre, elle est rétractée et approchée du centre du micropuits. Une fois que tous les micropuits ont été visités, la pointe est rétractée et déplacée vers le premier micropuits. La platine est alors activée pour déplacer l'échantillon et apporter de nouvelles cellules pour l'analyse. Ce processus est répété jusqu'à ce que toutes les zones de balayage (calculées au début de l'exécution) aient été visitées.

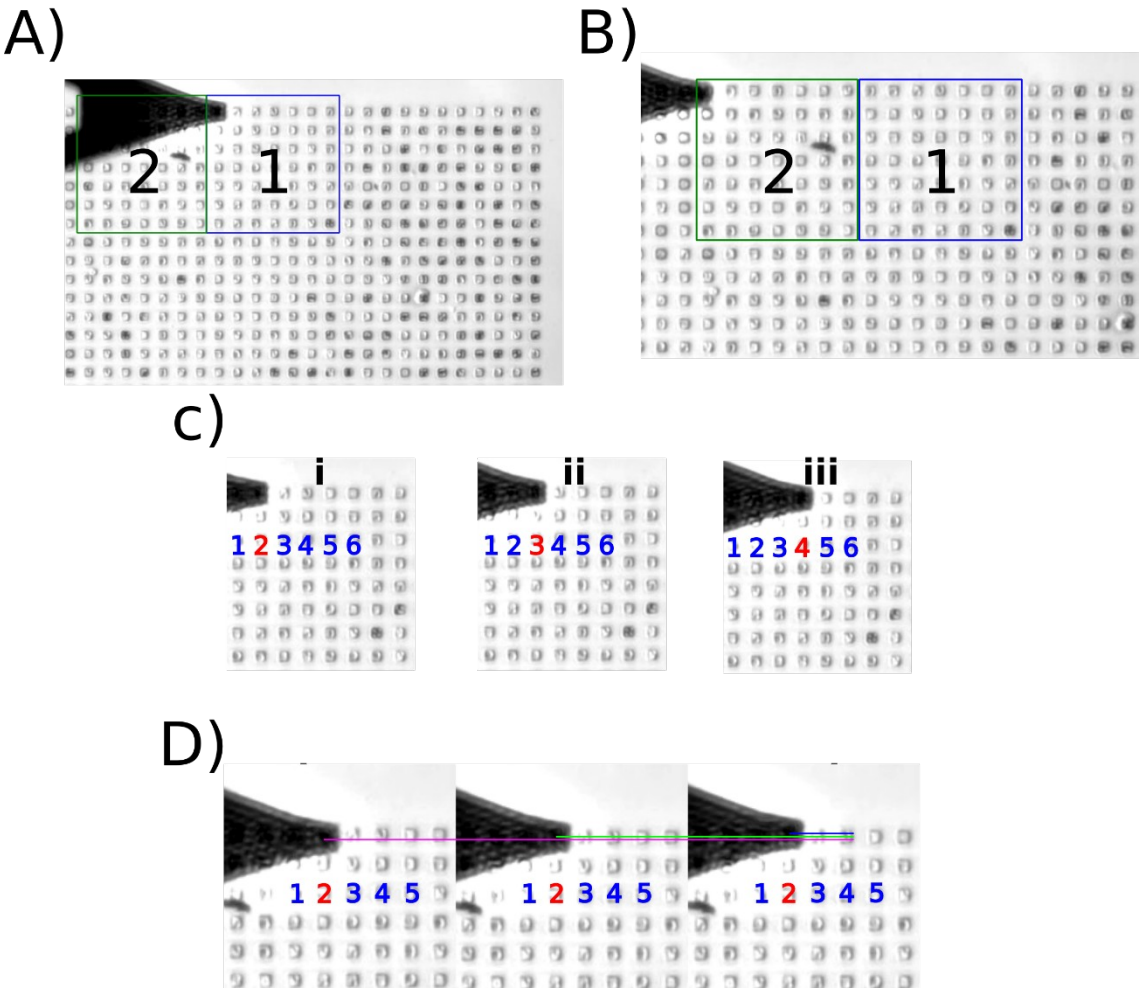

Figure 9. Exécution de scripts sur des cellules de levure. Images optiques prises à des moments précis pendant l'exécution du script. A) Emplacement du centre du premier micropuits dans la zone de balayage actuelle. B) Position de la pointe après le déplacement de la platine moteur, la zone 2 est la zone de balayage active à ce moment. C) Montre l'acquisition de données à travers différents micropuits (i-iii). D) Montre l'acquisition de données à l'intérieur d'un micropuits, l'indentation est réalisée dans différentes zones du même micropuits (magenta/vert/bleu).

Analyse statistique

Quatre expériences ont été menées pour établir la répétabilité et la fiabilité des résultats. Les cellules natives et les cellules traitées à la caspofongine ont été préparées indépendamment, comme mentionné dans le chapitre sur les matériaux et la méthode, et immobilisées le jour de leur utilisation. La décision d'utiliser la caspofongine est due au fait que son action sur la paroi cellulaire de la levure est encore en débat[48,51]. Après l'exécution du script, 1021 cellules ont été analysées pour la première expérience (cellules natives), 957 cellules pour la deuxième expérience (cellules natives), 1000 cellules pour la troisième (caspofungine) et 574 cellules pour la quatrième expérience (caspofungine). Pour les expériences 1 et 3, 16 indentations par cellules ont été prises, tandis que pour les expériences 2 et 4, 9 nanoindentations ont été prises.

Les expériences 1, 2, 3 et 4 sont des duplications indépendantes. Les cultures cellulaires étaient indépendantes et n'ont pas été effectuées le même jour. Quatre expériences ont été réalisées, dont

deux (expériences 1 et 2) avec des cellules natives et deux (expériences 3 et 4) avec des cellules traitées à la caspofongine. L'objectif de ce montage était d'obtenir un nombre comparable de cellules analysées (pour les cellules natives et traitées) et de déterminer le nombre maximum de cellules analysées dans un temps fixe (4 h).
Les courbes de force obtenues ont été analysées à l'aide du logiciel de traitement de données JPK, sur la base des travaux publiés par El-Kirat-Chatel51 . Nous avons extrait la constante élastique de la cellule de toutes les courbes de force. Cependant, le taux de remplissage du tampon PDMS n'est pas de 100 % (en réalité ~86 %). Le chapitre 2 présente la méthodologie utilisée pour l'analyse des courbes et explique comment la séparation entre les courbes de force des cellules et les courbes qui ne correspondent pas aux cellules (PDMS) a été effectuée. Le filtre des courbes de force était le suivant :

- Le point de contact est utilisé pour déterminer si les courbes de force sont à partir du fond du puits, donc toutes les courbes avec une valeur de point de contact inférieure à 4,15 µm sont rejetées.
- Les courbes ayant une pente négative sont rejetées.
- L'hypothèse selon laquelle la constante de ressort de la cellule devrait être inférieure à celle du PDMS mesuré à 150 pN/nm a été faite. Par conséquent, toutes les courbes de force donnant une constante de ressort supérieure à 150 pN/nm ont été rejetées.

Conformément aux critères précédents, le tableau 1 présente le nombre de cellules analysées, le nombre de courbes de force rejetées et le temps nécessaire pour analyser chaque puits.

Tableau 1. Résumé de l'information tirée des expériences.

	Expriment	Force Curves	Wells analyse	Cells analyse	Time per well(s)	Discorde force curves (%)
Native cells	1	15927	1021	1021	9	4.31
	2	8620	959	957	12	12.87
Treated cells	3	15457	1018	1000	9	8.19
	4	5180	579	574	12	20.88

La figure 10 présente les histogrammes de rigidité (constante de printemps) des cellules de C. albicans en conditions naturelles (A et B) et traitées à la caspofongine (C et D). 10A et 10B (à gauche) montrent les histogrammes de rigidité, le nombre de cellules analysées dans les deux premières expériences était de 1021 et 959, respectivement ; les deux sont obtenues en analysant indépendamment les cellules natives cultivées. En analysant les deux histogrammes avec la méthode des moyennes k, ils ont été déconvolués en 2 populations qui sont légèrement différentes dans les 2 expériences. La première population a une constante de printemps moyenne de 21 ±6 pN/nm (expérience 1) et 30 ±13 pN/nm (expérience 2) tandis que l'autre population a une constante de printemps de 48 ±9 pN/nm (expérience 1) et 80 ±18 pN/nm (expérience 2). Pour les expériences 3 et 4 (figures 10C et 10D, à gauche), 1018 et 579 cellules ont été analysées selon la littérature51 , les cellules traitées présentent un ramollissement de la paroi cellulaire en raison du traitement à la caspofongine. Ce changement est visible dans la figure 10, qui compare les expériences 1 et 3.

La crête présente à 21 pN/nm (10A, gauche) passe à 13 pN/nm (10C, gauche) et la crête à 48 pN/nm passe à 42 pN/nm. Pour les expériences 2 et 4 (10B et 10D, à gauche respectivement), la crête présente à 30 pN/nm passe à 15 pN/nm et la crête à 80 pN/nm passe à 52 pN/nm. Les figures 10E et 10F montrent l'essai d'ANOVA unidirectionnel, 10E-gauche a été obtenu en comparant les données de rigidité 10A et 10C, réduisant les deux ensembles à 1018 cellules, tandis que 10F-gauche a été obtenu en comparant les données de rigidité 10B et 10D, réduisant les deux ensembles à 579. Le test unidirectionnel est utilisé pour comparer les résultats des cellules natives aux cellules traitées en obtenant un p<0,001 (représenté par ***).

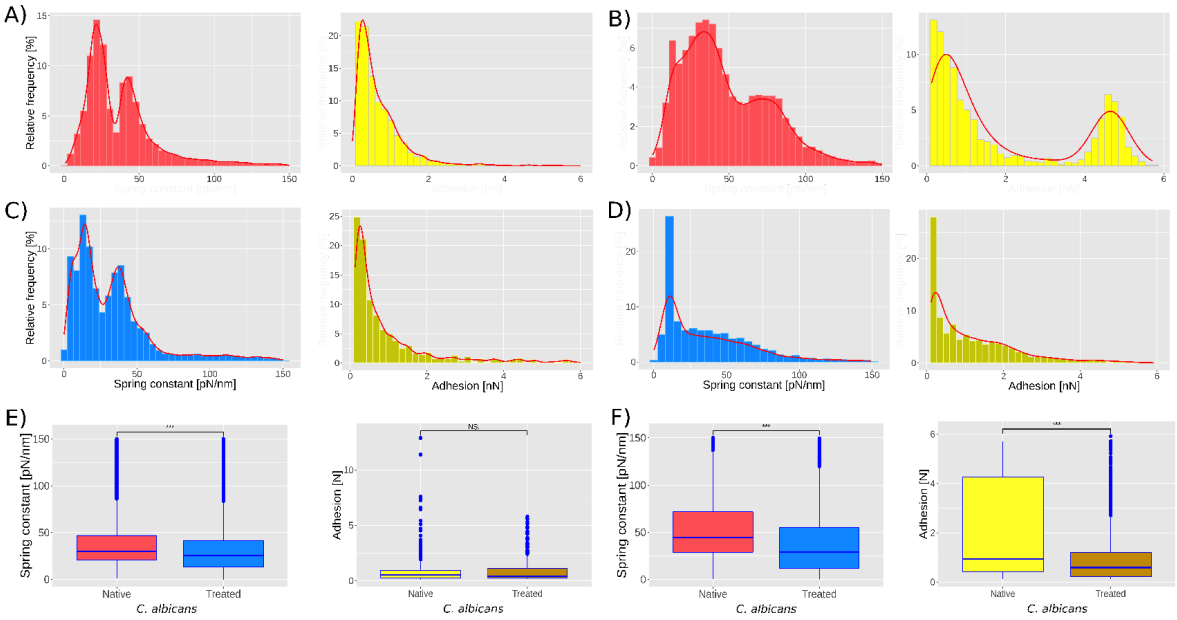

*Figure 10. Histogrammes des constantes de printemps pour C. albicans, natif et traité à la caspofungine. A et B (à gauche) montrent les histogrammes de la constante de printemps pour les expériences 1 et 2 des cellules de C. albicans natif (1021 et 959 cellules analysées respectivement). Alors que C et D (à gauche) montrent les histogrammes de la constante de printemps pour les expériences 3 et 4 de cellules de C. albicans traitées (1018 et 579 cellules analysées respectivement). A et B (à droite) montrent les résultats obtenus par l'analyse d'adhésion des expériences 1 et 2. C et D montrent les résultats de l'analyse d'adhésion pour les expériences 3 et 4. E et F montrent l'essai d'ANOVA unidirectionnelle réalisé en utilisant la constante de rappel et les données d'adhésion des expériences 1-3 et 2-4 respectivement. *** = valeur p < 0,001, NS = aucune différence significative. La largeur du bac a été déterminée par la règle de Freedman-Diaconis.*

La figure 10A (à droite) montre que la force d'adhésion entre la pointe nue et la cellule native était de 0,64 ±0,6 nN dans la première expérience, alors que dans la deuxième expérience, toujours sur des cellules natives, 2 sous-populations ont été trouvées : la première a une force d'adhésion moyenne de 0,7±1,4 nN alors que la seconde est de 4,5±1,5 nN. Le traitement à la caspofongine n'a pas d'effet significatif sur l'adhérence si l'on considère les expériences 1 et 3 (test ANOVA unidirectionnel, la figure E droite ne montre pas de différence significative) ; il semble que la caspofongine induit une diminution de l'adhérence à la pointe et une réduction de l'hétérogénéité de l'adhérence de la population.

Cellules HeLa

Réseaux de cellules et immobilisation

Pour les cellules HeLa, nous avons utilisé deux marques différentes de matrices de cellules BIOSOFT et CYTOO. Cependant, l'immobilisation d'une seule cellule s'est avérée difficile car il a été difficile d'obtenir quelque chose de similaire aux timbres PDMS (figure 8, à droite). Nous avons rencontré au moins deux problèmes : premièrement, le taux de remplissage obtenu avec le protocole standard n'est que de 20-25% et deuxièmement, beaucoup de positions n'étaient pas occupées par des cellules individuelles. Une étape d'optimisation de l'immobilisation sera donc nécessaire pour poursuivre dans cette direction.

Malgré ces difficultés, nous avons pu faire la preuve du concept. En utilisant les matrices BIOSOFT et notre script, adapté à un déplacement plus important, il a été possible d'enregistrer des courbes de force sur au moins 80 cellules de mammifères en une heure. Cela représente déjà un changement par rapport aux expériences standard de l'AFM Bio. Les résultats sur l'immobilisation HeLa sont présentés au chapitre 3 Matériels et méthodes.

Exécution de l'algorithme

La figure 11 montre les résultats de l'immobilisation des puces BIOSOFT (11A). Les images ont été prises à des moments précis afin de montrer comment la pointe passe d'un groupe de cellules à un autre (11B) et les différentes indentations (vert / bleu / magenta) sur la position de chaque groupe de cellules (11C). Pour les indentations individuelles, nous avons défini une petite région carrée de 5 µm x 5 µm qui simule la région d'indentation utilisée dans les cellules de C. albicans.

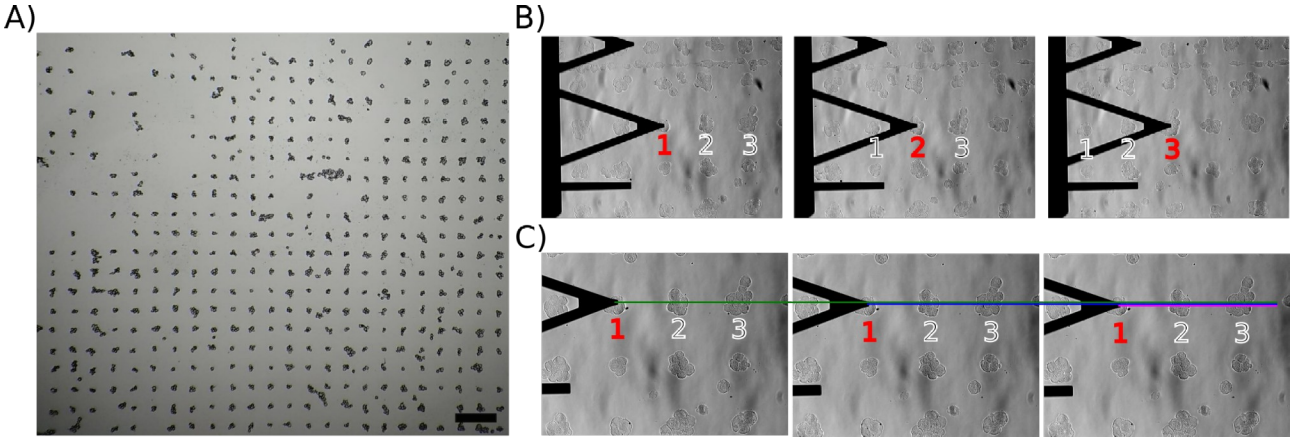

Figure 11. Images optiques des réseaux de cellules BIOSOFT. A) Les résultats de l'immobilisation, sur chaque spot, permettent de voir des petits groupes de cellules (clusters de cellules), la barre est de 250 µm. B) Montre le mouvement de la pointe d'une cellule à l'autre. C) montre les trois premières positions d'indentation (vert / bleu / magenta) sur la première cellule.

Analyse statistique

Deux expériences ont été réalisées, l'une avec des cellules HeLa natives et l'autre avec des cellules HeLa fixes. L'objectif des deux expériences était de pouvoir obtenir un nombre élevé de cellules mesurées en peu de temps. Neuf indentations ont été réalisées sur chaque cellule (~6 secondes par cellule), permettant d'obtenir des mesures de 80 cellules natives et 70 cellules fixes en ~28 minutes. La figure 12 montre les histogrammes du module d'Young (élasticité) extraits à l'aide du logiciel

JPK Data Processing. La figure 12A montre les résultats d'élasticité pour les cellules HeLa natives et la figure 12B montre les résultats d'élasticité pour les cellules fixes, les résultats montrent, comme prévu, que les cellules fixes présentent un incrément du module d'Young (125 - 1000 kPa) avec une valeur moyenne de 435 ±203 kPa. Par rapport aux cellules natives (2,5 - 30 kPa) avec une valeur moyenne de 6,2 ± 5 kPa.

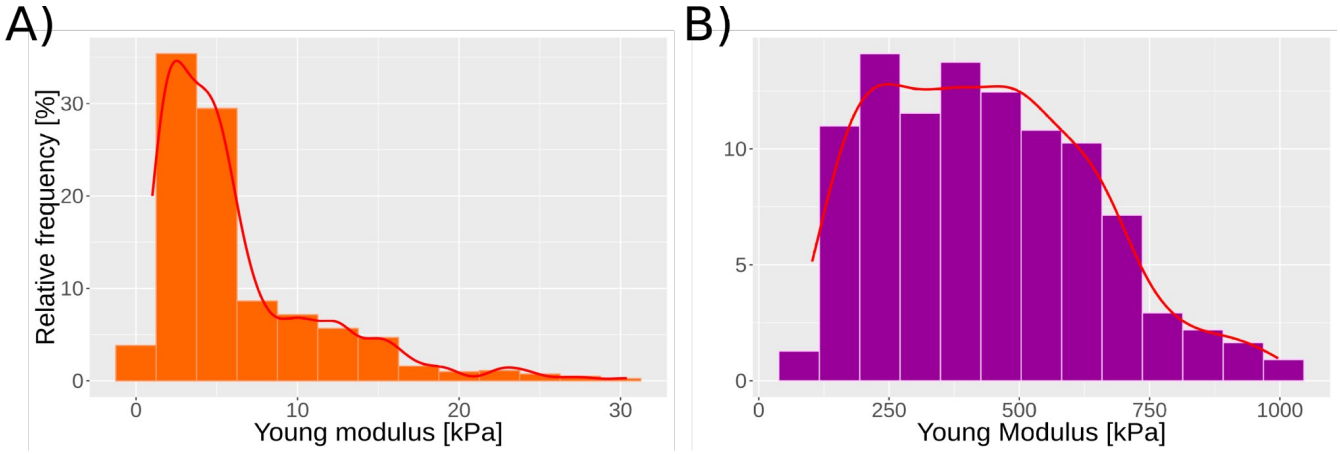

Figure 12. Histogrammes du module jeune des cellules HeLa natives et fixes. A) montrent l'histogramme du module de Young pour les cellules HeLa natives (80 cellules analysées). B) présentez l'histogramme du module de Young pour les cellules HeLa fixées (70 cellules analysées).

Glycanes et réseaux de matériaux

Les RayBio Glycan Array 300 ont été acquis, ces puces ont différents types de glycocalyx (environnement de revêtement polymère extracellulaire présenté dans les cellules procaryotes et eucaryotes) immobilisés à des régions circulaires spécifiques sur une lame de verre. Les points où les glycanes sont immobilisées sont séparés de 400 µm. Les spots sont répartis en 34 rangées par 27 colonnes, et pour aligner l'orientation de la lame de verre sur le mouvement de la platine moteur, les spots témoins positifs (POS1 et POS2) ont été utilisés. Il est important de noter que ces glycans sont destinés à la microscopie fluorescente, et qu'ils comportent une erreur sur la position des spots. Cette erreur est significative (>200 µm), et c'est un paramètre important à considérer lors du développement de l'algorithme pour déplacer le cantilever et mesurer l'adhésion sur les spots automatiquement. La position des points est prise en compte lors de l'étiquetage des mesures pour identifier à quel glycan les mesures correspondent. Il est possible d'implémenter le script développé pour les réseaux de glycanes à mesurer sur différents matériaux (par exemple, en utilisant SCFS sur un réseau de matériaux).

Analyse de la courbe de force

Le nombre de courbes de force obtenues par l'application de notre méthodologie automatisée était d'environ 45000 courbes de force, c'est un nombre important et il n'est pas si facile de les analyser manuellement, à cause de cela nous avons développé un script en python pour que l'analyse puisse être automatisée. Le processus en général est le suivant : pour convertir tous les fichiers jpk-force en fichiers txt, sur les fichiers txt les colonnes nommées "Vertical Deflection" et "Head hight (measured & smoothed)" ont été sélectionnées. La figure 13 montre le traitement appliqué aux données sélectionnées :

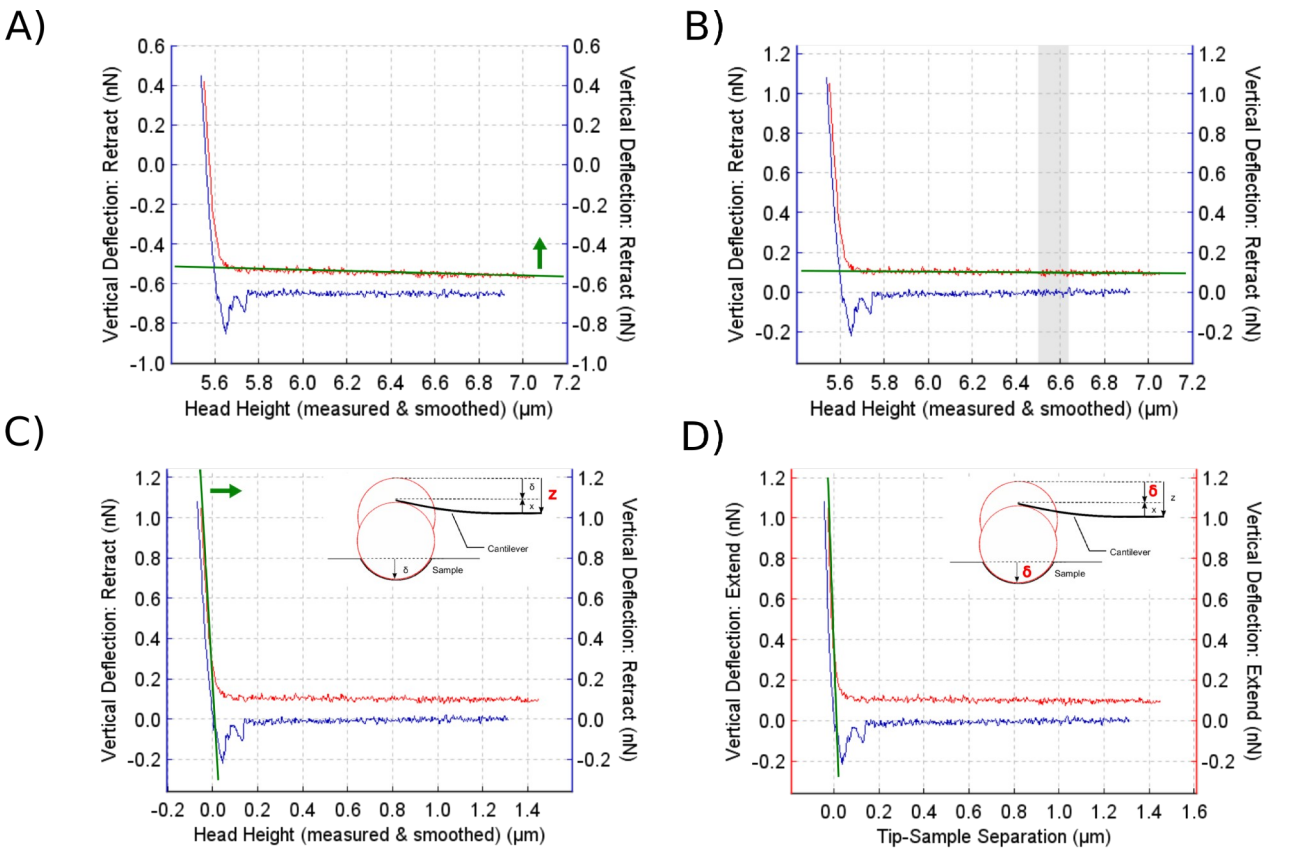

Figure 13. Traitement des données des courbes de force. La courbe rouge est la courbe d'approche et la courbe bleue est la courbe de retrait. A) montre l'inclinaison sur les courbes de force, la ligne verte aide à voir l'inclinaison sur les courbes et la flèche verte aide à voir la direction dans laquelle la correction sera faite. B) l'inclinaison de la courbe de force corrigée, la zone grise montre la partie des données utilisées pour calculer un ajustement linéaire qui est utilisé pour la correction. C) montre l'indentation totale sur l'échantillon (z) et la flèche verte indique la direction dans laquelle les courbes seront corrigées. D) montre l'indentation réelle sur l'échantillon (δ), après cette correction les courbes de force sont prêtes à extraire les caractéristiques mécaniques.

Une fois les courbes traitées, il est possible de calculer la rigidité et la force d'adhérence maximale. Il est important de noter que toutes les courbes utilisées pour le calcul de la rigidité ne peuvent pas être utilisées pour obtenir la force d'adhérence maximale, la figure 14 montre quelques exemples de courbes de force qui sont rejetées dans l'analyse de la force d'adhérence maximale. Le script est capable de traiter ce type de courbes et de les omettre de l'analyse. L'omission se fait en considérant les valeurs de la courbe d'extension, comme le montre la figure 13 : la courbe d'extension (courbe rouge) est au-dessus de zéro (voir Axe de déviation verticale), sur les mauvaises courbes cela ne se produit pas. Une autre caractéristique prise en compte pour l'omission est une courbe de force de rétraction coupée. La figure 14B montre la courbe de coupe, le programme analyse la courbe et détermine que le point minimum (qui représente la force d'adhérence maximale) se répète plusieurs fois et en utilisant cette information, la courbe est rejetée. Pour la figure 14C, les deux procédures énumérées ci-dessus permettent d'éliminer ce type de courbe de force.

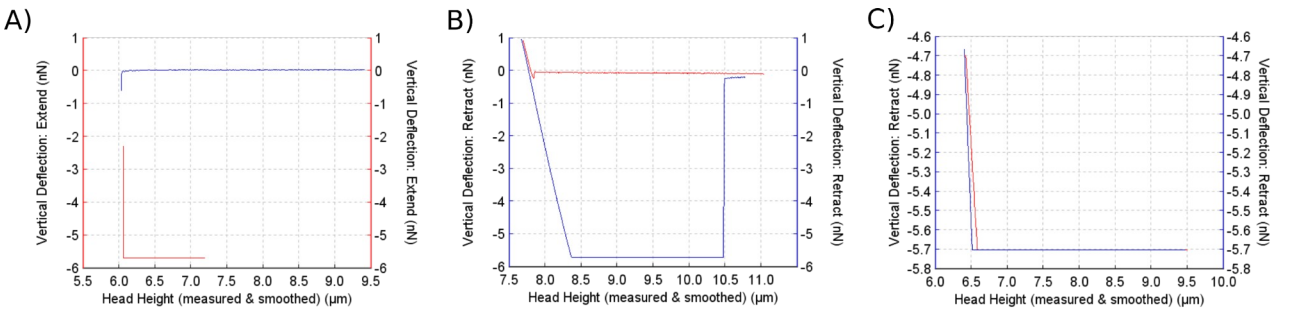

Figure 14. Exemples de courbes de force rejetées dans l'analyse de la force d'adhérence maximale. La courbe rouge est la courbe d'approche et la courbe bleue est la courbe de retrait.

Enfin, le programme est capable d'obtenir la force d'adhérence maximale de 8000 courbes de force en 3 minutes environ (2 h s'il doit tracer et enregistrer les images de chaque courbe de force). Avec cet outil, il est possible d'analyser rapidement l'énorme quantité de données (comme celle obtenue avec la méthodologie présentée ici) par rapport à une analyse manuelle, qui prendrait environ 8h. La description complète de l'algorithme peut être consultée dans le chapitre 3 Matériels et méthodes.

Analyse de l'apprentissage machine

L'apprentissage machine peut être défini comme l'application de méthodes statistiques pour détecter des modèles à partir d'ensembles de données spécifiques et ensuite utiliser les modèles découverts pour prédire les données futures ou prendre d'autres types de décisions en cas d'incertitude[52,53]. L'apprentissage machine est divisé en deux types, supervisé et non supervisé. L'apprentissage supervisé (aussi appelé prédictif) utilise un ensemble de formation ; l'ensemble de formation est étiqueté (comme la taille ou le poids d'une personne). Chaque classe ou type dans l'ensemble de formation est appelé caractéristiques, attributs ou covariables[52]. L'objectif est d'utiliser l'ensemble de formation pour trouver des modèles et ensuite appliquer ces connaissances dans un nouvel ensemble de données et le classer. Le deuxième type d'apprentissage machine est le type non supervisé (aussi appelé descriptif)[52]. Il utilise un ensemble de formation non étiqueté ; c'est ce qu'on appelle parfois la découverte de connaissances et c'est un problème moins bien défini parce qu'on ne dit pas à la machine quel type de motifs il faut regarder.

Dans ce travail de thèse, l'analyse de l'apprentissage machine a été faite en collaboration avec le Dr Marie Véronique Le Lann. Le Dr Le Lann a assigné un de ses étudiants à notre projet, et il a utilisé l'outil P3S pour l'analyse, qui est un logiciel développé par le Laboratoire d'Analyse et d'Architecture des Systèmes (LAAS). Il utilise trois algorithmes (binomial flou, centré flou et gaussien normal). Pour l'ensemble d'entraînement, 80 % des données (respectivement natives et traitées) ont été utilisées, et les 20 % restants ont été utilisés pour le test. Les algorithmes d'apprentissage machine utilisés étaient du type supervisé. La figure 15 montre les attributs utilisés pour l'apprentissage, la rigidité, l'adhérence et le travail d'adhérence. La figure 15A montre une courbe de force, pour calculer la rigidité un ajustement linéaire est fait à la courbe de rétraction, l'ajustement linéaire est fait seulement dans les premiers 150 pN/nm (c'est parce que la rigidité montrée dans les histogrammes de la figure 10 est obtenue de cette façon). Les figures 15B et 15C montrent l'adhérence maximale et le travail d'adhérence, respectivement.

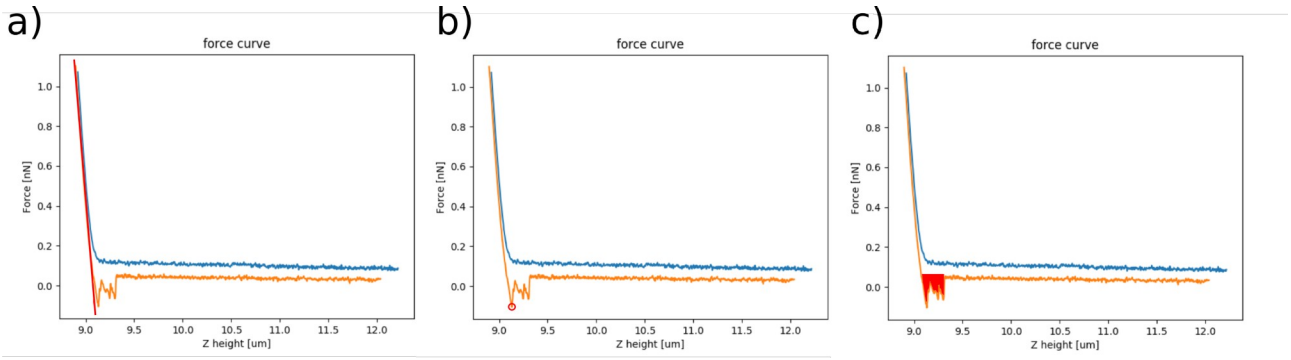

Figure 15. Analyse des propriétés mécaniques des courbes de force. a) Montre l'ajustement linéaire fait à la courbe de rétraction (orange) en prenant seulement les premiers 150 pN/nm. b) Montre la force d'adhérence maximale (cercle rouge), déterminée à partir de la courbe de rétraction (orange). c) Montre le travail d'adhérence (zone rouge), également déterminé à partir de la courbe de rétraction (orange).

Les résultats obtenus avec le logiciel P3S ont été comparés aux algorithmes d'apprentissage de machine conventionnels tels que les voisins proches (K-NN) et la machine à vecteur d'appui (SVM). Le tableau 2 montre les différents pourcentages de performance pour chaque algorithme afin d'identifier quelles courbes de force correspondent aux cellules natives, et lesquelles correspondent aux cellules traitées. On peut observer que le MinMax Gaussien normal a la meilleure performance (86,10%), comparable aux résultats obtenus avec l'algorithme SVM (85,62%).

Tableau 2. Résultats de l'apprentissage machine. Les résultats ont été obtenus en utilisant 80 % des ensembles de données pour la formation et les 20 % restants pour les essais.

	Algorithmes d'apprentissage de la machine							
	Fuzzy binomial Poba	Fuzzy binomial MinMax	Fuzzy centered Poba	Fuzzy centered MinMax	Normal Gaussian Poba	Normal Gaussian MinMax	K-NN	SVM
Taux de classification	85.51%	85.84%	85.38%	86.10%	86.10%	86.29%	82.67%	85.62%

Discussion

C. albicans

Le protocole utilisé pour immobiliser les cellules est celui décrit par Formosa et al.[47], Néanmoins, dans ce travail, une étape supplémentaire a été franchie, l'ajout du surnageant sur le tampon PDMS avant le dépôt des cellules. Après diverses observations, nous avons déterminé que le dépôt des cellules sur le timbre était augmenté après que le PDMS ait été en contact avec le surnageant. Avec cette modification, il a été possible de remplir rapidement les micropuits avec des cellules, de ~50% à ~85% (voir chapitre 3 matériaux et méthodes). Ce comportement est probablement dû aux polymères de mannose fondés sur la couche externe de C. albicans. Le nombre de nanoindentations était de 16 pour les expériences 1 et 3 et de 9 pour les expériences 2 et 4. L'objectif de faire varier le

nombre de nanoindentations était d'observer si un changement significatif serait présent dans les histogrammes, cependant, deux sous-populations ont commencé à fusionner lorsque nous avons diminué le nombre de mesures. Néanmoins, avec neuf indentations, il était encore possible d'observer les deux sous-populations (Figure 10).

La constante de ressort de chaque courbe de force obtenue avec la procédure automatisée a été extraite. Sur la base des résultats publiés par El-Kirat-Chatel[51], on s'attendait à un changement dans les résultats des cellules traitées par rapport aux cellules natives. Ces résultats peuvent être confirmés en examinant la figure 10 (A et B, et C et D). Au contraire, la présence des deux pics observés dans les histogrammes des quatre expériences était inattendue. En effet, les expériences réalisées sur des cellules individuelles[48,51] a montré une distribution homogène des propriétés nanomécaniques. Nous pensons que les deux pics dans les distributions montrées dans la figure 10 correspondent à la somme des analyses significatives sur une seule cellule, montrant la complexité de la paroi cellulaire étudiée à partir des populations cellulaires. La différence de rigidité (valeur absolue de la constante de ressort) pour les deux expériences indépendantes sur des cellules natives peut provenir de différences incontrôlables dans les cultures cellulaires. La force maximale appliquée, la vitesse de la pointe, la constante de ressort en porte-à-faux, le tampon, la température étaient les mêmes. Il est important de noter que la paroi cellulaire de *C. albicans* est complexe, et qu'elle n'est pas statique ; elle évolue en fonction des conditions de croissance, du développement morphologique, et en réponse aux conditions difficiles[54]. *C. albicans* est un microbe extrêmement polyvalent[55] capable de sentir et de s'adapter à son environnement. Il a été signalé que le traitement à la caspofongine augmente les sites de liaison de la Dectine-1, ce qui affecte la couche externe des mannoprotéines et a un impact sur l'élasticité de la paroi cellulaire[56].

Par conséquent, les phases de croissance de *C. albicans* sont difficiles à contrôler, et une différence non mesurable dans les conditions initiales de culture peut résulter de l'effet papillon à la différence que nous observons entre les expériences 1 et 3. Dans ce travail, on présente la reproduction réussie de la distribution des cellules dans deux populations bien définies. L'hétérogénéité sur le module jeune des cellules de *Saccharomyces cerevisiae* a été signalée par Dague E. et al.[57] Néanmoins, les cellules analysées étaient peu nombreuses (5 cellules), et il était donc impossible de prévoir une conclusion générale à l'échelle de la population. Pour les cellules uniques, la présence de sous-populations est quelque chose d'inattendu et de nouveau. Mais, sur le terrain des biofilms, certains chercheurs ont signalé sa présence comme Harrison et al.[58] a déclaré que des sous-populations étaient responsables de la résistance des biofilms aux agents chélatineux. Khot et al.[59], qui rencontre des sous-populations responsables de la résistance des biofilms à l'amphotéricine B. Dans cette dernière publication, les auteurs ont démontré que la sous-population était associée aux gènes de la voie de l'ergostérol et du bêta 1-6 glucane. Ces deux gènes sont une composante essentielle de la paroi cellulaire du champignon, et l'étude précédente de notre équipe[60] montre que leur niveau d'expression est corrélé avec les propriétés nanomécaniques des cellules. Plus récemment, Rosenberg et al.[61] a montré que la tolérance aux antifongiques était un effet de sous-population. Dans ce travail, il n'y a pas de raison particulière responsable des 2 sous-populations, et plus de travail doit être fait pour présenter un argument confiant sur son origine. Globalement, il est possible d'émettre l'hypothèse que les sous-populations, chez *C. albicans*, sont un mécanisme d'adaptation probablement responsable de la remarquable expansion de ce microbe.

Pour prouver que les sous-populations ne sont pas liées à des positions d'indentation spécifiques ou à un moment précis au cours des expériences, les graphiques des figures 16A et 16B montrent les

valeurs de la constante de printemps au fur et à mesure que le temps évolue, on peut voir que les contributions des pics sont présentes à chaque heure, ce qui permet d'écarter l'idée que les pics sont présents en raison du temps qu'il a fallu pour réaliser l'expérience. Les figures 16C et 16D montrent quatre points d'indentation (points centraux de la cellule) pour les expériences 1 et 3 et neuf points d'indentation pour les expériences 2 et 4 liés aux valeurs de rigidité; si la présence des pics devait être liée à la position de l'indentation, le graphique montrerait des contributions spécifiques en fonction d'une position.

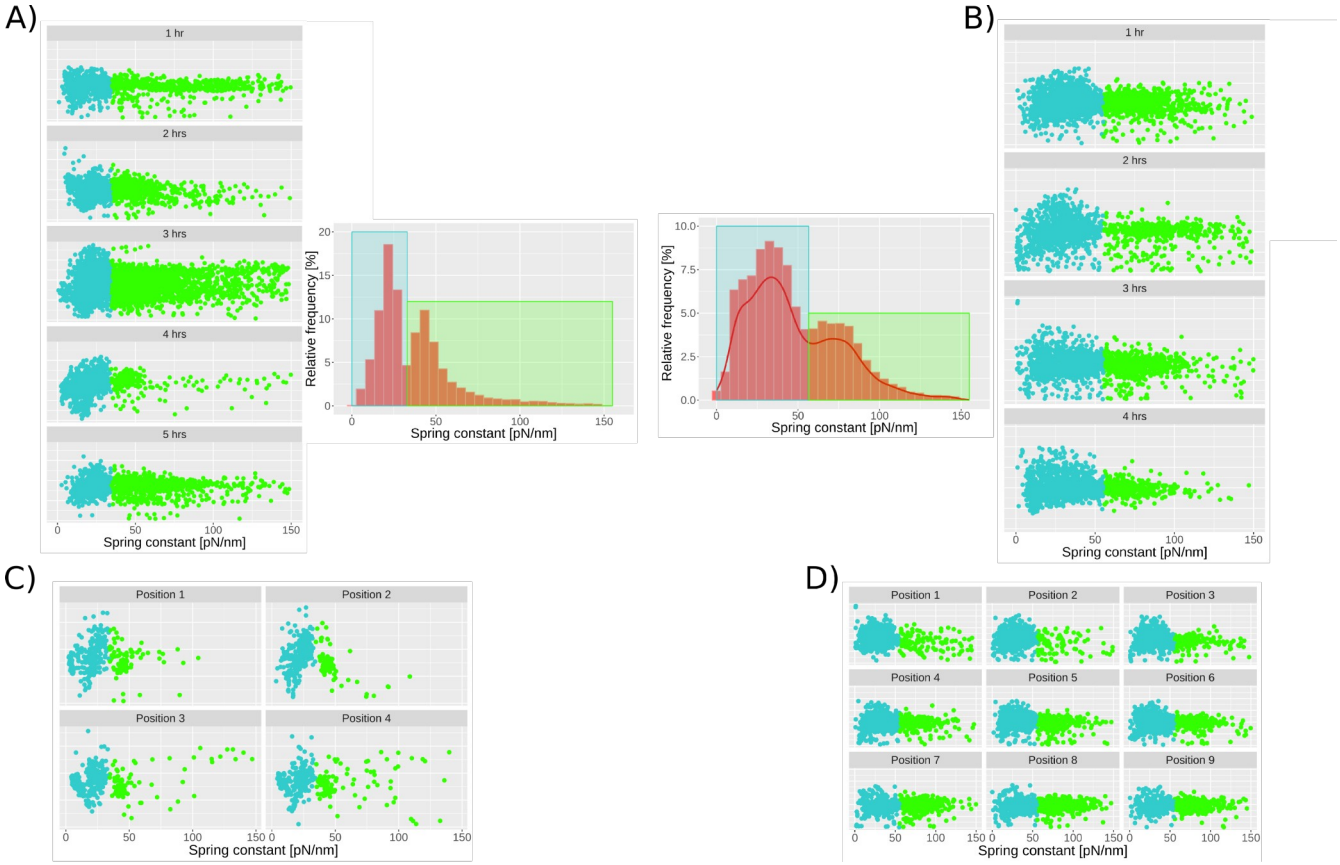

Figure 16. Dépendance des valeurs par rapport au temps et à la position. Les histogrammes dans les carrés bleus sont les données originales qui sont divisées en différents sous-groupes correspondant aux sous-populations fondées (histogramme de gauche cyan/vert ; histogramme de droite cyan/vert). A et B : montrent la présence des trois populations à chaque heure de l'expérience. C et D : montrent les positions de l'indentation, sur chacune d'elles il est possible de voir la présence des sous-populations (cyan/vert) en fonction de la position de l'indentation à l'intérieur du puits. L'organisation des sous-groupes a été faite en utilisant l'algorithme des k-means.

Pour confirmer la présence des deux sous-populations, la figure 17 montre la valeur moyenne de chaque cellule et présente ces valeurs sur les histogrammes. Elle confirme la présence des deux sous-populations centrées sur les mêmes valeurs que celles des distributions globales.

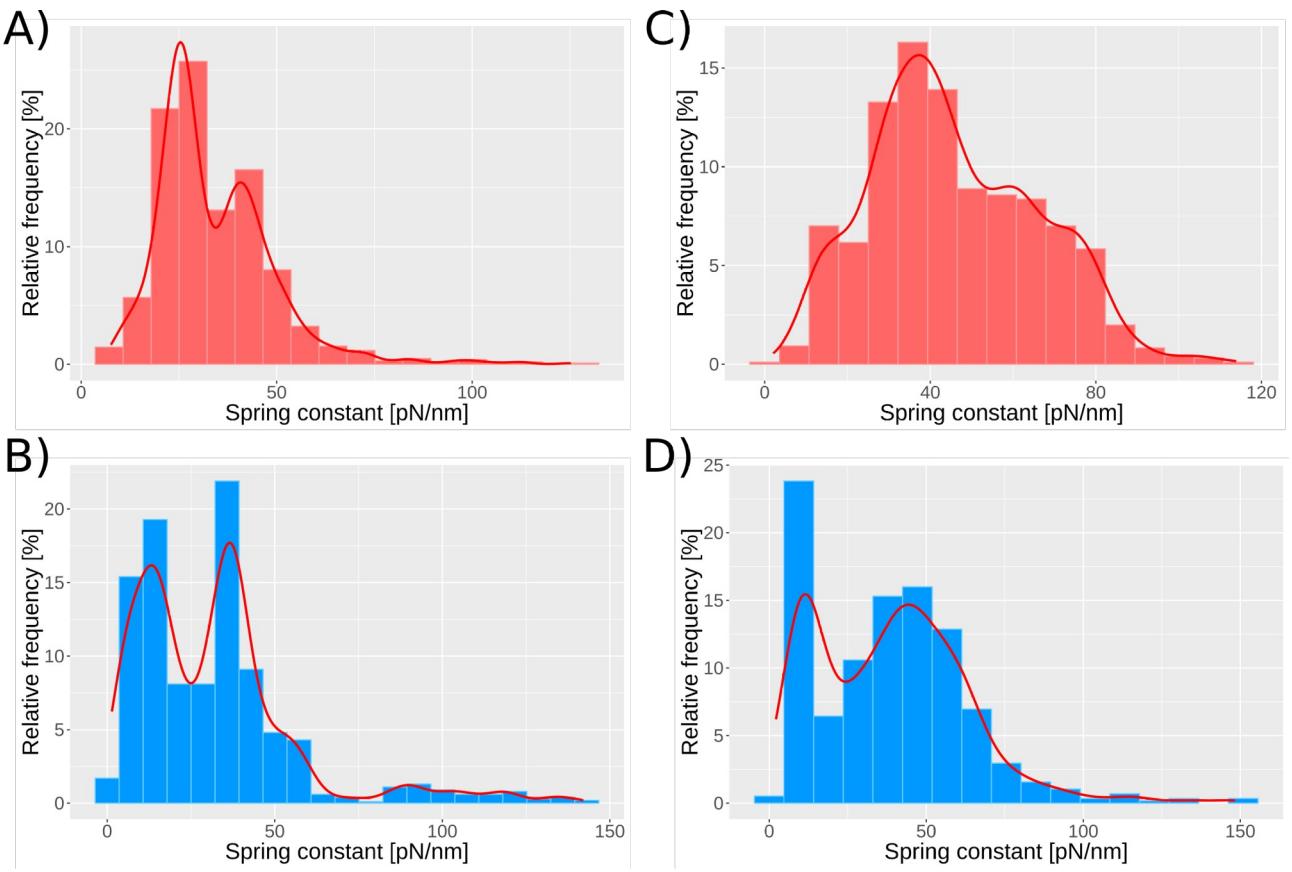

Figure 17. Histogrammes des valeurs médianes de la constante de printemps. A et B : Montrer les résultats médians par cellule pour les cellules natives et les cellules traitées à la caspofongine, expériences 1 et 3. C et D : Représenter les résultats médians par cellule pour les cellules natives et les cellules traitées à la caspofongine, expériences 2 et 4.

La stratégie que nous présentons pour prendre seulement quelques courbes de force (9 à 16) sur un grand nombre de cellules est nouvelle et différente de l'approche traditionnelle sur les mesures mécaniques par AFM sur des cellules vivantes. Néanmoins, il est nécessaire de comparer nos résultats avec la littérature pour valider notre approche. Nous avons comparé nos résultats à deux travaux publiés la même année. La figure 18A présente les résultats de ces travaux. El Kirat-Chatel[51] a réalisé 256 indentations sur une seule cellule et a trouvé une valeur de rigidité de 51±9 pN/nm pour les cellules natives et de 27±10 pN/nm pour les cellules traitées par la caspofongine. Nos résultats s'avèrent du même ordre de grandeur (constante de ressort variant de 21±6 à 81±19 pN/nm pour les cellules naïves), et la même diminution peut être observée sur le traitement à la caspofongine (constante de ressort variant de 13 à 52 pN/nm). La figure 18B montre les résultats publiés par Formosa et al.[48], et ils ont montré que les *C. albicans* traités à la caspofungine sont devenus plus durs que les cellules natives. Le nombre d'indentations faites par eux était de 1024. Cette incohérence peut s'expliquer si les auteurs sélectionnent une cellule native de la sous-population la plus molle et une cellule traitée de la sous-population la plus dure. Le manque de technologie pour évaluer la population cellulaire à ce moment-là fait qu'il est impossible de voir que les deux résultats étaient exacts mais incomplets. La nouvelle méthodologie automatisée présentée ici peut jeter un peu de lumière sur ce type d'incohérences.

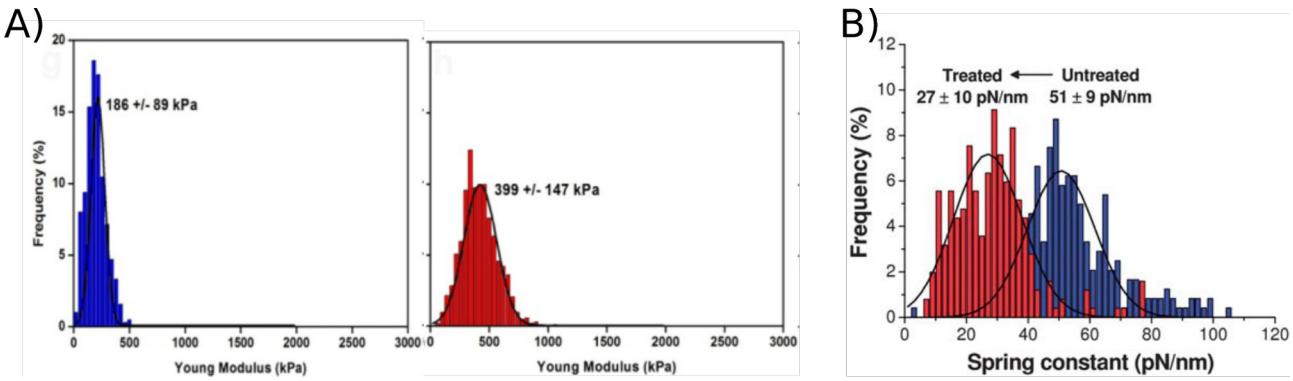

Figure 18. Comparaison des propriétés mécaniques publiées. A) montre les résultats publiés par El Kirat-Chatel et al.[51] prouvant qu'après un traitement à la caspofongine, la paroi cellulaire se ramollit. B) les résultats publiés par Formosa et al.[48] prouver qu'après un traitement à la caspofungine, la paroi cellulaire durcit.

Les résultats des mesures d'adhérence mettent en évidence la limite à laquelle cette méthodologie peut être confrontée. Il a été prouvé que C. albicans peut exprimer un grand nombre d'adhérences sur sa surface[55,62]. Mais, la méthode automatisée présentée ici n'est pas conçue pour analyser en détail les cellules individuelles. Cependant, cela signifie que l'approche traditionnelle n'est pas antagoniste avec notre nouvelle méthode et qu'elles fournissent des informations supplémentaires. De plus, les différences de constante de printemps entre les nanodomaines et la paroi cellulaire " normale " ne sont pas de l'ordre de grandeur des 2 sous-populations. Les nanodomaines les plus rigides sont de 13,4±0,2 nN/µm alors que le reste de la paroi cellulaire est de 12,4±0,3 nN/µm53. Dans ce travail, nous rapportons une sous-population à 21±6 nN/µm et la seconde à 48±9 nN/µm. Cela signifie que la différence due aux nanodomaines est incluse dans la barre d'erreur de notre mesure. Ainsi, nos résultats ne seraient plus incomplets parce qu'ils ne prendraient pas en compte l'hétérogénéité de la population cellulaire mais incomplets parce que nous n'aurions pas de contrôle sur l'échantillon biologique produit. Les Candida albicans sont connus pour leur polyvalence[55] et dans ce contexte, ce type de cellules s'est avéré être un excellent test pour notre méthodologie.

Enfin, l'analyse par apprentissage machine a montré qu'il n'était pas possible de différencier les cellules de levure natives des cellules de levure traitées avec une seule propriété mécanique. L'analyse par apprentissage machine a été répétée, en tenant compte des propriétés mécaniques mentionnées (rigidité, adhérence et travail d'adhésion), et avec les trois valeurs, un pourcentage acceptable des données peut être identifié. Cependant, les 9 ou 16 indentations n'ont pas toutes été prises en compte. Au lieu de cela, une valeur moyenne par propriété mécanique de la cellule a été calculée et entrée dans les algorithmes. Avec la méthodologie présentée ici, nous pensons qu'il est possible d'appliquer, bientôt, des algorithmes d'apprentissage machine pour détecter les cellules saines des cellules malades, et peut-être que ces algorithmes deviendront une partie fondamentale d'un outil de diagnostic basé sur la AFM et les propriétés mécaniques.

Cellules HeLa

Les résultats présentés dans ce chapitre ont été conformes aux attentes ; les cellules fixes ont présenté une augmentation de leur module de Young (les cellules sont devenues plus rigides). Les valeurs du module de Young obtenues à partir de cellules natives sont, selon la littérature[63]. Cependant, comme l'immobilisation d'une seule cellule n'a pas été réalisée sur tous les sites d'immobilisation des timbres, il n'est pas possible d'établir si les valeurs proviennent du noyau de la

cellule ou des régions plus molles[64]. Le temps nécessaire pour la mesure des cellules était de ~6 s par cellule, soit un total de 8 min pour obtenir les courbes de force de 80 cellules. Cependant, le temps d'exécution total était de ~30 min, ce qui signifie que l'engagement et le désengagement de l'étage moteur prend la majeure partie du temps. Une modification est nécessaire pour réduire le temps d'engagement et de désengagement de l'étage moteur.

Perspectives

Ce travail a présenté des expériences spécifiques avec un type particulier de levure (C. albicans) ; cependant, il existe beaucoup d'autres variétés de levures et de microbes sur lesquels la méthodologie automatisée peut être appliquée pour accéder aux résultats des populations cellulaires et voir les différences par rapport à l'analyse unicellulaire, ce qui peut aider à comprendre le comportement, les caractéristiques et peut-être des caractéristiques étroites et incontrôlables dans les échantillons analysés.

Un autre domaine d'intérêt est celui des cellules de mammifères. Dans ce travail, une preuve de concept a été présentée, la principale difficulté lors de l'expérimentation avec des cellules de mammifères était la préparation de l'échantillon. Les matrices de cellules choisies pour l'immobilisation des cellules se sont avérées inadéquates pour la méthodologie automatisée. Cela peut s'expliquer par le fait qu'habituellement, lors de l'analyse d'échantillons avec l'AFM, toute la manipulation est faite manuellement. Si tous les modèles ne contiennent pas de cellules, le chercheur doit se déplacer vers les zones où les cellules sont présentes. A ce moment, le nombre de cellules analysées dépend fortement du nombre de cellules immobilisées, et si ce nombre n'est pas assez élevé, alors les mesures proviendront principalement du réseau de cellules et non des cellules. Cette méthodologie peut encore être améliorée; beaucoup de nouvelles caractéristiques peuvent être mises en œuvre.

La méthodologie automatisée présentée ici pourrait ouvrir la porte non seulement à une signification statistique avec la AFM, mais elle peut aussi être considérée comme la première étape de la transformation de la AFM en un outil de diagnostic ou une procédure de diagnostic. Pour ce faire, il y a encore beaucoup de choses à considérer, comme par exemple:

Le montage automatisé des puces en porte-à-faux.- Il est pratique que cette étape soit automatisée, car le fait de travailler avec des cellules vivantes tend à modifier la pointe (en la salissant) et, par conséquent, les mesures obtenues sont compromises. Certains protocoles ont été établis pour nettoyer la pointe, ce qui prend beaucoup de temps. Le montage automatique de la puce qui contient les cantilevers peut contribuer à améliorer le temps nécessaire pour nettoyer et, si nécessaire, remplacer une pointe qui ne peut être nettoyé

Automatisation de l'alignement et de l'étalonnage.- L'automatisation de ces étapes contribuera à faire de l'AFM une technique plus conviviale et à prolonger l'exécution du script car, avec le temps, la déviation verticale commence à se déplacer dans une direction ou une autre (-11 V à +11 V) et si l'alignement peut être automatique, il est alors possible de corriger ce déplacement de déviation pendant l'exécution du script.

Vérification de la pointe.- La vérification de l'état de la pointe est cruciale pour un AFM entièrement automatisé, car l'expérience est en cours de développement; diverses situations peuvent se produire lorsque la pointe s'use ou s'écrase, ou lorsque des particules se fixent à la pointe. Ces

situations établissent le besoin de vérifier fréquemment la clarté de la pointe. Jusqu'à présent, la vérification est effectuée par le technicien, généralement à vue.

Reconnaissance des espaces vides.- La reconnaissance d'images peut être mise en œuvre pour éviter les zones sans cellules. Elle permet d'augmenter la vitesse et le nombre de cellules analysées. Cependant, pour mettre en œuvre cette fonctionnalité, une amélioration de l'immobilisation des cellules sur les puces doit être obtenue car jusqu'à présent l'immobilisation des cellules de mammifères n'est pas optimale (seulement environ 30 % des modèles contiennent des cellules individuelles).

Apprentissage machine / analyse de l'apprentissage approfondi.- La méthodologie présentée ici permet d'analyser un nombre élevé de cellules, et de ce fait, le nombre de courbes de force est augmenté de façon exponentielle. Cette information massive ouvre le champ de l'analyse mécanique à de nouvelles méthodes d'analyse et à de nouveaux outils de calcul. L'apprentissage machine tel que l'apprentissage profond est un domaine de l'informatique qui a été utilisé ces dernières années pour résoudre des problèmes liés à la biomédecine, entre autres, et nous pensons qu'il peut être utilisé pour la classification et l'analyse des courbes de force.

Je pense que l’ensemble de ces innovations réunies ouvriront la voie à l’utilisation en routine des propriétés biomécaniques de cellules comme outils de diagnostic et de pronostique médical.

Références

(1) Binnig, G.; Rohrer, H.; Gerber, Ch.; Weibel, E. Surface Studies by Scanning Tunneling Microscopy. *Phys. Rev. Lett.* **1982**, *49* (1), 57–61. https://doi.org/10.1103/PhysRevLett.49.57.

(2) Bottomley, L. A.; Gadsby, E. D.; Poggi, M. A. MICROSCOPY TECHNIQUES | Atomic Force and Scanning Tunneling Microscopy. In *Encyclopedia of Analytical Science (Second Edition)*; Worsfold, P., Townshend, A., Poole, C., Eds.; Elsevier: Oxford, 2005; pp 143–151. https://doi.org/10.1016/B0-12-369397-7/00386-1.

(3) Piontek, M. C.; Roos, W. H. Atomic Force Microscopy: An Introduction. In *Single Molecule Analysis: Methods and Protocols*; Peterman, E. J. G., Ed.; Methods in Molecular Biology; Springer New York: New York, NY, 2018; pp 243–258. https://doi.org/10.1007/978-1-4939-7271-5_13.

(4) Formosa, C.; Dague, E. Imaging Living Yeast Cells and Quantifying Their Biophysical Properties by Atomic Force Microscopy. In *Advanced Microscopy in Mycology*; Dahms, T. E. S., Czymmek, K. J., Eds.; Fungal Biology; Springer International Publishing: Cham, 2015; pp 125–141. https://doi.org/10.1007/978-3-319-22437-4_7.

(5) Malkin, A. J.; Land, T. A.; Kuznetsov, Yu. G.; McPherson, A.; DeYoreo, J. J. Investigation of Virus Crystal Growth Mechanisms by In Situ Atomic Force Microscopy. *Phys. Rev. Lett.* **1995**, *75* (14), 2778–2781. https://doi.org/10.1103/PhysRevLett.75.2778.

(6) Rief, M.; Gautel, M.; Oesterhelt, F.; Fernandez, J. M.; Gaub, H. E. Reversible Unfolding of Individual Titin Immunoglobulin Domains by AFM. *Science* **1997**, *276* (5315), 1109–1112. https://doi.org/10.1126/science.276.5315.1109.

(7) Tao, N. J.; Lindsay, S. M.; Lees, S. Measuring the Microelastic Properties of Biological Material. *Biophys. J.* **1992**, *63* (4), 1165–1169.

(8) Meister, A.; Gabi, M.; Behr, P.; Studer, P.; Vörös, J.; Niedermann, P.; Bitterli, J.; Polesel-Maris, J.; Liley, M.; Heinzelmann, H.; et al. FluidFM: Combining Atomic Force Microscopy and Nanofluidics in a Universal Liquid Delivery System for Single Cell Applications and Beyond. *Nano Lett.* **2009**, *9* (6), 2501–2507. https://doi.org/10.1021/nl901384x.

(9) Ando, T.; Kodera, N.; Takai, E.; Maruyama, D.; Saito, K.; Toda, A. A High-Speed Atomic Force Microscope for Studying Biological Macromolecules. *Proc. Natl. Acad. Sci.* **2001**, *98* (22), 12468–12472. https://doi.org/10.1073/pnas.211400898.
(10) Syahir, A.; Usui, K.; Tomizaki, K.; Kajikawa, K.; Mihara, H. Label and Label-Free Detection Techniques for Protein Microarrays. *Microarrays* **2015**, *4* (2), 228–244. https://doi.org/10.3390/microarrays4020228.
(11) Lekka, M.; Laidler, P.; Gil, D.; Lekki, J.; Stachura, Z.; Hrynkiewicz, A. Z. Elasticity of Normal and Cancerous Human Bladder Cells Studied by Scanning Force Microscopy. *Eur. Biophys. J.* **1999**, *28* (4), 312–316. https://doi.org/10.1007/s002490050213.
(12) Cross, S. E.; Jin, Y.-S.; Rao, J.; Gimzewski, J. K. Nanomechanical Analysis of Cells from Cancer Patients. *Nat. Nanotechnol.* **2007**, *2* (12), 780–783. https://doi.org/10.1038/nnano.2007.388.
(13) Omidvar, R.; Tafazzoli-shadpour, M.; Shokrgozar, M. A.; Rostami, M. Atomic Force Microscope-Based Single Cell Force Spectroscopy of Breast Cancer Cell Lines: An Approach for Evaluating Cellular Invasion. *J. Biomech.* **2014**, *47* (13), 3373–3379. https://doi.org/10.1016/j.jbiomech.2014.08.002.
(14) Bastatas, L.; Martinez-Marin, D.; Matthews, J.; Hashem, J.; Lee, Y. J.; Sennoune, S.; Filleur, S.; Martinez-Zaguilan, R.; Park, S. AFM Nano-Mechanics and Calcium Dynamics of Prostate Cancer Cells with Distinct Metastatic Potential. *Biochim. Biophys. Acta BBA - Gen. Subj.* **2012**, *1820* (7), 1111–1120. https://doi.org/10.1016/j.bbagen.2012.02.006.
(15) Smolyakov, G.; Thiebot, B.; Campillo, C.; Labdi, S.; Severac, C.; Pelta, J.; Dague, É. Elasticity, Adhesion, and Tether Extrusion on Breast Cancer Cells Provide a Signature of Their Invasive Potential. *ACS Appl. Mater. Interfaces* **2016**, *8* (41), 27426–27431. https://doi.org/10.1021/acsami.6b07698.
(16) Lekka, M.; Fornal, M.; Pyka-Fościak, G.; Lebed, K.; Wizner, B.; Grodzicki, T.; Styczeń, J. Erythrocyte Stiffness Probed Using Atomic Force Microscope. *Biorheology* **2005**, *42* (4), 307–317.
(17) Dulińska, I.; Targosz, M.; Strojny, W.; Lekka, M.; Czuba, P.; Balwierz, W.; Szymoński, M. Stiffness of Normal and Pathological Erythrocytes Studied by Means of Atomic Force Microscopy. *J. Biochem. Biophys. Methods* **2006**, *66* (1), 1–11. https://doi.org/10.1016/j.jbbm.2005.11.003.
(18) Benech, J. C.; Benech, N.; Zambrana, A. I.; Rauschert, I.; Bervejillo, V.; Oddone, N.; Damián, J. P. Diabetes Increases Stiffness of Live Cardiomyocytes Measured by Atomic Force Microscopy Nanoindentation. *Am. J. Physiol.-Cell Physiol.* **2014**, *307* (10), C910–C919. https://doi.org/10.1152/ajpcell.00192.2013.
(19) Dague, E.; Genet, G.; Lachaize, V.; Guilbeau-Frugier, C.; Fauconnier, J.; Mias, C.; Payré, B.; Chopinet, L.; Alsteens, D.; Kasas, S.; et al. Atomic Force and Electron Microscopic-Based Study of Sarcolemmal Surface of Living Cardiomyocytes Unveils Unexpected Mitochondrial Shift in Heart Failure. *J. Mol. Cell. Cardiol.* **2014**, *74*, 162–172. https://doi.org/10.1016/j.yjmcc.2014.05.006.
(20) Braga, P. C.; Ricci, D. Differences in the Susceptibility of Streptococcus Pyogenes to Rokitamycin and Erythromycin A Revealed by Morphostructural Atomic Force Microscopy. *J. Antimicrob. Chemother.* **2002**, *50* (4), 457–460. https://doi.org/10.1093/jac/dkf180.
(21) Formosa, C.; Grare, M.; Duval, R. E.; Dague, E. Nanoscale Effects of Antibiotics on P. Aeruginosa. *Nanomedicine Nanotechnol. Biol. Med.* **2012**, *8* (1), 12–16. https://doi.org/10.1016/j.nano.2011.09.009.
(22) Wang, N.; Butler, J. P.; Ingber, D. E. Mechanotransduction across the Cell Surface and through the Cytoskeleton. *Science* **1993**, *260* (5111), 1124–1127. https://doi.org/10.1126/science.7684161.

(23) Puig-De-Morales, M.; Grabulosa, M.; Alcaraz, J.; Mullol, J.; Maksym, G. N.; Fredberg, J. J.; Navajas, D. Measurement of Cell Microrheology by Magnetic Twisting Cytometry with Frequency Domain Demodulation. *J. Appl. Physiol. Bethesda Md 1985* **2001**, *91* (3), 1152–1159. https://doi.org/10.1152/jappl.2001.91.3.1152.
(24) Zhang, Y.; Wei, F.; Poh, Y.-C.; Jia, Q.; Chen, J.; Chen, J.; Luo, J.; Yao, W.; Zhou, W.; Huang, W.; et al. Interfacing 3D Magnetic Twisting Cytometry with Confocal Fluorescence Microscopy to Image Force Responses in Living Cells. *Nat. Protoc.* **2017**, *12* (7), 1437–1450. https://doi.org/10.1038/nprot.2017.042.
(25) Ashkin, A.; Dziedzic, J. M.; Yamane, T. Optical Trapping and Manipulation of Single Cells Using Infrared Laser Beams. *Nature* **1987**, *330* (6150), 769–771. https://doi.org/10.1038/330769a0.
(26) Svoboda, K.; Block, S. M. Biological Applications of Optical Forces. *Annu. Rev. Biophys. Biomol. Struct.* **1994**, *23* (1), 247–285. https://doi.org/10.1146/annurev.bb.23.060194.001335.
(27) Hénon, S.; Lenormand, G.; Richert, A.; Gallet, F. A New Determination of the Shear Modulus of the Human Erythrocyte Membrane Using Optical Tweezers. *Biophys. J.* **1999**, *76* (2), 1145–1151.
(28) "Next-generation" optical tweezers trap tightly without overheating | Harvard John A. Paulson School of Engineering and Applied Sciences https://www.seas.harvard.edu/news/2011/09/next-generation-optical-tweezers-trap-tightly-without-overheating (accessed Dec 13, 2019).
(29) Wirtz, D. Particle-Tracking Microrheology of Living Cells: Principles and Applications. *Annu. Rev. Biophys.* **2009**, *38* (1), 301–326. https://doi.org/10.1146/annurev.biophys.050708.133724.
(30) Panorchan, P.; Lee, J. S. H.; Daniels, B. R.; Kole, T. P.; Tseng, Y.; Wirtz, D. Probing Cellular Mechanical Responses to Stimuli Using Ballistic Intracellular Nanorheology. In *Methods in Cell Biology*; Cell Mechanics; Academic Press, 2007; Vol. 83, pp 113–140. https://doi.org/10.1016/S0091-679X(07)83006-8.
(31) Chu, K. K.; Mojahed, D.; Fernandez, C. M.; Li, Y.; Liu, L.; Wilsterman, E. J.; Diephuis, B.; Birket, S. E.; Bowers, H.; Martin Solomon, G.; et al. Particle-Tracking Microrheology Using Micro-Optical Coherence Tomography. *Biophys. J.* **2016**, *111* (5), 1053–1063. https://doi.org/10.1016/j.bpj.2016.07.020.
(32) Gómez-González, M. One- and Two-Point Particle Tracking Microrheology of Complex Viscoelastic Fluids, UC San Diego, 2015.
(33) Thoumine, O.; Ott, A. Time Scale Dependent Viscoelastic and Contractile Regimes in Fibroblasts Probed by Microplate Manipulation. *J. Cell Sci.* **1997**, *110* (17), 2109–2116.
(34) Hellström, L. H. O.; Samaha, M. A.; Wang, K. M.; Smits, A. J.; Hultmark, M. Errors in Parallel-Plate and Cone-Plate Rheometer Measurements Due to Sample Underfill. *Meas. Sci. Technol.* **2014**, *26* (1), 015301. https://doi.org/10.1088/0957-0233/26/1/015301.
(35) Fernández, P.; Heymann, L.; Ott, A.; Aksel, N.; Pullarkat, P. A. Shear Rheology of a Cell Monolayer. *New J. Phys.* **2007**, *9* (11), 419–419. https://doi.org/10.1088/1367-2630/9/11/419.
(36) Guck, J.; Ananthakrishnan, R.; Mahmood, H.; Moon, T. J.; Cunningham, C. C.; Käs, J. The Optical Stretcher: A Novel Laser Tool to Micromanipulate Cells. *Biophys. J.* **2001**, *81* (2), 767–784. https://doi.org/10.1016/S0006-3495(01)75740-2.
(37) Guck, J.; Schinkinger, S.; Lincoln, B.; Wottawah, F.; Ebert, S.; Romeyke, M.; Lenz, D.; Erickson, H. M.; Ananthakrishnan, R.; Mitchell, D.; et al. Optical Deformability as an Inherent Cell Marker for Testing Malignant Transformation and Metastatic Competence. *Biophys. J.* **2005**, *88* (5), 3689–3698. https://doi.org/10.1529/biophysj.104.045476.
(38) Yang, T.; Bragheri, F.; Minzioni, P. A Comprehensive Review of Optical Stretcher for Cell Mechanical Characterization at Single-Cell Level. *Micromachines* **2016**, *7* (5), 90. https://doi.org/10.3390/mi7050090.

(39) Carlo, D. D. A Mechanical Biomarker of Cell State in Medicine. *J. Lab. Autom.* **2012**, *17* (1), 32–42. https://doi.org/10.1177/2211068211431630.
(40) Wang, Z.; Liu, L.; Wang, Y.; Xi, N.; Dong, Z.; Li, M.; Yuan, S. A Fully Automated System for Measuring Cellular Mechanical Properties. *J. Lab. Autom.* **2012**, *17* (6), 443–448. https://doi.org/10.1177/2211068212460236.
(41) Roy, R.; Chen, W.; Cong, L.; Goodell, L. A.; Foran, D. J.; Desai, J. P. A Semi-Automated Positioning System for Contact-Mode Atomic Force Microscopy (AFM). *IEEE Trans. Autom. Sci. Eng.* **2013**, *10* (2), 462–465. https://doi.org/10.1109/TASE.2012.2226154.
(42) Favre, M.; Polesel-Maris, J.; Overstolz, T.; Niedermann, P.; Dasen, S.; Gruener, G.; Ischer, R.; Vettiger, P.; Liley, M.; Heinzelmann, H.; et al. Parallel AFM Imaging and Force Spectroscopy Using Two-Dimensional Probe Arrays for Applications in Cell Biology. *J. Mol. Recognit.* **2011**, *24* (3), 446–452. https://doi.org/10.1002/jmr.1119.
(43) Sadeghian, H.; Herfst, R.; Dekker, B.; Winters, J.; Bijnagte, T.; Rijnbeek, R. High-Throughput Atomic Force Microscopes Operating in Parallel. *Rev. Sci. Instrum.* **2017**, *88* (3), 033703. https://doi.org/10.1063/1.4978285.
(44) Dujardin, A.; Wolf, P. D.; Lafont, F.; Dupres, V. Automated Multi-Sample Acquisition and Analysis Using Atomic Force Microscopy for Biomedical Applications. *PLOS ONE* **2019**, *14* (3), e0213853. https://doi.org/10.1371/journal.pone.0213853.
(45) Martínez-Rivas, A.; Dague, E.; Proa-Coronado, S.; Séverac, C.; González-Quijano, G. Process by Atomic Force Microscopy for the Massive Physical and Mechanical Analysis of Materials, arrays and structures of biomaterials. PCT/MX2018/050027.
(46) Dague Etienne; Proa Coronado Sergio; Severac Childerick; Martinez Rivas Adrian. *AUTOMATIP: Automation of Biophysical Measurements on Cells by Atomic Force Microscope (AFM)*; Instituto Politecnico Nacional: Mexico, D.F., 2017.
(47) Formosa, C.; Pillet, F.; Schiavone, M.; Duval, R. E.; Ressier, L.; Dague, E. Generation of Living Cell Arrays for Atomic Force Microscopy Studies. *Nat. Protoc.* **2015**, *10* (1), 199–204. https://doi.org/10.1038/nprot.2015.004.
(48) Formosa, C.; Schiavone, M.; Martin-Yken, H.; François, J. M.; Duval, R. E.; Dague, E. Nanoscale Effects of Caspofungin against Two Yeast Species, Saccharomyces Cerevisiae and Candida Albicans. *Antimicrob. Agents Chemother.* **2013**, *57* (8), 3498–3506. https://doi.org/10.1128/AAC.00105-13.
(49) Heinisch, O. Cochran, W. G.: Sampling Techniques, 2. Aufl. John Wiley and Sons, New York, London 1963. Preis s. *Biom. Z.* **1965**, *7* (3), 203–203. https://doi.org/10.1002/bimj.19650070312.
(50) Yamane, T. *Statistics: An Introductory Analysis*; Harper & Row, 1967.
(51) El-Kirat-Chatel, S.; Beaussart, A.; Alsteens, D.; Jackson, D. N.; Lipke, P. N.; Dufrêne, Y. F. Nanoscale Analysis of Caspofungin-Induced Cell Surface Remodelling in Candida Albicans. *Nanoscale* **2013**, *5* (3), 1105–1115. https://doi.org/10.1039/c2nr33215a.
(52) Press, T. M. Machine Learning https://mitpress.mit.edu/books/machine-learning-1 (accessed Dec 3, 2019).
(53) Mccarthy, J. F.; Marx, K. A.; Hoffman, P. E.; Gee, A. G.; O'neil, P.; Ujwal, M. L.; Hotchkiss, J. Applications of Machine Learning and High-Dimensional Visualization in Cancer Detection, Diagnosis, and Management. *Ann. N. Y. Acad. Sci.* **2004**, *1020* (1), 239–262. https://doi.org/10.1196/annals.1310.020.
(54) Dague, E.; Bitar, R.; Ranchon, H.; Durand, F.; Yken, H. M.; François, J. M. An Atomic Force Microscopy Analysis of Yeast Mutants Defective in Cell Wall Architecture. *Yeast* **2010**, *27* (8), 673–684. https://doi.org/10.1002/yea.1801.
(55) Poulain, D. Candida Albicans, Plasticity and Pathogenesis. *Crit. Rev. Microbiol.* **2015**, *41* (2), 208–217. https://doi.org/10.3109/1040841X.2013.813904.

(56) Hwang, G.; Liu, Y.; Kim, D.; Li, Y.; Krysan, D. J.; Koo, H. Candida Albicans Mannans Mediate Streptococcus Mutans Exoenzyme GtfB Binding to Modulate Cross-Kingdom Biofilm Development in Vivo. *PLOS Pathog.* **2017**, *13* (6), e1006407. https://doi.org/10.1371/journal.ppat.1006407.
(57) Dague, E.; Jauvert, E.; Laplatine, L.; Viallet, B.; Thibault, C.; Ressier, L. Assembly of Live Micro-Organisms on Microstructured PDMS Stamps by Convective/Capillary Deposition for AFM Bio-Experiments. *Nanotechnology* **2011**, *22* (39), 395102. https://doi.org/10.1088/0957-4484/22/39/395102.
(58) Harrison, J. J.; Turner, R. J.; Ceri, H. A Subpopulation of Candida Albicans and Candida Tropicalis Biofilm Cells Are Highly Tolerant to Chelating Agents. *FEMS Microbiol. Lett.* **2007**, *272* (2), 172–181. https://doi.org/10.1111/j.1574-6968.2007.00745.x.
(59) Khot, P. D.; Suci, P. A.; Miller, R. L.; Nelson, R. D.; Tyler, B. J. A Small Subpopulation of Blastospores in Candida Albicans Biofilms Exhibit Resistance to Amphotericin B Associated with Differential Regulation of Ergosterol and β-1,6-Glucan Pathway Genes. *Antimicrob. Agents Chemother.* **2006**, *50* (11), 3708–3716. https://doi.org/10.1128/AAC.00997-06.
(60) Schiavone, M.; Déjean, S.; Sieczkowski, N.; Castex, M.; Dague, E.; François, J. M. Integration of Biochemical, Biophysical and Transcriptomics Data for Investigating the Structural and Nanomechanical Properties of the Yeast Cell Wall. *Front. Microbiol.* **2017**, *8*. https://doi.org/10.3389/fmicb.2017.01806.
(61) Rosenberg, A.; Ene, I. V.; Bibi, M.; Zakin, S.; Segal, E. S.; Ziv, N.; Dahan, A. M.; Colombo, A. L.; Bennett, R. J.; Berman, J. Antifungal Tolerance Is a Subpopulation Effect Distinct from Resistance and Is Associated with Persistent Candidemia. *Nat. Commun.* **2018**, *9* (1), 2470. https://doi.org/10.1038/s41467-018-04926-x.
(62) Groot, P. W. J. de; Bader, O.; Boer, A. D. de; Weig, M.; Chauhan, N. Adhesins in Human Fungal Pathogens: Glue with Plenty of Stick. *Eukaryot. Cell* **2013**, *12* (4), 470–481. https://doi.org/10.1128/EC.00364-12.
(63) Sajeesh, P.; Raj, A.; Doble, M.; Sen, A. K. Characterization and Sorting of Cells Based on Stiffness Contrast in a Microfluidic Channel. *RSC Adv.* **2016**, *6* (78), 74704–74714. https://doi.org/10.1039/C6RA09099K.
(64) Tománková, K. B.; Kolar, P.; Malohlava, J.; Kolářová, H. Mechanical Characterisation of HeLa Cells Using Atomic Force Microscopy; 2012.

Chapter 1: Methods of micropatterning

This chapter is a summary of one of the papers done in collaboration between the two countries. This paper was one of the pillars for our research, and it mentions different methods of micropatterning and manipulation of cells. The methods to manipulate cells are essential because they are the first step of the methodology developed in this thesis work.

The objective of micropatterning and manipulating mammalian and bacterial cells is to have better controls, a deeper understanding, and to apply these in practical biomedical microelectromechanical systems (bioMEMS), point-of-care (POC) devices, and organs-on-chips (OOC). Cell micropatterning and cell manipulation currently represent the basic steps to perform drug testing experiments, to understand biochemical processes, to design microfluidic devices for medical applications, and to conduct fundamental studies in biological areas.

It is straightforward to consider characteristics of the substrate where cells are patterned, such as conductivity, hydrophobicity, hydrophilicity, thermal, and environmental factors together with cost, and accessibility. In this context, predominant substrates or platforms are composed of polymers such as polydimethylsiloxane (PDMS), polymethylmethacrylate (PMMA), cyclic olefin copolymer (COC), and polyimide (PI). At the same time, other biomaterials are gaining popularity, such as alginate, chitosan, or functionalized surfaces, with the use of low-cost materials like graphene. The methods of micropatterning presented here are being classified into three categories and are listed next.

1.1 Physical cell patterning.

Inkjet bioprinting.- This technique uses an ink solution to generate droplets containing cells. There are three types of inkjet printing methodologies known as continuous inkjet (CIJ) printing, drop-on-demand (DOD) printing, and electrohydrodynamic jet printing. The DOD inkjet printing method has been largely used to fabricate 3D structures for biomedical applications. The DOD technique to elaborate live-cell-based biosensors has also been explored. Inkjet printing has a moderate cost and good controllability; however, some parameters related to droplet formation had to be considered.

Optical and Optoelectronic Tweezers.- This technology uses optical forces to move cells; some optical tweezers use radiation pressure emitted by a laser beam and other infrared lasers. Cell arrays using optical methods allow remote manipulation and monitoring due to the intrinsic charge and dielectric properties of cells. Optical tweezers provide high precision of positioning for small arrays and small dielectric objects. However, they have a limited manipulation area, which means that at large-scale and heterogeneous patterns, the resolution is reduced. Non-contact optoelectronic can be applied for some bacteria that have high movability. Optoelectronic manipulation of cells is a feasible option for cell trapping and elaboration of microfluidic devices, due to remote and large-scale manipulation. Currently, microfabrication techniques are enlarging their applications.

Nonetheless, thermal effects and photodamage of cells must be critical factors in designing experimental systems with this methodology.

Laser-Based Cell Patterning.- Laser-based direct writing technique to pattern cells uses a laser to transfer or propel cells from one source film (donor, ribbon, or target) to a receiving or acceptor substrate. This technique could be divided as follows: Laser-induced forward transfer (LIFT), absorbing film-assisted laser-induced forward transfer (AFA-LIFT), biological laser processing (BioLP), matrix-assisted pulsed laser evaporation direct writing (MAPLE DW), and laser-guided direct writing (LGDW). LIFT, AFA-LIFT, BioLP, and MAPLE DW have a similar configuration, and nowadays, these techniques are referred to as laser direct-write (LDW). The last laser-based cell pattering called laser-guided direct writing (LGDW) is a variation technique of the commonly used optical trap (laser tweezers, optical tweezers), capable of depositing cells on different matrices such as collagen or Matrigel, but is limited by the size of the specific cell. LGDW is a technique that consists of guiding and propelling a stream of cells onto a target surface by using optical forces of a laser (700–1000 nm, which is above the wavelength absorption of most proteins).

Acoustic Force Patterning.- Acoustic methodologies use surface acoustic waves (SAWs) for microscale manipulation with less energy than optical and optoelectronic approaches. SAWs, made of electrodes, are excited at different frequencies and deposited onto piezoelectric substrates. Common frequencies to generate SAW wavelengths from 1 to 300 nm are around 10 to 1000 MHz. Most of the works have been focused on the reduction of time and energy required to pattern cells, conserving their functionality and viability as mentioned by Ding et al. The migration of cells, subjected to acoustic waves is called acoustophoresis, and is dependent on the physical properties of cells such as size, compressibility, and density but also on the viscosity and fluidic properties of the medium. Most of the cells have a positive acoustic contrast factor that implies an attraction to nodes.

Electrokinetic Forces (Dielectrophoresis).- Dielectrophoresis (DEP) is considered an active method of cell manipulation because it requires energy to move cells. This technique combines electrokinetic forces with hydrodynamic effects to achieve cell trapping or lead cells to specific areas without damaging them. A cell has polarization in the surrounding media caused by an electric field. A dipole moment is induced by the electric field, thereby moving cells, and depending on their permittivity and the polarizability of the surrounding media, the cells can be attracted to the electric field in the direction of the gradient (positive) or repelled, opposite to the gradient (negative).

Magnetic Cell Manipulation.- Magnetic force and magnetic biomaterials can guide cells for tissue engineering applications that require complex and tissue organization. Some have used magnetic manipulation to form patterns with complex architectures. The necessity of single-cell studies of cell membrane functionality, the interaction with new drugs, the detection, and sorting among other biological applications are now boosting single-cell arrays with magnetic approaches. In this context, magnetic patterning is specific for mammalian and bacterial cells. However, the technique requires cell labeling with biocompatible magnetic particles.

1.2 Chemical Patterning for Cells Assembly

Surface Chemistry Methodologies.- Cells also have the ability to sense the environment around them, especially the surface where they adhere. It is thus possible to take advantage of this property to pattern adhesive and anti-adhesive molecules and therefore order the cells on a surface. Proteins from the extracellular matrix, like fibronectin, laminin, or collagen, are preferred to glass or Poly(L -lysine)-graft-poly(ethylene glycol) (PLL-g-PEG) by the cells. This makes it possible to control the localization of the cells. In microbiology, matrix proteins have not been used to immobilize bacteria or yeast. On the contrary, some work relies on electrostatic interactions between a positively charged surface and negatively charged microbes. Polyethylenimine Poly- L-Lysine (PLL) or 3-aminopropyltriethoxysilane (APTES) were used to immobilize microbes.

1.3 Physical and Chemical Patterning

Microcontact Printing.- Microcontact printing (μCP) is an accessible lithography technique first introduced by the Whiteside group. It relies on a stamp made of an elastomeric material, usually polydimethylsiloxane (PDMS), cast on a master mold (usually silicon). The unmold stamp is inked and let to dry. Finally, the ink is transferred onto a surface by contact. Although microcontact printing can be used to produce nanoscale patterns down to 40 nm line grating and even 2 nm using nanotubes to mold the stamp, nano-lithographic facilities are required and are quite expensive and not necessary for cell adhesion.
Fabricating a master mold is both expensive and time-consuming. One way to avoid breaking the original silicon master mold is to make replicas in epoxy or polyurethane using PDMS stamps made from the original mold. Automation and robotics have improved the robustness of the printing process. These commercial systems can align prints with sub-10 μm precision in a repetitive fashion, and several different molecules can be printed. This opens the path to more complex devices with different specific cells at specific positions. However, the robustness of the printing process is dominated by the interaction between the ink and the surface.

Microwells and Filtration.- In an attempt to minimize the surface chemistry, microstructured surfaces or used porous membranes to immobilize round-shaped cells have been developed. Unfortunately, the filling rate of the pores is often very low, and it is time-consuming to localize a cell and perform statistically relevant experiments.

Deep UV Micropatterning.- This methodology applies wavelengths below 280 nm in the region of deep UV (DUV) to obtain micropatterns; it requires a predesigned photomask sensitive to those wavelengths. The material used in a photomask, especially for deep UV, is normally natural quartz, synthetic quartz, or fused silica. However, this technology has also been used for glass and PDMS combined with a coating of PLL and PLL-g-PEG to facilitate cell adhesion.

1.4 Conclusions

Physical and chemical micropatterning techniques have improved rapidly, and several methodologies are emerging. The selection of the best technique will depend primarily on the purpose as well as the biomaterials involved, the experimental design, and the micro-nano

fabrication techniques. On the one hand, physical methods for cell trapping such as inkjet printing, optoelectronic, acoustic, dielectrophoretic, laser-based, and magnetic techniques provide high specificity to sort and collocate cells in predesigned patterns. These physical-active techniques can be efficient, highly specific, and reproducible, but it is necessary to identify the critical factors for each technique to conserve viability and cell functionality.

On the other hand, the use of surface chemistry based methodologies provide an efficient way to fix cells on surfaces taking advantage of biomolecule specific recognition by cell receptors and chemical bonding between different functional groups, which allow high adhesion, specificity, or the opposite effect such as repelling adhesion. All these technological advances have greatly expanded the development of biomedical microdevices and high-performance platforms to automatically analyze cells as medical applications are emerging, with great academic and industrial impact.

micromachines

MDPI

Review

Methods of Micropatterning and Manipulation of Cells for Biomedical Applications

Adrian Martinez-Rivas [1,*], Génesis K. González-Quijano [2], Sergio Proa-Coronado [3], Childérick Séverac [4] and Etienne Dague [5,*]

1 CIC, Instituto Politécnico Nacional (IPN), Av. Juan de Dios Bátiz S/N, Nueva Industrial Vallejo, 07738 Mexico City, Mexico
2 CONACYT-CNMN, Instituto Politécnico Nacional (IPN), Av. Luis Enrique Erro s/n, Nueva Industrial Vallejo, 07738 Mexico City, Mexico; gkgonzalez@conacyt.mx
3 ENCB, Instituto Politécnico Nacional (IPN), Av. Wilfrido Massieu, Unidad Adolfo López Mateos, 07738 Mexico City, Mexico; sergio.prc81@gmail.com
4 ITAV-CNRS, Université de Toulouse, CNRS, Toulouse, France; childerick.severac@itav.fr
5 LAAS-CNRS, Université de Toulouse, CNRS, Toulouse, France
* Correspondence: nanobiomex@hotmail.com or amartinezri@cic.ipn.mx (A.M.-R.); edague@laas.fr (E.D.); Tel.: +52-55-5729-6000 (ext. 56606) (A.M.-R.); +33-56-133-7841 (E.D.)

Received: 7 November 2017; Accepted: 28 November 2017; Published: 29 November 2017

Abstract: Micropatterning and manipulation of mammalian and bacterial cells are important in biomedical studies to perform in vitro assays and to evaluate biochemical processes accurately, establishing the basis for implementing biomedical microelectromechanical systems (bioMEMS), point-of-care (POC) devices, or organs-on-chips (OOC), which impact on neurological, oncological, dermatologic, or tissue engineering issues as part of personalized medicine. Cell patterning represents a crucial step in fundamental and applied biological studies in vitro, hence today there are a myriad of materials and techniques that allow one to immobilize and manipulate cells, imitating the 3D in vivo milieu. This review focuses on current physical cell patterning, plus chemical and a combination of them both that utilizes different materials and cutting-edge micro-nanofabrication methodologies.

Keywords: cell patterning and manipulation; mammalian and bacterial cells; micro-nanofabrication; microfluidics; organs-on-chips (OOC); biomedical microelectromechanical systems (bioMEMS); point-of-care (POC); soft lithography

1. Introduction

The objective of micropatterning and manipulating mammalian and bacterial cells is to have better controls, a deeper understanding, and to apply these in practical biomedical microelectromechanical systems (bioMEMS), point-of-care (POC) devices, and organs-on-chips (OOC) [1]. In this regard, (nano)biotechnologists have developed and implemented novel methodologies to fix cells on substrates, in a controlled manner, so-called micropatterning. It is a challenging task, however, new micro and nanofabrication methodologies have contributed to the achievement of satisfactory outcomes. Cell micropatterning and cell manipulation currently represent the basic steps to perform drug testing experiments [2,3], to understand biochemical processes [4,5], to design microfluidic devices for medical applications, and to conduct fundamental studies in biological areas [6,7]. In this context, in vitro assays have increased their efficiency because of the simplicity of cell micropatterning and manipulation, which permit the carrying out of 3D human cells assays, replacing animal in vivo models [8]. Additionally, because of the versatility of these cell micropatternings, they can be applied to biomolecules [9], bacteria [10], yeasts [11], and other bioparticles involved in therapies [12], diagnosis [13], or interaction with numerous biochemical processes [14].

Single-cell manipulating models allow more in depth studies of membrane functionalities, cell interaction with particles, as well as drugs and external stimulus that a few years ago would have been difficult to analyze, including the advantage of performing high throughput measurements [15]. On the other hand, parallel-cell manipulation enables cell-arrays to mimic in vivo conditions, representing enormous progress in biomedical areas due to the fact that the conventional 2D culture is being replaced by 3D approaches which are more accurate and nearer to humans, both physiologically and metabolically [16].

It is straightforward to consider characteristics of the substrate where cells are patterned, such as conductivity, hydrophobicity, hydrophilicity, thermal, and environmental factors together with cost, and accessibility [17]. In this context, predominant substrates or platforms are composed of polymers such as polydimethylsiloxane (PDMS), polymethylmethacrylate (PMMA), cyclic olefin copolymer (COC), and polyimide (PI), while other biomaterials are gaining popularity such as alginate, chitosan, or functionalized surfaces with the use of low cost materials like graphene [18].

In this review, separated or combined physical and chemical techniques for micropatterning and manipulating mammalian and bacterial cells are described, focusing on microfabricated biomedical devices and surveying significant reported articles as well as the contributions of the present authors, in this area.

2. Techniques and Methods

2.1. Physical Cell Patterning

2.1.1. Inkjet Cell Printing

Inkjet bioprinting uses an ink solution to generate droplets containing cells. There are three types of inkjet printing methodologies known as: continuous inkjet (CIJ) printing, drop-on demand (DOD) printing, and electrohydrodynamic jet printing. As there is high controllability and less contamination; the DOD inkjet printing method has been largely used to fabricate 3D structures for biomedical applications. Hence, Yusof et al. [19] reported a non-contact approach to pattern single cells by using an Inkjet printing technique that consisted of a dispenser chip to deposit droplets, a sensor to detect the cells, and an automation tool to print on specific substrates such as microscope slides and microtiter plates. They put emphasis on diagnostic and therapeutic applications by patterning a cervical cancer line (HeLa), obtaining a printing efficiency of 87% and a cell viability rate of 75%. This technique has also been used to implement 3D micro-tissue arrays [20], and then 440 micro-arrays or 3D liver tissue chips with different layer numbers and hepatocytes and endothelial cells were elaborated, as part of organ-on-chips developments.

The DOD technique to elaborate live-cell-based biosensors has also been explored [21]. In this work the concentration of reactive oxygen species (ROS) was studied, as this is thought to be related to the change of hydrogen peroxide (H_2O_2) and then implicated in some human health conditions, including aging. A Surface Patterning Tool (SPT) substrate made of SU-8 resist was elaborated. They placed mammalian cells and modified a commercial Bioforce Nano eNablerTM (Bioforce Nanosciences, Inc., Ames, IA, USA), to print onto a hydrogel-based anchoring matrix. Inkjet printing has a moderate cost and good controllability; however, some parameters related to droplet formation had to be considered. Then in a recent paper [22] a ligament flow of a droplet formation process was obtained, when patterning cells and their effect on the viability and distribution were studied.

In another paper, an electrohydrodynamic jet printing (e-jet) approach was employed [23] to print bioinks such as fibronectin (FN), extracellular matrix (ECM) glycoprotein, and 3-aminopropyltriethoxysilane (APTES) to subsequently pattern mouse embryonic fibroblast cells (NIH-3T3). This methodology uses a rapid nozzle-free jet process called pyroelectrohydrodynamic jet (p-jet), because it uses a pyroelectric effect that modifies the bioink fluid, modulating the dot sizes from 200 μm down to 0.5 μm.

Relating to pattering of bacteria, Zheng et al. [24], modified a commercial thermal inkjet printer to pattern *Escherichia coli* on agar-coated substrates, making different bacterial colonies which enabled the evaluation of the antimicrobial activity of antibiotics. To perform the printing of bacteria onto microscope glass slides and microtiter plates, a commercial four-color thermal inkjet printer (Canon PIXMA ip1880) was employed (Figure 1). Srimongkon et al. [25] elaborated a prototype of a bacterial culture system by combining commercial inkjet printers and paper substrates to pattern cells in a culture media based on hydrogels such as poly(vinyl alcohol) and standard calcium alginate, as an alternative to the commonly used agarose.

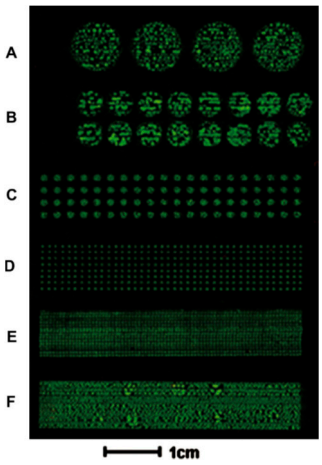

Figure 1. Microscope glass slide where a bacterial array was printed, showing different dot sizes in the letters **A** to **F**. Reproduced with permission from [24].

2.1.2. Optical and Optoelectronic Tweezers

This technology uses optical forces to move cells, some optical tweezers use radiation pressure emitted by a laser beam and others use infrared lasers. Cell arrays using optical methods allow remote manipulation and monitoring due to the intrinsic charge and dielectric properties of cells.

Ozkan et al. [26] fabricated an electro-optical system which employed both an electrophoretic array and remote optical manipulation by vertical-cavity surface. They were able to monitor the expression of a fluorescent protein in aseptic conditions.

Optical tweezers provide high precision of positioning for small arrays and small dielectric objects. However, they have a limited manipulation area which means that at large-scale and heterogeneous patterns, the resolution is reduced [26,27]. To reduce optical radiation forces, optoelectronic methodologies can be applied to trap cells. Optoelectronic tweezers (OET) can reduce energy 100,000 times compared with optical tweezers as mentioned by Chiou et al. [28] when used with a halogen lamp and a digital micromirror for parallel manipulation of cells that were trapped on a 1.3×1.0 mm^2 area with direct optical imaging control. They placed cells between an upper indium tin oxide-coated glass (ITO-coated glass), and lower multiple layers of photosensitive surfaces. This technique utilizes high-resolution virtual electrodes for single-cell manipulation and direct imaging to control live human B-cells and differentiates between dead cells, according to the image obtained and their dielectric properties. In addition, this technique permits high-resolution patterning using electric fields with less optical intensity than optical tweezers, therefore the differences in permeability, capacitance, conductivity, internal conductivity, and size allow one to discriminate between live cells and dead cells.

Furthermore, levels of radiation can reach ~10^7 W/cm^2 which could cause photodamage to cells (opticution) [29]. There are other variants such as plasmonic tweezers, and photonic crystal waveguides, however they are limited by heat generation and light intensity and could cause cell damage [30].

Non-contact optoelectronic manipulation can be applied for some bacteria that have high movability. Mishra et al. [29] used an electrokinetic technique to manipulate *Enterobacter aerogenes* that in suspension

reach >20 μm/s. They proved the optical radiation effect, laser-induced heating, and the electric field on bacteria viability. The system consisted of parallel-plate ITO-coated transparent electrodes separated by a 100 μm spacer to form a microchannel, a 1064 nm laser projecting into the microchannel through a 40X lens, and dark field imaging of bacteria cells. They used 10% BSA to avoid unspecific adherence to the electrodes and an AC electric field. Their experiments demonstrated that optical radiation and laser-induced heating have negligible effect on cell membranes. However, high electric field strength $\geq$200 KV_{pp} (peak to peak voltage), the combination of laser-induced temperature, and electrothermal flow can accelerate the poration of cells after ~5 min.

It is possible, by the use of OET, to reach large-scale parallel manipulation and low-intensity optical trapping. Jing et al. [30] proposed modulated light fields to trap mammalian, yeast, and *Escherichia coli* cells, on the surface of a two-dimensional photonic crystal. They fabricated a silicon photocrystal coated with parylene-C to planarize the surface and provide an adequate refractive index. Circular patterns were obtained by photolithography as parallel holes of 500 nm in depth. By using this methodology, they trapped different single cells at the pattern's surface without compromising their viability. They also proved that the aperture number of the lens did not affect the effectiveness of cell trapping and their methodology could be applied to miniaturize devices used for several types of cells.

Optoelectronic manipulation of cells is a feasible option for cell trapping and elaboration of microfluidic devices, due to remote and large-scale manipulation. Currently microfabrication techniques are enlarging their applications. Nonetheless, thermal effects and photodamage of cells must be critical factors in designing experimental systems with this methodology.

2.1.3. Laser-Based Cell Patterning

Laser-based direct writing technique to pattern cells, uses a laser to transfer or propel cells from one source film (donor, ribbon or target) to a receiving or acceptor substrate. This technique could be divided as follows [31]: Laser-induced forward transfer (LIFT), absorbing film-assisted laser-induced forward transfer (AFA-LIFT), biological laser processing (BioLP), matrix-assisted pulsed laser evaporation direct writing (MAPLE DW), and laser-guided direct writing (LGDW). LIFT, AFA-LIFT, BioLP, and MAPLE DW have a similar configuration and nowadays these techniques are referred to as laser direct-write (LDW). Hence, LDW combined with rat mesentery culture tissue have been employed to reproducibly print breast cancer cells (MDA-MB-231 and MCF-7) and fibroblasts on this ex vivo tissue [32]. In this article, it was recently demonstrated that by using this bioprinting technique, it was possible to locally pattern breast cancer cell groups to characterize cell movements during the angiogenesis.

The last laser-based cell pattering called laser-guided direct writing (LGDW), is a variation technique of the commonly used optical trap (laser tweezers, optical tweezers), capable of depositing cells on different matrices such as collagen or Matrigel, but is limited by the size of the specific cell [33]. LGDW is a technique that consists of guiding and propelling a stream of cells onto a target surface by using optical forces of a laser (700–1000 nm which is above the wavelength absorption of most proteins). It has been used to propel embryonic chick spinal cord cells of a distance of around 300 μm, through their culture medium, and deposited in an untreated glass coverslip (as target surface) [31]. A total of 76 cells were guided with an average deposition rate of 2.5 cells/min. To increase the distance of the cell guidance to the maximum of 7 mm, light was coupled into hollow optical fibers, verifying the cell viability. It was finally claimed that this technique, in comparison to laser tweezers, has the advantage of presenting a continuous stream of cells for deposition and a position precision of 1 μm, being adaptable to microfabrication methodologies.

2.1.4. Acoustic Force Patterning

Acoustic methodologies use surface acoustic waves (SAWs) for microscale manipulation with less energy than optical and optoelectronic approaches. SAWs, made of electrodes, are excited at different frequencies and deposited onto piezoelectric substrates. Common frequencies to generate SAW wavelengths from 1 to 300 nm are around 10 to 1000 MHz [34]. In acoustic manipulation systems,

the displacement resolution depends on the formed nodes and frequency because of the applied energy [35]. Most of the works have been focused on the reduction of time and energy required to pattern cells, conserving their functionality and viability as mentioned by Ding et al. [35]. Their system consisted of a lithium niobate ($LiNbO_3$) piezoelectric substrate collocated asymmetrically between two orthogonal pairs of interdigitated transducers (IDTs), with an independent radiofrequency signal. The orthogonal array formed four nodes around a polydimethylsiloxane (PDMS)-based microchannel that allowed total control in the displacement area. They found that the power density required to manipulate 10 μm polystyrene beads was ~0.5 $nW/\mu m^2$ for a particle, reaching velocities of ~30 μm/s at 18.5 MHz to 37 MHz. They patterned (letters) with bovine red blood cells and polystyrene beads, furthermore under the same conditions they immobilized a multicellular microorganism *Caenorhabditis elegans*, not finding significant generated heat. The viability of these cells did not deteriorate.

Acoustic methods can be applied for 3D microsystems as well. Recently Nasser et al. [36] used self-assembled monolayers (SAMs) to align cardiomyocytes mixed with cardiac fibroblasts in an extracellular matrix-based gelatin methacryloyl (GelMA). The piezoelectric substrate was lithium niobate ($LiNbO_3$) and slanted-finger interdigital transducers (SFITs) were fabricated. The alignment was obtained in less than 10 s. The cells conserved their functionality after 5–7 days, this indicated that this methodology is suitable to create 3D biomimetic structures for rapidly encapsulating cells.

The migration of cells, subjected to acoustic waves is called acoustophoresis, and is dependent on the physical properties of cells such as size, compressibility, and density but also on the viscosity and fluidic properties of the medium. Most of the cells have a positive acoustic contrast factor that implies an attraction to nodes [37]. The principle of acoustophoretic microdevices is the same, that is, a piezoelectric platform and IDTs are needed to produce SAWs to generate cell movements in a continuous flow due to the acoustic force. The design created by Ai et al. [37] to separate *Escherichia coli* (*E. coli*) from human peripheral blood mononuclear cells (PBMCs) in a silicon-based microchannel demonstrated that the pressure nodes created on the sidewalls of the microchannel were perpendicular to the piezoelectric base, and the biggest cells (PBMCs) were attracted to nodes which were separated in different outlets, with an efficacy of 95.65% in continuous flow.

An acoustic method does not compromise cell viability, it is a chemical free technique to manipulate cells with less energy compared with an optical method and it is a rapid contactless technique, nonetheless a previous simulation process with the corresponding mathematical models could predict the behavior of cells, improving the results as in other physical methods.

2.1.5. Electrokinetic Forces (Dielectrophoresis)

Dielectrophoresis (DEP) is considered an active method of cell manipulation because it requires energy to move cells. This technique combines electrokinetic forces with hydrodynamic effects to achieve cell trapping or lead cells to specific areas without damaging them. A cell has polarization in the surrounding media caused by an electric field. A dipole moment is induced by the electric field thereby moving cells, and depending on their permittivity and the polarizability of the surrounding media, the cells can be attracted to the electric field in the direction of the gradient (positive) or repelled, opposite to the gradient (negative) [38,39]. These considerations are important because cells can be separated from a mixture, as a positive and negative charge at first approach and then selecting the appropriate frequency, cells can be separated into groups usually at frequencies between 10 kHz to 100 MHz [13]. Cells can also be separated using combined methods such as flow separation, field-flow fractionation (FFF) (by sedimentation, temperature or viscosity), and travelling-wave mechanisms [38]. However, the displacement of cells becomes slow when the dielectric force decreases due to the separation distance of electrodes along the test area. To solve this problem, modern micro-nanofabrication techniques permit the elaboration of different geometries of nanometer-scale electrodes that can improve the area and the distribution of the electric field, using different arrays. These arrays have been widely used for medical microdevices. For example, Gascoyne et al. [13], detected malaria-infected cells from human blood by dielectrophoretic manipulation, using two types of microelectrode arrays. An interdigitated

electrode array, operated at 5 V_{pp} and 200 kHz, was used to separate the parasitized erythrocytes by negative electrophoresis, and then a spiral electrode array operated with four-phase excitation at 3 V_{pp} and 2 MHz to concentrate parasitized erythrocytes at the center of the spiral was presented. In this particular case, parasitized erythrocytes, having pores due to the infection, they exhibited a loss of ions, changing their permittivity and membrane properties which facilitated their dielectric differentiation.

Actually, not only nanometer electrode arrays, and dielectrophoresis traps have improved cell manipulation, but control mechanisms have been integrated for this purpose. Recently, Sadeghian et al. [39] elaborated a microfluidic actuator with gold interdigitated electrode patterns to separate white blood cells (k562-cells) from polystyrene particles. They performed an optimization by finite element simulation in COMSOL Multiphysics 5, and according to their results, geometric parameters such as pitch, width to pitch ratio, and channel height are important because the gradient of the generated electric field depends on these factors. Efficiency of recovery was 93% with 100% of purity at 7.5 V_{pp} and 800 MHz. It was concluded that in their interdigitated electrode array the electrodes-pitch should be as close as possible. The channel must have a minimum height, and the voltage should be as high as possible but avoiding cell damage to achieve cell separation [39].

Furthermore, dielectrophoretic manipulation of cells has been applied to tissue engineering to align different types of cells in complex tissues as demonstrated by Ho et al. [40]; through positive dielectrophoresis (DEP), biomimetic alignment of lobular liver tissue was achieved, employing a concentric-stellate-type electrode array that generates radial-pattern electric fields to guide individual cells. This cell-patterning microfluidic chip was fabricated on glass and PDMS, and planar electrodes were placed in a concentric ring array which provided the formation of pearl-chain like patterns. These patterns were stabilized because of the stellate-tip designed in the electrodes, which enhanced the distribution of the electric field with local maximum gradients inside the concentric-ring array, tangentially between the adjacent stellate-tip electrode rings.

Dielectric differentiation and manipulation could be applied not only to stem cells, cancer cells, and other biomolecules and particles associated with many pathologies, but also to microorganisms which may cause diseases in humans. D'Amico et al. [41] employed a 4-pole microelectrode geometry to detect low levels of *Escherichia coli* [41] and *Staphylococcus aureus* from human blood using a combined membraneless microdialysis and dielectrophoresis system. They isolated 79% of *E. coli* and 78% of *S. aureus* from minimal blood sample volumes. To reach bacteria separation, they used monensin to permeabilize blood cells and alter their cytoelectric properties to separate cells in their microfluidic system (Figure 2). This label-free methodology can be applied to detect other pathogens directly from biological samples reducing costs, time, instrumentation, cross contamination, and sample amounts through the microfabrication techniques for miniaturization procedures.

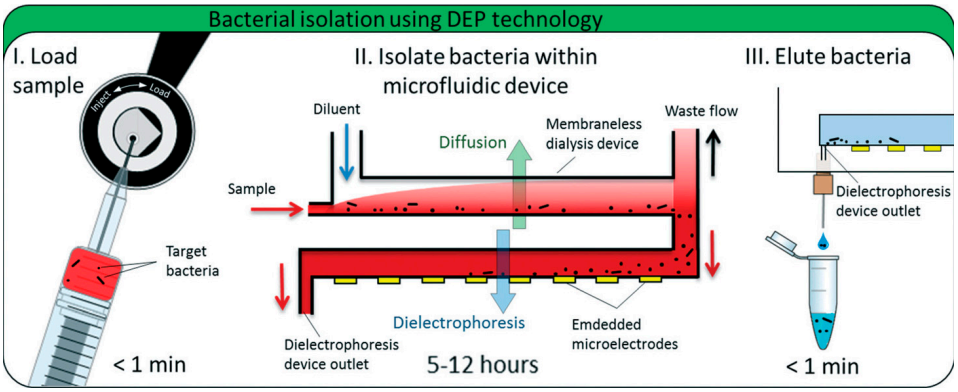

Figure 2. A microfluidic device to detect and separate pathogen bacteria from human blood. (**I**) Blood sample mixed with permeabilizing agent is loaded and injected, (**II**) The sample is pumped to the microfluidic device, (**III**) Target bacteria are eluted for further analysis. Reproduced with permission from [41].

2.1.6. Magnetic Cell Manipulation

Magnetic force and magnetic biomaterials can guide cells for tissue engineering applications which require complex and functional tissue organization. Some have used magnetic manipulation to form patterns with complex architectures, Ino et al. [42] used magnetite cationic liposomes (MCLs) to label mouse NIH/3T3 fibroblasts (FB) and human umbilical vein endothelial cells (HUVECs) to form different patterns by using steel plates and a magnet (Figure 3). They proved variants such as cell patterning by laser-cut devices, and cell patterning of HUVECs onto Matrigel to create complex capillaries. Their results show non-toxic effects on cells, and very good formation of capillaries and branches by sequenced patterning.

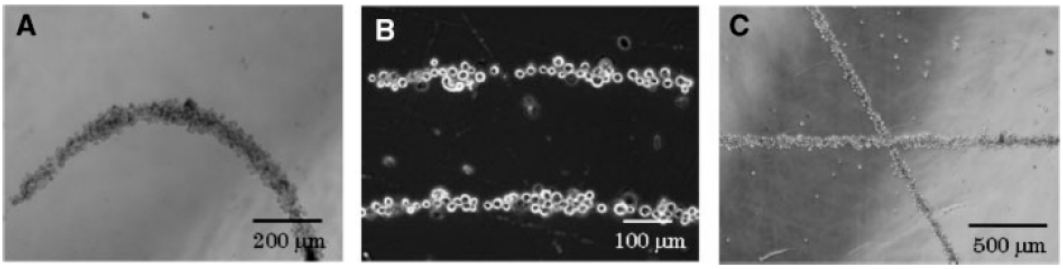

Figure 3. Phase-microscope images of cell patterns created by magnetic forces. (**A**) Fibroblasts (FB) curve patterns; (**B**) FB parallel patterns; (**C**) FB crossing patterns. Reproduced with permission from [42].

Another novel system using magnetic force, was a 3D magnetic bioprinting system to carry out uterine rings from patient cells. Souza et al. [43] obtained uterine rings of human myometrial cells. The cells were magnetized with biocompatible gold nanoparticles, iron oxide, and Poly-L-Lysine, which do not alter the behavior of cells. After a magnetization procedure, re-suspended cells were collocated under 384-well plates on the magnets to form tight ring structures per well. This fast patterning was used to study contractility of different inhibitors simultaneously with interesting results. Their multiple test in vitro showed differences in contractility response even when all the cells were from women. This fact demonstrates the differences between biological samples and the importance of personalized medicine in the near future as well as rapid patterning techniques.

The necessity of single-cell studies of cell membrane functionality, the interaction with new drugs, the detection and sorting among other biological applications are now boosting single-cell arrays with magnetic approaches. Magnetic arrays are suitable for bacteria patterning despite the fact that bacteria cells are smaller than mammalian cells. Pivetal et al. [44] fabricated, by using reversed magnetization with thermomagnetic patterning, a patterned array of 7.5 × 7.5 mm^2 micromagnets. Bacteria were labelled magnetically by immunomagnetic in situ hybridization to increase specificity and guarantee bacteria fixation (Figure 4). The above paper reported that both labelling techniques and fixed bacteria conserved their membranes thus being suitable for further studies.

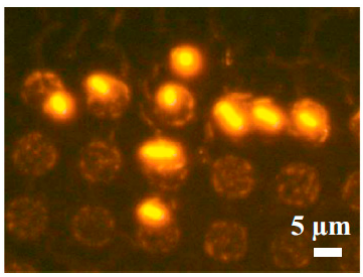

Figure 4. *E. coli* stained with ethidium bromide to observe individual cell-trapping on a micro-magnet array. Reproduced with permission from [44].

In this context, magnetic patterning is specific for mammalian and bacteria cells. However, the technique requires cell labelling with biocompatible magnetic particles.

Micromachines **2017**, *8*, 347 8 of 20

In this context, magnetic patterning is specific for mammalian and bacteria cells. However, the technique requires cell labelling with biocompatible magnetic particles.

2.2. Chemical Patterning for Cells Assembly

Surface Chemistry Methodologies

Cells also have the ability to sense the environment around them, especially the surface where they are adhered. It is thus possible to take advantage of this property to pattern adhesive and anti-adhesive molecules and therefore order the cells on a surface. Proteins from the extra cellular matrix, like fibronectin, laminin or collagen, are preferred to glass or Poly(L-lysine)-graft-poly(ethylene glycol) (PLL-g-PEG) by the cells. This makes it possible to control the localization of the cells. Moreover, patterning special forms of adhesive molecules has been performed. Disc, crossbow, H, Y, L and many more were created and are commercially available for fundamental research in cancer cell adhesion, architecture or mechanotransduction [45–48].

Surface Chemistry Methodologies

Cells also have the ability to sense the environment around them, especially the surface where they are adhered. It is thus possible to take advantage of this property to pattern adhesive and anti-adhesive molecules and therefore order the cells on a surface. Proteins from the extra cellular matrix, like fibronectin, laminin or collagen, are preferred to glass or Poly(L-lysine)-graft-poly(ethylene glycol) (PLL-g-PEG) by the cells. This makes it possible to control the localization of the cells. Moreover, patterning special forms of adhesive molecules has been performed. Disc, crossbow, H, Y, L and many more were created and are commercially available for fundamental research in cancer cell adhesion, architecture or mechanotransduction [45–48].

This technique has been used by Théry et al. [47], to better understand the role of the adhesive microenvironment and of the cell internal organization on the polarity. They demonstrated that the microtubule distribution, the position of the nucleus, centrosome and Golgi apparatus, depend on the shape of the printed ECM proteins. Thanks to this approach they established a link between the extracellular adhesion, the organelles organization, and the cell polarity. In the same study, the concept of the average cell was proposed. Fluorescence coming from different dyes is collected and several cells immobilized on the same sort of pattern. The pattern has the advantage of imposing a shape to the cells. Thus, combining several fluorescence images of several cells is possible. This was strictly impossible with cells freely sticking on a surface, because each cell would take a different shape. There is a clear statistical interest to pattern and create arrays of cells having the same shape. Thereby, it is easier to compare the behavior of cells having the same shape.

This technique has been used by Théry et al. [47], to better understand the role of the adhesive microenvironment and of the cell internal organization on the polarity. They demonstrated that the microtubule distribution, the position of the nucleus, centrosome and Golgi apparatus, depend on the shape of the printed ECM proteins. Thanks to this approach they established a link between the extracellular adhesion, the organelles organization, and the cell polarity. In the same study, the concept of the average cell was proposed. Fluorescence coming from different dyes is collected and several cells immobilized on the same sort of pattern. The pattern has the advantage of imposing a shape to the cells. Thus, combining several fluorescence images of several cells is possible. This was strictly impossible with cells freely sticking on a surface, because each cell would take a different shape. There is a clear statistical interest to pattern and create arrays of cells having the same shape. Thereby, it is easier to compare the behavior of cells having the same shape.

In microbiology, matrix proteins have not been used to immobilize bacteria or yeast. On the contrary some work relies on electrostatic interactions between a positively charged surface and negatively charged microbes. Polyethylenimine (PEI), Poly-L-Lysine (PLL) or 3-aminopropyltriethoxysilane (APTES) were used to immobilize microbes [49–53]. Only recently have researchers been interested in patterning positive charges to create bacteria arrays. In 2008, Ressier et al. [54] used Atomic Force Microscope (AFM) oxidation lithography to create patterns of SiO_x on a hydrophobic Self Assembled Mono-lay (SAM) of octadecyltrimethoxysilane (OTMS). The convective/capillary technique to direct the assembly of *E. coli* cells on the SiOx pattern was used (Figure 5). A more uniform pattern was achieved.

In microbiology, matrix proteins have not been used to immobilize bacteria or yeast. On the contrary some work relies on electrostatic interactions between a positively charged surface and negatively charged microbes. Polyethylenimine (PEI), Poly-L-Lysine (PLL) or 3-aminopropyltriethoxysilane (APTES) were used to immobilize microbes [49–53]. Only recently have researchers been interested in patterning positive charges to create bacteria arrays. In 2008, Ressier et al. [54] used Atomic Force Microscope (AFM) oxidation lithography to create patterns of SiO_x on a hydrophobic Self Assembled Mono-lay (SAM) of octadecyltrimethoxysilane (OTMS). The convective/capillary technique to direct the assembly of *E. coli* cells on the SiOx pattern was used (Figure 5). A more uniform pattern was achieved.

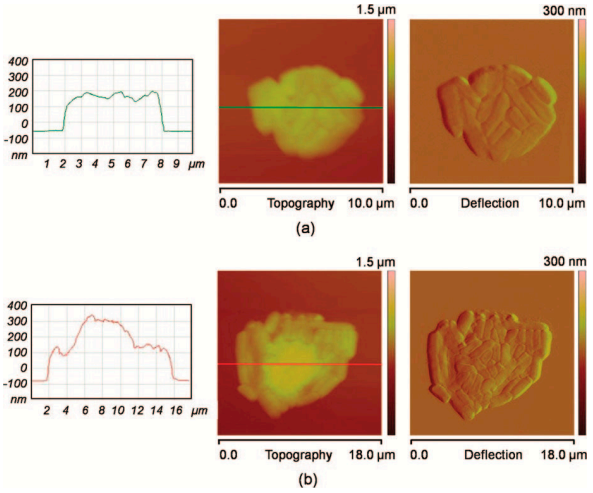

Figure 5. *E. coli* bacteria onto SiO_x patterns, observed by atomic force microscope (AFM) in contact mode: meniscus dragging speeds of (**a**) 1 µm/s and (**b**) 0.5 µm/s. Reproduced with permission from [54].

Figure 5. *E. coli* bacteria onto SiO_x patterns, observed by atomic force microscope (AFM) in contact mode: meniscus dragging speeds of (**a**) 1 µm/s and (**b**) 0.5 µm/s. Reproduced with permission from [54].

In another study, Cerf et al. [55], used micro contact printing to create an anti-adhesive sea made of octadecyltrichlorosilane (OTS) and organized positively charged islands made of APTES. Thanks to this development they were able to assemble arrays of *E. coli* cells that were analyzed by AFM nanomechanical experiments. Cells killed by heating, were found to be stiffer than normal cells deposited on the pattern. Figure 6 shows the array of bacteria prepared on the bifunctional (adhesive: APTES positive charges and anti-adhesive: OTS) surface.

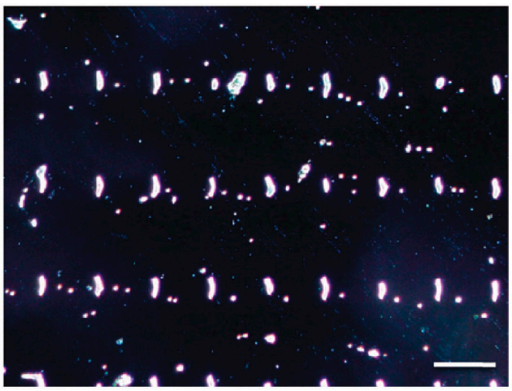

Figure 6. Patterned bacteria onto functionalized surface with 3-aminopropyltriethoxysilane (APTES) (1100 × 1000 μm^2 dark field image with a scale bar that measures 30 μm). Reproduced with permission from [55].

More recently Jauvert et al. [56], used high molecular weight PEI molecules to create a pattern of positive charges. In this work, negative patterns are created on a PMMA thin film, by nanoxerography or electrical micro contact printing. The surfaces were then immersed in PEI solution, and finally dried after a final immersion in ethanol. The PEI thickness is controlled by the amount of charge injected during the nanoxerography process, resulting in a control of the positive charge on the pattern and finally on the number of bacteria immobilized on each pattern. Figure 7 shows this dependency.

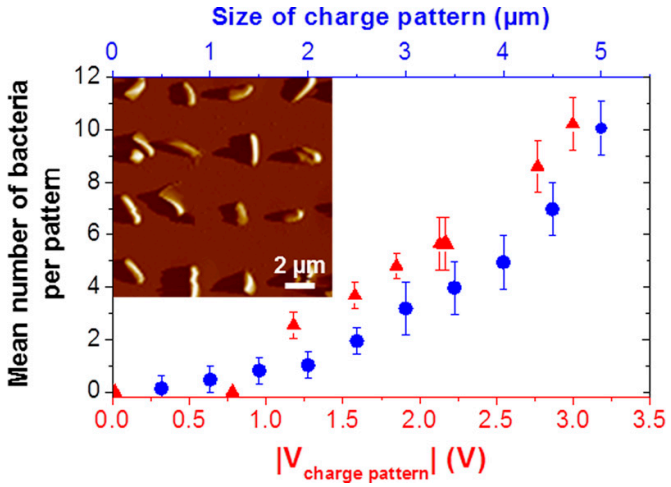

Figure 7. AFM deflection image, in a buffer medium, of an arrays of single *Pseudomonas aeruginosa* bacteria immobilized on polyethylenimine (PEI) patterns, with the lateral size (blue disk symbols) and charge patterns (red triangle symbols). Reproduced with permission from [56].

2.3. Physical and Chemical Patterning

2.3.1. Microcontact Printing Overview

Microcontact printing (μCP) is an accessible lithography technique first introduced by the Whiteside group [57]. It relies on a stamp made of an elastomeric material usually polydimethylsiloxane (PDMS) cast on a master mold (usually silicon). The unmold stamp is inked and let to dry. Finally, the ink is transferred onto a surface by contact. The contact is said to be conformational as the stamp elastic properties allow it to make conformal contact even on rough surfaces resulting in a high-quality transfer of the ink onto the surface. Although microcontact printing can be used to produce nanoscale patterns down to 40 nm line grating [58] and even 2 nm using nanotubes to mold the stamp [59], nano-lithographic facilities are required and are quite expensive and not necessary for cell adhesion. Microcontact printing is often presented as an accessible technology necessitating only a simple laser printer, spin coating and UV lamp to perform rapid prototyping of master molds [60] with features larger than 20 μm largely sufficient for cell patterning. Features larger than 2 μm have since become easily affordable as master molds can be ordered from specialized companies for a few hundred dollars and can then be used to produce an unlimited number of PDMS stamps. Since the first publication revealing cells attached to surface patterns using μCP [61], several reviews on microcontact printing have addressed in part the use of microcontact printing to attach cells onto surfaces [62–64]. Here we highlight some of the recent advances that have been made in the different steps involved in the μCP process: mold, inking process, stamping process or stamped surface/material.

Fabricating a master mold is both expensive and time consuming. One way to avoid breaking the original silicon master mold is to make replicas in epoxy or polyurethane using PDMS stamps made from the original mold [65]. Fabricating a mold is often time consuming as it requires time to design it, instead why not use natural materials to produce patterns? Wong et al. [66] have used the vascular system of a leaf to produce a bioinspired PDMS mold. This mold was successfully used to grow endothelial cells into vascular channels.

Often when considering technical options offered by μCP, the choice of ink seems the most viable. Which molecule will attach best to the cells used? What influence will the ink molecules have on the attached cells? Which molecule will prevent attachment outside the defined patterns? (These questions have mostly been answered in previously cited reviews.). Yet, cells are seldom considered as the actual ink. Malaquin et al. [67] used an inking technique derived from capillary assembly where a meniscus displacement was used to push and capture particles into grooves at the surface of a PDMS stamp. Capillary assembly has also been used to improve inking of molecules onto PDMS stamps resulting in much improved prints [68,69], using specific antibody coated at the surface of the particles and targeting cell membrane proteins. Delapierre et al. were able to capture and place specific types of cells onto the stamp [70]. Alternate grooves at 90° angle to each others allowed the alternate capture of particles coated with different antibodies capable of attaching two different cell types on the stamp.

Automation [71] and robotics [72,73] have improved the robustness of the printing process. These commercial systems can align prints with sub-10 μm precision in a repetitive fashion and several different molecules can be printed. This opens the path to more complex devices with different specific cells at specific positions. However, the robustness of the printing process is dominated by the interaction between the ink and the surface. Humidified Microcontact printing is a new process for printing biomolecules susceptible to attach cells onto low energy surfaces such as plastic Petri-dishes. In this respect Ricoult et al. [74] showed that flowing water in channels next to proteins at the contact area between the stamp and the surface, improves the quality of prints on both low and high energy surfaces while increasing the distance from the water channel decreases print quality. Relative humidity at 88% in the stamp was found to be the threshold to increase the transfer of proteins and the overall robustness of the printing process.

If glass and plastic Petri-dish surfaces are more commonly used for μCP, improvements in μCP can come from the surface on which molecules or cells are immobilized. Polio and Smith [75] developed

a methodology to perform μCP on poly-acrylamide hydrogels to study 2D cellular traction forces. They advantageously used a microcontact printed coverslip to transfer alternate patterns of gelatin and fibronectin onto the surface of the hydrogel. Gels and scaffolds are increasingly being used for tissue engineering and to understand cells and tissue mechanobiology. An example of such an experiment is illustrated in the study by Vedula et al. [76] which shows that epithelial bridges between cells separated by tracks maintain tissue integrity during cell migration. In this case microcontact printing was performed to print fibronectin on top of non-adherent polymer tracks. A suspended membrane formed between the tracks as collective cellular migration took place. This last example illustrates how microcontact printing has become a versatile accessible technique for biology.

The use of PDMS based stamps in biology is not limited to microcontact printing and has also led to a new form of cell patterning using physical capture through microwells and using microfluidic devices that are shown in the following sections.

2.3.2. Microwells and Filtration

In an attempt to minimize the surface chemistry, microstructured surfaces or used porous membranes to immobilize round shaped cells have been developed. Figure 8 presents a single *Lactococcus lactis* cell trapped in a pore of a polycarbonate membrane. This technique has been extensively used to trap bacteria and yeast for AFM experiments [77].

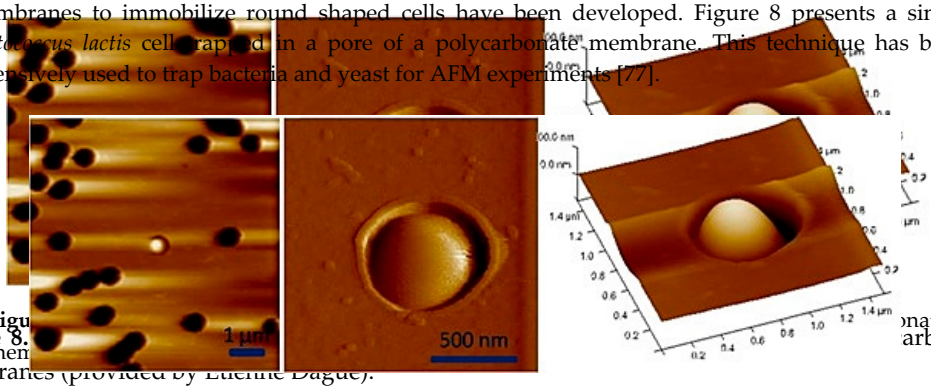

Figure 8. AFM images of the immobilization of *Lactococcus lactis* cell in pores of polycarbonate membranes (provided by Etienne Dague).

Unfortunately, the filling rate of the pores is often very low, and it is time consuming to localize a cell and perform topographical experiments. In order to overcome this problem Kailas et al. [78] developed a lithographically patterned substrate to immobilize *Staphylococcus aureus* cells (Figure 9). In this method, no chemicals are used to immobilize the cell and the confinement is minimized as compared to the filter solution because no sucking step is performed. However, an evaporation step of 15 to 20 min is required to allow the cells to settle into the patterns. Thanks to this device, it was possible to follow the cell division process under AFM.

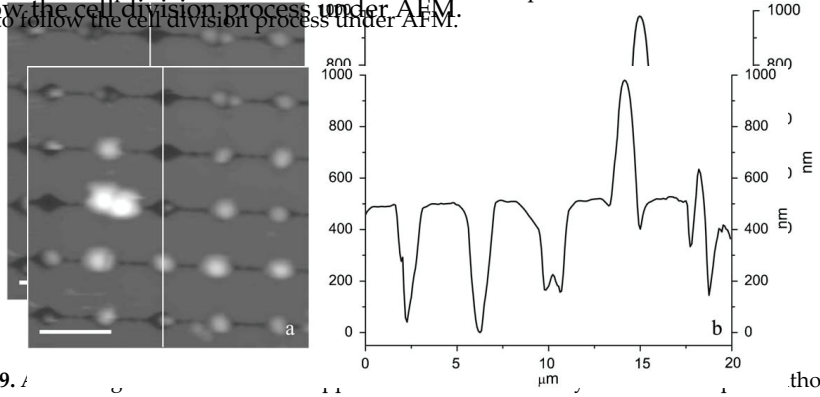

Figure 9. AFM image of *S. aureus* cells trapped in holes elaborated by contact mask photolithography and their variation in height measured by AFM. Reproduced with permission from [78].

Furthermore, Dague et al. [13,79] developed a microstructured PDMS stamp presenting various holes size, ranging from 1.5×1.5 μm^2 to 6×6 μm^2. The stamp is prepared by molding PDMS on a silicon master with negative patterns (Figure 10). The silicon master is elaborated by performing conventional photolithography and reactive ion etching. The authors demonstrated that the PDMS

Furthermore, Dague et al. [15,79] developed a microstructured PDMS stamp presenting various holes size, ranging from 1.5 × 1.5 μm^2 to 6 × 6 μm^2. The stamp is prepared by molding PDMS on a silicon master with negative patterns (Figure 10). The silicon master is elaborated by performing conventional photolithography and reactive ion etching. The authors demonstrated that the PDMS stamp is suitable for immobilizing not only bacteria and yeasts, but also algae and eukaryotic cell nuclei [15]. To achieve a higher filling rate of the hole, the authors took advantage of convective/capillary deposition and achieved a filling rate of up to 85%. Such a development is a step toward the fabrication of reproducible microbial cell arrays where each cell can be probed individually. Thanks to such developments, it will be possible in the near future to access the population heterogeneity, which is known to be a key factor in bacterial resistance acquisition, for instance.

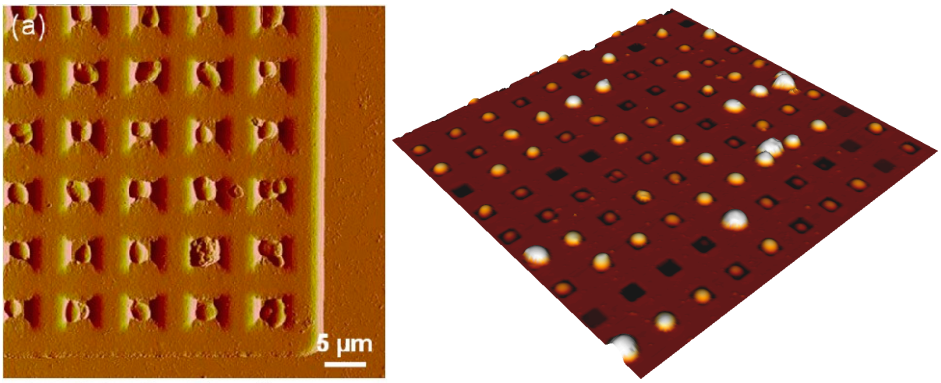

Figure 10. AFM images of *S. cerevisiae* yeast trapped in polydimethylsiloxane (PDMS) patterns functionalized by Concanavalin A (on the left) reproduced with permission from [79] and AFM 3D height image of *C. albicans* cell array trapped in microwells made of PDMS stamps (on the right). Reproduced with permission from [15].

2.3.3. Cell Patterning in Microfluidic Devices Combined with Microcontact Printing

Micropatterning cells inside microfluidic devices has enormous research application; to implement 3D culture of a specific cell line for instance and then to study cell signaling, proliferation or cell migration. In this context, a method to pattern cell culture inside a microfluidic device was reported [80] in which success was achieved in implementing the binding and sterilization, in one step, of human umbilical vein endothelial cells (HUVEC), MDA-MB-231 breast cancer cells, and NIH 3T3 mouse fibroblasts. As it is a physicochemical patterning methodology, a substrate with PLL, collagen, and other extracellular matrix (ECM) proteins (cell-adhesive) was functionalized, by using microcontact printing (μCP) and the plasma-based dry etching process to bond and etch away some parts that were not in contact with the PDMS, to finally integrate a PDMS-based microchannel piece and to complete the microfluidic device. In a more recent article [81], a microfluidic cell patterning method was developed to form patterned 3D multicellular aggregates (spheroids) of multiple cell types. This device was composed of one top PDMS channel, sandwiching a semi-porous polycarbonate membrane and a bottom PDMS channel, so that the flow and cells pass through them. Finally, the group of Xuesong Ye et al. [82], in a very recent experiment, developed a microfluidic chip to pattern two cancer cell lines; HeLa and human gallbladder carcinoma cells (SGC-996) and were able to observe phenomena such as colony formation, cell migration, and cell proliferation. Firstly, PLL and Laminin proteins were printed with μCP and then a PDMS stamp, carrying paired microwells, was incubated on the substrate of the microfluidic chip (Figure 11). They employed a SU-8 photolithographical process to elaborate the different utilized pieces to finally implement cell patterning in 5 min, the loading of cells was performed by a syringe pump.

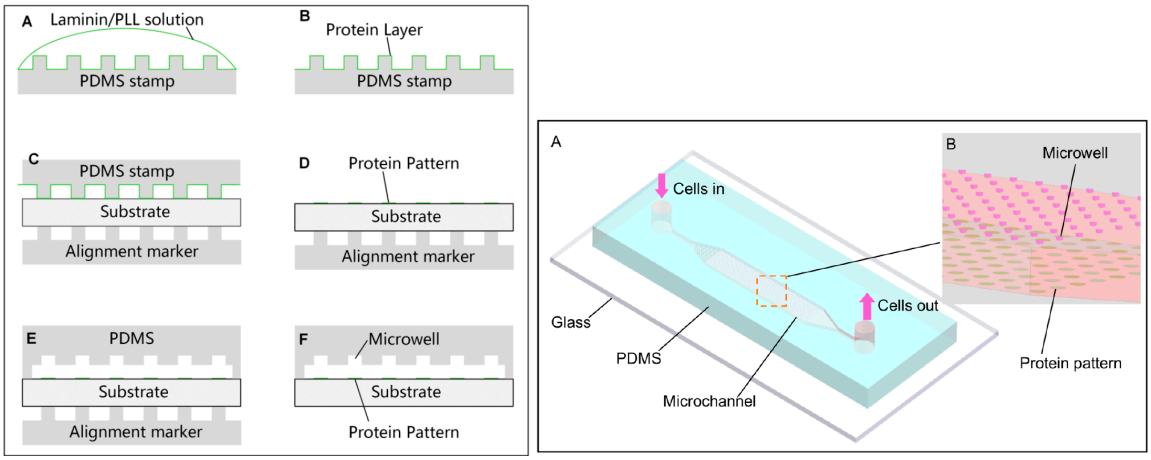

Figure 11. On the left, a schema of a PDMS stamp with microwells to fabricate the microfluidic device, showing protein incubation (**A**,**B**), patterned proteins on the substrate (**C**,**D**) and microwell paring with a PDMS alignment marker. On the right, a schema of the final microfluidic chip showing triangular microwells where cells are captured. Reproduced with permission from [82].

2.3.4. Deep UV Micropatterning

This methodology applies wavelengths of below 280 nm in the region of deep UV (DUV) to obtain micropatterns, it requires a predesigned photomask sensitive to those wavelengths. The material used in a photomask especially for deep UV is normally natural quartz, synthetic quartz or fused silica [83]. However, this technology has also been used for glass and PDMS combined with a coating of PLL and PLL-g-PEG to facilitate cell adhesion [84,85]. Alvéole PRIMO® technology [86], based on light induced molecular adsorption of proteins (LIMAP), enables protein micropatterning to adhere specific cells. The photoactivable reagent is exposed to UV light (PRIMO module) to obtain patterns of up to 1.2 µm resolution. This approach facilitates the manipulation and elaboration of cell arrays for measuring and it is possible to combine this technique with conventional processes.

Hulshof et al. [87] used deep UV lithography in combination with conventional lithography to fabricate more than 1200 different nanotopographies for cell cultivation. U2OS osteosarcoma cells were cultured in their chip to measure cell spreading, orientation, and actin morphology in their topography designs which include lines, circles, and triangles in different arrays of 200 nm to 700 nm. They observed relevant changes in cell behavior related to their topographies.

This technology is mainly used by biologists because it does not require expensive facilities to perform the process and it is a better method for cell manipulation.

3. Perspective: Automatic Biophysical Measurements on Patterned Cells

Based on the variety of techniques to pattern different kinds of cells, it seems that the next step is to perform biophysical measurements on them automatically (e.g., mechanical, force distribution). At present only a few researchers are taking advantage of cell arrays to develop automated systems. For instance Li et al. [88] designed a nanomanipulator to integrate it in an Atomic Force Microscope (AFM). They tested this system analyzing lymphoma Raji cells. Pillars (5 µm in height and 10 µm in diameter) were elaborated and then coated with Poly-L-Lysine (PLL) so the lymphoma cells were vertically trapped. Another example was published by Fortier et al. [89] where microwells were elaborated onto a glass coverslip coated with SU-8 film using a soft lithography technique to obtain an array of circular wells (20 µm in diameter, 7 µm in height). Then, the mechanical properties of fixed leukemia cells (NB4) were measured, implementing an automated system for the data analysis; their software processed 147 force curves taken at different applied forces with the objective of determining which geometry tip (spherical or conical) was more convenient for NB4

cells. Eleonora Minelli et al. [90], recently reported a fully automated neural network based algorithm to analyze 200 approach/retract force-distance (FD) curves, taken by AFM, applied to brain cancer tissues. In this respect, we are developing a methodology which permits us to obtain and analyze automatically thousands of biophysical measurements of both mammalian and bacterial cells, in a few hours.

4. Conclusions and Perspective

Physical and chemical micropatterning techniques have improved rapidly and several methodologies are emerging. The selection of the best technique will depend primarily on the purpose as well as the biomaterials involved, the experimental design, and the micro-nanofabrication techniques. On the one hand, physical methods for cell trapping such as inkjet printing, optoelectronic, acoustic, dielectrophoretic, laser-based, and magnetic techniques provide high specificity to sort and collocate cells in predesigned patterns. This may simplify further tests and considerably reduce costs, the amount of material used and biological samples for high-throughput analysis. However, with these methods collateral effects on cells such as opticution, poration, or cell damage can appear because of the thermal effects caused by external energy sources. These physical-active techniques can be efficient, highly specific and reproducible, but it is necessary to identify the critical factors for each technique (Table 1), to conserve viability and cell functionality.

On the other hand, the use of surface chemistry based methodologies provide an efficient way to fix cells on surfaces taking advantage of biomolecule specific recognition by cell receptors and chemical bonding between different functional groups which allow high adhesion, specificity or the opposite effect such as repelling adhesion. Micropatterning techniques such as microcontact printing have extended their applications even in the microfluidic area and novel in vitro models with patterned cells are increasing and impacting on future studies related to intracellular sensing; 3D portable in vitro models for diagnosis and therapy, used in point-of-care (POC) biomedical devices. All these technological advances have greatly expanded the development of biomedical microdevices and high-performance platforms to automatically analyze cells as medical applications are emerging, with great academic and industrial impact.

Table 1. Advantages and disadvantages of cell patterning and manipulation techniques.

Technique	Advantage	Disadvantage
Inkjet printing (Physical)	Moderate cost Good controllability	Droplet formation Requires an external power source
Optical and optoelectronic cell trapping (Physical)	Remote and large-scale manipulation Highly specific due to the intrinsic charge and dielectric properties of cells	Thermal effects and photodamage in cells Requires an external power source
Laser-based cell patterning (Physical)	Cells and any particles can be manipulated	Large instrumentation Complex set-up
Acoustic patterning (Physical)	No significant heat generation and no effects on cell viability	Requires an external power source, piezoelectric surface, and electrode fabrication.
Dielectrophoresis (Physical)	Combine electrokinetic forces with hydrodynamic effects High-resolution patterning Large-scale parallel manipulation	Requires an external power source Dielectric force decreases due to the separation distance of electrodes
Magnetic techniques (Physical)	Remote manipulation High-resolution patterning, No stress behavior on cells	Magnets and labelling cells with magnetic particles are required
Surface chemistry methodologies (Chemical)	High precision and recognition by receptor or specific functional groups between the surface and cells	Pretreated surface is required The surface chemistry could modify the functionality of cells
Microcontact printing (Physicochemical)	Low cost, rapid prototyping	Difficulty in controlling the ink and the surface robustness
Microwells and filtration (Physicochemical)	Minimize the surface chemistry and conservation of cell functionality	Time consuming placing numerous cells inside microwells
DUV patterning (Physicochemical)	It does not require expensive facilities	The resolution depends on the photomask design and patterning substrate.
Cell patterning in microfluidic devices combined with microcontact printing (Physicochemical)	Study 3D culture cells and specialized biomedical microdevices	Requires specialized facilities, integration of techniques

Acknowledgments: We want to acknowledge FONCYCYT of CONACYT (Mexico), the Ministry of Foreign Affairs of France the Université Paris 13, through the financial support of the collaborative ECOS-NORD project named Nano-palpation for diagnosis, No. 263337 (Mexico) and M15P02 (France). AMR would like to thank the financial support of SIP-IPN through the project No. 20170067. GKGQ thanks to CONACYT for the Catedra program and to the CNMN-IPN for the support of developing her research activities. SPC is supported by a PhD fellowship from CONACYT (No. 288029).

Conflicts of Interest: The authors declare no conflict of interest.

References

1. Martinez-Rivas, A.; González-Quijano, G.K. Micro and nanoengineering advances for the development and commercialization of organ-on-chips. *Biol. Eng. Med.* **2017**, *2*, 2. [CrossRef]
2. Shirure, V.S.; George, S.C. Design considerations to minimize the impact of drug absorption in polymer-based organ-on-a-chip platforms. *Lab Chip* **2017**, *17*, 681–690. [CrossRef] [PubMed]
3. Ware, B.R.; Berger, D.R.; Khetani, S.R. Prediction of Drug-Induced Liver Injury in Micropatterned Co-cultures Containing iPSC-Derived Human Hepatocytes. *Toxicol. Sci.* **2015**, *145*, 252–262. [CrossRef] [PubMed]
4. Griep, L.M.; Wolbers, F.; de Wagenaar, B.; ter Braak, P.M.; Weksler, B.B.; Romero, I.A.; Couraud, P.O.; Vermes, I.; van der Meer, A.D.; van den Berg, A. BBB on chip: Microfluidic platform to mechanically and biochemically modulate blood-brain barrier function. *Biomed. Microdevices* **2013**, *15*, 145–150. [CrossRef] [PubMed]
5. Zhao, J.; Cao, Y.; DiPietro, L.A.; Liang, J. Dynamic cellular finite-element method for modelling large-scale cell migration and proliferation under the control of mechanical and biochemical cues: A study of re-epithelialization. *J. R. Soc. Interface* **2017**, *14*, 20160959. [CrossRef] [PubMed]
6. Phan, D.T.; Bender, R.H.F.; Andrejecsk, J.W.; Sobrino, A.; Hachey, S.J.; George, S.C.; Hughes, C.C. Blood–brain barrier-on-a-chip: Microphysiological systems that capture the complexity of the blood–central nervous system interface. *Exp. Biol. Med.* **2017**, *242*, 1669–1678. [CrossRef] [PubMed]
7. Huh, D.; Matthews, B.D.; Mammoto, A.; Montoya-Zavala, M.; Hsin, H.Y.; Ingber, D.E. Reconstituting Organ-Level Lung Functions on a Chip. *Science* **2010**, *328*, 1662–1668. [CrossRef] [PubMed]
8. Beißner, N.; Lorenz, T.; Reichl, S. Chapter 11: Organ on chip. In *Microsystems for Pharmatechnology: Manipulation of Fluids, Particles, Droplets, and Cells*; Dietzel, A., Ed.; Springer: Cham, Switzerland, 2016; pp. 299–339. [CrossRef]
9. Städler, B.; Falconnet, D.; Pfeiffer, I.; Höök, F.; Vörös, J. Micropatterning of DNA-Tagged Vesicles. *Langmuir* **2004**, *20*, 11348–11354. [CrossRef] [PubMed]
10. Estevam-Alves, R.; Ferreira, P.H.D.; Coatrini, A.C.; Oliveira, O.N.; Fontana, C.R.; Mendonca, C.R. Femtosecond Laser Patterning of the Biopolymer Chitosan for Biofilm Formation. *Int. J. Mol. Sci.* **2016**, *17*, 1243. [CrossRef] [PubMed]
11. Huang, G.; Mei, Y.; Thurmer, D.J.; Coric, E.; Schmidt, O.G. Rolled-up transparent microtubes as two-dimensionally confined culture scaffolds of individual yeast cells. *Lab Chip* **2009**, *9*, 263–268. [CrossRef] [PubMed]
12. Credi, C.; De Marco, C.; Molena, E.; Pla Roca, M.; Samitier Martí, J.; Marques, J.; Fernàndez-Busquets, X.; Levi, M.; Turri, S. Heparin micropatterning onto fouling-release perfluoropolyether-based polymers via photobiotin activation. *Colloids Surf. B Biointerfaces* **2016**, *146*, 250–259. [CrossRef] [PubMed]
13. Gascoyne, P.; Mahidol, C.; Ruchirawat, M.; Satayavivad, J.; Watcharasit, P.; Becker, F.F. Microsample preparation by dielectrophoresis: Isolation of malaria. *Lab Chip* **2002**, *2*, 70–75. [CrossRef] [PubMed]
14. Lee, Y.; Lee, H.J.; Jin Son, K.; Koh, W.-G. Fabrication of hydrogel-micropatterned nanofibers for highly sensitive microarray-based immunosensors having additional enzyme-based sensing capability. *J. Mater. Chem.* **2011**, *21*, 4476–4483. [CrossRef]
15. Formosa, C.; Pillet, F.; Schiavone, M.; Duval, R.E.; Ressier, L.; Dague, E. Generation of living cell arrays for atomic force microscopy studies. *Nat. Protoc.* **2015**, *10*, 199–204. [CrossRef] [PubMed]
16. Imamura, Y.; Mukohara, T.; Shimono, Y.; Funakoshi, Y.; Chayahara, N.; Toyoda, M.; Kiyota, N.; Takao, S.; Kono, S.; Nakatsura, T.; et al. Comparison of 2D- and 3D-culture models as drug-testing platforms in breast cancer. *Oncol. Rep.* **2015**, *33*, 1837–1843. [CrossRef] [PubMed]
17. Langer, R.; Tirrell, D.A. Designing materials for biology and medicine. *Nature* **2004**, *428*, 487–492. [CrossRef] [PubMed]

18. Martinez-Rivas, A.; González-Quijano, G.K. Capítulo 8: Nanobiosensores con aplicaciones en biomedicina. In *Nanobiotecnología: Fundamentos y Perspectivas*; Ramón-Gallegos, E., Ed.; Editorial Académica Española: Saarbrücken, Deutschland, Alemania, 2016; p. 371, ISBN 978-3-8417-5270-3.
19. Yusof, A.; Keegan, H.; Spillane, C.D.; Sheils, O.M.; Martin, C.M.; O'Leary, J.J.; Zengerle, R.; Koltay, P. Inkjet-like printing of single-cells. *Lab Chip* **2011**, *11*, 2447–2454. [CrossRef] [PubMed]
20. Matsusaki, M.; Sakaue, K.; Kadowaki, K.; Akashi, M. Three-Dimensional Human Tissue Chips Fabricated by Rapid and Automatic Inkjet Cell Printing. *Adv. Healthc. Mater.* **2013**, *2*, 534–539. [CrossRef] [PubMed]
21. Hynes, W.F.; Doty, N.J.; Zarembinski, T.I.; Schwartz, M.P.; Toepke, M.W.; Murphy, W.L.; Atzet, S.K.; Clark, R.; Melendez, J.A.; Cady, N.C. Micropatterning of 3D Microenvironments for Living Biosensor Applications. *Biosensors* **2014**, *4*, 28–44. [CrossRef] [PubMed]
22. Zhang, M.; Krishnamoorthy, S.; Song, H.; Zhang, Z.; Xu, C. Ligament flow during drop-on-demand inkjet printing of bioink containing living cells. *J. Appl. Phys.* **2017**, *121*, 124904. [CrossRef]
23. Mecozzi, L.; Gennari, O.; Rega, R.; Battista, L.; Ferraro, P.; Grilli, S. Simple and Rapid Bioink Jet Printing for Multiscale Cell Adhesion Islands. *Macromol. Biosci.* **2017**, *17*. [CrossRef] [PubMed]
24. Zheng, Q.; Lu, J.; Chen, H.; Huang, L.; Cai, J.; Xu, Z. Application of inkjet printing technique for biological material delivery and antimicrobial assays. *Anal. Biochem.* **2011**, *410*, 171–176. [CrossRef] [PubMed]
25. Srimongkon, T.; Mandai, S.; Enomae, T. Application of Biomaterials and Inkjet Printing to Develop Bacterial Culture System. *Adv. Mater. Sci. Eng.* **2015**, *2015*, e290790. [CrossRef]
26. Ozkan, M.; Pisanic, T.; Scheel, J.; Barlow, C.; Esener, S.; Bhatia, S.N. Electro-Optical Platform for the Manipulation of Live Cells. *Langmuir* **2003**, *19*, 1532–1538. [CrossRef]
27. Kim, J.J.; Bong, K.W.; Reátegui, E.; Irimia, D.; Doyle, P.S. Porous microwells for geometry-selective, large-scale microparticle arrays. *Nat. Mater.* **2017**, *16*, 139–146. [CrossRef] [PubMed]
28. Chiou, P.Y.; Ohta, A.T.; Wu, M.C. Massively parallel manipulation of single cells and microparticles using optical images. *Nature* **2005**, *436*, 370–372. [CrossRef] [PubMed]
29. Mishra, A.; Maltais, T.R.; Walter, T.M.; Wei, A.; Williams, S.J.; Wereley, S.T. Trapping and viability of swimming bacteria in an optoelectric trap. *Lab Chip* **2016**, *16*, 1039–1046. [CrossRef] [PubMed]
30. Jing, P.; Wu, J.; Liu, G.W.; Keeler, E.G.; Pun, S.H.; Lin, L.Y. Photonic Crystal Optical Tweezers with High Efficiency for Live Biological Samples and Viability Characterization. *Sci. Rep.* **2016**, *6*. [CrossRef] [PubMed]
31. Schiele, N.R.; Corr, D.T.; Huang, Y.; Raof, N.A.; Xie, Y.; Chrisey, D.B. Laser-based direct-write techniques for cell printing. *Biofabrication* **2010**, *2*, 032001. [CrossRef] [PubMed]
32. Phamduy, T.B.; Sweat, R.S.; Azimi, M.S.; Burow, M.E.; Murfee, W.L.; Chrisey, D.B. Printing cancer cells into intact microvascular networks: A model for investigating cancer cell dynamics during angiogenesis. *Integr. Biol.* **2015**, *7*, 1068–1078. [CrossRef] [PubMed]
33. Nahmias, Y.; Odde, D.J. Micropatterning of living cells by laser-guided direct writing: application to fabrication of hepatic–endothelial sinusoid-like structures. *Nat. Protoc.* **2006**, *1*, 2288–2296. [CrossRef] [PubMed]
34. Collins, D.J.; Devendran, C.; Ma, Z.; Ng, J.W.; Neild, A.; Ai, Y. Acoustic tweezers via sub–time-of-flight regime surface acoustic waves. *Sci. Adv.* **2016**, *2*, e1600089. [CrossRef] [PubMed]
35. Ding, X.; Lin, S.-C.S.; Kiraly, B.; Yue, H.; Li, S.; Chiang, I.-K.; Shi, J.; Benkovic, S.J.; Huang, T.J. On-chip manipulation of single microparticles, cells, and organisms using surface acoustic waves. *Proc. Natl. Acad. Sci. USA* **2012**, *109*, 11105–11109. [CrossRef] [PubMed]
36. Naseer, S.M.; Manbachi, A.; Samandari, M.; Walch, P.; Gao, Y.; Zhang, Y.S.; Davoudi, F.; Wang, W.; Abrinia, K.; Cooper, J.M.; et al. Surface acoustic waves induced micropatterning of cells in gelatin methacryloyl (GelMA) hydrogels. *Biofabrication* **2017**, *9*, 015020. [CrossRef] [PubMed]
37. Ai, Y.; Sanders, C.K.; Marrone, B.L. Separation of Escherichia coli Bacteria from Peripheral Blood Mononuclear Cells Using Standing Surface Acoustic Waves. *Anal. Chem.* **2013**, *85*, 9126–9134. [CrossRef] [PubMed]
38. Hughes, M.P. Strategies for dielectrophoretic separation in laboratory-on-a-chip systems. *Electrophoresis* **2002**, *23*, 2569–2582. [CrossRef]
39. Sadeghian, H.; Hojjat, Y.; Soleimani, M. Interdigitated electrode design and optimization for dielectrophoresis cell separation actuators. *J. Electrost.* **2017**, *86*, 41–49. [CrossRef]
40. Ho, C.-T.; Lin, R.-Z.; Chang, W.-Y.; Chang, H.-Y.; Liu, C.-H. Rapid heterogeneous liver-cell on-chip patterning via the enhanced field-induced dielectrophoresis trap. *Lab Chip* **2006**, *6*, 724–734. [CrossRef] [PubMed]

41. D'Amico, L.; Ajami, N.J.; Adachi, J.A.; Gascoyne, P.R.C.; Petrosino, J.F. Isolation and concentration of bacteria from blood using microfluidic membraneless dialysis and dielectrophoresis. *Lab Chip* **2017**, *17*, 1340–1348. [CrossRef] [PubMed]
42. Ino, K.; Ito, A.; Honda, H. Cell patterning using magnetite nanoparticles and magnetic force. *Biotechnol. Bioeng.* **2007**, *97*, 1309–1317. [CrossRef] [PubMed]
43. Souza, G.R.; Tseng, H.; Gage, J.A.; Mani, A.; Desai, P.; Leonard, F.; Liao, A.; Longo, M.; Refuerzo, J.S.; Godin, B. Magnetically Bioprinted Human Myometrial 3D Cell Rings as A Model for Uterine Contractility. *Int. J. Mol. Sci.* **2017**, *18*, 683. [CrossRef] [PubMed]
44. Pivetal, J.; Royet, D.; Ciuta, G.; Frenea-Robin, M.; Haddour, N.; Dempsey, N.M.; Dumas-Bouchiat, F.; Simonet, P. Micro-magnet arrays for specific single bacterial cell positioning. *J. Magn. Magn. Mater.* **2015**, *380*, 72–77. [CrossRef]
45. Wei, S.C.; Fattet, L.; Tsai, J.H.; Guo, Y.; Pai, V.H.; Majeski, H.E.; Chen, A.C.; Sah, R.L.; Taylor, S.S.; Engler, A.J.; et al. Matrix stiffness drives epithelial-mesenchymal transition and tumour metastasis through a TWIST1-G3BP2 mechanotransduction pathway. *Nat. Cell Biol.* **2015**, *17*, 678–688. [CrossRef] [PubMed]
46. Kwon, M.; Godinho, S.A.; Chandhok, N.S.; Ganem, N.J.; Azioune, A.; Thery, M.; Pellman, D. Mechanisms to suppress multipolar divisions in cancer cells with extra centrosomes. *Genes Dev.* **2008**, *22*, 2189–2203. [CrossRef] [PubMed]
47. Théry, M.; Racine, V.; Piel, M.; Pépin, A.; Dimitrov, A.; Chen, Y.; Sibarita, J.-B.; Bornens, M. Anisotropy of cell adhesive microenvironment governs cell internal organization and orientation of polarity. *Proc. Natl. Acad. Sci. USA* **2006**, *103*, 19771–19776. [CrossRef] [PubMed]
48. Théry, M.; Racine, V.; Pépin, A.; Piel, M.; Chen, Y.; Sibarita, J.-B.; Bornens, M. The extracellular matrix guides the orientation of the cell division axis. *Nat. Cell Biol.* **2005**, *7*, 947–953. [CrossRef] [PubMed]
49. Formosa, C.; Grare, M.; Jauvert, E.; Coutable, A.; Regnouf-de-Vains, J.B.; Mourer, M.; Duval, R.E.; Dague, E. Nanoscale analysis of the effects of antibiotics and CX1 on a Pseudomonas aeruginosa multidrug-resistant strain. *Sci. Rep.* **2012**, *2*. [CrossRef] [PubMed]
50. Formosa, C.; Herold, M.; Vidaillac, C.; Duval, R.E.; Dague, E. Unravelling of a mechanism of resistance to colistin in Klebsiella pneumoniae using atomic force microscopy. *J. Antimicrob. Chemother.* **2015**, *70*, 2261–2270. [CrossRef] [PubMed]
51. Camesano, T.A.; Natan, M.J.; Logan, B.E. Observation of changes in bacterial cell morphology using tapping mode atomic force microscopy. *Langmuir* **2000**, *16*, 4563–4572. [CrossRef]
52. Emerson, R.J.; Camesano, T.A. Nanoscale investigation of pathogenic microbial adhesion to a biomaterial. *Appl. Environ. Microbiol.* **2004**, *70*, 6012–6022. [CrossRef] [PubMed]
53. Cerf, A.; Cau, J.-C.; Vieu, C. Controlled assembly of bacteria on chemical patterns using soft lithography. *Colloids Surf. B Biointerfaces* **2008**, *65*, 285–291. [CrossRef] [PubMed]
54. Ressier, L.; Viallet, B.; Beduer, A.; Fabie, D.; Fabié, L.; Palleau, E.; Dague, E. Combining convective/capillary deposition and AFM oxidation lithography for close-packed directed assembly of colloids. *Langmuir* **2008**, *24*, 13254–13257. [CrossRef] [PubMed]
55. Cerf, A.; Cau, J.-C.; Vieu, C.; Dague, E. Nanomechanical properties of dead or alive single-patterned bacteria. *Langmuir* **2009**, *25*, 5731–5736. [CrossRef] [PubMed]
56. Jauvert, E.; Palleau, E.; Dague, E.; Ressier, L. Directed Assembly of Living Pseudomonas aeruginosa Bacteria on PEI Patterns Generated by Nanoxerography for Statistical AFM Bioexperiments. *ACS Appl. Mater. Interfaces* **2014**, *6*, 21230–21236. [CrossRef] [PubMed]
57. Kumar, A.; Biebuyck, H.A.; Whitesides, G.M. Patterning Self-Assembled Monolayers: Applications in Materials Science. *Langmuir* **1994**, *10*, 1498–1511. [CrossRef]
58. Thibault, C.; Severac, C.; Trevisiol, E.; Vieu, C. Microtransfer molding of hydrophobic dendrimer. *Microelectron. Eng.* **2006**, *83*, 1513–1516. [CrossRef]
59. Hua, F.; Sun, Y.; Gaur, A.; Meitl, M.A.; Bilhaut, L.; Rotkina, L.; Wang, J.; Geil, P.; Shim, M.; Rogers, J.A.; et al. Polymer Imprint Lithography with Molecular-Scale Resolution. *Nano. Lett.* **2004**, *4*, 2467–2471. [CrossRef]
60. Kane, R.S.; Takayama, S.; Ostuni, E.; Ingber, D.E.; Whitesides, G.M. Patterning proteins and cells using soft lithography. *Biomaterials* **1999**, *20*, 2363–2376. [CrossRef]
61. Mrksich, M.; Whitesides, G.M. Using self-assembled monolayers to understand the interactions of man-made surfaces with proteins and cells. *Annu. Rev. Biophys. Biomol. Struct.* **1996**, *25*, 55–78. [CrossRef] [PubMed]

62. Zhang, S.; Yan, L.; Altman, M.; Lässle, M.; Nugent, H.; Frankel, F.; Lauffenburger, D.A.; Whitesides, G.M.; Rich, A. Biological surface engineering: A simple system for cell pattern formation. *Biomaterials* **1999**, *20*, 1213–1220. [CrossRef]
63. Ruiz, S.A.; Chen, C.S. Microcontact printing: A tool to pattern. *Soft Matter* **2007**, *3*, 168–177. [CrossRef]
64. Long, M.; Sato, M.; Lim, C.T.; Wu, J.; Adachi, T.; Inoue, Y. Advances in Experiments and Modeling in Micro- and Nano-Biomechanics: A Mini Review. *Cell. Mol. Bioeng.* **2011**, *4*, 327–339. [CrossRef]
65. Foncy, J.; Cau, J.-C.; Bartual-Murgui, C.; François, J.M.; Trévisiol, E.; Sévérac, C. Comparison of polyurethane and epoxy resist master mold for nanoscale soft lithography. *Microelectron. Eng.* **2013**, *110*, 183–187. [CrossRef]
66. Wong, L.; Pegan, J.D.; Gabela-Zuniga, B.; Khine, M.; McCloskey, K.E. Leaf-inspired microcontact printing vascular patterns. *Biofabrication* **2017**, *9*, 021001. [CrossRef] [PubMed]
67. Malaquin, L.; Kraus, T.; Schmid, H.; Delamarche, E.; Wolf, H. Controlled Particle Placement through Convective and Capillary Assembly. *Langmuir* **2007**, *23*, 11513–11521. [CrossRef] [PubMed]
68. Fredonnet, J.; Foncy, J.; Lamarre, S.; Cau, J.-C.; Trévisiol, E.; Peyrade, J.-P.; François, J.M.; Séverac, C. Dynamic PDMS inking for DNA patterning by soft lithography. *Microelectron. Eng.* **2013**, *111*, 379–383. [CrossRef]
69. Cayron, H.; Berteloite, B.; Vieu, C.; Paveau, V.; Cau, J.-C.; Cerf, A. Controlled deposition and multi-layer architecturing of single biomolecules using automated directed capillary assembly and nano-contact printing processes. *Microelectron. Eng.* **2015**, *135*, 1–6. [CrossRef]
70. Delapierre, F.-D.; Mottet, G.; Taniga, V.; Boisselier, J.; Viovy, J.-L.; Malaquin, L. High throughput micropatterning of interspersed cell arrays using capillary assembly. *Biofabrication* **2017**, *9*, 015015. [CrossRef] [PubMed]
71. Lagraulet, A.; Foncy, J.; Berteloite, B.; Esteve, A.; Blatche, M.-C.; Malaquin, L.; Vieu, C. InnoStamp 40^{TM} and InnoScan 1100AL^{TM}: A complete automated platform for microstructured cell arrays. *Nat. Methods* **2015**, *12*. [CrossRef]
72. McNulty, J.D.; Klann, T.; Sha, J.; Salick, M.; Knight, G.T.; Turng, L.-S.; Ashton, R.S. High-precision robotic microcontact printing (R-μCP) utilizing a vision guided selectively compliant articulated robotic arm. *Lab Chip* **2014**, *14*, 1923–1930. [CrossRef] [PubMed]
73. Knight, G.T.; Klann, T.; McNulty, J.D.; Ashton, R.S. Fabricating Complex Culture Substrates Using Robotic Microcontact Printing (R-μCP) and Sequential Nucleophilic Substitution. *J. Vis. Exp. JoVE* **2014**. [CrossRef] [PubMed]
74. Ricoult, S.G.; Sanati Nezhad, A.; Knapp-Mohammady, M.; Kennedy, T.E.; Juncker, D. Humidified Microcontact Printing of Proteins: Universal Patterning of Proteins on Both Low and High Energy Surfaces. *Langmuir* **2014**, *30*, 12002–12010. [CrossRef] [PubMed]
75. Polio, S.R.; Smith, M.L. Patterned Hydrogels for Simplified Measurement of Cell Traction Forces. *Methods Cell Biol.* **2014**, *121*, 17–31. [CrossRef] [PubMed]
76. Vedula, S.R.K.; Hirata, H.; Nai, M.H.; Brugués, A.; Toyama, Y.; Trepat, X.; Lim, C.T.; Ladoux, B. Epithelial bridges maintain tissue integrity during collective cell migration. *Nat. Mater.* **2014**, *13*, 87–96. [CrossRef] [PubMed]
77. El Kirat, K.; Burton, I.; Dupres, V.; Dufrene, Y.F. Sample preparation procedures for biological atomic force microscopy. *J. Microsc.* **2005**, *218*, 199–207. [CrossRef] [PubMed]
78. Kailas, L.; Ratcliffe, E.C.; Hayhurst, E.J.; Walker, M.G.; Foster, S.J.; Hobbs, J.K. Immobilizing live bacteria for AFM imaging of cellular processes. *Ultramicroscopy* **2009**, *109*, 775–780. [CrossRef] [PubMed]
79. Dague, E.; Jauvert, E.; Laplatine, L.; Viallet, B.; Thibault, C.; Ressier, L. Assembly of live micro-organisms on microstructured PDMS stamps by convective/capillary deposition for AFM bio-experiments. *Nanotechnology* **2011**, *22*, 395102. [CrossRef] [PubMed]
80. Rhee, S.W.; Taylor, A.M.; Tu, C.H.; Cribbs, D.H.; Cotman, C.W.; Jeon, N.L. Patterned cell culture inside microfluidic devices. *Lab Chip* **2005**, *5*, 102–107. [CrossRef] [PubMed]
81. Torisawa, Y.; Mosadegh, B.; Luker, G.D.; Morell, M.; O'Shea, K.S.; Takayama, S. Microfluidic hydrodynamic cellular patterning for systematic formation of co-culture spheroids. *Integr. Biol.* **2009**, *1*, 649–654. [CrossRef] [PubMed]
82. Tu, C.; Huang, B.; Zhou, J.; Liang, Y.; Tian, J.; Ji, L.; Liang, X.; Ye, X. A Microfluidic Chip for Cell Patterning Utilizing Paired Microwells and Protein Patterns. *Micromachines* **2017**, *8*. [CrossRef]

83. Azioune, A.; Carpi, N.; Tseng, Q.; Théry, M.; Piel, M. Chapter 8—Protein Micropatterns: A Direct Printing Protocol Using Deep UVs. In *Methods in Cell Biology*; Cassimeris, L., Tran, P., Eds.; Academic Press: Cambridge, MA, USA, 2010; Volume 97, pp. 133–146, ISBN 978-0-12-381349-7.
84. Carpi, N.; Piel, M.; Azioune, A.; Cuvelier, D.; Fink, J. Micropatterning on silicon elastomer (PDMS) with deep UVs. *Protoc. Exch.* **2011**. [CrossRef]
85. Carpi, N.; Piel, M.; Azioune, A.; Fink, J. Micropatterning on glass with deep UV. *Protoc. Exch.* **2011**. [CrossRef]
86. Alvéole. Available online: http://www.alveolelab.com/primo.html (accessed on 20 November 2017).
87. Hulshof, F.F.B.; Zhao, Y.; Vasilevich, A.; Beijer, N.R.M.; de Boer, M.; Papenburg, B.J.; van Blitterswijk, C.; Stamatialis, D.; de Boer, J. NanoTopoChip: High-throughput nanotopographical cell instruction. *Acta Biomater.* **2017**, *62*, 188–198. [CrossRef] [PubMed]
88. Li, M.; Liu, L.; Xi, N.; Wang, Y. Biological Applications of a Nanomanipulator Based on AFM: In situ visualization and quantification of cellular behaviors at the single-molecule level. *IEEE Nanotechnol. Mag.* **2015**, *9*, 25–35. [CrossRef]
89. Fortier, H.; Variola, F.; Wang, C.; Zou, S. AFM force indentation analysis on leukemia cells. *Anal. Methods* **2016**, *8*, 4421–4431. [CrossRef]
90. Minelli, E.; Ciasca, G.; Sassun, T.E.; Antonelli, M.; Palmieri, V.; Papi, M.; Maulucci, G.; Santoro, A.; Giangaspero, F.; Delfini, R.; et al. A fully-automated neural network analysis of AFM force-distance curves for cancer tissue diagnosis. *Appl. Phys. Lett.* **2017**, *111*, 143701. [CrossRef]

Chapter 2: State of the art

This chapter shows some works published about the main components of the methodology developed for this thesis work, scanning probe microscopy, and cell arrays. Also, works improving the speed of mechanical measurements and the number of measurements done with an AFM are listed. Automation seems to be the suitable way to improve speed and the number of mechanical measurements as the mechanical measurements on AFM are usually done manually.

2.1. Scanning Probe Microscopy

Scanning probe microscopy (SPM) is a set of microscopy techniques that provide information about the atomic level process and structures. The first technique was scanning tunneling microscopy (STM) developed by Binning and Rohrer in 1981, awarded the Nobel Prize in 1986 for their invention. Atomic force microscopy (AFM) is another SPM technique invented by Binning, Quate, and Gerber in 1986. STM is considered the father of the AFM, because these techniques have some features in common; both uses a tip to obtain images from the sample, and they obtain topographical images. These techniques were rapidly adopted in many fields, and the work presented in this thesis uses one of these techniques, so the next sections described them.

2.1.1 Atomic Force Microscopy

AFM is capable of achieving atomic-resolution under certain conditions, it overcomes the optical resolution limitations but also the requirements for the sample to be conductive[1]. The principle of working consists of a sharp tip mounted on a flexible cantilever, and this cantilever is attached to a piezoelectric ceramic that moves on x, y, and z positions. A laser beam reflects on the back of the cantilever to a four-quadrant photodiode, so as the tip scans the surface, it is possible to obtain topographical images based on the position of the laser in the photodiode[2].

AFM not only captures images, it also allows mechanical studies by performing force spectroscopy. The results of this analysis are known as force curves (force vs. distance plots) from these is possible to obtain, mechanical properties such as, Young modulus values, stiffness, adhesion.

Figure 2.1 shows a typical force curve. As the tip approaches the sample, no bending on the cantilever can be observed until the tip and the sample is close enough. Then the cantilever is pulled down due to the van der Waals interactions between the tip and surface or by the presence of a thin hydration layer on the surface. After the contact rising the sample produces an upward bend in the cantilever. The load is calculated by multiplying the reference (cantilever deflection value) times its spring constant. On the downward movement of the scanner, the cantilever flattens, and if there is a presence of adhesive forces, a downward deflection in the cantilever maybe be observed. When the restoring forces of the cantilever exceed these forces, the tip releases from the surface, and the cantilever returns to its original position[3].

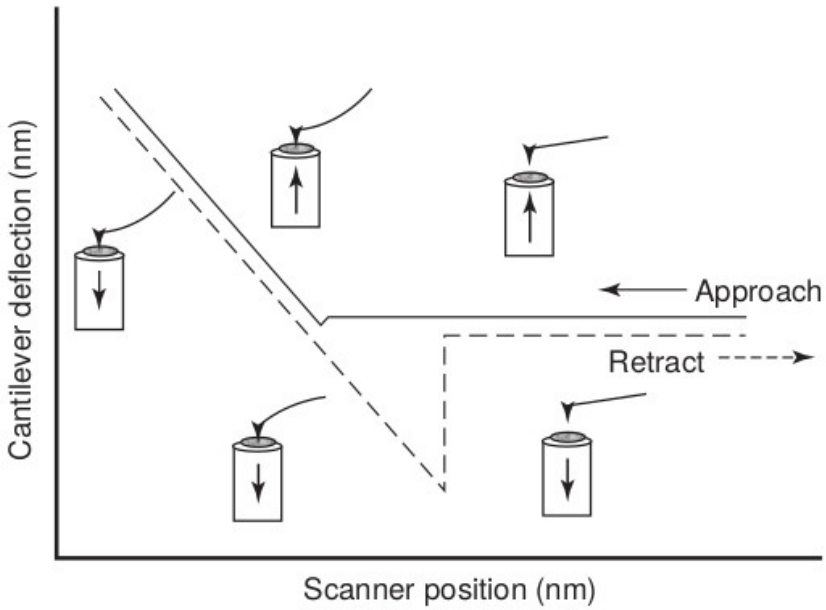

Figure 2.1. Force curve formation in air. The force curve is monitored by cantilever deflection as the piezoelectric rises and withdraws the sample surface from the tip. The approach and retract curves are dissimilar when strong chemical or physical attraction exists between the tip and the surface. Image was taken from[3].

AFM is a technique that from the start demonstrate potential for applications in the biological area. For example Malkin et al.[4] reported the imaging of virus crystal growth dynamics. Another example is the work from Rief et al.[5] reports the use of single-molecule force spectroscopy to unfold titin, the giant sarcomeric protein of striated muscle. They report that a force of 150 to 300 piconewtons is needed to unfold and obtain a characteristic sawtooth plot for larger individual titin molecules. Tao et al.[6] used the AFM to extract the mechanical properties of hydrated cow tibia. The extraction of the rigidity was done using images, and they reported dramatic variations in elastic properties when comparing low versus high resolution images.

The AFM technique has been modified to include other functionalities such as the work from Meister A. et al.[7], they published a liquid delivery system (FluidFM) based on hollow cantilevers capable of dispense soluble molecules, stimulation, and extraction of specific components from the cell under physiological conditions. Ando T. et al.[8] reported in 2001 the first high-speed AFM used to image myosin V molecules moving on mica. The AFM generates an image every 80 ms, the modification of the cantilevers was necessary (high resonance frequencies and small spring constants) to reach higher speed.

This thesis work focuses on developing a methodology that uses the AFM capabilities to obtain the mechanical properties (such as Young modulus, stiffness, and adhesion) and cell array immobilization, which helps organize cells, so the analysis is performed faster than with the classical method.

2.2. Mechanical properties

Mechanical properties (also known as the mechanical phenotype) are considered as label-free biomarkers. They do not need chemical reactions to be detected because they depend on the biophysical properties of the target molecules, and usually, the interactions detected are mechanical,

electrical, or optical signals[9]. In the literature, many works exist that report the mechanical properties of different types of cells. However, many of those works use a limited number of cells (<100) to report their findings. In the next sections, some of the works on mechanical properties reported on literature are listed.

2.2.1 Mechanical properties of microbes

Atomic force microscope has helped achieving important structural information on microbes such as the work reported by Touhami et al.[10] they analyzed *S. cerevisiae* cell wall during cell division. They found that the region of the bud scar has a higher elastic modulus because of an accumulation of chitin. Their study was the first to report distinct regions of different elasticity at the surface. Alsteens et al.[11] confirmed the behavior on *S. cerevisiae*, but for *Saccharomyces carlsbergensis*, cell wall elasticity has no distinctive regions. Other studies on S. cerevisiae by Pillet et al.[12] showed that heat stress induces the formation of circular structures on the cell wall of the yeasts and an increment in these circular regions of their Young modulus. They performed 3 independent experiments and analyzed 10-12 yeast cells per experiment. Schiavone et al.[13] report an exciting work on which they evaluated the effects of the autolysis process on yeast. They evaluated two types of strains (L71 and L69) and found that for L71, the autolysis process profoundly affects the surface structure of the yeast, but no significant adhesion modifications were found.
Meanwhile, for the L69, no visible differences on the surface were found between the normal yeast and the re-hydrated cells. However, an increase in the roughness of the re-hydrated cells and the presence of adhesion regions in the cell surface was observed. They performed 3 experiments using 11 cells per experiment (a total of 33 cells for its study).

C. albicans is an opportunistic pathogen capable of adhering to mammalian cells. Its study is essential because it can be found in many hospitals, and its a very adaptable pathogen. Formosa et al.[14] reported the mapping of the adhesive properties (nanodomains) to understand the virulence of *C. albicans*. They probed that Als proteins participated in the nanodomains. They performed single-cell analysis on living wild type yeast and used 3 cells in their study. Martin-Yken et al.[15] reported a study of the *C. albicans* SMi1 proteins and founded that in the absence of these proteins, the Young modulus of the cell wall decreases 85% and the over-expression of SMi1 increases adhesion. They used 12 cells for their study, and from each cell, a force volume was obtained, collecting between 1024 and 4160 force curves.
In the field of microbiology, mechanical properties have been used to analyze the response of *Streptococcus pyogenes* to rokitamicyn[16]. And to analyze the elongation of *Pseudomonas aeruginosa* cells under ticarcillin antibiotic[17] among many other examples.
The study of different microbes can help obtaining a better understanding of their behavior and the way they react to different treatments, giving not only a basic answer if the treatment works or not, but to describe the different changes the microbes go through when exposed to different drugs.

2.2.2 Mechanical properties of mammalian cells

Usually, the mechanical properties of mammalian cells are extracted with other techniques because AFMs found in commerce do not have high throughput. Nevertheless, AFM is still a valuable tool when the mechanical properties of cells are to be extracted. For mammalian cells, their mechanical phenotype can be associated with some diseases, such as, Lekka et al.[18] compared to two types of

human epithelial cells (Hu609 and HCV29) against BC3726 (HCV29 cells transfected), T24, and bladder transitional cell carcinoma (T24 and ATCC HTB4). They found that normal cells have a higher Young modulus (one order of magnitude) compared with the Young modulus of cancerous cells. They reported the analysis of 20 cells per cell line. Cross et al.[19], studying cancerous cells, analyzed metastatic cells taken from patients with lung, breast, and pancreas cancer and founded a decrease in the stiffness by 70 % when comparing cancer cells with healthy cells. Omidvar et al.[20] compared the adhesion of two cancerous cell lines (MCF-7, T47D, and MDA-MB-231) using single-cell force spectroscopy (SCFS). A cell (T47D) was attached to the cantilever to function as a tip, and then indentations were performed onto the cancerous cells. They founded that the adhesion force decreases as their invasion potential increases.

Bastatas et al.[21] reported that combined biomechanical signatures (adhesion and calcium dynamics) of prostate cancer cells (LNCaP, CL-1, and CL-2) indicate the metastatic potential of the cells. For their studies, they used 17 to 35 cells per cell line. Smolyakov et al.[22] studied four breast cancer cell lines (SKBR3, MCF7, BT474, and MDA-MB231). They founded a relation between invasiveness, and Young modulus (more invasive cells have a lower Young modulus) increased adhesion in cancer cells, which contributes to invasion. Also, they found that adhesion increases as the cells become more invasive.

Sanyour et al.[23] reported an analysis of membrane cholesterol content in vascular smooth muscle cells (VSMCs). With the AFM, they measured VSMCs stiffness. They found that cholesterol-enrichment increase cytoskeleton stiffness and cell adhesion compared to their control.

The mechanical properties have been used to identify some diseases such as erythrocyte stiffness that has been linked to diabetes mellitus, coronary diseases[24], G6PD deficiency, and hereditary spherocytosis[25]. In the field of cardiovascular diseases, the mechanical properties of cardiomyocytes have been studied by Benech et al.[26]. They reported an increase in stiffness of live cardiomyocytes of diabetic mice. Dague et al.[27] also found a mitochondrial shift on cardiomyocytes from mice with heart failure and a general increase in the stiffness of cardiomyocyte's surface.

2.3. Cell arrays

Cell micropatterning and cell manipulation help in many scientific tests, such as the designing of microfluidic devices for medical applications, drug testing, and understand biochemical processes[28]. Cell micropatternings can be applied to biomolecules[29], bacteria[30], yeast[31], and other bioparticles involved in therapies[32]. In this section, a variety of techniques are presented. The techniques presented are a combination of different processes of fabrication, and some require surface functionalization.

2.3.1 Optical tweezers

Optical tweezers provide high precision of positioning for small arrays. Some optical tweezers use radiation pressure emitted by a laser beam, and others use infrared lasers. They allow remote manipulation, and the monitorization can be done by tracking the intrinsic charge and dielectric properties of cells. Optoelectronic tweezers (OET) can reduce the energy 100,000 times compared to conventional optical tweezers, as claimed by Chiou et al.[33] their system uses a halogen lamp and a digital micromirror for parallel manipulation of cells. They placed cells between an upper indium tin oxide-coated glass (ITO-coated glass), and lower multiple layers of photosensitive surfaces.

Their technique utilizes virtual electrodes, and they can differentiate dead cells by their dielectric properties. Their technique also guarantees high-resolution patterning.
Another example is the work of Jing et al.[34]; they modulated light fields to trap mammalian, yeast, and microbial cells, on the surface of a photonic crystal. On the surface of silicon photocrystal, by using the phtotolithography technique, they microfabricate circular patterns (500 nm depth). Their methodology allows them to trap different single cells without compromising cell viability, and they proved that the aperture number of the lens does not affect the effectiveness of cell trapping.

2.3.2 Inkjet cell printing

This technique is divided into three types, continuous inkjet printing (CIJ), drop-on-demand printing (DOD), and electrohydrodynamic jet printing. DOD is the most controllable and causes less contamination. One example is the work of Yusof et al.[35], which reported a non-contact printing of single cells. They used a dispenser chip to deposit droplets, a sensor detects the cells, and an automated printer generates the patterns on specific substrates such as microscope slides and microtiter plates. Their printing efficiency is 87%, and cell viability is 75%. Relating to bacteria, Zheng et al.[36] reports the use of a modified thermal inkjet printer to pattern Escherichia coli on agar substrates so that they can evaluate the antimicrobial activity of antibiotics.

2.3.3 Acoustic force patterning

These methods use surface acoustic waves (SAWs) for manipulating, and they use less energy than optical and optoelectronic techniques. In acoustic systems, the displacement resolution depends on the formed nodes and frequency[37]. The migration of cells subjected to acoustic waves is called acustophoresis, and it depends on cells size, compressibility, density, and also the fluidic properties of the medium. Nasser et al.[38] used a piezoelectric substrate of lithium niobate ($LiNbO_3$) and slanted-finger interdigitated transducers to align cardiomyocytes mixed with cardiac fibroblast. The alignment was obtained in less than 10 s.
Acoustic methods are a chemical-free technique to manipulate cells, they do not compromise cell viability, and they are a rapid contactless technique.

2.3.4 Magnetic cell manipulation

Magnetic forces and magnetic materials can manipulate cells when a complex organization is required. Magnetic arrays are suitable for bacteria and mammalian cells, despite bacteria cells are smaller. For example the work of pivetal et al.[39], they used reverse magnetization along with thermomagnetic patterning to fabricate an array of 7.5×7.5 mm^2. They labeled magnetically E. coli bacteria to increase specificity and guarantee bacteria fixation. Another example is the work of Souza et al.[40]; they magnetized myometrial cells with biocompatible gold nanoparticles, iron oxide, and Poly-L-Lysine. Then they deposited the cells on 384-well plates on the magnets to form ring structures per well.
The magnetic techniques require cell labeling with biocompatible magnetic particles.

2.3.5 Surface chemistry methodology

The methodologies involving surface chemistry take advantage of the cell's capacity to detect their environment. Patterns of adhesive and anti-adhesive molecules should be printed on the surface to

take advantage of this property. Adhesive and anti-adhesive patterns make it possible to control the locations of the cells and immobilize them inside specific geometries. The work of Thery et al.[41] demonstrated the microtubule distribution, the position of the Golgi apparatus and the nucleus depend on the shape of the extracellular matrix proteins. Because of their work, a better understanding of the adhesive microenvironment and cell internal organization.

Regarding microbes, the immobilization is done by electrostatic interactions between positively charged surfaces and negatively charged microbes. For example, Cerf et al.[42] immobilized E. coli cells onto APTES islands (positive charges) deposited on a surface of octadecyltrichlorosilane (negative charges). Also, Ressier et al.[43] reported the immobilization of E. coli cells onto silicon oxide patterns (fabricated using the AFM oxidation lithography), the substrate was treated with a SAM of octadecyltrimethoxysilane (OTMS). Convective/capillary assembly technique was used to drag the cells into the patterns.

2.3.6 Microcontact printing

Microcontact printing (μCP) is a lithography technique on which a stamp (made of an elastomeric material) is used to transfer patterns previously designed. The stamp is made from a master mold (usually of silicon), and many stamps can be fabricated from the master. The stamp is inked and let to dry, and then the ink is transferred onto a surface by contact. Features of 20 μm are good enough for cell patterning. However, for smaller features, nano-lithographic facilities are required. The conventional method uses an ink (which can be the cell culture itself). However, Malaquin et al.[44] used a technique derived from capillary assembly where a meniscus displacement was used to push the cells into the grooves at the PDMS stamp surface.

Dague et al.[45,46] developed a microstructured PDMS stamp with various hole sizes, ranging from 1.5 x 1.5 mm2 to 6 x 6 mm^2. Their stamp with negative patterns is suitable for immobilizing bacteria, yeast, algae, and eukaryotic cell nuclei. They achieve a high filling rate (85%), and each cell can be probed individually.

2.3.7 Deep UV micropatterning

This methodology uses wavelengths in the region of deep UV (DUV), below 280 nm, to obtain micropatterns. A specialized mask designed for DUV is needed to fabricate the micropatterns; usually, it is made of quartz, synthetic quartz, or fused silica. Hulshof et al.[47] reported the immobilization of U2OS osteosarcoma cells in more than 1200 different topographies. Their designs include lines, circles, and triangles in different arrays of 200 nm to 700 nm. Alvéole PRIMO®[48] is another type of DUV technique; it is based on light-induced molecular adsorption of proteins (LIMAP). The PRIMO module is where the photoactivable reagent is exposed to UV light, and patterns of up to 1.2 μm can be obtained.

2.4. AFM automation

In preview sections the tools to implement an automated methodology (AFM and cell immobilization techniques) were described, and also, in the preview sections, the interest and utility of the mechanical biomarkers can be seen. In this section, works related to AFM automation are being studied, the challenges another authors have encountered, and the solutions they have proposed.

Wang et al.[49] reported an automated system for measuring the mechanical properties of Raji cells. Their system used image processing to identify the cells, and then the cantilever was moved automatically, so the tip was located on top of the cell. Within 3 s the location and measurement of the cells were completed. One important requirement needed to execute their system is that the shape of the cells needs to be round (which is usually a sign of dying cells). And the substrate of the cell needs to be completely flat, and cell agglomeration was to be avoided because their system did not withdraw the tip from the sample. To test their system, they used 4 cells per scanning area; however, they did not report the number of cells the system can analyze within an hour.

Another example of automation is the work from Roy et al.[50]; they developed a system capable of analyzing tissue. The system uses image processing to align the tip to a region of interest (80 µm x 150 µm) and can obtain up to 480 force curves from there. The process takes ~80 min and is not adapted for single-cell analysis. Both the works from Wang and Roy focus on finding the target cells or tissue and then perform the mechanical measurements they want.

A different approach is reported in the work of Favre et al.[51]. They fabricated an array of cantilevers controlled by one AFM (figure 2.2a); this permits them to obtain images from different regions of the sample at the same time. Applying this technology in the cell population is possible if the arrays of cantilevers are to be organized as the cell arrays. Sadeghian et al.[52] developed a set of 44 miniaturized AFMs in an area of 450 mm (figure 2.2b). Each AFM is capable of performing independent analysis on the sample. To test the system, the authors obtained images from gold nanoparticles (10 nm in diameter) deposited on mica. The regions of interest are determined manually, and the cell arrays must be adapted to the distribution of the AFMs.

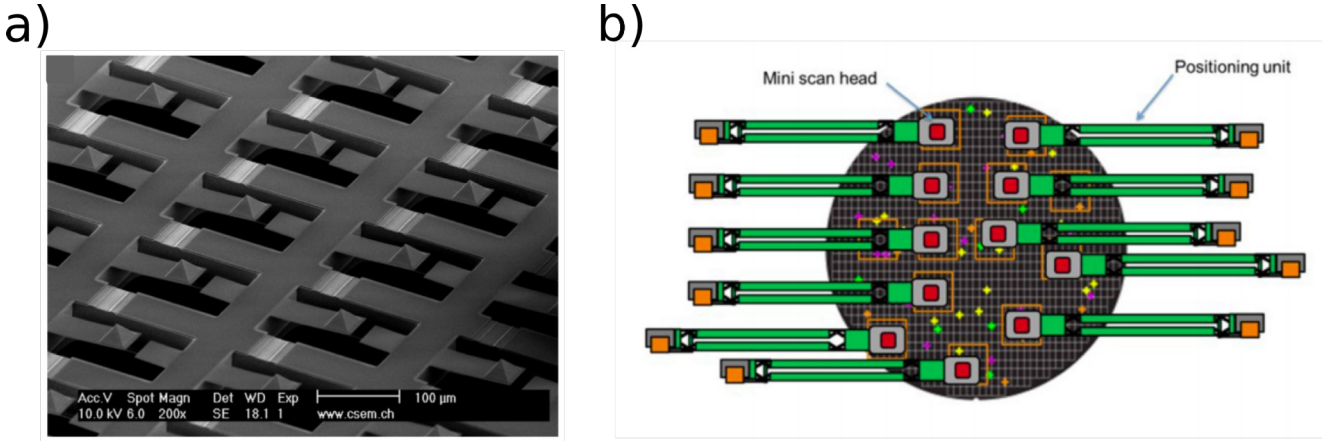

Figure 2.2. Parallel AFMs. a) Arrays of cantilevers (17 per column), all cantilevers are controlled by one AFM head. Taken from[51]*. b) Distribution of the miniaturized AFMs on a wafer like surface (450 mm). Every mini scan head works independently and the positioning unit approaches the AFMs to perform the analysis. Image was taken from*[52].

A published paper that is very similar to our methodology is the work of Dujardin et al.[53]. They reported an automated procedure to obtain AFM images but just on bacteria. They implemented a python script in a Dimension Fast Scan-Bio AFM (Bruker, Santa Barbara, CA, USA); the process spent most of the time aligning the photodetector and performing engagement each time, giving a total of 501 areas imaged in 8 h 35 min. The system takes a force volume of the sample and, based on heights, identifies the position of all cells. Then an image is taken in a 2x2 μm^2 area. Their analysis is of the height and Peak-Force error signals. The cells used to test their system were *Yersinia pseudotuberculosis* and living *Mycobacterium bovis* BCG bacteria.

2.5. Conclusions

In this chapter, an overview of the works relating to AFM origins and breakthrough publications, mechanical properties of cells, cell immobilization, and the advances made in AFM automation published in recent years has been listed. There are many works published about AFM, cell arrays, and some works reported successful accomplishment of automation to a certain degree. However, many of the works focus on analyzing a sample faster, but they do not give importance to increase the number of samples analyzed. The main difference between those works and the work presented in this thesis is that this work looks to maximize the number of samples analyzed so it can be possible to assess the cell population and obtain statistical significance in the results.

2.6. References

(1) Piontek, M. C.; Roos, W. H. Atomic Force Microscopy: An Introduction. In *Single Molecule Analysis: Methods and Protocols*; Peterman, E. J. G., Ed.; Methods in Molecular Biology; Springer New York: New York, NY, 2018; pp 243–258. https://doi.org/10.1007/978-1-4939-7271-5_13.

(2) Formosa, C.; Dague, E. Imaging Living Yeast Cells and Quantifying Their Biophysical Properties by Atomic Force Microscopy. In *Advanced Microscopy in Mycology*; Dahms, T. E. S., Czymmek, K. J., Eds.; Fungal Biology; Springer International Publishing: Cham, 2015; pp 125–141. https://doi.org/10.1007/978-3-319-22437-4_7.

(3) Bottomley, L. A.; Gadsby, E. D.; Poggi, M. A. MICROSCOPY TECHNIQUES | Atomic Force and Scanning Tunneling Microscopy. In *Encyclopedia of Analytical Science (Second Edition)*; Worsfold, P., Townshend, A., Poole, C., Eds.; Elsevier: Oxford, 2005; pp 143–151. https://doi.org/10.1016/B0-12-369397-7/00386-1.

(4) Malkin, A. J.; Land, T. A.; Kuznetsov, Yu. G.; McPherson, A.; DeYoreo, J. J. Investigation of Virus Crystal Growth Mechanisms by In Situ Atomic Force Microscopy. *Phys. Rev. Lett.* **1995**, *75* (14), 2778–2781. https://doi.org/10.1103/PhysRevLett.75.2778.

(5) Rief, M.; Gautel, M.; Oesterhelt, F.; Fernandez, J. M.; Gaub, H. E. Reversible Unfolding of Individual Titin Immunoglobulin Domains by AFM. *Science* **1997**, *276* (5315), 1109–1112. https://doi.org/10.1126/science.276.5315.1109.

(6) Tao, N. J.; Lindsay, S. M.; Lees, S. Measuring the Microelastic Properties of Biological Material. *Biophys. J.* **1992**, *63* (4), 1165–1169.

(7) Meister, A.; Gabi, M.; Behr, P.; Studer, P.; Vörös, J.; Niedermann, P.; Bitterli, J.; Polesel-Maris, J.; Liley, M.; Heinzelmann, H.; et al. FluidFM: Combining Atomic Force Microscopy and Nanofluidics in a Universal Liquid Delivery System for Single Cell Applications and Beyond. *Nano Lett.* **2009**, *9* (6), 2501–2507. https://doi.org/10.1021/nl901384x.

(8) Ando, T.; Kodera, N.; Takai, E.; Maruyama, D.; Saito, K.; Toda, A. A High-Speed Atomic Force Microscope for Studying Biological Macromolecules. *Proc. Natl. Acad. Sci.* **2001**, *98* (22), 12468–12472. https://doi.org/10.1073/pnas.211400898.

(9) Syahir, A.; Usui, K.; Tomizaki, K.; Kajikawa, K.; Mihara, H. Label and Label-Free Detection Techniques for Protein Microarrays. *Microarrays* **2015**, *4* (2), 228–244. https://doi.org/10.3390/microarrays4020228.

(10) Touhami, A.; Nysten, B.; Dufrêne, Y. F. Nanoscale Mapping of the Elasticity of Microbial Cells by Atomic Force Microscopy. *Langmuir* **2003**, *19* (11), 4539–4543. https://doi.org/10.1021/la034136x.

(11) Alsteens, D.; Dupres, V.; Evoy, K. M.; Wildling, L.; Gruber, H. J.; Dufrêne, Y. F. Structure, Cell Wall Elasticity and Polysaccharide Properties of Living Yeast Cells, as Probed by AFM. *Nanotechnology* **2008**, *19* (38), 384005. https://doi.org/10.1088/0957-4484/19/38/384005.

(12) Pillet, F.; Lemonier, S.; Schiavone, M.; Formosa, C.; Martin-Yken, H.; Francois, J. M.; Dague, E. Uncovering by Atomic Force Microscopy of an Original Circular Structure at the Yeast Cell Surface in Response to Heat Shock. *BMC Biol.* **2014**, *12* (1), 6. https://doi.org/10.1186/1741-7007-12-6.
(13) Schiavone, M.; Sieczkowski, N.; Castex, M.; Dague, E.; Marie François, J. Effects of the Strain Background and Autolysis Process on the Composition and Biophysical Properties of the Cell Wall from Two Different Industrial Yeasts. *FEMS Yeast Res.* **2015**, *15* (2). https://doi.org/10.1093/femsyr/fou012.
(14) Formosa, C.; Schiavone, M.; Boisrame, A.; Richard, M. L.; Duval, R. E.; Dague, E. Multiparametric Imaging of Adhesive Nanodomains at the Surface of Candida Albicans by Atomic Force Microscopy. *Nanomedicine Nanotechnol. Biol. Med.* **2015**, *11* (1), 57–65. https://doi.org/10.1016/j.nano.2014.07.008.
(15) Martin-Yken, H.; Bedekovic, T.; Brand, A. C.; Richard, M. L.; Znaidi, S.; d'Enfert, C.; Dague, E. A Conserved Fungal Hub Protein Involved in Adhesion and Drug Resistance in the Human Pathogen Candida Albicans. *Cell Surf.* **2018**, *4*, 10–19. https://doi.org/10.1016/j.tcsw.2018.10.002.
(16) Braga, P. C.; Ricci, D. Differences in the Susceptibility of Streptococcus Pyogenes to Rokitamycin and Erythromycin A Revealed by Morphostructural Atomic Force Microscopy. *J. Antimicrob. Chemother.* **2002**, *50* (4), 457–460. https://doi.org/10.1093/jac/dkf180.
(17) Formosa, C.; Grare, M.; Duval, R. E.; Dague, E. Nanoscale Effects of Antibiotics on P. Aeruginosa. *Nanomedicine Nanotechnol. Biol. Med.* **2012**, *8* (1), 12–16. https://doi.org/10.1016/j.nano.2011.09.009.
(18) Lekka, M.; Laidler, P.; Gil, D.; Lekki, J.; Stachura, Z.; Hrynkiewicz, A. Z. Elasticity of Normal and Cancerous Human Bladder Cells Studied by Scanning Force Microscopy. *Eur. Biophys. J.* **1999**, *28* (4), 312–316. https://doi.org/10.1007/s002490050213.
(19) Cross, S. E.; Jin, Y.-S.; Rao, J.; Gimzewski, J. K. Nanomechanical Analysis of Cells from Cancer Patients. *Nat. Nanotechnol.* **2007**, *2* (12), 780–783. https://doi.org/10.1038/nnano.2007.388.
(20) Omidvar, R.; Tafazzoli-shadpour, M.; Shokrgozar, M. A.; Rostami, M. Atomic Force Microscope-Based Single Cell Force Spectroscopy of Breast Cancer Cell Lines: An Approach for Evaluating Cellular Invasion. *J. Biomech.* **2014**, *47* (13), 3373–3379. https://doi.org/10.1016/j.jbiomech.2014.08.002.
(21) Bastatas, L.; Martinez-Marin, D.; Matthews, J.; Hashem, J.; Lee, Y. J.; Sennoune, S.; Filleur, S.; Martinez-Zaguilan, R.; Park, S. AFM Nano-Mechanics and Calcium Dynamics of Prostate Cancer Cells with Distinct Metastatic Potential. *Biochim. Biophys. Acta BBA - Gen. Subj.* **2012**, *1820* (7), 1111–1120. https://doi.org/10.1016/j.bbagen.2012.02.006.
(22) Smolyakov, G.; Thiebot, B.; Campillo, C.; Labdi, S.; Severac, C.; Pelta, J.; Dague, É. Elasticity, Adhesion, and Tether Extrusion on Breast Cancer Cells Provide a Signature of Their Invasive Potential. *ACS Appl. Mater. Interfaces* **2016**, *8* (41), 27426–27431. https://doi.org/10.1021/acsami.6b07698.
(23) Sanyour, H. J.; Li, N.; Rickel, A. P.; Childs, J. D.; Kinser, C. N.; Hong, Z. Membrane Cholesterol and Substrate Stiffness Co-Ordinate to Induce the Remodelling of the Cytoskeleton and the Alteration in the Biomechanics of Vascular Smooth Muscle Cells. *Cardiovasc. Res.* **2019**, *115* (8), 1369–1380. https://doi.org/10.1093/cvr/cvy276.
(24) Lekka, M.; Fornal, M.; Pyka-Fościak, G.; Lebed, K.; Wizner, B.; Grodzicki, T.; Styczeń, J. Erythrocyte Stiffness Probed Using Atomic Force Microscope. *Biorheology* **2005**, *42* (4), 307–317.
(25) Dulińska, I.; Targosz, M.; Strojny, W.; Lekka, M.; Czuba, P.; Balwierz, W.; Szymoński, M. Stiffness of Normal and Pathological Erythrocytes Studied by Means of Atomic Force

Microscopy. *J. Biochem. Biophys. Methods* **2006**, *66* (1), 1–11. https://doi.org/10.1016/j.jbbm.2005.11.003.
(26) Benech, J. C.; Benech, N.; Zambrana, A. I.; Rauschert, I.; Bervejillo, V.; Oddone, N.; Damián, J. P. Diabetes Increases Stiffness of Live Cardiomyocytes Measured by Atomic Force Microscopy Nanoindentation. *Am. J. Physiol.-Cell Physiol.* **2014**, *307* (10), C910–C919. https://doi.org/10.1152/ajpcell.00192.2013.
(27) Dague, E.; Genet, G.; Lachaize, V.; Guilbeau-Frugier, C.; Fauconnier, J.; Mias, C.; Payré, B.; Chopinet, L.; Alsteens, D.; Kasas, S.; et al. Atomic Force and Electron Microscopic-Based Study of Sarcolemmal Surface of Living Cardiomyocytes Unveils Unexpected Mitochondrial Shift in Heart Failure. *J. Mol. Cell. Cardiol.* **2014**, *74*, 162–172. https://doi.org/10.1016/j.yjmcc.2014.05.006.
(28) Martinez-Rivas, A.; González-Quijano, G. K.; Proa-Coronado, S.; Séverac, C.; Dague, E. Methods of Micropatterning and Manipulation of Cells for Biomedical Applications. *Micromachines* **2017**, *8* (12), 347. https://doi.org/10.3390/mi8120347.
(29) Städler, B.; Falconnet, D.; Pfeiffer, I.; Höök, F.; Vörös, J. Micropatterning of DNA-Tagged Vesicles. *Langmuir* **2004**, *20* (26), 11348–11354. https://doi.org/10.1021/la0482305.
(30) Estevam-Alves, R.; Ferreira, P. H. D.; Coatrini, A. C.; Oliveira, O. N.; Fontana, C. R.; Mendonca, C. R. Femtosecond Laser Patterning of the Biopolymer Chitosan for Biofilm Formation. *Int. J. Mol. Sci.* **2016**, *17* (8), 1243. https://doi.org/10.3390/ijms17081243.
(31) Huang, G.; Mei, Y.; Thurmer, D. J.; Coric, E.; Schmidt, O. G. Rolled-up Transparent Microtubes as Two-Dimensionally Confined Culture Scaffolds of Individual Yeast Cells. *Lab. Chip* **2009**, *9* (2), 263–268. https://doi.org/10.1039/B810419K.
(32) Credi, C.; De Marco, C.; Molena, E.; Pla Roca, M.; Samitier Martí, J.; Marques, J.; Fernàndez-Busquets, X.; Levi, M.; Turri, S. Heparin Micropatterning onto Fouling-Release Perfluoropolyether-Based Polymers via Photobiotin Activation. *Colloids Surf. B Biointerfaces* **2016**, *146*, 250–259. https://doi.org/10.1016/j.colsurfb.2016.06.020.
(33) Chiou, P. Y.; Ohta, A. T.; Wu, M. C. Massively Parallel Manipulation of Single Cells and Microparticles Using Optical Images. *Nature* **2005**, *436* (7049), 370–372. https://doi.org/10.1038/nature03831.
(34) Jing, P.; Wu, J.; Liu, G. W.; Keeler, E. G.; Pun, S. H.; Lin, L. Y. Photonic Crystal Optical Tweezers with High Efficiency for Live Biological Samples and Viability Characterization. *Sci. Rep.* **2016**, *6* (1), 1–7. https://doi.org/10.1038/srep19924.
(35) Yusof, A.; Keegan, H.; Spillane, C. D.; Sheils, O. M.; Martin, C. M.; O'Leary, J. J.; Zengerle, R.; Koltay, P. Inkjet-like Printing of Single-Cells. *Lab. Chip* **2011**, *11* (14), 2447–2454. https://doi.org/10.1039/C1LC20176J.
(36) Zheng, Q.; Lu, J.; Chen, H.; Huang, L.; Cai, J.; Xu, Z. Application of Inkjet Printing Technique for Biological Material Delivery and Antimicrobial Assays. *Anal. Biochem.* **2011**, *410* (2), 171–176. https://doi.org/10.1016/j.ab.2010.10.024.
(37) Ding, X.; Lin, S.-C. S.; Kiraly, B.; Yue, H.; Li, S.; Chiang, I.-K.; Shi, J.; Benkovic, S. J.; Huang, T. J. On-Chip Manipulation of Single Microparticles, Cells, and Organisms Using Surface Acoustic Waves. *Proc. Natl. Acad. Sci.* **2012**, *109* (28), 11105–11109. https://doi.org/10.1073/pnas.1209288109.
(38) Naseer, S. M.; Manbachi, A.; Samandari, M.; Walch, P.; Gao, Y.; Zhang, Y. S.; Davoudi, F.; Wang, W.; Abrinia, K.; Cooper, J. M.; et al. Surface Acoustic Waves Induced Micropatterning of Cells in Gelatin Methacryloyl (GelMA) Hydrogels. *Biofabrication* **2017**, *9* (1), 015020. https://doi.org/10.1088/1758-5090/aa585e.
(39) Pivetal, J.; Royet, D.; Ciuta, G.; Frenea-Robin, M.; Haddour, N.; Dempsey, N. M.; Dumas-Bouchiat, F.; Simonet, P. Micro-Magnet Arrays for Specific Single Bacterial Cell Positioning. *J. Magn. Magn. Mater.* **2015**, *380*, 72–77. https://doi.org/10.1016/j.jmmm.2014.09.068.

(40) Souza, G. R.; Tseng, H.; Gage, J. A.; Mani, A.; Desai, P.; Leonard, F.; Liao, A.; Longo, M.; Refuerzo, J. S.; Godin, B. Magnetically Bioprinted Human Myometrial 3D Cell Rings as A Model for Uterine Contractility. *Int. J. Mol. Sci.* **2017**, *18* (4), 683. https://doi.org/10.3390/ijms18040683.
(41) Théry, M.; Racine, V.; Piel, M.; Pépin, A.; Dimitrov, A.; Chen, Y.; Sibarita, J.-B.; Bornens, M. Anisotropy of Cell Adhesive Microenvironment Governs Cell Internal Organization and Orientation of Polarity. *Proc. Natl. Acad. Sci.* **2006**, *103* (52), 19771–19776. https://doi.org/10.1073/pnas.0609267103.
(42) Cerf, A.; Cau, J.-C.; Vieu, C.; Dague, E. Nanomechanical Properties of Dead or Alive Single-Patterned Bacteria. *Langmuir* **2009**, *25* (10), 5731–5736. https://doi.org/10.1021/la9004642.
(43) Ressier, L.; Viallet, B.; Beduer, A.; Fabre, D.; Fabie, L.; Palleau, E.; Dague, E. Combining Convective/Capillary Deposition and AFM Oxidation Lithography for Close-Packed Directed Assembly of Colloids. *Langmuir* **2008**, *24* (23), 13254–13257. https://doi.org/10.1021/la8028726.
(44) Malaquin, L.; Kraus, T.; Schmid, H.; Delamarche, E.; Wolf, H. Controlled Particle Placement through Convective and Capillary Assembly. *Langmuir* **2007**, *23* (23), 11513–11521. https://doi.org/10.1021/la700852c.
(45) Formosa, C.; Pillet, F.; Schiavone, M.; Duval, R. E.; Ressier, L.; Dague, E. Generation of Living Cell Arrays for Atomic Force Microscopy Studies. *Nat. Protoc.* **2015**, *10* (1), 199–204. https://doi.org/10.1038/nprot.2015.004.
(46) Dague, E.; Jauvert, E.; Laplatine, L.; Viallet, B.; Thibault, C.; Ressier, L. Assembly of Live Micro-Organisms on Microstructured PDMS Stamps by Convective/Capillary Deposition for AFM Bio-Experiments. *Nanotechnology* **2011**, *22* (39), 395102. https://doi.org/10.1088/0957-4484/22/39/395102.
(47) Hulshof, F. F. B.; Zhao, Y.; Vasilevich, A.; Beijer, N. R. M.; de Boer, M.; Papenburg, B. J.; van Blitterswijk, C.; Stamatialis, D.; de Boer, J. NanoTopoChip: High-Throughput Nanotopographical Cell Instruction. *Acta Biomater.* **2017**, *62*, 188–198. https://doi.org/10.1016/j.actbio.2017.08.023.
(48) PRIMO: Micropatterning, Microfabrication and Hydrogel Structuration. *alvéole*.
(49) Wang, Z.; Liu, L.; Wang, Y.; Xi, N.; Dong, Z.; Li, M.; Yuan, S. A Fully Automated System for Measuring Cellular Mechanical Properties. *J. Lab. Autom.* **2012**, *17* (6), 443–448. https://doi.org/10.1177/2211068212460236.
(50) Roy, R.; Chen, W.; Cong, L.; Goodell, L. A.; Foran, D. J.; Desai, J. P. A Semi-Automated Positioning System for Contact-Mode Atomic Force Microscopy (AFM). *IEEE Trans. Autom. Sci. Eng.* **2013**, *10* (2), 462–465. https://doi.org/10.1109/TASE.2012.2226154.
(51) Favre, M.; Polesel-Maris, J.; Overstolz, T.; Niedermann, P.; Dasen, S.; Gruener, G.; Ischer, R.; Vettiger, P.; Liley, M.; Heinzelmann, H.; et al. Parallel AFM Imaging and Force Spectroscopy Using Two-Dimensional Probe Arrays for Applications in Cell Biology. *J. Mol. Recognit.* **2011**, *24* (3), 446–452. https://doi.org/10.1002/jmr.1119.
(52) Sadeghian, H.; Herfst, R.; Dekker, B.; Winters, J.; Bijnagte, T.; Rijnbeek, R. High-Throughput Atomic Force Microscopes Operating in Parallel. *Rev. Sci. Instrum.* **2017**, *88* (3), 033703. https://doi.org/10.1063/1.4978285.
(53) Dujardin, A.; Wolf, P. D.; Lafont, F.; Dupres, V. Automated Multi-Sample Acquisition and Analysis Using Atomic Force Microscopy for Biomedical Applications. *PLOS ONE* **2019**, *14* (3), e0213853. https://doi.org/10.1371/journal.pone.0213853.

Chapter 3: Materials and methods

The methodology involves immobilization of cell in arrays and measurement automation done by AFM. This chapter starts by listing some of the methodologies used in the thesis work and then the methods in detail used to prepare cell arrays, the cell culture, the cell immobilization technique, and the automation of AFM measurements are described. The parameters used for each type of experiments are listed, and the experiments can be divided into three categories: microbes (*C. albicans*), mammalian cells (HeLa), and glycan arrays (RayBio 300). Finally a section describing the data analysis and some techniques used for data organization (Freedman-Diaconis rule and k-means method) are included in this chapter.

3.1. Fabrication methods

Different cell arrays (one type for microbes and one for mammalian) were fabricated. Optical lithography, also known as photolithography, is considered the precursor technique for all the modern methods on micro-nano fabrication. Figure 3.1 shows an example of photolithography and pattern transfer on a silicon wafer using a specific type of resist. Generally, a photoresist is deposited as a thin film and exposed to radiation to transfer the patterns to a substrate. Then, by developing and etching, the resist is removed from the silicon wafer and the patterns are embossed in the wafer which is then called the master mold. The maximum resolution acquired with this technique is ~1 ±0.1 μm[1].

Soft lithography is a set of techniques more suitable for biological applications because it uses elastomeric surfaces (soft materials) with defined pattern features for transferring molecules onto surfaces[2]. Soft lithography techniques are not expensive, simple to be applied, and do not require access to a cleanroom. In this thesis work the soft lithography technique was not fully applied, so no microcontact printing steps are involved. Once the master mold is fabricated, it can be treated with an anti-sticking layer to prevent the attachment of the polymer to the master mold. Figure 3.1B shows the PDMS stamp fabrication[1]. Several stamps can be generated from one master mold, and usually, they can be used more than once. The microstructures in the PDMS stamps are used to immobilize cells.

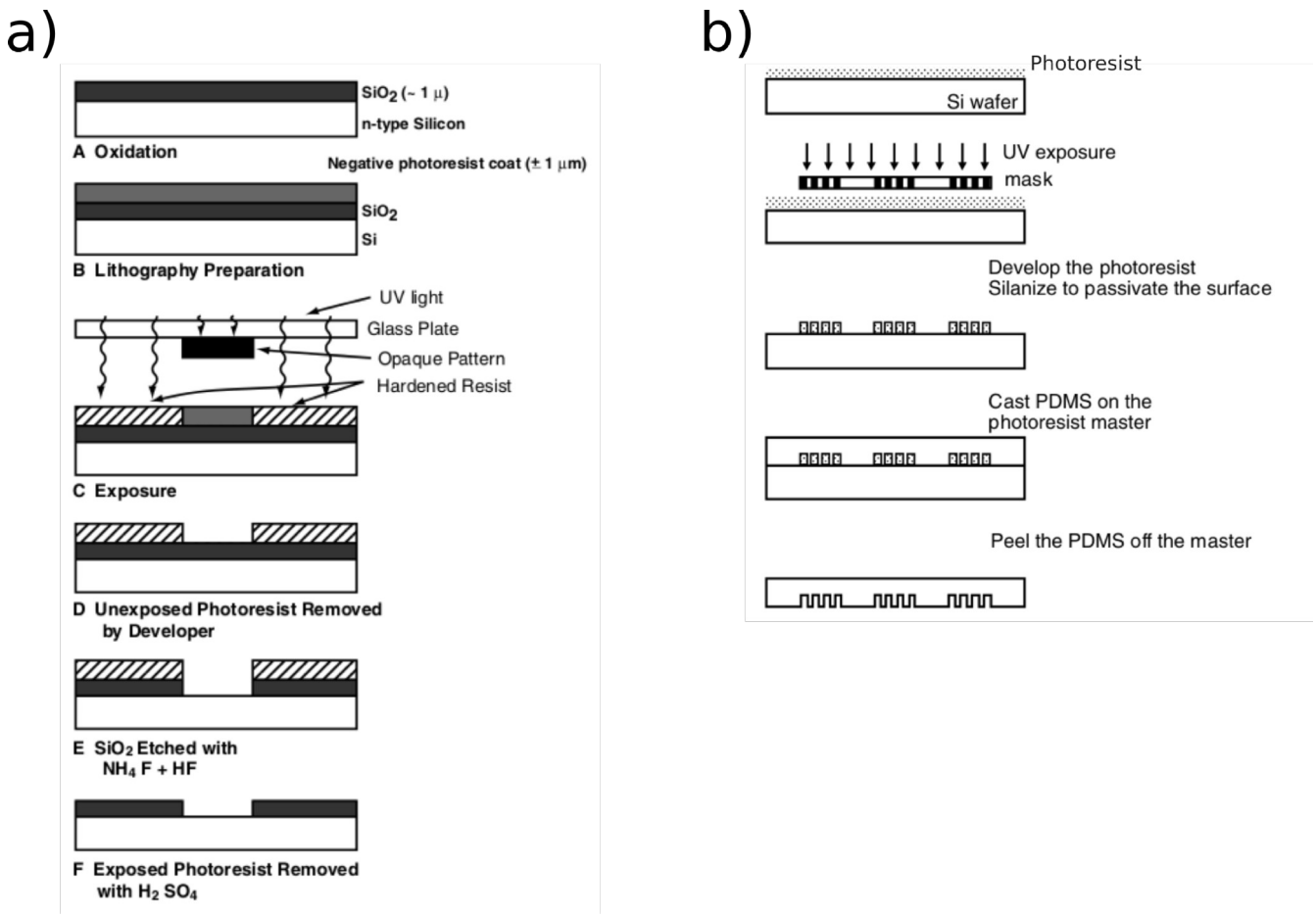

Figure 3.1. Lithography techniques. (a) Basic photolithography; the example uses an oxidized silicon wafer and a negative photoresist system. Steps in the process include exposure, development, oxide etching, and resist stripping. (b) Incomplete soft lithography process; the example starts with the master mold fabrication and proceeds to show the PDMS stamp fabrication process. The microstructures in the PDMS are used to immobilize cells. Image was modified from[1].

3.2. Cell culture

Many works around the world about diseases or the fabrication of drugs at some point are going to need to test their drugs or chemicals to verify their activity, the first systems used for this are the *in vitro* tests like cell cultures or separated tissues. For this thesis work, *C. albicans* cell culture methodology is described in Formosa et al.[3] paper meanwhile, the methodology for HeLa cells was done in collaboration with BIOSOFT company.

3.3. Immobilization techniques

3.3.1 Convective/Capillary assembly

Precise particle placement is one of the challenges to overcome when developing biodevices (involving cells, particles, among others). One reported technique is self-assembly. It relies on the interaction between the forces of the particles and the surface. Convective assembly (figure 3.2A) is a technique for depositing small particles or cells on a surface done by the evaporation of the solvent, meaning that both the temperature of the substrate and the solvent are not the same and the angle (θ_{rec}) is smaller than 20°[4,5]. As the surface of the substrate became hydrophobic is challenging

to deposit particles with convective assembly. To solve this problem, researchers founded that patterning the surface helps immobilizing because vertical structures can counter the forces on the meniscus (which are parallel to the surface), and also the angle (θ_{rec}) must be between 20° and 60° this technique is known as capillary assembly[5,6] (figure 3.2B).

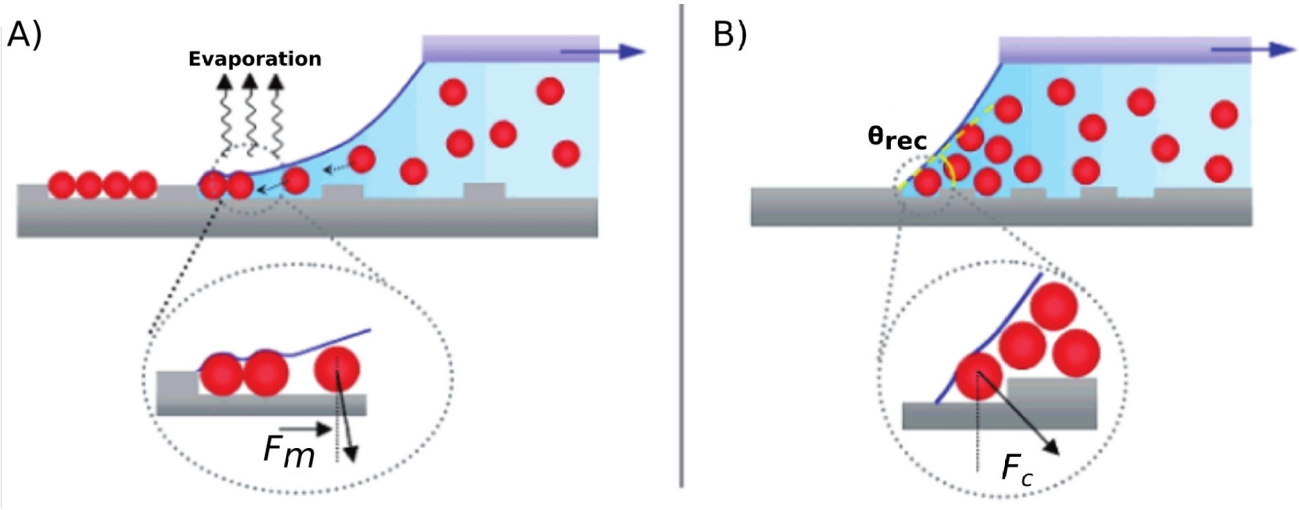

Figure 3.2. Convective/Capillary assembly techniques. A) The convective assembly is driven by the convective flow and induced evaporation at the contact line of the droplet, this leads to the formation of continuous 2D layers (F_m is the force exerted by the meniscus). B) On capillary assembly the combination of geometrical confinement and capillary forces (F_c) created by the meniscus make possible the deposit of only one or few particles, this deposition does not occur on flat surfaces. Image was modified from[5].

3.4. Automation of the indentations on the AFM

3.4.1 Atomic Force Microscopy (AFM)

This technique was derived from Scanning Tunneling Microscopy (STM). AFM is a very versatile technique because it can touch the samples and obtain topographical images, mechanical properties (elasticity, adhesion, stiffness, among others), apply voltages, or sense magnetic variations, in air or liquid. The components of an AFM are a sharp tip mounted on a cantilever beam which is attached to a piezoelectric ceramic (the piezo moves on x, y, and z). A laser strikes on the cantilever back (usually gold-coated), and it is reflected onto a four-quadrant photodiode which makes possible to track the deflection of the cantilever as it goes over the surface of the sample. The modes of AFM working are the following: contact, non-contact, and tapping. On contact mode, the tip is always touching the sample, it is faster than the other modes and it is used to obtain topographical images, mechanical properties, and friction tests. However, for fragile samples contact mode can induce some damage. In the non-contact mode the tip is far from the sample, and it is oscillating at its resonance frequency. The interaction between the forces changes the frequency of the cantilever, this mode is used for the analysis using electrical fields or magnetic forces. The tapping mode is used to obtain topographical images and also for mechanical properties; in this mode, the cantilever is oscillating with an amplitude higher than in non-contact mode. The tip touches the surface for a short time, as it is retracted continuously from the surface, and the damage that could be done to fragile samples is almost nonexistent, the feedback loop adjusts the cantilever height to maintain the amplitude constant.

However, the AFM is not only an imaging tool; the force spectroscopy mode (FS) is capable of detecting piconewton forces between the tip and the sample. In FS the tip is approached and retracted from the surface (no scan is made) the results obtained from this procedure are graphed as force versus distance curves (also known as force curves) and by using models like Hertz or Sneddon, it is possible to extract properties like Young modulus, maximum adhesion force, adhesion work, stiffness, among others[7].

3.4.2 Algorithm for the microbes

Figure 3.3A shows the flowchart for the algorithm. The first steps consist in acquiring the input parameters: two initial central coordinates (wells W1 and W2, Figure 3.3C), manually selected; the size of W1, the pitch between the well, and the size of the total area to be scanned (400 µm). The script calculates the scanning areas coordinates by using the Δ distance (distance between W1 and W2) plus half the size of W1. With those parameters, the algorithm divides the maximum area into scanning areas (Step 2, Figure 3.3B), and the centering algorithm developed for this work is executed (Step 3, see centering algorithm), to find the exact center of the initial wells (W1' and W2'). With this information, the positions of all the wells inside the scanning area and the tilt angle can be calculated accurately.

Then, the cantilever is moved toward each microwell, and inside each microwell, several nanoindentations are performed guaranteeing measurements on different regions of the cells (Step 4). To perform the nanoindentations inside the microwells it was defined a safe area (a confined square of 1,5 µm x 1,5 µm, see force data analysis section) to avoid obtaining measures at the microwell edge or on PDMS.

Once all the microwells of the scanning area have been measured the piezo is retracted, then the cantilever goes back to W1' and the motor stage activates and moves the sample to the next 100x100 μm^2 scanning area (Step 5). However, the motor stage creep prevents the cantilever from being precisely at the center of the new W1 microwell of this new 100x100 μm^2 scanning area. A centering algorithm is executed again to correct the problem. Nevertheless, the centering is executed only once, because now the tilt angle is known and it does not change in between scanning areas. The automated process described in the last paragraph can be seen in the supplementary video from Proa et al.[8].

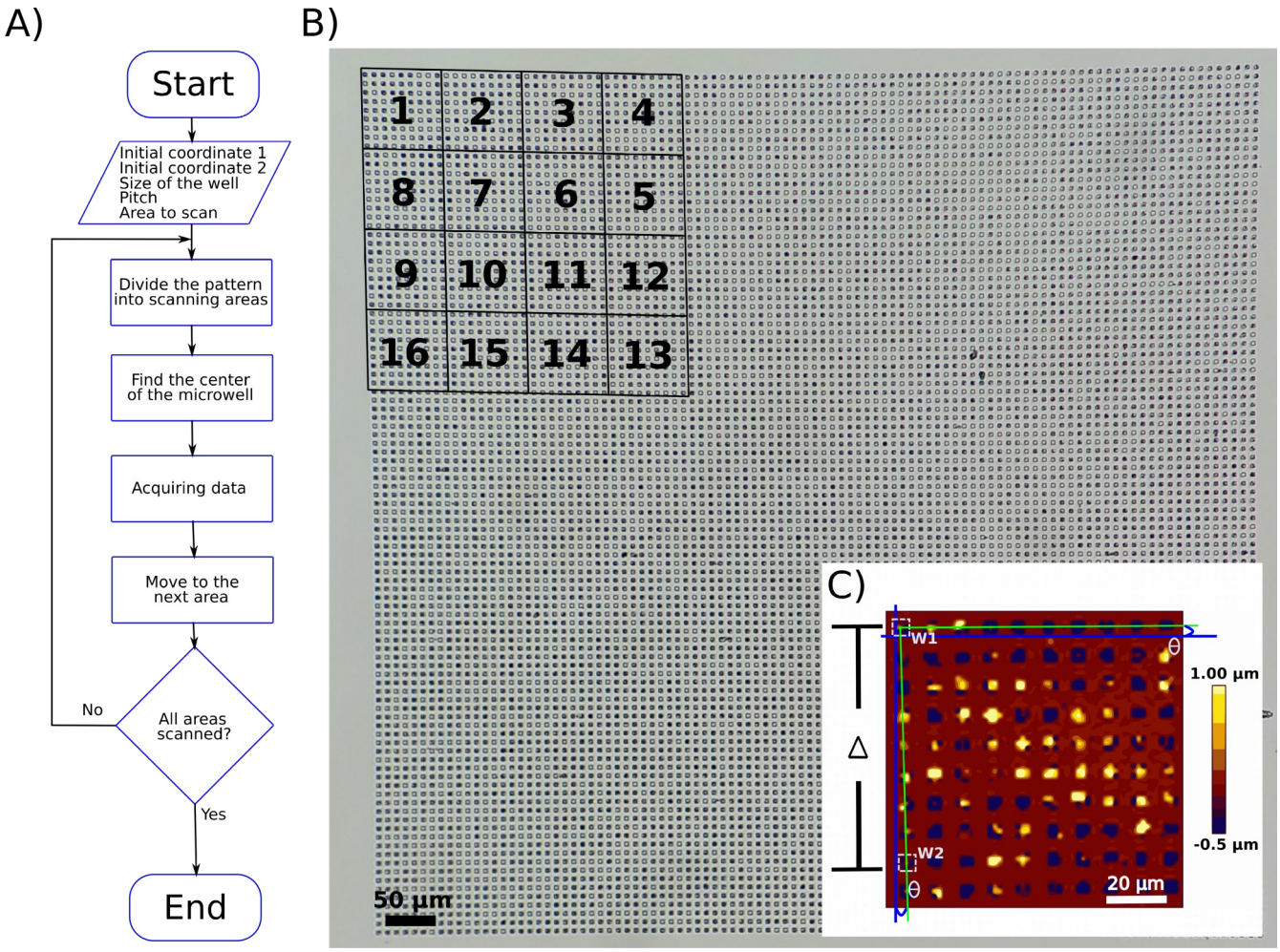

Figure 3.3. Initializing AFM automatic acquisition. A: Flowchart of the algorithm developed for automated measurements with the AFM. B: Optical image of the patterns after the cell immobilization process, the numbered squares represent the scanning areas. C: AFM topographical image recorded in force-volume mode. W1 and W2 are the initial microwells used to measure the distance Δ needed to divide the pattern into scanning areas. Blue lines represent the alignment axis of the piezo and the green lines are the axis of the pattern. Θ is the tilt angle between those two axes.

3.4.2.1 Centering algorithm

To find the center of a well the centering algorithm first creates a grid of 25 coordinates distributed in an area of 7.5 µm x 8.5 µm (Figure 3.4A), then the tip is approach to the first coordinate to be in contact with the surface (Figure 3.4B), once the tip touches the surface the height is stored (Figure 3.4B, red dotted line) and the tip is retracted. The process repeats for every coordinate in the grid. The coordinates marked C1, C2 and C3 are used for plane calculation, the plane is used to know the relative height of the flat PDMS surface. The definition of the plane equation is as Ax+By+Cz +D = 0 so it is necessary to find the coefficients A, B, C, and D, this is computed with the following equations.

$$A=(C_{3,y}-C_{1,y})(C_{2,z}-C_{1,z})-(C_{2,y}-C_{1,y})(C_{3,z}-C_{1,z}) \quad \text{(I)}$$

$$B=(C_{3,z}-C_{1,z})(C_{2,x}-C_{1,x})-(C_{2,z}-C_{1,z})(C_{3,x}-C_{1,x}) \quad \text{(II)}$$

$$C=(C_{3,x}-C_{1,x})(C_{2,y}-C_{1,y})-(C_{2,x}-C_{1,x})(C_{3,y}-C_{1,y}) \quad \text{(III)}$$

$$D=-(A)(C_{1,x})+B(C_{1,y})+C(C_{1,z}) \quad \text{(IV)}$$

Then the distance (d) between each of the 25 points (x, y, z) and the stamp plane is calculated thanks to equation V.

$$d = \frac{A(x)+B(y)+C(z)}{\sqrt{A^2+B^2+C^2}} \qquad \text{(V)}$$

Finally, this distance is used to determine which points fall inside the microwells and which are outside that is on the flat PDMS surface, conducted by assigning weights to each point, the points near or on the surface is assigned a zero weight, the points inside the well receive a weight>1. Discard the points with zero weight and, only points with weight>1 (Figure 3.4B, green dots) are used in equation VI to find the centroid of a polygon, which is thus considered as the more precise center of the well.

$$Centroid = \frac{\sum_{i=0}^{max} z_i(x_i, y_i)}{\sum_{i=0}^{max} z_i} \qquad \text{(VI)}$$

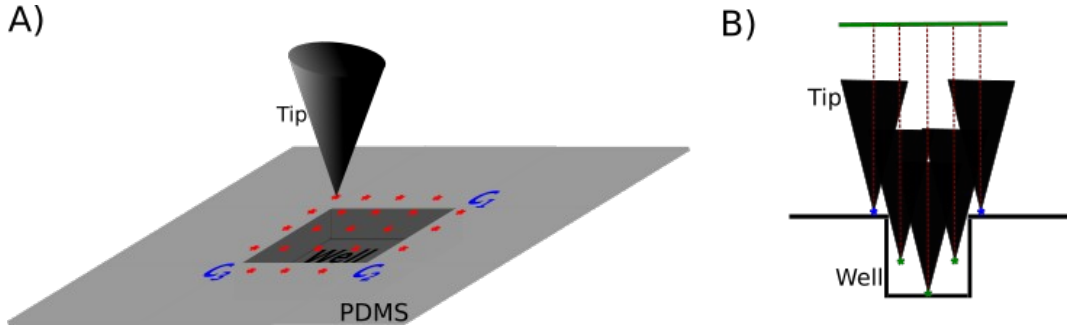

Figure 3.4. Centering algorithm. A: 3D schematic of a well and the grid of 25 points, C_1, C_2 and C_3 are the points used for plane calculation. B: schematic representation of the approaching of the tip to the well on different regions, the blue asterisks represent the points that fall on the PDMS surface and that will be used for plane calculation, the green asterisks represent the points used to find the center of the well, the green line represents the baseline of the piezo.

To move across the different scanning areas equation VII was used. The term C_{MS} was determined empirically and it helps minimizing the motor stage creep.

$$Coord_{(x+1),(y+1)} = (Coord_x - \Delta \sin\theta - C_{MS}), (Coord_y - \Delta \cos\theta) \qquad \text{(VII)}$$

$$C_{MS} = \frac{wellsize}{5}$$

3.4.3 Algorithm for the glycans and mammalian cells

The crucial modification done to the script was the movement of the motor stage for going from cell to cell. The previous section (algorithm used for microbes) mention that two different types of movements are used, the motor stage to move to different scanning areas and the movement on each microwell. Mammalian cells are larger than microbes, and the movement needs to be done via the motor stage and the mechanical measurements on different regions of the cell with the piezo. Hence, for this case, there is no need to compute the centering algorithm. Figure 3.5 left shows the flowchart conducted on mammalian cells. Some initial parameters are needed to start the execution of the script like “Initial coordinate” that refers to the center of two selected cells (represented in 3.5 right by Ic1 and Ic2). These two coordinates delimit the number of cells to be scanned (such as 2×2,

10×10, 50×50). The scanning region means the region where the force map or the individual indentations are going to be taken. The region can be the size of the cell or smaller to focus on a specific part of the cell. One of the differences between this script and the one used for microbes is that the script used for mammalian cells implements force maps acquisition, so now it is possible to select individual indentation or force maps. The number of indentations is for individual indentations option. The script makes a grid of the number of indentations x number of indentations inside the scanning region.

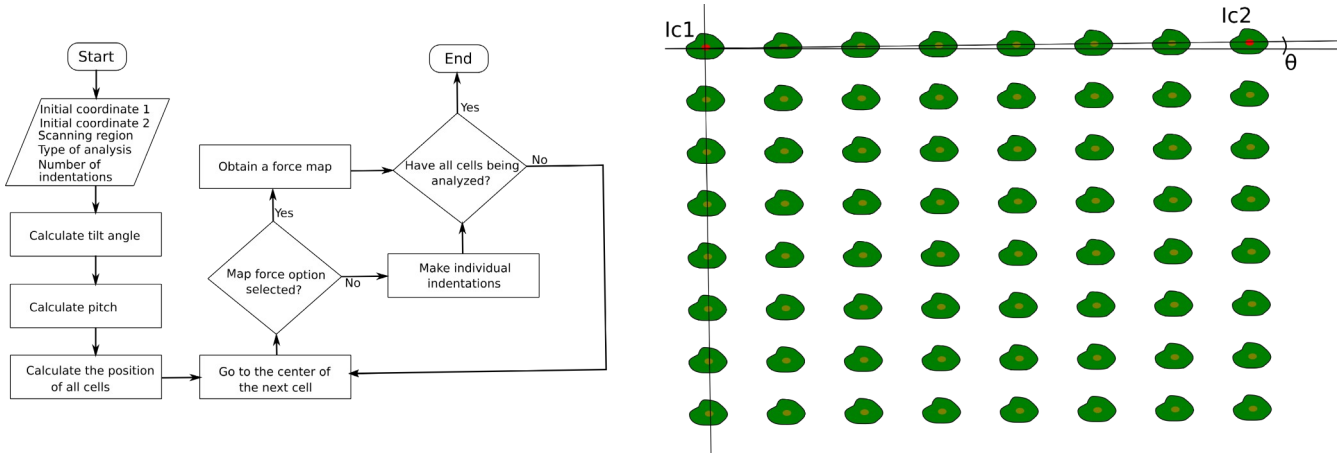

Figure 3.5. The flowchart and mammalian array schematic. Left: flowchart of the algorithm used for mammalian cells automated acquisition of the mechanical properties. Right: schematic of a mammalian cell array. Ic1 and Ic2 (red spot) represent the center of the cells. θ is the tilt angle of the array.

For glycan arrays, the script is planned to be the same as for the mammalian cells; however, two crucial modifications are considered. Firstly just one initial coordinate is needed because it is a commercial array, and all the spots have a molecule of interest. And secondly is the way the force curves are going to be stored which is important to identify the glycan measured.

3.5. Experiments

In this section it is described in detail how the experiments were performed, from the cell culture preparation, to the parameters used on the AFM. Only the PDMS stamp preparation was based on the work published by Formosa et. al.[9] and no modification was made to produce the stamp.

3.5.1 PDMS stamp preparation

The procedure reported in Formosa[9] paper is described as follows:

1. Design of the desired patterns of the silicon master using CleWin software.
2. The patterns are written using laser lithography to make a glass and chromium mask.
3. A silicon wafer is cleaned under oxygen plasma for 15 min at 800 W.
4. A solution of hexamethyldisilazane is used to promote adherence of the photoresist to the silicon wafer.
5. The photoresist AZ ECI 3012 is deposited on the silicon wafer using the EVG 120 automatic coating/developing machine (5 s of deposition and 30 s of spinning), and its bake for 60 s at 90 °C on a hot plate.

6. The silicon wafer covered by the photoresist is exposed through the glass and chromium mask for 10 s.
7. After exposure bake the silicon master for 60 s at 110 °C on a hot plate in ambient air to polymerize the resist.
8. Submerge the silicon master in a solution of MF CD-26 developer for 20 s.
9. Rinse the silicon master using deionized water and dry under nitrogen.
10. Perform RIE on the silicon master. This step must be realized under plasma of sulfur hexafluoride (SF_6, 200 sccm) and octafluorocyclobutane (C_4F_8, 400 sccm) at a pressure of 0.07 mBar and a power of 2,800 W.
11. Remove the remaining photoresist from the silicon master under oxygen plasma for 15 min at 800 W.
12. Put the silicon master in octadecyltrichlorosilane in liquid phase to render the silicon wafer anti-adhesive.
13. Prepare PDMS pre-polymer solution in a 10:1 mass ratio of PDMS olygomers and a reticular agent.
14. Degas the solution under vacuum.
15. Deposit the degassed PDMS solution on the silicon master.
16. Cure the PDMS solution on the silicon master for 1 h at 80 °C in ambient air.
17. Cut with a scalpel and detach the PDMS microstructures.

3.5.2 *Candida albicans*

C. albicans was stored at -80 °C. Four independent cultures were prepared with the *C. albicans* revivified on Yeast Peptone Dextrose (YPD) agar, and each was grown in 5 ml YPD broth for 20 h at 30 °C. Two of the cell cultures were added 9.4 µl of caspofungin at 0.1 mg ml^{-1} (4xMIC) concentration and let for 24 h at 30 °C. The four cultures were let under static conditions. The concentration of *C. albicans* cells was made by centrifugation, washed two times in acetate buffer, and resuspended in acetate buffer before performing AFM experiments.

Preparation of the stamp was as follows: 600 µl were taken from resuspended cell solution and centrifugated to separate the buffer from the cells. The supernatant was deposited onto the PDMS stamp and degassed for ~40 min. Then buffer is removed from the PDMS surface, and 200 µl of cell solution was deposited and allowed to stand for 15 min at room temperature. Then by using convective/capillary assembly the cells were placed into the microwells.

The measurements were done with a commercial JPK Nanowizard II, with a motorized precision stage MotStage Zeiss AxioObserver (S/N SM-01-0017) on an inverted optical microscope Zeiss Axiovert 200M. The AFM control software (SPM version 4). Tips used were commercially available silicon nitride triangular cantilevers (Bruker MLCT) with spring constants and sensitivity ranging respectively from 0.0110 N m-1 to 0.0405 N m-1 and from 31.8 nm V^{-1} to 54.2 nm V^{-1}. Calibration was done using the thermal tune method. The parameters used to engage the tip were: Igain = 70Hz, Pgain = 0.002, setpoint = 0.5 nN. The maximum applied force used to record force curves was set to 1 nN and the piezo and motor stage speed were 10 µm s^{-1} and 200 µm s^{-1} respectively. The AFM field was 100 µm x 100 µm. The script was written in Jython 2.5, it is a fusion between Python and Java language, and executed using the experiment planner module included in the SPM software control, which runs under Ubuntu 10.04 LTS (Lucid Lynx).

3.5.3 HeLa cells

The HeLa cells were prepared in collaboration with BIOSOFT company using the following procedure: from one flask of HeLa cells it was removed the media, the cells with 1 ml PBS buffer (Gibco™ DPBS 1X) were washed. Then 1 ml trypsin (HyClone trypsin 0.05% 1x) is added to the cells and let it rest for 3 min. Then 2 ml of medium (DMEM 1x + GlutaMAX™) was added.
To immobilize the HeLa cells two types of cell arrays were used; the ones provided by BIOSOFT (ready for use on the AFM). And the CYTOO chips (REF 10-900-13-06), prepared as recommended by the company. Every CYTOO chip is divided into 169 grid units which have coordinates printed on the underside of the chip. Each square grid unit has 144 identical micropatterns giving a total of ~20,000 micropatterns per chip. However, CYTOO Chips starter's user guide mention that only 10-30% of the micropatterns are occupied by a single cell. That is not a good filling rate to perform an analysis because the methodology presented in this thesis work is highly dependent on the number of cells immobilized.
The decision to select CYTOO or BIOSOFT was based on the immobilization results and in the end BIOSOFT was the choice because those chips had a higher filling rate despite not all the spots had single cells. An experiment to test the modified script working with this new chip was developed. The BIOSOFT immobilization was done using InnoStamp 40TM on glass slides[10], and three types of micropatterns were used (circles, triangles, and squares).
The measurements were done with the same commercial JPK Nanowizard II, the parameters are the same as the ones listed in the previous sub-section (*C. albicans*).

3.5.4 Glycan arrays

RayBio Glycan Array 300 was acquired to perform tests using the automated methodology in conjunction with single-cell force spectroscopy (SCFS). Figure 3.6 show the four identical sub-arrays delivered in one slide. The glycans printed per sub-array are 100 glycans from the RayBio Glycan-100 array, an additional 80 N-glycans, 50 glycolipid glycans, 18 tandem epitopes, and 50 human milk oligosaccharide glycans. Each glycan has a coordinate associated, but this coordinate is not printed on the slide. The procedure was to cut the glass slide to use only one of the sub-arrays per experiment and perform the analysis in liquid. The microscope parameters are the same as for the HeLa and *C. albicans cells*.
The glycan arrays are stored at -20°C and after initial use they are stored at 4°C. The cutting of the sub-array was done with a conventional diamond tip cutter. The main problem with the glycan array is that it was developed for fluorescent labeling, and its adaptation to our methodology is challenging because it has a considerable random error in the spots position, so the program would has to be modified for each subarray.

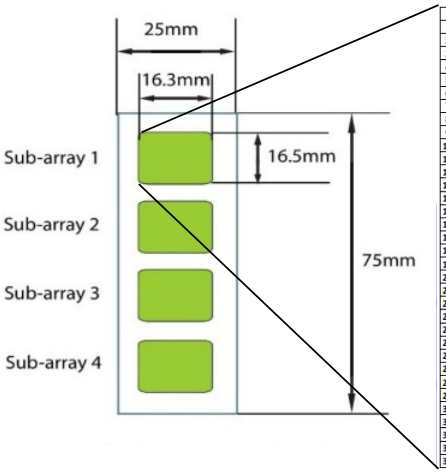

	1	2	3	4	5	6	7	8	9	10	11	12	13	14	15	16	17	18	19	20	21	22	23	24	25	26	27
1	POS1	POS1	POS1	POS2	POS2	POS2	NEG	NEG	NEG	G0001	G0001	G0001	G0002	G0002	G0002	G0003	G0003	G0003	G0004	G0004	G0004	G0005	G0005	G0005	G0006	G0006	G0006
2	G0007	G0007	G0007	G0008	G0008	G0008	G0009	G0009	G0009	G0010	G0010	G0010	G0011	G0011	G0011	G0012	G0012	G0012	G0013	G0013	G0013	G0014	G0014	G0014	G0015	G0015	G0015
3	G0016	G0016	G0016	G0017	G0017	G0017	G0018	G0018	G0018	G0019	G0019	G0019	G0020	G0020	G0020	G0021	G0021	G0021	G0022	G0022	G0022	G0023	G0023	G0023	G0024	G0024	G0024
4	G0025	G0025	G0025	G0026	G0026	G0026	G0027	G0027	G0027	G0028	G0028	G0028	G0029	G0029	G0029	G0030	G0030	G0030	G0031	G0031	G0031	G0032	G0032	G0032	G0033	G0033	G0033
5	G0034	G0034	G0034	G0035	G0035	G0035	G0036	G0036	G0036	G0037	G0037	G0037	G0038	G0038	G0038	G0039	G0039	G0039	G0040	G0040	G0040	G0041	G0041	G0041	G0042	G0042	G0042
6	G0043	G0043	G0043	G0044	G0044	G0044	G0045	G0045	G0045	G0046	G0046	G0046	G0047	G0047	G0047	G0048	G0048	G0048	G0049	G0049	G0049	G0050	G0050	G0050	G0051	G0051	G0051
7	G0052	G0052	G0052	G0053	G0053	G0053	G0054	G0054	G0054	G0055	G0055	G0055	G0056	G0056	G0056	G0057	G0057	G0057	G0058	G0058	G0058	G0059	G0059	G0059	G0060	G0060	G0060
8	G0061	G0061	G0061	G0062	G0062	G0062	G0063	G0063	G0063	G0064	G0064	G0064	G0065	G0065	G0065	G0066	G0066	G0066	G0067	G0067	G0067	G0068	G0068	G0068	G0069	G0069	G0069
9	G0070	G0070	G0070	G0071	G0071	G0071	G0072	G0072	G0072	G0073	G0073	G0073	G0074	G0074	G0074	G0075	G0075	G0075	G0076	G0076	G0076	G0077	G0077	G0077	G0078	G0078	G0078
10	G0079	G0079	G0079	G0080	G0080	G0080	G0081	G0081	G0081	G0082	G0082	G0082	G0083	G0083	G0083	G0084	G0084	G0084	G0085	G0085	G0085	G0086	G0086	G0086	G0087	G0087	G0087
11	G0088	G0088	G0088	G0089	G0089	G0089	G0090	G0090	G0090	G0091	G0091	G0091	G0092	G0092	G0092	G0093	G0093	G0093	G0094	G0094	G0094	G0095	G0095	G0095	G0096	G0096	G0096
12	G0097	G0097	G0097	G0098	G0098	G0098	G0099	G0099	G0099	G0100	G0100	G0100	N010	N010	N010	N011	N011	N011	N012	N012	N012	N013	N013	N013	N014	N014	N014
13	N015	N015	N015	N020	N020	N020	N021	N021	N021	N022	N022	N022	N023	N023	N023	N024	N024	N024	N025	N025	N025	N026	N026	N026	N022G	N022G	N022G
14	N023G	N023G	N023G	N025G	N025G	N025G	N030	N030	N030	N210	N210	N210	N040	N040	N040	N041	N041	N041	N042	N042	N042	N043	N043	N043	N044	N044	N044
15	N045	N045	N045	N050	N050	N050	N051	N051	N051	N052	N052	N052	N053	N053	N053	N054	N054	N054	N055	N055	N055	TE001	TE001	TE001	TE002	TE002	TE002
16	TE003	TE003	TE003	TE004	TE004	TE004	TE005	TE005	TE005	TE006	TE006	TE006	TE007	TE007	TE007	TE008	TE008	TE008	TE009	TE009	TE009	TE010	TE010	TE010	TE011	TE011	TE011
17	TE012	TE012	TE012	TE013	TE013	TE013	TE014	TE014	TE014	TE015	TE015	TE015	TE016	TE016	TE016	TE017	TE017	TE017	TE018	TE018	TE018	TE019	TE019	TE019	TE020	TE020	TE020
18	TE021	TE021	TE021	TE022	TE022	TE022	TE023	TE023	TE023	TE024	TE024	TE024	TE025	TE025	TE025	TE026	TE026	TE026	TE027	TE027	TE027	TE028	TE028	TE028	TE029	TE029	TE029
19	TE030	TE030	TE030	TE031	TE031	TE031	TE032	TE032	TE032	TE033	TE033	TE033	TE034	TE034	TE034	TE035	TE035	TE035	TE036	TE036	TE036	TE037	TE037	TE037	TE038	TE038	TE038
20	TE039	TE039	TE039	TE040	TE040	TE040	TE041	TE041	TE041	TE042	TE042	TE042	TE043	TE043	TE043	TE044	TE044	TE044	TE045	TE045	TE045	TE046	TE046	TE046	TE047	TE047	TE047
21	TE048	TE048	TE048	TE049	TE049	TE049	TE050	TE050	TE050	H0100	H0100	H0100	H0101	H0101	H0101	H0103	H0103	H0103	H0105	H0105	H0105	H0106	H0106	H0106	H0200	H0200	H0200
22	H0201	H0201	H0201	H0202	H0202	H0202	H0203	H0203	H0203	H0204	H0204	H0204	H0205	H0205	H0205	H0207	H0207	H0207	H0208	H0208	H0208	H0209	H0209	H0209	H0210	H0210	H0210
23	H0300	H0300	H0300	H0301	H0301	H0301	H0303	H0303	H0303	H0304	H0304	H0304	H0305	H0305	H0305	H0306	H0306	H0306	H0307	H0307	H0307	H0400	H0400	H0400	H0402	H0402	H0402
24	H0403	H0403	H0403	H0404	H0404	H0404	H0405	H0405	H0405	H0406	H0406	H0406	H0407	H0407	H0407	H0408	H0408	H0408	H0409	H0409	H0409	H0410	H0410	H0410	H0411	H0411	H0411
25	H0500	H0500	H0500	H0503	H0503	H0503	H0504	H0504	H0504	H0505	H0505	H0505	H0600	H0600	H0600	H0601	H0601	H0601	H0602	H0602	H0602	H0603	H0603	H0603	H0604	H0604	H0604
26	H0606	H0606	H0606	H0608	H0608	H0608	H0609	H0609	H0609	H0610	H0610	H0610	H0700	H0700	H0700	H0701	H0701	H0701	H0800	H0800	H0800	H0900	H0900	H0900	L1001	L1001	L1001
27	L1002	L1002	L1002	L1003	L1003	L1003	L1011	L1011	L1011	L1012	L1012	L1012	L1013	L1013	L1013	L1021	L1021	L1021	L1022	L1022	L1022	L1023	L1023	L1023	L1201	L1201	L1201
28	L1202	L1202	L1202	L1203	L1203	L1203	L1204	L1204	L1204	L1205	L1205	L1205	L1206	L1206	L1206	L1207	L1207	L1207	L1209	L1209	L1209	L1211	L1211	L1211	L1212	L1212	L1212
29	L1213	L1213	L1213	L1214	L1214	L1214	L1215	L1215	L1215	L1216	L1216	L1216	L1221	L1221	L1221	L1222	L1222	L1222	L1225	L1225	L1225	L1226	L1226	L1226	L2000	L2000	L2000
30	L2100	L2100	L2100	L2101	L2101	L2101	L2102	L2102	L2102	L2111	L2111	L2111	L2112	L2112	L2112	L2113	L2113	L2113	L2121	L2121	L2121	L2122	L2122	L2122	L2103	L2103	L2103
31	L2104	L2104	L2104	L2131	L2131	L2131	L2132	L2132	L2132	L2133	L2133	L2133	L2191	L2191	L2191	L2192	L2192	L2192	L2200	L2200	L2200	L2300	L2300	L2300	L2301	L2301	L2301
32	L2302	L2302	L2302	L2311	L2311	L2311	L2312	L2312	L2312	L2303	L2303	L2303	L2304	L2304	L2304	L2391	L2391	L2391	L2392	L2392	L2392	L2900	L2900	L2900	L2911	L2911	L2911
33	L2912	L2912	L2912	L2913	L2913	L2913	L3100	L3100	L3100	L3101	L3101	L3101	L3102	L3102	L3102	L3111	L3111	L3111	L3112	L3112	L3112	L3113	L3113	L3113	L3103	L3103	L3103
34	L3200	L3200	L3200	L3201	L3201	L3201	L3202	L3202	L3202	L3211	L3211	L3211	L3212	L3212	L3212	L3213	L3213	L3213	NEG	NEG	NEG	POS2	POS2	POS2	POS1	POS1	POS1

Figure 3.6. Glycan array schematic. The glass slide is composed of four sub-array and the distribution of each sub-array is shown. The array is composed of positive and negative controls (POS and NEG respectively), Glycans (G0001-G0100), N-Glycans (NYYY), Glycolipid Glycans (LYYY), Human Milk Oligosaccharides (HYYYY), Tandem epitopes (TEYYY). Y represents different numbers 0-9.

3.6. Data analysis

The script saves the force curves in folders organized by the number of area and the number of well inside the current area. However, the numbering of the wells is reset when the area is changed, this forced us to develop a script capable of changing the numbering of the force curves so we can have a continuous numbering. Executing the “Copy files” python script copy all the force curves files into a designated directory replacing the number of the well by a serial numbering.

Mechanical analysis is the study of the shape and volume of a solid body by applying external forces to change it. If the forces applied are not too large, the body should be capable of returning to its original shape and volume when the force is no longer present, this phenomenon is called elasticity, and it depends on how the forces are applied (longitudinal, volumetric, and shearing)[11]. Figure 3.7A shows the plot of longitudinal strain (ΔL/L) versus longitudinal stress (ΔF/A). It shows two behaviors elastic and plastic. To describe the elastic behavior it could be imagined a piece of wire or a metal bar of uniform cross-sectional area (A) under tension when the tensile force is applied the axial length of the bar changes. If the force is not too large, the longitudinal strain is proportional to the longitudinal stress, and when the force is removed, the bar retracts entirely to its original length. However, if the forces applied to the bar are sufficiently large, its behavior changes (plastic behavior) and the relation between stress and strain is no longer linear, and the bar is permanently stretched. The point P is called the elastic limit and is the point in which the behavior becomes nonlinear and irreversible.

The mechanical analysis of cells is done in the elastic region of the plot presented in figure 3.7A. Figure 3.7B depicts a force curve having two parts, the approaching part (also known as extend) and the retract part. In the approaching curve, a contact point (CP) is found, it is the point where the tip touches the sample for the first time, from this point forward the force applied to the tip is causing a deformation on the sample. When the maximum force is reached the cantilever stops and start detaching from the sample (retract curve), as the cantilever is moving away from the sample, it is possible to see a point when the tip suddenly release itself from the sample surface, this point is known as the maximum adhesion force. A segment of the approaching curve (from the CP to the

end of the curve) is used to calculate the Young modulus meanwhile the retract curve is used to obtain the maximum adhesion force (MA_F) and performing a linear fit (LF) on this curve give you the stiffness.

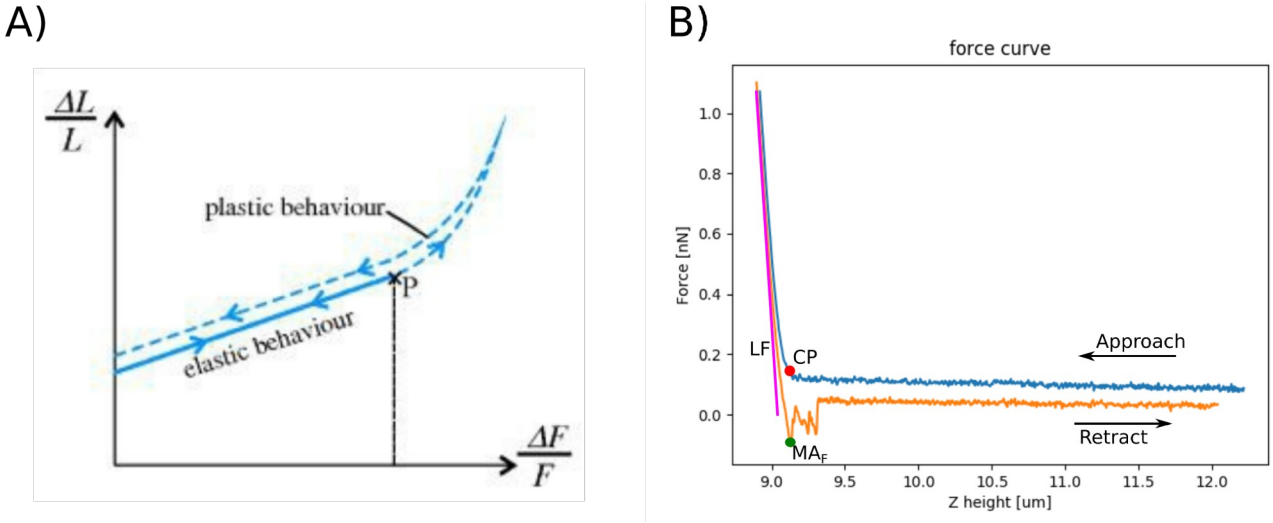

Figure 3.7. Mechanical plots. A) Plot of longitudinal strain versus longitudinal stress for a solid. For an applied stress below the elastic limit (P) the behavior of the deformation is linear and the body resumes its original length when the stress is removed (solid line). If the elastic limit is exceeded the strain depends on stress in a nonlinear manner and the body remains permanently extended (dashed line) after the stress has been removed. Image was taken from[11]*. B) Plot of a force curve showing the two components extend (blue) and retract (orange). The red spot indicates the contact point (CP) which is when the tip first touches the sample. The green dot represents the point of maximum adhesion force (MA_F) and the stiffness is obtained from a linear fit (LF) on the linear section of the retract curve.*

Young modulus is obtained mainly using two models, the Hertz model[12] and the Sneddon[13] model. The principal difference between those models is that Hertz considers only a circular indenter meanwhile Sneddon consider pyramidal indenter. In both cases, the CP is an important parameter to consider because when its lightly changed a considerable change in the calculated Young modulus is found, so the correct calculation of the CP it is crucial to produce repeatable results.

The extraction of the stiffness was done using the JPK data processing software. The procedure followed with the JPK software was as follows: In the top menu ‘File’ select open ‘batch of spectroscopy curves’. In the batch processing window, use the process we provide in the appendix. Select the last part of the process and click on ‘keep and apply to all'. All force curves will receive the same treatment. Briefly: The process uses the calibration from the FCs files to convert the deflection curves into force curves calibrated in N; a data smoothing algorithm is applied; the baseline is translated to rest on the zero axis; the contact point is extrapolated and the FC is offset to place the contact point at coordinate (0,0); the bending of the cantilever is subtracted to the FCs, the retract slope is fitted. At the end of the data treatment, the software generates a file that contains a table giving for each force curve such as its name, Young modulus, contact point, adhesion force, slopes.

3.6.1 Statistical analysis

The results from the JPK data processing software are stored into two different files (one for treated and another for native cells). The plotting of the histograms, and ANOVA statistical treatments were

done using an R script. The width of the bins in the histograms was done using the Freedman-Diaconis rule because it has been reported that it works on non-theoretical cases. The histograms presented two subpopulations, we used the k-means method to determine which data correspond to the first or the second subpopulation.

3.6.1.1 Freedman-Diaconis rule

In statistics, the Freedman-Diaconis rule is used to calculate the width of the bins to be used in a histogram[14]. Other approaches are Scott and Sturges rule, and the three rules behave almost the same for samples between 50 and 500 points. However, for larger samples only the Freedman-Diaconis rule gives 35% more bins and it is considered a rule that works for non-theoretical cases[15].

3.6.1.2 K-means method

The k-means method is based on the Hartigan and Wong algorithm[16]. It divides M points in N dimensions into K clusters, and the centers of the clusters are at the mean of their Voronoi set[17] (the set of data points which are nearest to the group center). The procedure is to minimize the within-cluster sum of squares, so the dimension of the clusters is changed until the items in the same cluster are similar as possible, and items in different clusters are different as possible.

The execution of the R script was done as follows: open the R script use R studio, and load the files containing the information extracted with the data processing software (.tsv). On the environment window use the “Import Dataset” button, from the list displayed select “from text (readr)” and in the new window select the Browser button and find the .tsv file. Once the file is loaded select the columns you want to include for the analysis. The script works with 4 datasets, consider two experiments both having native and treated cells. It is possible to execute blocks of the script and see how the variables change according to the functions executed. However, to run all the code just press ctrl+alt+r.

3.7. Conclusions

In this chapter, the methods and methodologies used to implement the automated methodology successfully have been listed. Fabrication of cell arrays (PDMS microstructures) was done following the Formosa et al. paper; however, for the cell immobilization step, some intermediate steps were added. Depositing of the cell culture supernatant and after degassing of the PDMS stamp improved cell attachment to the PDMS patterns.

Two AFM scripts were developed based on the type of cell to analyze. They have some similarities, like the tilt angle calculation and the movement across the stamp. However, for the mammalian cells script, the functionality of acquiring force maps has been implemented, and the movement from cell to cell is done using the motor stage. The problem of using motor stage movement is time consumption, it can duplicate the times of execution if used too often. Time consumption is a problem we think could be corrected with an update of the software control or a newer version of the microscope. Also, in commercial AFMs motor stage has a displacement error known as “creep”, the error to consider is ~2 µm but it is important to consider it when moving the stage.

Mechanical analysis of cells was done in the elastic region, and the stiffness was extracted from the force curves using the data treatment showed in the data analysis section. Freedman-Diaconis rule helped determine the optimal size of the bins in the histograms and k-mean method were used to

group the data contain in the *C. albicans* subpopulations, this provided us with a mathematical classification of the data and to analyze the grouped data.

3.8. References

(1) Madou, M. J. *Fundamentals of Microfabrication: The Science of Miniaturization, Second Edition*; CRC Press, 2002.

(2) Encyclopedia of Nanotechnology | SpringerLink https://link.springer.com/referencework/10.1007/978-90-481-9751-4 (accessed Aug 29, 2019).

(3) Formosa, C.; Schiavone, M.; Martin-Yken, H.; François, J. M.; Duval, R. E.; Dague, E. Nanoscale Effects of Caspofungin against Two Yeast Species, Saccharomyces Cerevisiae and Candida Albicans. *Antimicrob. Agents Chemother.* **2013**, *57* (8), 3498–3506. https://doi.org/10.1128/AAC.00105-13.

(4) Prevo, B. G.; Velev, O. D. Controlled, Rapid Deposition of Structured Coatings from Micro- and Nanoparticle Suspensions. *Langmuir* **2004**, *20* (6), 2099–2107. https://doi.org/10.1021/la035295j.

(5) Malaquin, L.; Kraus, T.; Schmid, H.; Delamarche, E.; Wolf, H. Controlled Particle Placement through Convective and Capillary Assembly. *Langmuir* **2007**, *23* (23), 11513–11521. https://doi.org/10.1021/la700852c.

(6) Yin, Y.; Lu, Y.; Gates, B.; Xia, Y. Template-Assisted Self-Assembly: A Practical Route to Complex Aggregates of Monodispersed Colloids with Well-Defined Sizes, Shapes, and Structures. *J. Am. Chem. Soc.* **2001**, *123* (36), 8718–8729. https://doi.org/10.1021/ja011048v.

(7) Formosa, C.; Dague, E. Imaging Living Yeast Cells and Quantifying Their Biophysical Properties by Atomic Force Microscopy. In *Advanced Microscopy in Mycology*; Dahms, T. E. S., Czymmek, K. J., Eds.; Fungal Biology; Springer International Publishing: Cham, 2015; pp 125–141. https://doi.org/10.1007/978-3-319-22437-4_7.

(8) Proa-Coronado, S.; Séverac, C.; Martinez-Rivas, A.; Dague, E. Beyond the Paradigm of Nanomechanical Measurements on Cells Using AFM: An Automated Methodology to Rapidly Analyse Thousands of Cells. *Nanoscale Horiz.* **2019**. https://doi.org/10.1039/C9NH00438F.

(9) Formosa, C.; Pillet, F.; Schiavone, M.; Duval, R. E.; Ressier, L.; Dague, E. Generation of Living Cell Arrays for Atomic Force Microscopy Studies. *Nat. Protoc.* **2015**, *10* (1), 199–204. https://doi.org/10.1038/nprot.2015.004.

(10) Lagraulet, A.; Foncy, J.; Berteloite, B.; Esteve, A.; Blatche, M.-C.; Malaquin, L.; Vieu, C. InnoStamp 40™ and InnoScan 1100AL™: A Complete Automated Platform for Microstructured Cell Arrays. *Nat. Methods* **2015**, *12*, 894–894. https://doi.org/10.1038/nmeth.f.383.

(11) Mansfield, M.; O'Sullivan, C. *Understanding Physics*; John Wiley & Sons, 2011.

(12) Johnson, K. L. One Hundred Years of Hertz Contact. *Proc. Inst. Mech. Eng.* **1982**, *196* (1), 363–378. https://doi.org/10.1243/PIME_PROC_1982_196_039_02.

(13) Sneddon, I. N. The Relation between Load and Penetration in the Axisymmetric Boussinesq Problem for a Punch of Arbitrary Profile. *Int. J. Eng. Sci.* **1965**, *3* (1), 47–57. https://doi.org/10.1016/0020-7225(65)90019-4.

(14) Freedman, D.; Diaconis, P. On the Histogram as a Density Estimator:L2 Theory. *Z. Für Wahrscheinlichkeitstheorie Verwandte Geb.* **1981**, *57* (4), 453–476. https://doi.org/10.1007/BF01025868.

(15) Scott, D. W. *Multivariate Density Estimation: Theory, Practice, and Visualization*; John Wiley & Sons, 1992.

(16) Hartigan, J. A.; Wong, M. A. Algorithm AS 136: A K-Means Clustering Algorithm. *J. R. Stat. Soc. Ser. C Appl. Stat.* **1979**, *28* (1), 100–108. https://doi.org/10.2307/2346830.
(17) R Core Team. *R: A Language and Enviroment for Statistical Computing*; R Foundation for Statistical Computing: Vienna, Austria, 2018.

Chapter 4: Automation and analysis of AFM measurements on cells

In this chapter, the results obtained during my Ph.D. are presented and discussed. In order to automatize AFM measurements on living cells, we applied an innovative strategy combining the directed assembly of cells and the development of a software able to move the AFM tip from cell to cell. In this chapter, I will, therefore, describe my results concerning these different points. The first part deals with the optimization of microbes (*Candida albicans)* immobilization into a PDMS microstructured stamp, the second part is dedicated to software development and explains the different steps that we had to validate to make the automatic displacement of the tip possible. In the third part, I present the data collected on *Candida albicans* and the nanomechanical comparison of native cells population with caspofungin treated cells population. It includes the analysis of the data by supervised machine learning. In the fourth part, I describe the results of the strategy that we decided to use to immobilize living mammalian cells. We thus decided to use another strategy, based on patterning of extracellular matrix proteins. In the fifth part, I focus on the script adaptation that has been required to achieve much longer displacement and the first results we obatined on mammalian cells. Finally, in the last part, it is discussed the possible extension of this strategy to arrays of proteins or glycans, as well as to material arrays.

4.1. Optimization of *C. albicans* immobilization in PDMS microstructured stamps

4.1.1 PDMS stamps fabrication

Stamps were previously fabricated from a Silicon master mold. The process of fabricating the master was by conventional photolithography. The design of the mask was done with CleWin software. Figure 4.1a shows the photolithography procedure to elaborate microwells master mold. First, the silicon wafer was cleaned with oxygen plasma and then a solution of hexamethyldisilazane to promote adherence of the photoresist was applied. After, the photoresist is deposited on the substrate and exposed to UV light to transfer the patterns to the photoresist. After developing and etching by reactive ion etching (RIE), the photoresist is removed, finishing the master mold. In the master mold several regions of microwells were designed, every region has different microwells sizes (1.5 – 6 µm); however, the pitch (0.5 µm) remains constant, the depth of the microwells varies from 1—4 µm (figure 4.1b, master mold in green). The total area covered by the microwells was 1mm x 1mm. Figure 4.1c shows the PDMS stamp casting procedure. First, the master mold is cleaned, so no photoresist residues are found on the surface. After, the master is submerged in octadecyltrichlorosilane to render the silicon master anti-adhesive. Then a solution (10:1) of PDMS oligomers and reticular agent is prepared and degassed. The solution is deposited on the master mold surface and cured. The motifs are cut and removed with a scalpel. The immobilization of the cells can be done by two methods, on a convective and capillary setups or manually. However, achieving a high filling ratio (>80 %) applying the manual method is difficult.

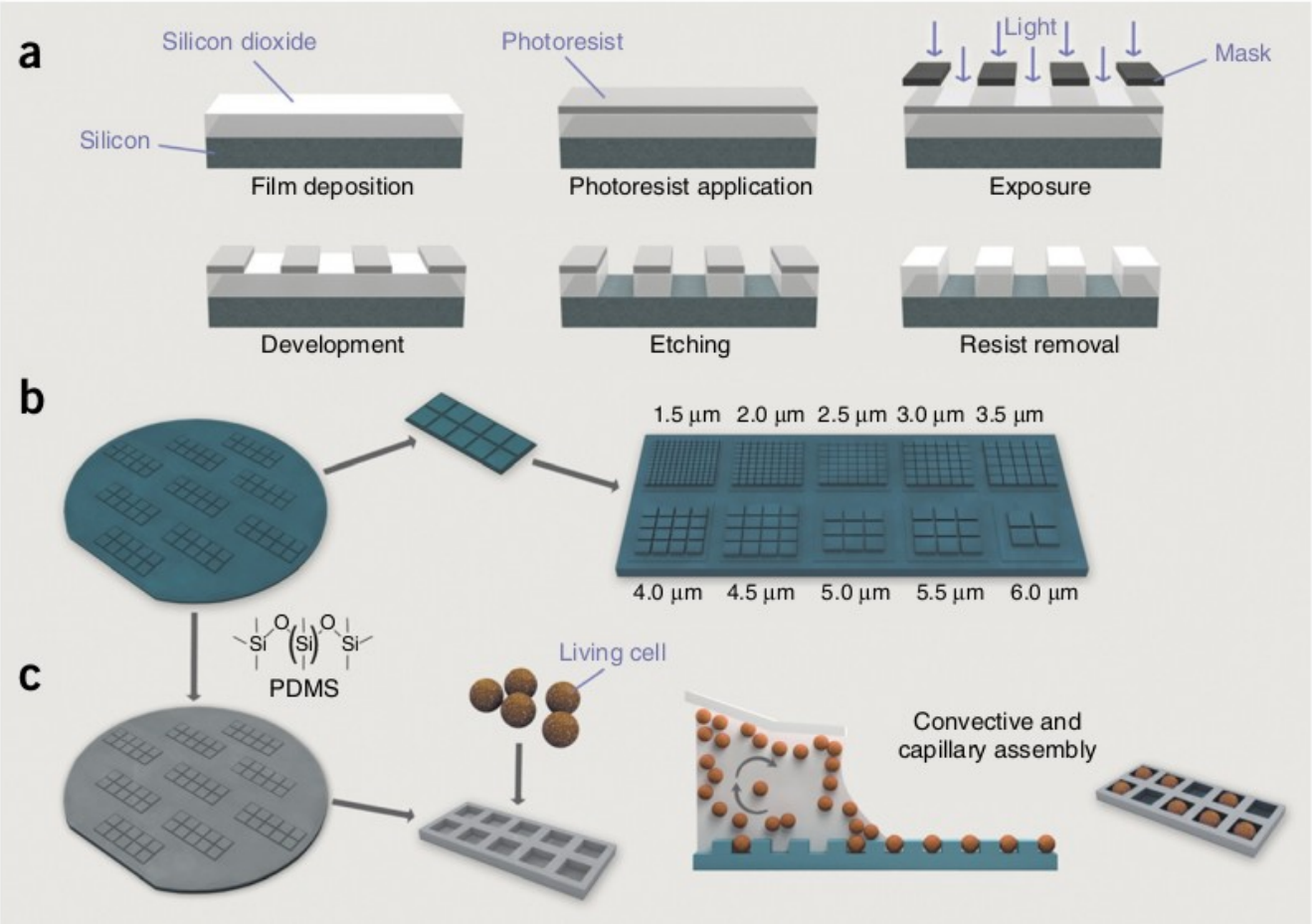

Figure 4.1. Design of the PDMS stamps and cell immobilization. a) Photolithography process to elaborate the silicon microstructured master. b) Microstructured pattern sizes, these patterns are going to be transferred to the PDMS. c) Living cells assembled inside the micropatterns by convective and capillary deposition forming a cell array. Image was taken from[1].

4.1.2 Optimizing filling rate

The technique used for cell immobilization was manual convective and capillary assembly described in Formosa et al.[1] paper. However, the filling rate is low, and to improve it, two steps can be taken. The first was changing to a setup of convective and capillary assembly; the second was to optimize the surface chemistry. We decided to use the second.

4.1.2.1 Optimization of the stamp surface chemistry

Observation of the PDMS stamp behavior after cell culture deposit leads to determine that using the cell culture supernatant before depositing a droplet of the cell culture improves the filling rate. The protocol was modified as follows: First, we deposited the supernatant, of the cell culture, on the PDMS stamp surface and degassed for 30 minutes. Second, the supernatant is eliminated from the stamp surface, and let it rest for 15 minutes. After, a glass slide is used to drag the cells into the microwells.

Figure 4.2 shows the results of the immobilization compared to a clean PDMS stamp. The filling rate is ~85 %, which is high enough to be used with the program that automates the measurements from the cells.

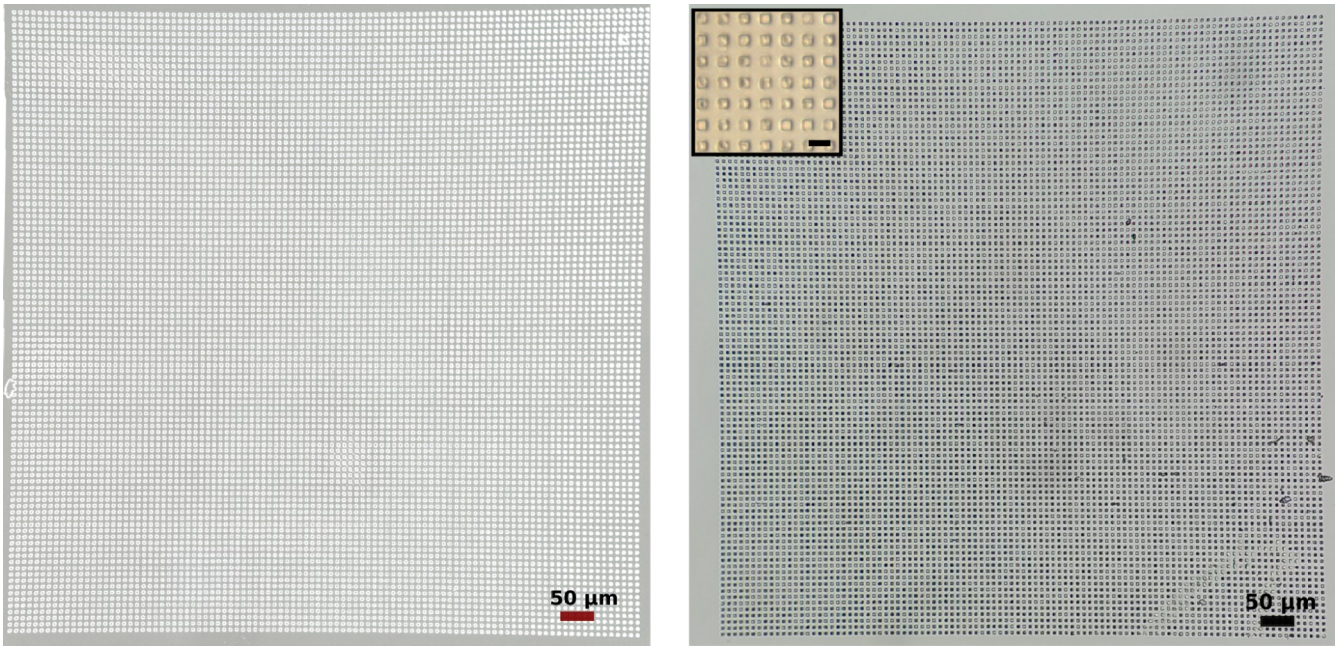

Figure 4.2. Optical images of the PDMS stamps. Left: Clean PDMS stamp. Right: PDMS stamp after cell immobilization, filling rate ~85%. Inlet shows an image captured with the AFM camera, scalebar is 10µm.

4.2. Development of the software that controls the AFM from cell to cell

The algorithm to automate the AFM measurements is shown in chapter 3 (Materials and methods). A total of three scripts were developed (one for microbes, another for mammalian cells, and another for glycan and material arrays). Each script is slightly modified to adapt to the requirements of each array. In this section, I show the results of the script executed on microbes.

4.2.1 The centering algorithm

The script receives the initial parameters (see Materials and methods, figure 4.3A) and then it divides the total scan area into smaller areas. Then the script goes to one of the scanning areas and executes the centering algorithm. The algorithm finds the centers of the initial microwells of that area. Figure 4.3A left shows the position of the cantilever and the tip (actually it is the base of the pyramidal tip, green dot) after the initial parameters have been entered. At this point, the tip is at the initial coordinates entered manually, and it is evident that the tip is not at the exact center of the microwell (red square). Figure 4.3B shows the position of the cantilever and the tip after the centering algorithm is executed, moving the tip to the center of the microwell. Figure 4.3A shows that the algorithm works for microwells of 4.5 µm x 4.5 µm size. However, the smallest microwell on which the centering algorithm works is shown in figure 4.3B (3.0 µm x 3.0 µm). We have a theory that reducing the size of the microwell down to 3.0 µm we are going to need a taller and sharper tip so the algorithm works. On the other hand, we believe that increasing the microwells size represents no problem for the algorithm.

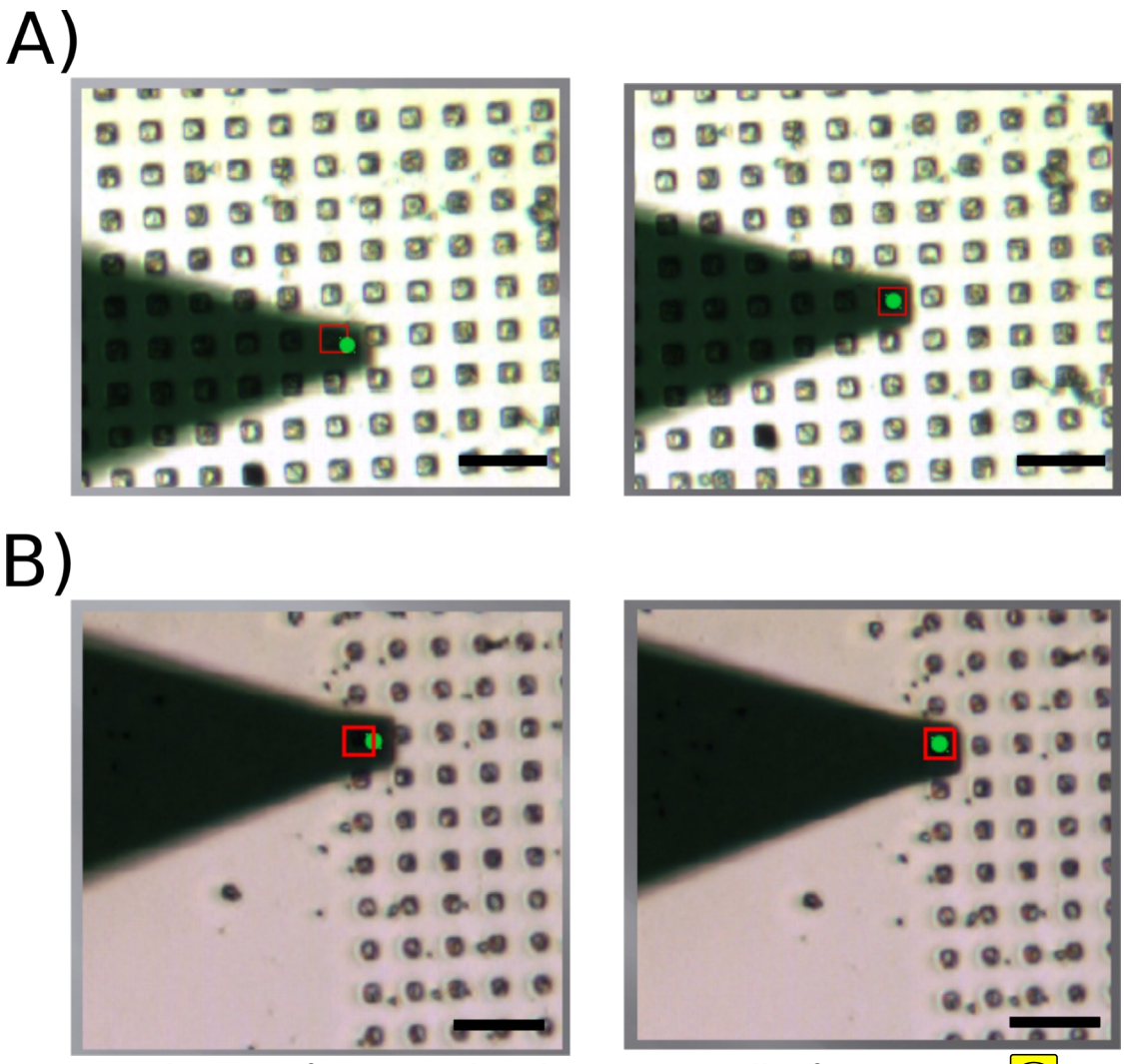

Figure 4.3. Optical images of centering algorithm. A) Microwells of 4.5 µm x 4.5 µm size and B) Microwells of 3.0 µm x 3.0 µm size. Left: It is the position of the cantilever at the beginning of the script execution. Right: The position of the cantilever after centering algorithm execution. Red squares illustrate the approximate position of the microwells hidden by the cantilever, and the green spot shows the approximate position of the pyramidal tip base. Scale bar is 20 µm length.

4.2.2 Definition of a "Safe area"

While running the software in test mode, we found that some of the force curves do not contain information about a cell or the PDMS substrate, these curves come mainly from the edges of the wells. A reduction of the measurement area was made to obtain reliable measurements related to cells. Figure 4.4A shows what we call the safe area, inside this area (green) the tip do not crash against the walls of the well, and figure 4.4B shows a schematic of the cell position inside the well, so the safe area also helps obtaining measurements from around the same area on the cell.

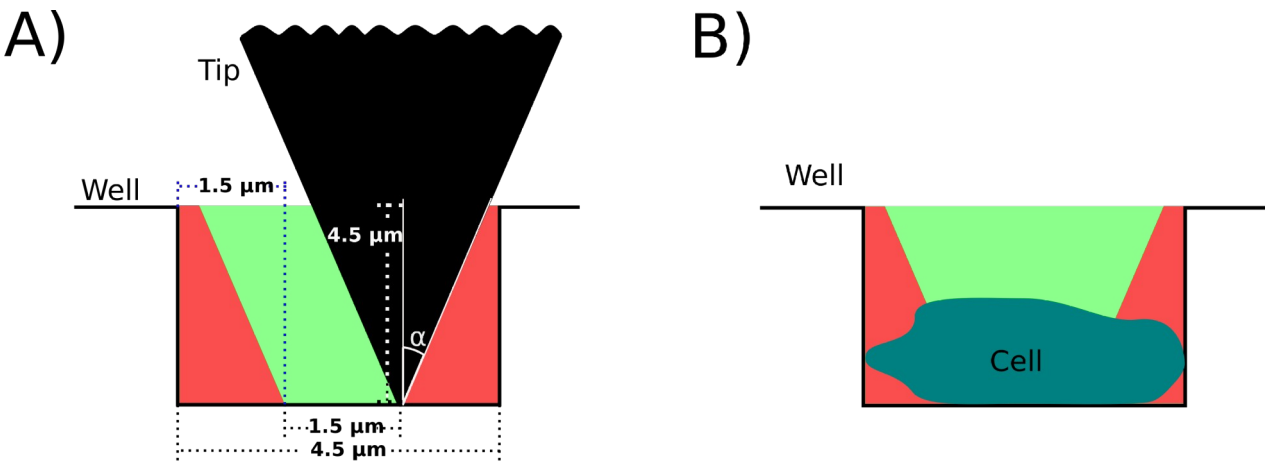

Figure 4.4. Safe area diagram. A) shows the safe area (green), which represents an area where the tip does not touch the walls of the microwells. A represents the semi-angle of the tip (17.5°). The area is calculated based on the tip geometries (black). B) Hypothetical immobilization of a cell showing the part of the cell that is expected to be inside the safe area (green).

4.2.3 Displacement between scanning areas

Figure 4.5 shows the execution of the program developed for this work. Figure 4.5A and 4.5B show how the cantilever moves from one scanning area to another. The centering algorithm takes ~40 s to be executed on each microwell. Figure 4.5C shows the displacement among the microwells in one scanning area. The movement is from the center of one microwell to the center of another microwell. Because the PDMS stamp is placed manually on the stage of the microscope, it is essential to consider that the stamp is tilted in the (x, y) direction. A tilt is present because the stage does not have any alignment marks. And the tilt must be considered when calculating the positions of all the microwells inside the current scanning area. The calculation of the stamp tilt is done after the execution of the centering algorithm, which allows a better tilt calculation. After the tilt is considered, the cantilever can accurately find the microwells positions. The program takes ~12 s to finish the 9 indentations per microwell and ~13 min per area, which is 64 wells per scanning area. Then Figure 4.5D shows the nanoindentation in different regions inside a microwell.

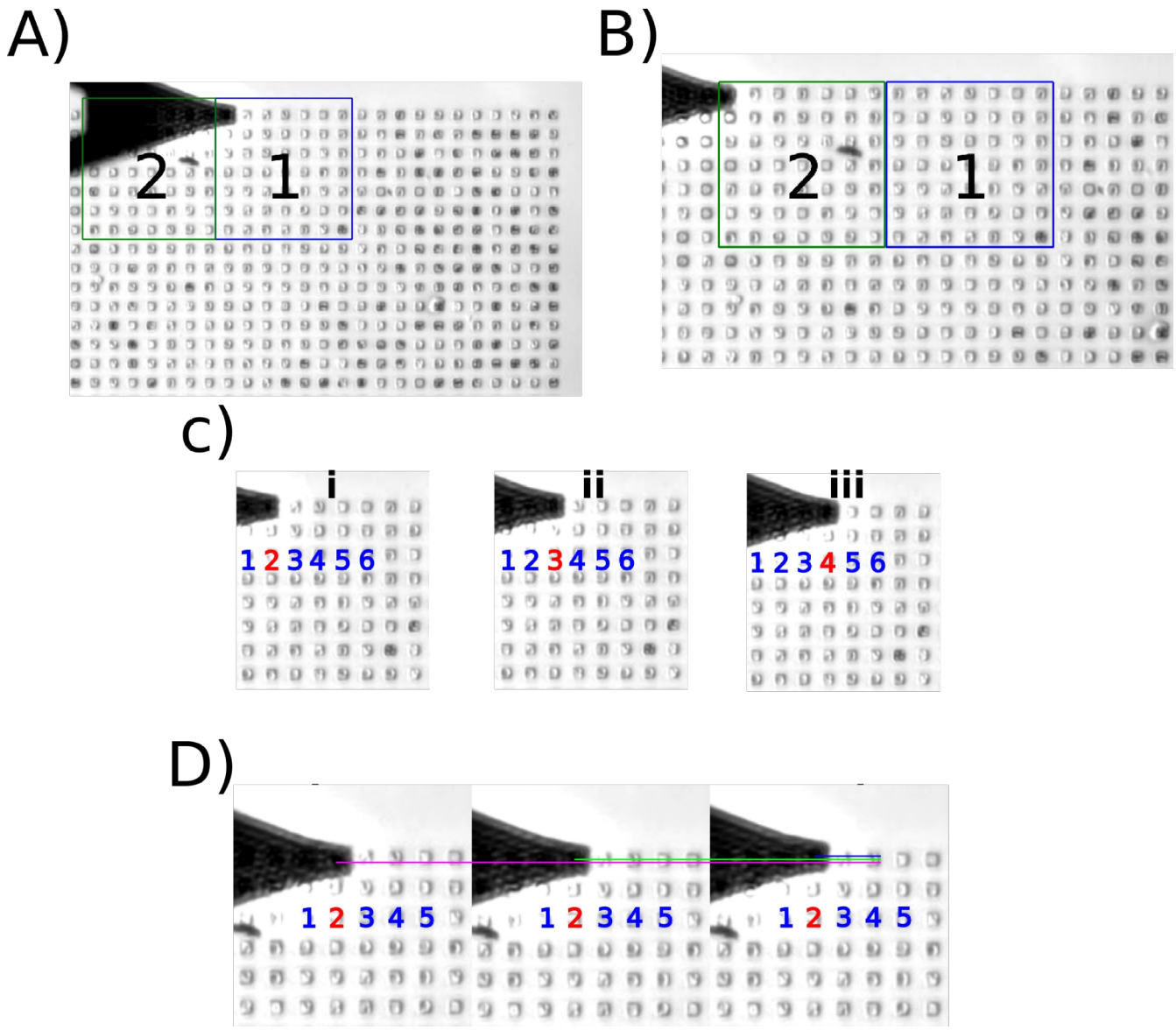

Figure 4.5. Optical images of algorithm execution. A: Location of the center of the first microwell in the current scanning area. B: Position of the tip after moving the motor stage, area 2 is the active scanning area at this moment. C: Shows data acquisition through different microwells (i-iii). D: Shows the data acquisition inside one microwell. The indentation is performed in different regions of the same microwell (magenta/green/blue).

4.3. Nanomechanical comparison of native cells population with caspofungin treated cells population

4.3.1 Background

C. albicans is a versatile fungus capable of adapting to different environments. Recently researchers around the globe have studied its relation with another pathogens and how it attached to surfaces. For example, Hwang et al.[2,3] reported the link between *C. albicans* and *Streptococcus mutants* mediated by the exoenzyme glucosyltransferase B (GtfB). The mannans in the outer layer of *C. albicans* interact with the GtfB to establish a strong bond highly stable[3]. However, the number of samples analyzed is small (10 – 20 cells per experiment, and usually, the experiments were

performed 3 – 4 times), which compromises the statistical significance of the results. Shengli et al[4] published work to understand better how the *Streptococcus Sanguinis* bacteriocin modifies the Young modulus and adhesion of thalli and hypha form of *C. albicans*. They obtained the results from 32 cells (4 survey lines, 8 cells each) in 2h.
Atomic force microscopy has been proved as a powerful technique to study mechanical properties of microbes and the effects of antifungal molecules on them[5]; also the need for a different measurement approach capable of interact with the new computational technologies like big data, artificial intelligence, and machine learning is evident. The examples mentioned establish that recently published works does not deal with high numbers of cells, even the latest model of AFM is not capable of increasing the number of cells analyzed which is essential because many works focus on the response of cells to drugs or chemicals and statistical significance of the results is an important parameter to achieve.

4.3.2 Acquiring AFM measurements

The force curves were obtained from *C. albicans* cells immobilized inside the micro-fabricated wells. Four experiments were conducted to establish the repeatability and reliability of the results. Native and caspofungin treated cells were independently prepared, as mentioned in the materials & method chapter and immobilized the day they were used. The decision to use caspofungin is because its action on the yeast cell wall is still under debate[6,7]. The script was executed, and then 1021 and 957 cells were analyzed for the first and the second experiment (native cells) respectively. 1000 cells and 574 cells for the third and the fourth experiment (caspofungin). For experiments 1 and 3, sixteen indentations per cells were taken, meanwhile, for experiments 2 and 4, nine nanoindentations were conducted.
Experiments 1, 2, 3, and 4 are independent duplicates. The cell cultures were independent and were not performed the same day; Experiments 1 and 2 with native cells and experiments 3 and 4 with caspofungin treated cells. The objective of this setup was to obtain a comparable number of analyzed cells (for native and treated) and to determine the maximum number of cells analyzed in a fixed time (4 h).

4.3.3 Force curves analysis 

The force curves obtained were firstly analyzed using the JPK data processing software, based on the work published by El-Kirat-Chatel[7] we extracted the cell spring constant from all the force curves. However, the filling rate of the PDMS stamp is not 100 % but ~85 %.
The algorithm developed allows the tip to indent on different regions inside the well; however, not all the wells have a cell and become necessary to develop a process to discard these measurements. First, it is possible to discard the force curves from empty wells by obtaining the contact point. Empty wells height was acquired on an independent experiment (along with the mechanical properties of PDMS), using this information it was possible to establish that the force curves from inside of an empty well have a contact point at 4.15 µm.
To obtain the spring constant, the retract curve were used (Figure 4.6A), and the values obtained from PDMS are different than the ones from the cells, so this parameter is considered for filtering. Figure 4.6B shows an example of a force curve obtained from inside the well showing that the contact point is the height at which the tip first touches the PDMS. In the end, three parameters are considered to discard empty wells:

- The contact point is used to determine if the force curves are from the bottom of the well, so all the curves with a contact point value below 4.15 µm are discarded (fig 4.6B).
- Not all the measurements acquire a usable force curves; as a consequence, the curves with a negative slope are discarded.
- The cell spring constant is assumed to be lower than that of the PDMS measured at 150 pN/nm; hence, all force curve giving a spring constant higher than 150 pN/nm were discarded.

Following the previous criteria, Table 1 presents the number of cells analyzed, the number of force curves discarded, and the time taken to analyze each well.

Table 1. Summary of the force curves obtained/analyzed and the times of acquisition per experiment.

	Experiment	Force Curves	Wells analyzed	Cells analyzed	Time per well(s)	Discarded force curves (%)
Native cells	1	15927	1021	1021	9	4.31
	2	8620	959	957	12	12.87
Treated cells	3	15457	1018	1000	9	8.19
	4	5180	579	574	12	20.88

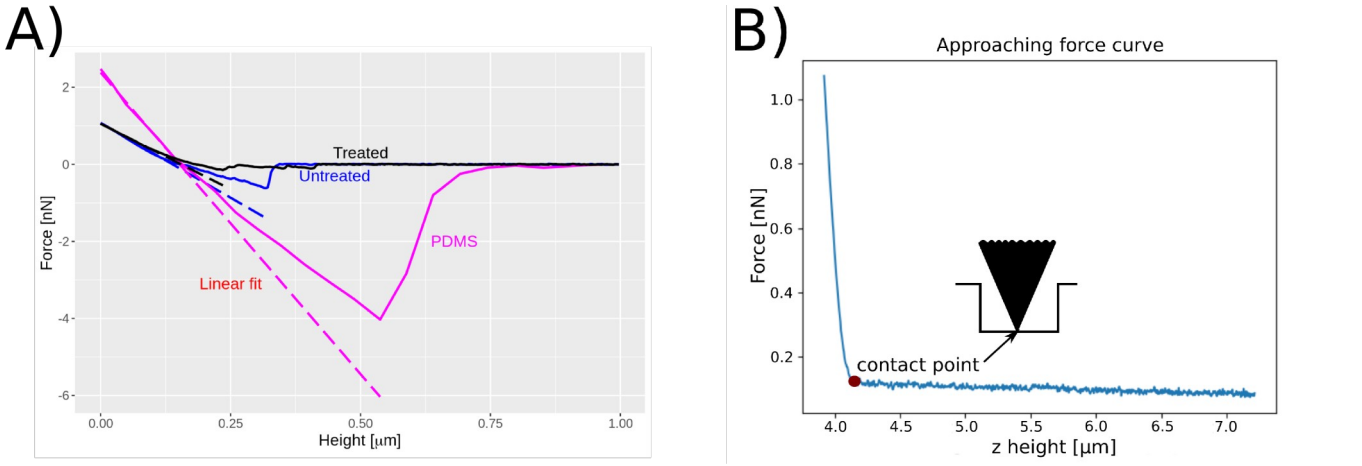

Figure 4.6. Acquisition method. A: Force-Height curves (retract segment) of the different cells analyzed, The linear fit shows the segment of the curve used to extract the spring constant value. B: Approaching force curve showing the contact point and its relation with the depth of the well.

The percentage of discarded force curves increases for the treated cells because the tip gets dirty really fast so the tip sometimes did not detach from the surface (resulting in useless curves)

4.3.4 Nanomechanical properties at the population scale

Figure 4.7 presents the stiffness (spring constant) and adhesion histograms for *C. albicans* cells in native conditions (A and B) and treated with caspofungin (C and D). 4.7A and B, left, show the stiffness histograms, the number of cells analyzed in the first two experiments were 1021 and 959, respectively; both are obtained by analyzing the native cells independently. Analyzing the two

histograms with the k-means method, they can be deconvoluted into 2 populations that are slightly different in the 2 experiments. The first population has a mean spring constant of 21 ±6 pN/nm (experiment 1) and 30 ±13 pN/nm (experiment 2) while the other population has a spring constant of 48 ±9 pN/nm (experiment 1) and 80 ±18 pN/nm (experiment 2). For experiments 3 and 4 (Figure 4.7C and D, left) 1018 and 579 cells were analyzed. According to the literature[7], treated cells present a softening of the cell wall because of the caspofungin treatment.

This shift can be seen in Figure 4.7, comparing experiments 1 and 3. The peak present at 21 pN/nm (35A-left) shift to 13 pN/nm (35C-left) and the peak at 48 pN/nm shifts to 42 pN/nm. For experiments 2 and 4 (4.7B and 4.7D, -left, respectively) the peak present at 30 pN/nm shifts to 15 pN/nm and the peak at 80 pN/nm shifts to 52 pN/nm. Figure 4.7E and 4.7F show the one-way ANOVA test, 4.7E-left was obtained comparing 4.7A and 4.7C spring constant data reducing both sets to 1018 cells. Meanwhile, 4.7F-left was obtained by comparing 4.7B and 4.7D spring constant data reducing both sets to 579. The one-way test is used to compare the native cells results against treated cells obtaining a $p<0.001$ (represented by ***).

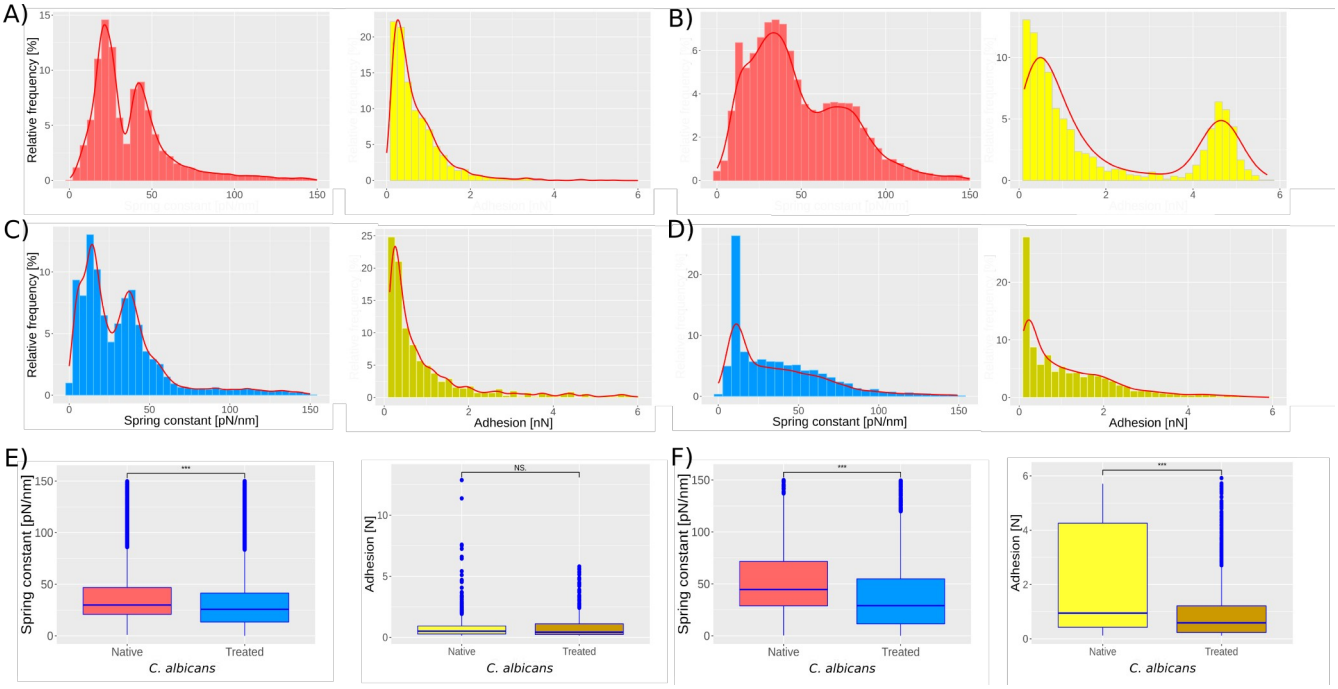

*Figure 4.7. Stiffness histograms for C. albicans, native and treated with caspofungin. A and B (left) show the spring constant histograms for experiments 1 and 2 of native C. albicans cells (1021 and 959 cells analyzed respectively). While C and D (left) show the spring constant histograms for the experiments 3 and 4 of treated C. albicans cells (1018 and 579 cells analyzed respectively). A and B (right) show the results obtained from the adhesion analysis on experiments 1 and 2. C and D show the adhesion results for experiments 3 and 4. E and F show the one-way ANOVA test performed using the spring constant and adhesion data from 1-3 and 2-4 respectively. *** = p value < 0.001, NS = no significant difference. Bin width was determined by Freedman-Diaconis rule.*

Figure 4.7A-right shows that the adhesion force between the bare tip and native cells was 0.64 ±0.6 nN in the first experiment, while in the second experiment still on native cells, 2 subpopulations were found: the first has a mean adhesion force of 0.7±1.4 nN while the second is 4.5±1.5 nN. The treatment with caspofungin has no significant effect on the adhesion if experiment 1 and 3 are

considered (one way ANOVA test, figure 4.7E-right shows no significant difference) but it seems that caspofungin induces a decrease in the adhesion to the tip and a reduction of the population adhesion heterogeneity.

4.3.5 Machine Learning analysis

The previous section showed that our results are in line with the works reported in the literature. However, the range of values between the native and treated cells are not clearly separated, so we looked for a solution that helped us differentiate the cells. The mechanical sensing is being done with an AFM, it is considered as an equivalent of the palpation method at the nanoscale. The sense of touch used for palpation is complex and we think that most of the analysis and comprehension obtained from touching involves several features that we can recognize (such as rigidity, porosity, elasticity, among others). Translating the sense of touch to the AFM is not going to be an easy task and we think using only one mechanical property to differentiate among cells is not enough.
Machine learning is a computational technique able to detect patterns from the data and then use those patterns to predict new data or classify new data[8,9]. Machine learning can be divided into two types:

i. Supervised learning which uses a training set previously classified or grouped (the groups are called descriptors), the objective is to use the training set to find patterns and then apply those parameters to classify a new set of data[8].
ii. Unsupervised learning also uses a training set, but the set has not been classified in any way, so the algorithm finds interesting ways to group the data, the algorithm is not told what kind of patterns it must search[8].

The machine learning (ML) analysis was done in collaboration with Dr. Marie Véronique Le Lann and one of her students Digaly Tcholna. They used the tool P3S for the ML analysis, which is a software developed by the Laboratoire de analyse et d'architecture des systèmes (LAAS). It uses three algorithms (fuzzy binomial, fuzzy centered, and normal Gaussian). The combination of machine learning with fuzzy logic is used to minimize the effect of the noise in the data, so it is possible to improve classification results[10]. The machine learning algorithms used were of the supervised type. Figure 4.8 shows the attributes used for learning, the stiffness, adhesion, and work of adhesion (a, b, and c respectively).

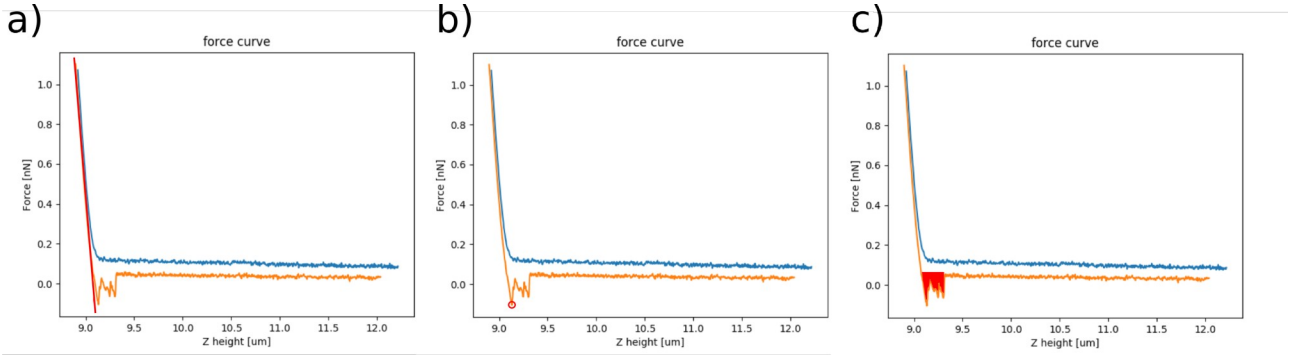

Figure 4.8. Force Vs distance curves of C. albicans cells. a) Linear fit done to the retract curve (orange) taking only the first 150 pN/nm. b) Maximum adhesion force (red circle), determined from

the retract curve (orange). c) Work of adhesion (red area), also determined from the retract curve (orange).

80 % of the data (native and treated respectively) was used for the training set, and the other 20% of the data was used for the tests. Table 2 show the confusion matrices, one for each algorithm applied. A total of 1532 predictions were done, the numbers in red show the false positive predictions (Native column) and false negative predictions (Treated column).

Table 2. Confusion matrices. The matrices were obtained using P3S LAAS software.

Fuzzy Binomial Poba

	Treated	Native	Total
Treated	540	187	727
Native	35	770	805
Total	575	957	1532

Fuzzy Centreated Poba

	Treated	Native	Total
Treated	523	172	695
Native	52	785	837
Total	575	957	1532

Normal Gaussian Proba

	Treated	Native	Total
Treated	539	177	716
Native	36	780	816
Total	575	957	1532

Fuzzy Binomial MinMax

	Treated	Native	Total
Treated	546	188	734
Native	29	769	798
Total	575	957	1532

Fuzzy Centread MinMax

	Treated	Native	Total
Treated	546	184	730
Native	29	773	802
Total	575	957	1532

Normal Gaussian MinMax

	Treated	Native	Total
Treated	549	184	733
Native	26	773	799
Total	575	957	1532

The results from the P3S software were compared to conventional machine learning algorithms, such as, nearest neighbors (K-NN) and support vector machines (SVM). The results are shown in table 3 and demonstrate the ability of supervised machine learning to adequately separate native and treated cells in 85% of the cases. Gaussian MinMax have the best performance (86.10%) when differentiating native from treated cells, followed by the SVM algorithm (85.62%).

Table 3.Machine learning results. The results were obtained using 80% of the data sets for training and the remaining 20% for testing.

	Machine learning algorithms							
	Fuzzy binomial Poba	Fuzzy binomial MinMax	Fuzzy centered Poba	Fuzzy centered MinMax	Normal Gaussian Poba	Normal Gaussian MinMax	K-NN	SVM
Classification rate	85.51%	85.84%	85.38%	86.10%	86.10%	86.29%	82.67%	85.62%

4.4. Mammalian cells immobilization

4.4.1 Background

HeLa cells are essential in cancer research, and many labs use them to understand the behavior of the disease and the effective mechanism to eliminate or improve detection. AFM is a methodology that has been used for the study of cancer cells, authors report the genetic modification of the cancer cell to suppress Glucose-6-phosphate dehydrogenase (G6PD) function to lower the Young modulus, proliferation, and migration of the HeLa cells[11] or implant suicide genetic nanoparticles (like G4AcFaHSTK + ganciclovir) to induce cytoplasmic shrinkage, cell membrane liquefaction, and cytoskeleton structure loss[12]. Also, the AFM is a useful tool in the study of HeLa cells interaction

with single-wall carbon nanotubes (SWCNTs) and how they affect the mechanical properties of the cells[13]. However, these examples have a common feature they all report the use of ~30 cells (at the best) to perform their studies, a meager number if the results are to be considered for medical treatments or diagnosis.

4.4.2 Mammalian cell arrays fabrication

4.4.2.1 CYTOO cell arrays

Figure 4.9a and 4.9b show the organization and the micropatterns printed in the cell arrays, respectively. The starter kit includes 6 chips, like the ones shown in figure 4.9a. Each chip can be easily identified with the chip identification letter, and the chips are divided into blocks. Each block can be identified with the column number and row letter. A total of 144 blocks (12×12) compose each CYTOO chip, and inside each block, a matrix of 12×12 micropatterns is present, all the micropatterns are covered with fibronectin protein. Figure 4.9b shows the different micropatterns used in the CYTOO chips and how the cell modifies its membrane to adapt to the geometry. Figure 4.9c shows the immobilization of HeLa cells in the chips; the red circles mark the single cells.

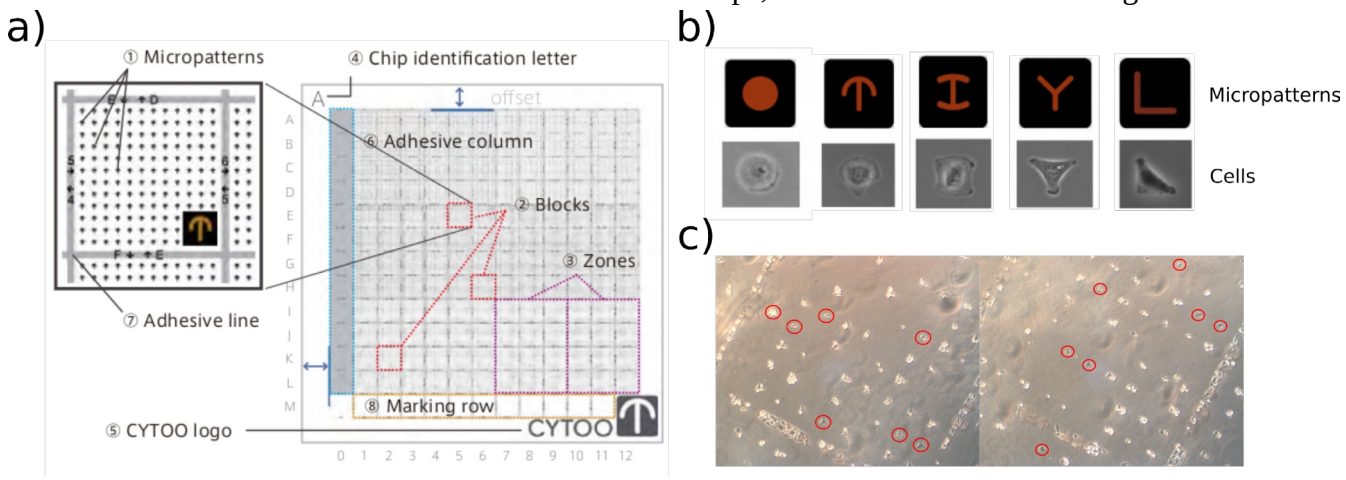

*Figure 4.9. CYTOO chips immobilization. (a) Schematic of a CYTOO chip. **1** indicate the micropatterns printed in the chips a total of 144 micropatterns are inside each block. **2** indicate the blocks, a total of 144 blocks compose a chip. **3** the zones are subsections where the type of the micropattern changes. **4** The letter helps identifying the chip that is being used. **5** The CYTOO logo helps knowing the orientation of the chip if the logo is in the position shown means the micropatterns are on the surface. **6** The adhesive column is covered with an adhesive protein; it is a marked area. **7** Similar to number 6, it is an adhesive protein and helps dividing the blocks. **8** The space destined for the logo or numbers. (b) The micropatterns printed in the CYTOO chips and the adaptation cells suffer after immobilization (HeLa cells). For the starter kit, these patterns are present in small and medium-size. (c) Immobilization results for HeLa cells, the red circles remarks the single cells. (a) and (b) taken from[14].*

4.4.2.2 BIOSOFT cell arrays

Figure 4.10 shows the patterns designed for the HeLa cells immobilization, a variety of patterns were designed with different sizes from 20 µm – 40 µm and distances between them from 40 µm to 80 µm. We tried different sizes and distances to establish which combination gives the better results for us to obtain a large quantity of cells immobilized. Figure 4.10A shows squares of different sizes separated by specific distances, these geometries resembles the ones used for the *C. albicans*

immobilization. Figure 4.10B shows patterns having geometries other than circles, squares, and rectangles (Y, L, T, H), this geometries have been reported that change the organization of the cell membrane[15,16]. Figure 4.10C shows part of the mask area to see the distribution on the mask of the different patterns.

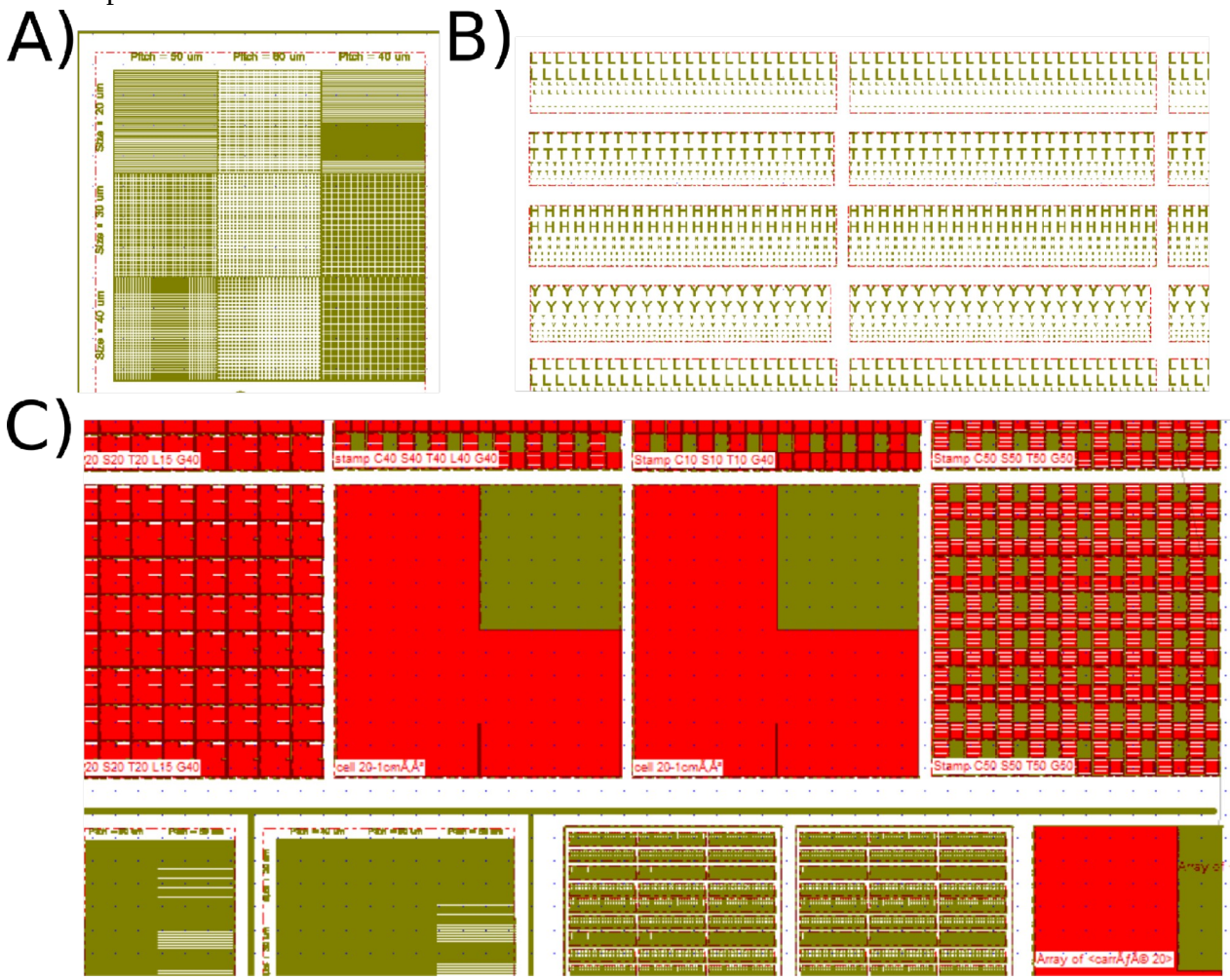

Figure 4.10. Design of the patterns for HeLa inmobilization. A: Show square patterns with different sizes (20, 30, 40 µm) separated by 40, 50, and 80 µm. B: Show different geometries bigger patterns are 100 µm height x 80 µm long and 10 µm width, medium are 30 µm x 24 µm and 4 µm width, and small patterns are 10 µm x 8 µm with 1.2 µm width. C: shows a region of the wafer to give an idea of the distribution of the patterns alongside the wafer.

The transfer of the patterns was made with the InnoStamp technology[17]. Figure 4.11 shows the procedure to fabricate the microstructured stamps (a – g). First, the magnetic PDMS stamps with the desired patterns are inked with different extracellular matrix proteins (ECM) at 100 µg ml-1 for 1 min. After drying, the magnetic stamp is automatically carried out to the printing area, aligned and brought into contact with a chemically treated glass slide for 1 min with a controlled force. Once the ECM components have been transferred to the substrate, the stamp is treated with polylysine-grafted polyethyleneglycol (PLL-g-PEG) to prevent the adhesion of cells outside the ECM patterns. From this point, the slides can be incubated with the desired cell (such as HeLa, PC3).

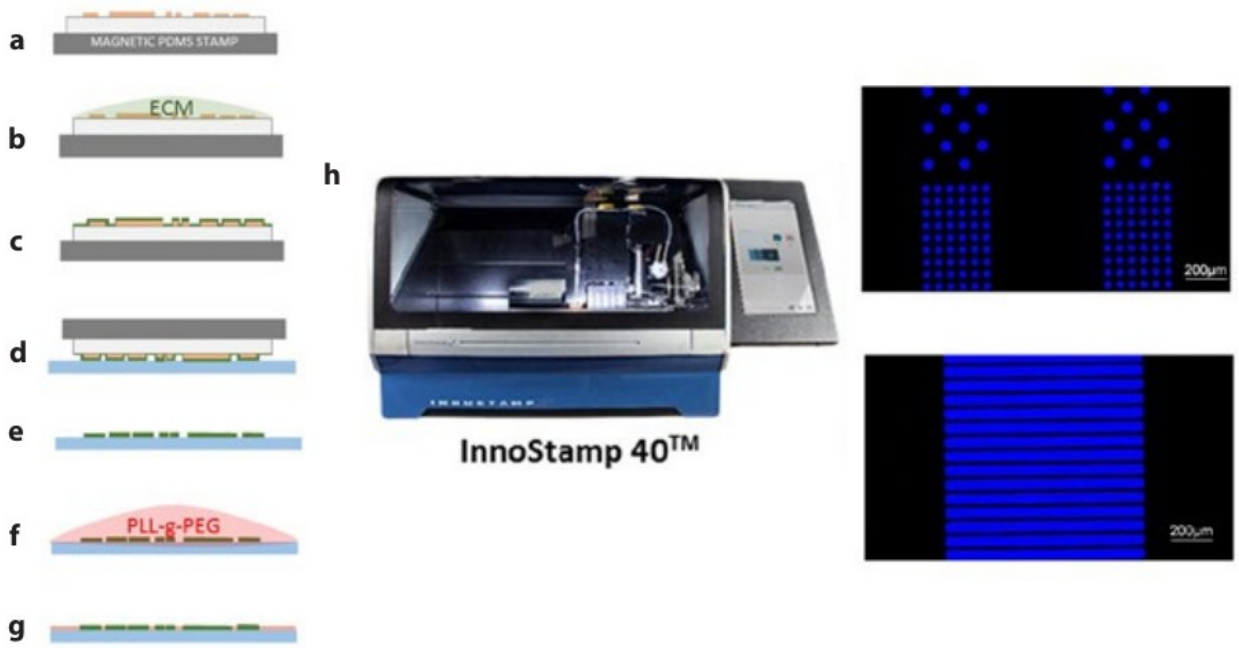

Figure 4.11. Automatic microstructured cell array process used in InnoStamp 40. (a) Magnetic PDMS stamp that contains the features (transfer stamp). (b) The magnetic stamp is inked with ECM components. (c) The stamp is air-dried. (d) The magnetic stamp is put in contact with the substrate. (e) ECM components are transferred to the substrate according to the stamp pattern. (f) The substrate is treated with non-adhesive molecules such as PLL-g-PEG. (g) The antifouling molecule covers the regions around the ECM pattern. (h) The innoStamp 40 automated microcontact printer together with some examples of ECM patterned slides. The spot diameter and line width range from 50 µm – 150 µm. Image was modified from[17].

4.4.3 Automatic measurements on mammalian cells

Figure 4.12A shows the optical images of the immobilization results done in collaboration with the BIOSOFT company. Single-Cell immobilization was not achieved. However, the results are better than the CYTOO chips, and we decided to use them for the proof of principle. Figure 4.12B and 4.12C shows the execution of the script with the new stamps and show the movement across the different cells on the stamp and the different indentations at the center regions of immobilization.

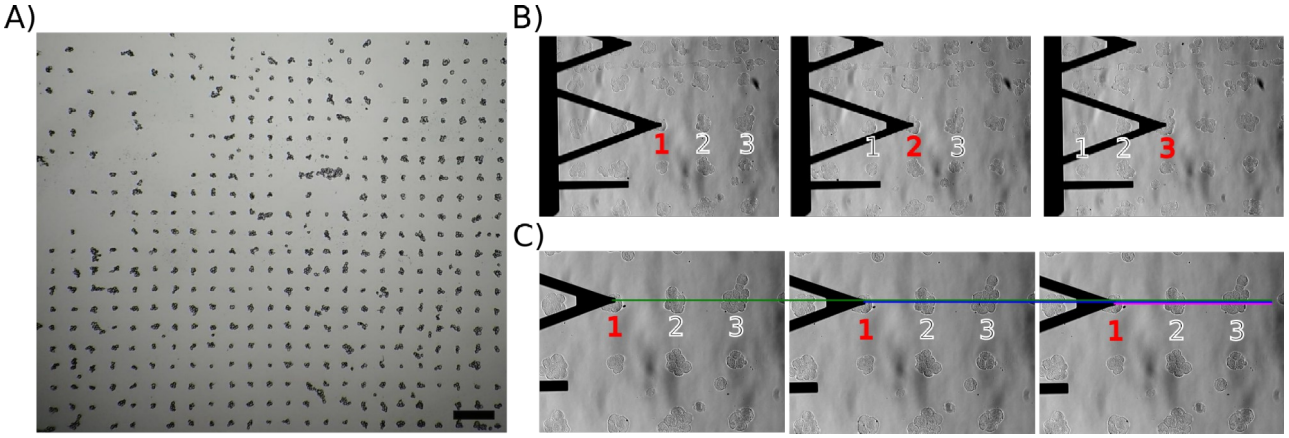

Figure 4.12. Optical images of BIOSOFT cell arrays. A) Immobilization results, on each spot, is possible to see small groups of cells (cell clusters), the bar is 250 µm. B) Shows the movement of the tip from cell to cell. C) shows the first three indentation positions (green/blue/magenta) on the first cell.

Two experiments were performed, one with native HeLa cells and another with fixed HeLa cells. The objective of the two experiments was to obtain a high number of cells measured in a short time. Nine indentations were performed on each cell (~6 seconds per cell), obtaining measurements from 80 native cells and 70 fixed cells in ~28 minutes. Figure 4.13 show the histograms of the Young modulus (elasticity) extracted using the JPK Data Processing software. Figure 4.13A show the elasticity results for native HeLa cells and 4.13B show the elasticity results for fixed cells, the results show, as expected, that the fixed cells present an increment in Young modulus (125 – 1000 kPa) with a mean value of 435 ±203 kPa. Compared to native cells (2.5 – 30 kPa) with a mean value of 6.2 ± 5 kPa.

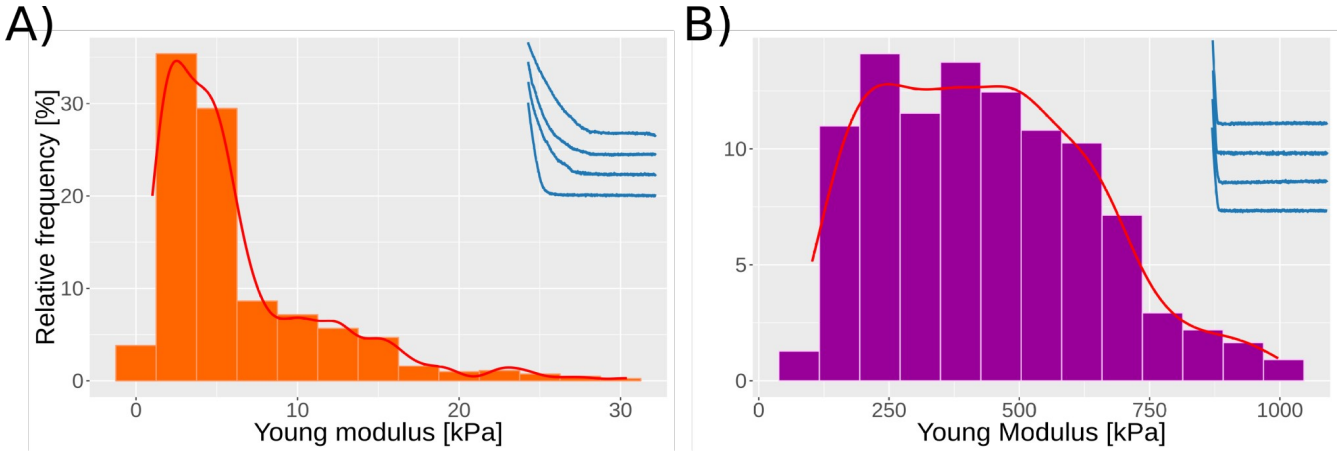

Figure 4.13. Young modulus histograms of native and fixed HeLa cells. A) Young modulus histogram for native HeLa cells (80 cells analyzed), inlet shows examples of the force curves treated. B) Young modulus histogram for fixed HeLa cells (70 cells analyzed), inlet shows examples of the force curves treated.

4.5. Discussion

4.5.1 *C. albicans*

The protocol used to immobilize the cells is the one described by Formosa et al.[6], nevertheless, in this work, one extra step was made, the addition of the supernatant taken from the cell culture and deposited onto the PDMS stamp before depositing the cells. The modifications allow going quickly (~1h) from ~50 % to ~85 % of microwells filled with cells (see chapter 3 materials & methods). This behavior probably comes from the mannose polymers founded on the outer layer of *C. albicans*[18] and its interaction between them and the surface of the PDMS, changing surface roughness and increasing the hydrophilicity of PDMS[17]. The number of nanoindentations was sixteen for experiments 1 and 3 and nine for experiments 2 and 4. The objective of varying the number of nanoindentations was to observe if a significant change is present in the histograms. The two subpopulations start to merge when we decrease the number of measurements; however, with nine indentations, it is still possible to see the two subpopulations.

The spring constant from every force curve obtained with the automated procedure was extracted. Based on the results published by El-Kirat-Chatel[7] a shift on the results for the treated cells compared to the native cells was expected, as shown in Figure 4.7 (A and B, C and D). On the contrary, the presence of the two peaks observed in the histograms in all four experiments was unexpected. Indeed, experiments performed on single cell[6,7] demonstrated the homogeneous

distribution of the nanomechanical properties. The difference in the stiffness (spring constant absolute value) for the two independent experiments on native cells may come from uncontrollable differences in the cell cultures. The maximum applied force, the tip velocity, the cantilever spring constant, the buffer, and the temperature were the same. It is important to note that *C. albicans* is an extremely versatile microbe[8] able to sense and adapt to its environment. As a consequence, the growth phases of *C. albicans* are challenging to control, and an unmeasurable difference in the initial culture conditions may result through the butterfly effect to the difference that we observe in between experiment 1 and 3. In this work, the successful reproduction of the distribution of the cells in two well-defined populations is presented. Heterogeneity on the young modulus of Saccharomyces cerevisiae cells was reported by Dague E. et al.[19] Nevertheless, the cells analyzed were just a few (5 cells), and it was, therefore, impossible to foresee a general conclusion at a population scale. For single-cell, the presence of subpopulations is something unexpected and new. However, on the field of biofilms, some researchers have reported its presence, like Harrison et al.[20] reported subpopulations as responsible on biofilms for its resistance to chelatin agents. Khot et al.[21] encounter subpopulations responsible for biofilms resistance to amphotericin B. In this last publication, the authors demonstrated that the sub-population was associated with ergosterol and beta 1-6 glucan pathway genes. They both are an essential component of the fungal cell wall, and the previous investigation from our team[22] shows that their expression level is correlated with the nanomechanical properties of the cells. More recently, Rosenberg et al.[23] showed that antifungal tolerance was a sub-population effect. In this work, there is no particular reason responsible for the 2 sub-populations, and more work needs to be done to present a confident argument about its origin. Globally, it is possible to hypothesize that sub-populations, in *C. albicans*, are an adaptation mechanism probably responsible for the remarkable expansion of this microbe.

To prove that sub-populations are not related to specific indentation positions or to a specific time during the experiments the plots in Figure 4.14A and 4.14B show the values of Spring constant as time evolves, it can be seeing that the contributions from the peaks are present at every hour which help discard the idea of the peaks are present because of the time it took to perform the experiment. Figure 4.14C and 4.14D show four points of indentation (central points of the cell) for experiments 1 and 3 and nine points of indentation for experiments 2 and 4 related to the stiffness values; if the presence of peaks were to be related to the position of indentation, the plot would show specific contributions according to a position.

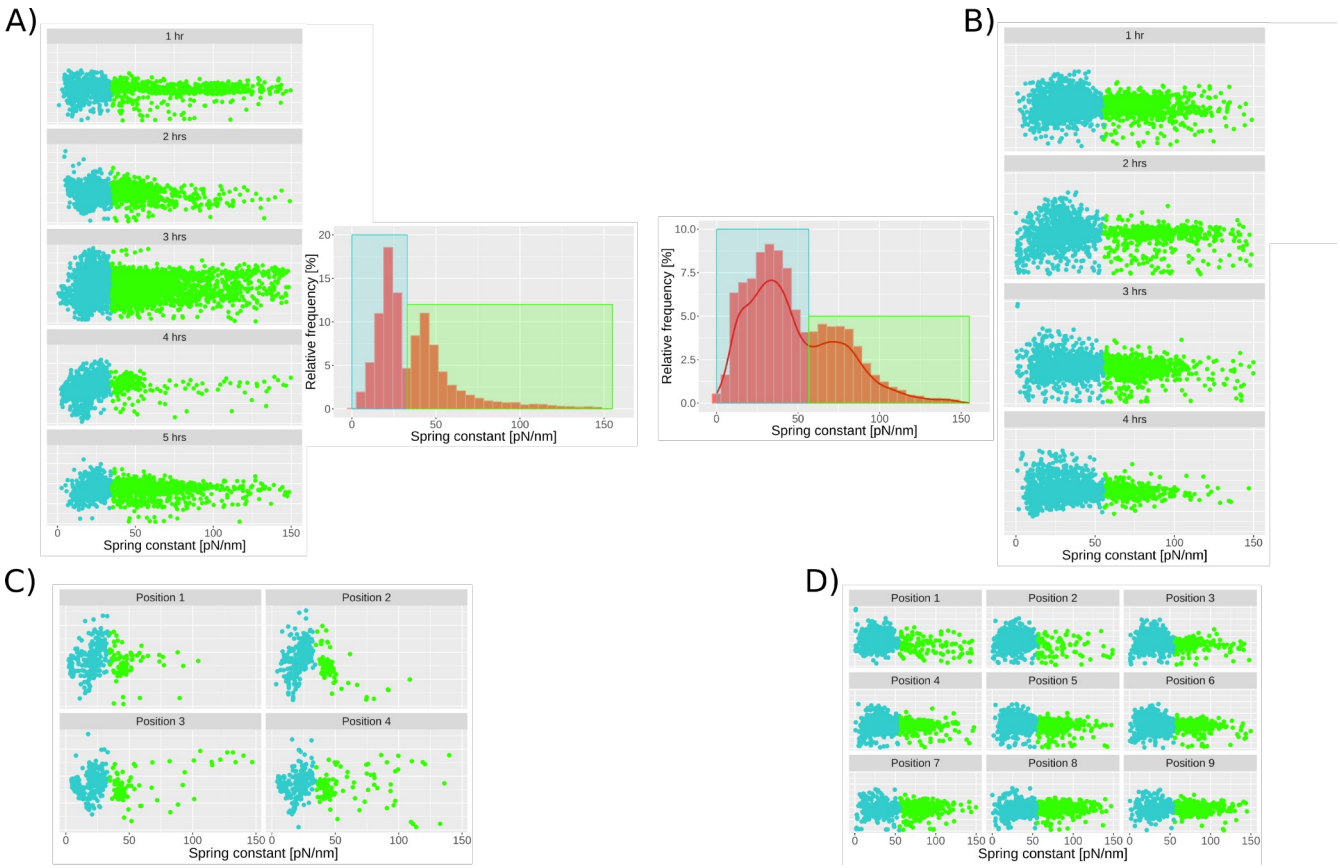

Figure 4.14. Time-position dependency of values. Histograms in the blue squares are the original data which is divided into the different subgroups corresponding to the subpopulations founded (left histogram cyan/green; right histogram cyan/green). A and B: Show the presence of the three populations at every hour in the experiment. C and D: show the positions of indentation, on each are possible to see the presence of the subpopulations (cyan/green) regarding the position of indentation inside the well. Subgroup organization was done using the k-means algorithm.

To confirm the presence of the two sub-populations figure 4.15 illustrates the average value of each cell showing those values on histograms. It confirms the presence of the two subpopulations centered on the same values as the ones for the global distributions.

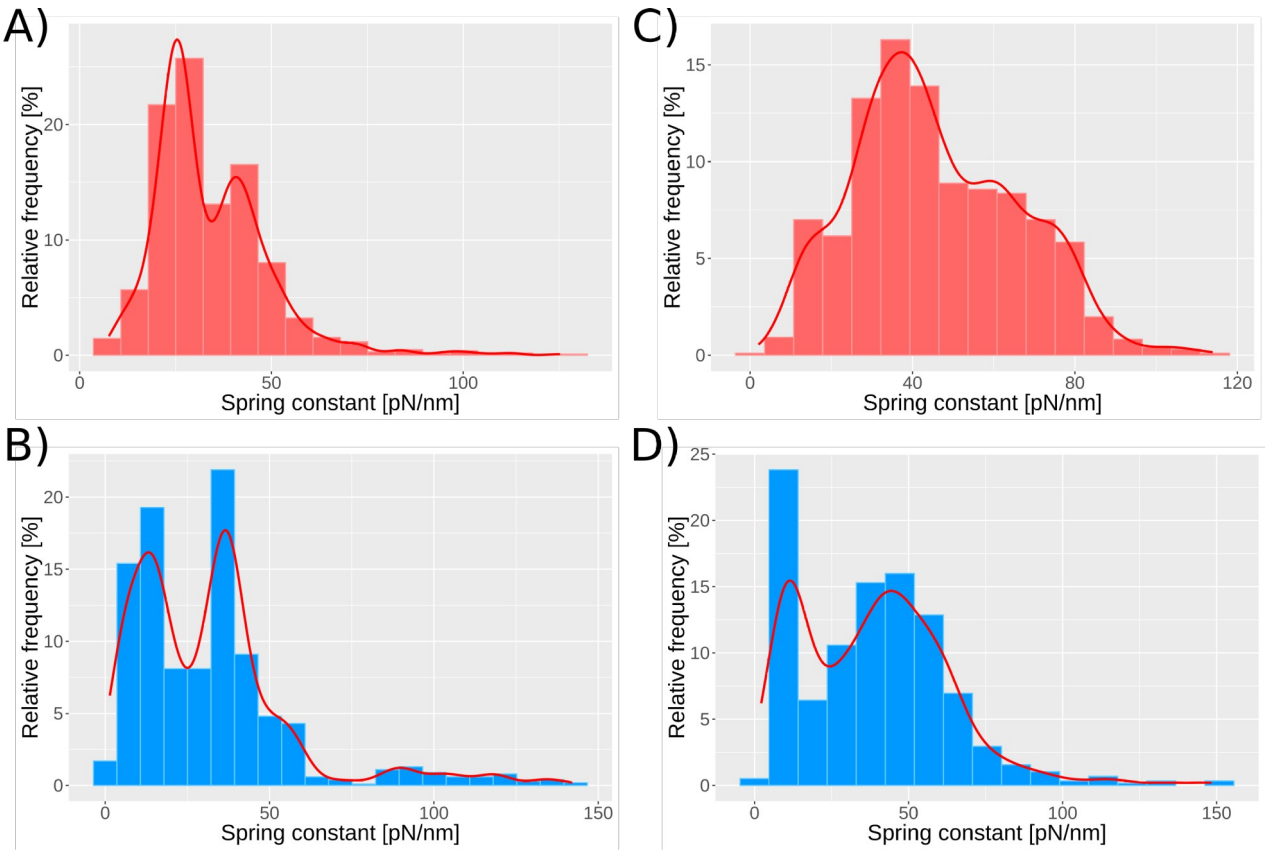

Figure 4.15. Histograms of the median spring constant values. A, B: Show the median results per cell for native and caspofungin treated cells, experiments 1 and 3. C and D: Show the median results per cell for native and caspofungin treated cells, experiments 2 and 4.

The strategy we present to take just a few force curves (9 to 16) over a large number of cells is novel and different compared to the traditional approach followed to conduct nanomechanical measurements, by AFM on living cells. Nevertheless, it is necessary to compare our results with the literature to validate our approach. We compared our results to two recent works; figure 4.16A shows the results from those works. El Kirat-Chatel[7] performed 256 indentations on single-cell and found stiffness value of 51±9 pN/nm for native cells and 27±10 pN/nm for cells treated with caspofungin. Our results proved to be on the same order of magnitude (spring constant ranging from 21±6 to 81±19 pN/nm for naive cells), and the same decrement can be observed on the caspofungin treatment (spring constant ranging from 13 to 52 pN/nm). Figure 4.16B shows the results published by Formosa et al.[6] showed that *C. albicans* treated with caspofungin becomes harder compared to native cells. The number of indentations made by them was 1024. This inconsistency can be explained if the authors select a native cell from the softest subpopulation and a treated cell from the hardest sub-population. The lack of technology to assess cell population at that time make it impossible to see that both results were accurate but incomplete. The new automated methodology presented here can shed some light into this type of inconsistencies.

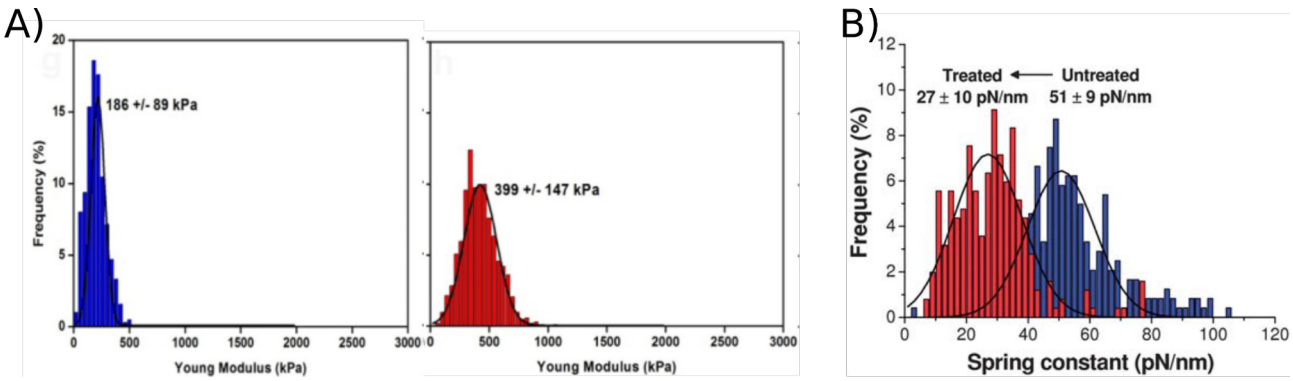

Figure 4.16. Comparison of published mechanical properties. A) Results published by El Kirat-Chatel et al.[7] proving that after caspofungin treatment the cell wall softens. B) Results published by Formosa et al.[6] prove that after caspofungin treatment the cell wall hardens.

Results of the adhesion measurements highlighted the limit with which this methodology can be confronted. It has been proved that *C. albicans* can express a large number of adhesives on its surface[8,24], but, the automated method presented here is not designed to analyze in great detail single cells. However, it means that the traditional approach is not antagonist with our new method and that they provide additional information relating to adhesion. Moreover, the differences in spring constant between the nanodomains and the "native" cell wall are not in the order of magnitude of the 2 subpopulations. Stiffer nanodomains are 13.4±0.2 nN/µm when the rest of the cell wall is 12.4±0.3 nN/µm[25]. In this work, we report a sub-population at 21±6 nN/µm and the second at 48±9 nN/µm. It means that the difference due to the nanodomains are included in the error bar of our measurement. Thus, our results would no longer be incomplete because they would not consider the heterogeneity of the cell population but incomplete because we would lack control over the biological sample produced. *Candida albicans* is known for its versatility[8] and in this context this demonstration serves better than any other cell model would have done.

The results obtained from machine learning analysis have helped us to conclude that differentiation using only one mechanical property is not reliable. In this work we report the use of three descriptors (adhesion, stiffness, and work of adhesion) to discern between native and treated cells with ~86% confidence. The massive amount of data obtained with our methodology allowed the implementation of computational techniques such as machine learning and with them we believe the AFM is one step closer to become a diagnostic tool.

4.5.2 HeLa cells

The results shown in this chapter were as expected; fixed cells presented an increment in their Young modulus (cells are becoming stiffer). The Young modulus values obtained from native cells are according to the literature[26]. However, because single cell immobilization was not accomplished on all the specified immobilization sites of the stamps, it is not possible to establish if the values come from the nucleus of the cell or from other softer regions[27]. The time taken for cell measurement was ~6 s per cell that means a total of 8 min to obtain the force curves from 80 cells, however, the time was ~30 min this means that the motor stage manipulation expends most of the time. A modification is needed to reduce the time spend on motor stage engage and disengage.

4.6. References

(1) Formosa, C.; Pillet, F.; Schiavone, M.; Duval, R. E.; Ressier, L.; Dague, E. Generation of Living Cell Arrays for Atomic Force Microscopy Studies. *Nat. Protoc.* **2015**, *10* (1), 199–204. https://doi.org/10.1038/nprot.2015.004.

(2) Hwang, G.; Marsh, G.; Gao, L.; Waugh, R.; Koo, H. Binding Force Dynamics of Streptococcus Mutans–Glucosyltransferase B to Candida Albicans. *J. Dent. Res.* **2015**, *94* (9), 1310–1317. https://doi.org/10.1177/0022034515592859.

(3) Hwang, G.; Liu, Y.; Kim, D.; Li, Y.; Krysan, D. J.; Koo, H. Candida Albicans Mannans Mediate Streptococcus Mutans Exoenzyme GtfB Binding to Modulate Cross-Kingdom Biofilm Development in Vivo. *PLOS Pathog.* **2017**, *13* (6), e1006407. https://doi.org/10.1371/journal.ppat.1006407.

(4) Ma, S.; Ge, W.; Yan, Y.; Huang, X.; Ma, L.; Li, C.; Yu, S.; Chen, C. Effects of Streptococcus sanguinis Bacteriocin on Deformation, Adhesion Ability, and Young's Modulus of Candida albicans https://www.hindawi.com/journals/bmri/2017/5291486/ (accessed Sep 20, 2019). https://doi.org/10.1155/2017/5291486.

(5) Formosa-Dague, C.; Duval, R. E.; Dague, E. Cell Biology of Microbes and Pharmacology of Antimicrobial Drugs Explored by Atomic Force Microscopy. *Semin. Cell Dev. Biol.* **2018**, *73*, 165–176. https://doi.org/10.1016/j.semcdb.2017.06.022.

(6) Formosa, C.; Schiavone, M.; Martin-Yken, H.; François, J. M.; Duval, R. E.; Dague, E. Nanoscale Effects of Caspofungin against Two Yeast Species, Saccharomyces Cerevisiae and Candida Albicans. *Antimicrob. Agents Chemother.* **2013**, *57* (8), 3498–3506. https://doi.org/10.1128/AAC.00105-13.

(7) El-Kirat-Chatel, S.; Beaussart, A.; Alsteens, D.; Jackson, D. N.; Lipke, P. N.; Dufrêne, Y. F. Nanoscale Analysis of Caspofungin-Induced Cell Surface Remodelling in Candida Albicans. *Nanoscale* **2013**, *5* (3), 1105–1115. https://doi.org/10.1039/c2nr33215a.

(8) Poulain, D. Candida Albicans, Plasticity and Pathogenesis. *Crit. Rev. Microbiol.* **2015**, *41* (2), 208–217. https://doi.org/10.3109/1040841X.2013.813904.

(9) Binnig, G.; Rohrer, H.; Gerber, Ch.; Weibel, E. Surface Studies by Scanning Tunneling Microscopy. *Phys. Rev. Lett.* **1982**, *49* (1), 57–61. https://doi.org/10.1103/PhysRevLett.49.57.

(10) Monrousseau, T.; Travé-Massuyès, L.; Le Lann, M.-V. Processing Measure Uncertainty into Fuzzy Classifier. In *26th International Workshop on Principles of Diagnosis*; Paris, France, 2015.

(11) Fang, Z.; Jiang, C.; Feng, Y.; Chen, R.; Lin, X.; Zhang, Z.; Han, L.; Chen, X.; Li, H.; Guo, Y.; et al. Effects of G6PD Activity Inhibition on the Viability, ROS Generation and Mechanical Properties of Cervical Cancer Cells. *Biochim. Biophys. Acta BBA - Mol. Cell Res.* **2016**, *1863* (9), 2245–2254. https://doi.org/10.1016/j.bbamcr.2016.05.016.

(12) Abdelhady, H. G.; Abdel-Salam, H. A.; Niazy, E. M.; Mueller, A.; Quast, M. J.; Effat, A. M.; Elbehairi, S.-E. I. Spatiotemporal PFQNM Visualization of the Effect of Suicide Dendriplexes on Dividing HeLa Cells. *Nanomedicine Nanotechnol. Biol. Med.* **2016**, *12* (8), 2365–2371. https://doi.org/10.1016/j.nano.2016.06.005.

(13) Dulínska-Molak, I.; Mao, H.; Kawazoe, N.; Chen, G. Variation of Mechanical Property of Single-Walled Carbon Nanotubes-Treated Cells Explored by Atomic Force Microscopy https://www.ingentaconnect.com/content/asp/jbn/2014/00000010/00000004/art00011%3bjsessionid=cjk1khtkl5ff.x-ic-live-01 (accessed Sep 20, 2019). https://doi.org/info:doi/10.1166/jbn.2014.1745.

(14) CYTOOchips™ Starter's A x18 https://cytoo.com/micropattern-products/chips/cytoochips%E2%84%A2-starters-x18 (accessed Oct 22, 2019).

(15) Albert, P. J.; Schwarz, U. S. Dynamics of Cell Shape and Forces on Micropatterned Substrates Predicted by a Cellular Potts Model. *Biophys. J.* **2014**, *106* (11), 2340–2352. https://doi.org/10.1016/j.bpj.2014.04.036.
(16) Petridou, N. I.; Skourides, P. A. FAK Transduces Extracellular Forces That Orient the Mitotic Spindle and Control Tissue Morphogenesis. *Nat. Commun.* **2014**, *5* (1), 1–16. https://doi.org/10.1038/ncomms6240.
(17) Lagraulet, A.; Foncy, J.; Berteloite, B.; Esteve, A.; Blatche, M.-C.; Malaquin, L.; Vieu, C. InnoStamp 40™ and InnoScan 1100AL™: A Complete Automated Platform for Microstructured Cell Arrays. *Nat. Methods* **2015**, *12*, 894–894. https://doi.org/10.1038/nmeth.f.383.
(18) Gow, N. A. R.; van de Veerdonk, F. L.; Brown, A. J. P.; Netea, M. G. Candida Albicans Morphogenesis and Host Defence: Discriminating Invasion from Colonization. *Nat. Rev. Microbiol.* **2011**, *10* (2), 112–122. https://doi.org/10.1038/nrmicro2711.
(19) Dague, E.; Jauvert, E.; Laplatine, L.; Viallet, B.; Thibault, C.; Ressier, L. Assembly of Live Micro-Organisms on Microstructured PDMS Stamps by Convective/Capillary Deposition for AFM Bio-Experiments. *Nanotechnology* **2011**, *22* (39), 395102. https://doi.org/10.1088/0957-4484/22/39/395102.
(20) Harrison, J. J.; Turner, R. J.; Ceri, H. A Subpopulation of Candida Albicans and Candida Tropicalis Biofilm Cells Are Highly Tolerant to Chelating Agents. *FEMS Microbiol. Lett.* **2007**, *272* (2), 172–181. https://doi.org/10.1111/j.1574-6968.2007.00745.x.
(21) Khot, P. D.; Suci, P. A.; Miller, R. L.; Nelson, R. D.; Tyler, B. J. A Small Subpopulation of Blastospores in Candida Albicans Biofilms Exhibit Resistance to Amphotericin B Associated with Differential Regulation of Ergosterol and β-1,6-Glucan Pathway Genes. *Antimicrob. Agents Chemother.* **2006**, *50* (11), 3708–3716. https://doi.org/10.1128/AAC.00997-06.
(22) Schiavone, M.; Déjean, S.; Sieczkowski, N.; Castex, M.; Dague, E.; François, J. M. Integration of Biochemical, Biophysical and Transcriptomics Data for Investigating the Structural and Nanomechanical Properties of the Yeast Cell Wall. *Front. Microbiol.* **2017**, *8*. https://doi.org/10.3389/fmicb.2017.01806.
(23) Rosenberg, A.; Ene, I. V.; Bibi, M.; Zakin, S.; Segal, E. S.; Ziv, N.; Dahan, A. M.; Colombo, A. L.; Bennett, R. J.; Berman, J. Antifungal Tolerance Is a Subpopulation Effect Distinct from Resistance and Is Associated with Persistent Candidemia. *Nat. Commun.* **2018**, *9* (1), 2470. https://doi.org/10.1038/s41467-018-04926-x.
(24) Groot, P. W. J. de; Bader, O.; Boer, A. D. de; Weig, M.; Chauhan, N. Adhesins in Human Fungal Pathogens: Glue with Plenty of Stick. *Eukaryot. Cell* **2013**, *12* (4), 470–481. https://doi.org/10.1128/EC.00364-12.
(25) Formosa, C.; Schiavone, M.; Boisrame, A.; Richard, M. L.; Duval, R. E.; Dague, E. Multiparametric Imaging of Adhesive Nanodomains at the Surface of Candida Albicans by Atomic Force Microscopy. *Nanomedicine Nanotechnol. Biol. Med.* **2015**, *11* (1), 57–65. https://doi.org/10.1016/j.nano.2014.07.008.
(26) Sajeesh, P.; Raj, A.; Doble, M.; Sen, A. K. Characterization and Sorting of Cells Based on Stiffness Contrast in a Microfluidic Channel. *RSC Adv.* **2016**, *6* (78), 74704–74714. https://doi.org/10.1039/C6RA09099K.
(27) Tománková, K. B.; Kolar, P.; Malohlava, J.; Kolářová, H. Mechanical Characterisation of HeLa Cells Using Atomic Force Microscopy; 2012.

Chapter 5: Conclusions and future work

5.1 Conclusions

This thesis work is the fruit of the collaboration between Mexico and France. The effort the team has put has been enormous. Also, many challenges raised for the duration of the thesis, not only intellectual but also technical, like working from a distance, trying to connect from lab to lab, the difference between time zones. However, in the end, everything was successfully accomplished and different reports were published.

The fabrication of the PDMS stamps was done following the protocol published by Formosa et al.[1] The repeatability was confirmed, and all the yeast immobilization experiments were done in these cell arrays. However, the fabrication of micropatterns smaller than 3 µm is useless for us because the centering algorithm does not work with cantilever sizes like the MLCT Bruker model.

A modification of the procedure for manual immobilization published by Formosa et al.[1] has been implemented here, acquiring high filling rates (~85%), almost the same as with the motorized setup. The modification impacted not only the filling rate but also the time needed for cell immobilization, going from 1 – 2 hours to 20 min; this is a significant contribution because it represents a more achievable and cheaper solution for single-cell immobilization on PDMS cell arrays. Becasue of the time it was imposible to test the convective/capillary assembly modification on the mammalian cells, maybe at first sight one can think that is not going to work with this type of cells. However, is worth giving a try and see if the higher filling rates can be reached with this methodology.

Relating to the automation algorithm, the centering algorithm permits to find the microwells and positions the tip on the center of the microwells (x,y position). For wells of size greater than 3.0 µm the algorithm works, the tests were performed on sizes of 3.0 µm, 4.5 µm, and 6.0 µm and for bigger sizes it is assumed that the algorithm performance is fine. The cells tested for immobilization in the PDMS stamps were *C. albicans* and *C. glabrata*, the technique employed was manual convective/capillary assembly. It is important to take into consideration the microwell sizes and cell types tested, when performing the automatic process developed and presented in this thesis. The centering algorithm permits to find the center of the microwells without using image processing, and it allows us to compensate for the creep of the motor stage, which is present every time the stage is moved to bring a new array of cells. However, its execution takes more time than the time of nanoindentation of the cells (40 s against 12 s). Because of this, the algorithm execution for every microwell is not recommended, and was the main reason to avoid its implementation in the mammalian cell script.

It is important to implement a cleaning protocol because results from the yeast cells have shown that is greatly needed. A big percentage of the force curves had to be discarded because they were of no use and that is because the tip gets dirty really fast so the program had to be stoped so the tip can be cleaned and then the program restarts. To obtain better results in the near future, two possibilities

can be developed: first, a cleaning protocol (which can be an intermediate step in the automation process) can be developed and then the verification of the tip can tell if the tip was effectively cleaned. Second, a modification on the tip must be done, like some surface chemistry so the attachment of particles or proteins can be prevented.

The JPK automation script was developed in Python 2.7 because this version contains almost the same features as Jython 2.5. Jython language is a fusion between Python and Java and is the default language that is installed along with the software to control the AFM. It is important to note that modules like numpy or scipy are not compatible with Jython language, and to avoid having execution problems; one must not include functions or classes from these modules. The script for the yeast cells is capable of calculating the position of the microwells inside the scanning area. However, it is not capable of discriminating against the empty microwells and the state of the tip; these limitations prevent the unsupervised execution of the methodology presented in this thesis work.

In this work, we also presented a way to manage, select, and organize the force curves extracted from the AFM in a more automated way. The scripts included here permit to select and rename the force curves files so they can be analyzed automatically accordingly to the parameters presented in chapter 4. However, to increase the efficiency of this process a way to decode the files in their .jpk-force format is needed. Opening the force curves in a jpk-force format will reduce the amount of time needed to process the curves because so far the program needs the force curves files in .txt format.

The results showed two subpopulations for the analysis, and increasing the number of indentations lead to more defined subpopulations. The results presented (stiffness) prove the heterogeneity of the cell population. This heterogeneity is essential because works reported in the literature presents conflicting results. That conflict, we think, can be explained by looking at the cell population and not only a few cells. The results confirmed the hypothesis presented in this thesis. It is possible to obtain significant results from cells when the number of indentations is lowered, and the number of cells analyzed increases. Works in the literature usually report several indentations done to cells from hundreds to thousands. However, in this work, the number of indentations was from 9 to 16. More experiments are needed to establish if the number of indentations can be lowered even more.

The massive amount of data (> 20,000 force curves) obtained here, made possible to use computational techniques that were not considered at the beggining, hence machine learning. Machine learning algorithms allowed us to determine that using only one mechanical property is not enough to differentiate native cells from treated cells. The preliminary results show that by using adhesion, stiffness, and work of adhesion, it is possible to differentiate with 86% of confidence.

5.2 Future work

This thesis work enabled AFM to assess the cell population. However, much work can still be done to improve not only the number of cells but the autonomous execution of the AFM. The algorithm is capable of finding the microwells and measure inside them. However, it is not capable of distinguishing between empty and filled microwells. Implementing image recognition for instance can be used to identify the empty microwells and then ignore those wells. Ignoring the empty wells

can improve the number of cells analyzed because the methodology presented here filters the results from the empty wells.

The script has been executed for about 4 h but, the program does not verify the state of the tip. Feedback of the state of the tip is essential to achieve complete autonomous execution. An additional step that verifies the condition of the tip and clean (if necessary) is needed in the algorithm. Also, tailoring the shape of the tip can help studying the effect of its geometry in the measurements.

The results showed a difference between native and treated cells. However, the results obtained were acquired from independent experiments. In the future, experiments tracking the state of the cells before and after the treatment must be done. The script does the labeling of cells, so it's easy to go to the previous cells and measure again after treatment. In this thesis work, a theory has been presented, which establishes that from the two subpopulations founded, the cells after treatment react differently to the caspofungin.
Sets of AFM force curves have been analyzed by algorithms derived from artificial intelligence. These data classification methods, however, have shown their power[2–4] and have only been considered for the analysis of AFM[5] images. From a bench-marking perspective and in order to really demonstrate the advantages of our methodology, we will deploy these methods for the analysis and comparison of cellular populations (MCF73, MCF710A[6], in particular) which have also been analyzed in a classical way. The machine learning results presented in this work were obtained using three mechanical properties, adhesion, stiffness, and work of adhesion. The results obtained establish with 86% confidence that it is possible to distinguish diseased cells from healthy cells. However, there are other factors such as Young modulus or the number of force curves that can be tested and see if the percentage increases or decreases. Because of the massive amount of data (> 20,000 force curves) obtained with the methodology presented here, it was possible to use computational techniques that were not considered before. Machine learning algorithms allowed us to determine that using only one mechanical property is not enough to differentiate native cells from treated cells. The preliminary results show that by using adhesion, stiffness, and work of adhesion is possible to differentiate with 86% of confidence.

5.3 References

(1) Formosa, C.; Pillet, F.; Schiavone, M.; Duval, R. E.; Ressier, L.; Dague, E. Generation of Living Cell Arrays for Atomic Force Microscopy Studies. *Nat. Protoc.* **2015**, *10* (1), 199–204. https://doi.org/10.1038/nprot.2015.004.

(2) Hedjazi, L.; Aguilar-Martin, J.; Le Lann, M.-V. Similarity-Margin Based Feature Selection for Symbolic Interval Data. *Pattern Recognit. Lett.* **2011**, *32* (4), 578–585. https://doi.org/10.1016/j.patrec.2010.11.018.

(3) Hedjazi, L.; Aguilar-Martin, J.; Le Lann, M.-V.; Kempowsky-Hamon, T. Membership-Margin Based Feature Selection for Mixed Type and High-Dimensional Data: Theory and Applications. *Inf. Sci.* **2015**, *322*, 174–196. https://doi.org/10.1016/j.ins.2015.06.007.

(4) Kempowsky-Hamon, T.; Valle, C.; Lacroix-Triki, M.; Hedjazi, L.; Trouilh, L.; Lamarre, S.; Labourdette, D.; Roger, L.; Mhamdi, L.; Dalenc, F.; et al. Fuzzy Logic Selection as a New

Reliable Tool to Identify Molecular Grade Signatures in Breast Cancer – the INNODIAG Study. *BMC Med. Genomics* **2015**, *8* (1), 3. https://doi.org/10.1186/s12920-015-0077-1.

(5) Huang, B.; Li, Z.; Li, J. Artificial Intelligent Atomic Force Microscope Enabled by Machine Learning. *ArXiv180709985 Cond-Mat Physicsphysics* **2018**.

(6) Smolyakov, G.; Thiebot, B.; Campillo, C.; Labdi, S.; Severac, C.; Pelta, J.; Dague, É. Elasticity, Adhesion, and Tether Extrusion on Breast Cancer Cells Provide a Signature of Their Invasive Potential. *ACS Appl. Mater. Interfaces* **2016**, *8* (41), 27426–27431. https://doi.org/10.1021/acsami.6b07698.

List of communications

Publications in interantional Peer reviewed journals

1. JoVe 2020; doi: 10.3791/61315.
Childérick Séverac, Sergio Proa-Coronado, Cécile Formosa-Dague, Adrian Martinez-Rivas, Etienne Dague.
Automation of Bio-Atomic Force Microscope Measurements on Hundreds of C. albicans Cells.

2. Nanoscale Horizons 2020 doi:10.1039/C9NH00438F.
S. Proa-Coronado, C. Séverac, A. Martínez-Rivas, E. Dague.
Beyond the paradigm of nanomechanical measurements on cells using AFM: an automated methodology to rapidly analyse thousands of cells.

3. Micromachines 2017, 8(12), 347; https://doi.org/10.3390/mi8120347.
A. Martinez-Rivas, K. Génesis González-Quijano, S. Proa-Coronado, C. Séverac, E. Dague.
Methods of micropatterning and manipulation of cells for biomedical applications.

Patent

1. WO2019112414 (A1). PCT/MX2018/050027, 2017, Mexico.
A. Martínez Rivas, E. Dague, S. Proa Coronado, C. Séverac, Génesis K. González Quijano
Proceso por medio de microscopía de fuerza atómica para el análisis masivo físico y mecánico en materiales, arreglos de biomateriales y estructuras.

Software Copyright

1. Número de registro: 03-2017-113012552200-01. 1 de diciembre 2017, Mexico D.F.
E. Dague, S. Proa Coronado, C. Séverac, A. Martinez Rivas
Automatip: Automatización de mediciones biofísicas en células por medio del microscopio de fuerza atómica (AFM).

Oral Communications in International conferences

1. BiophysAdh: International symposium on biophysics of microbial adhesion. 10-11 September 2018, Toulouse, France.

S. Proa-Coronado, C. Séverac, E. Dague, A. Martinez-Rivas
Automatic nanomechanical analysis on cell populations by Atomic Force Microscopy.

2. ICTNN2018: International congress on transdisciplinary nanoscience & nanotechnology. 28th-31th October 2018, Mexico city, Mexico
S. Proa-Coronado, C. Séverac, E. Dague, A. Martinez-Rivas
Automatic nanomechanical analysis on cell populations by atomic force microscopy.

Poster Communications in International conferences

1. **IMRC 2017:** XXVI International Materials Research Congress. August 20th25th 2017, Cancún Mexico; Labs-On-A-Chip and Organ-on-a-Chip Symposium, S. Proa-Coronado, C. Severac, E. Dague, A. Martinez-Rivas.

Algorithm to automate physical measurement of cells by Atomic Force Microscope immobilized in elastomeric microstrctures.

2. Nanobio-Tecnopoli: NanoBio meeting, 04 April 2018, CDMX, Mexico. Poster.
S. Proa-Coronado, C; Severac, E. Dague, A. Martinez-Rivas. Automation of cell measurement process on an atomic force microscope for cell population. NanoBio meeting.

3. MNE 2018: Micro & Nano Engineering. 24-27 September 2018, Copenhagen, Denmark. Poster.
S. Proa-Coronado, C. Séverac, A. Martínez-Rivas, E. Dague.
Automation of nanomechanical analysis on cell micropatternings by Atomic Force Microscopy.

4. Linz winter workshop: XXI Annual Linz Winter Workshop. 1-4 February 2019. Linz, Austria. Poster.
S. Proa-Coronado, C. Séverac, A. Martínez-Rivas, E. Dague.
Automated Atomic Force Microscopy for accessing cell population nanomechanical properties.

5. IMRC 2019: XXVIII International Materials Research Congress. August 18th to 23th 2019, Cancún México; Labs-On-A-Chip and Organ-on-a-Chip Symposium,
S. Proa-Coronado, C. Séverac, E. Dague, A. Martínez-Rivas
Atomic Force Microcopy for analyzing the nanomechanical properties of candida albicans cell population and its massive data.

Communications in local conferences

1. Bruker AFM user meeting: 27-28 Novembre 2018, Montpellier, France.
oral communication
S. Proa-Coronado, A. Martínez-Rivas, E. Dague, C. Séverac. AFM automation on living cells

2. BIOSURF 2019: École thématique CNRS «BIOSURF 2019». 3-7 June 2019, Porquerolles, France.
S. Proa-Coronado, C. Séverac, A. Martínez-Rivas, E. Dague.
Nanomechanical properties of *Candida albicans* cell population using Atomic Force Microscopy.

micromachines

MDPI

Review

Methods of Micropatterning and Manipulation of Cells for Biomedical Applications

Adrian Martinez-Rivas [1,*], Génesis K. González-Quijano [2], Sergio Proa-Coronado [3], Childérick Séverac [4] and Etienne Dague [5,*]

1 CIC, Instituto Politécnico Nacional (IPN), Av. Juan de Dios Bátiz S/N, Nueva Industrial Vallejo, 07738 Mexico City, Mexico
2 CONACYT-CNMN, Instituto Politécnico Nacional (IPN), Av. Luis Enrique Erro s/n, Nueva Industrial Vallejo, 07738 Mexico City, Mexico; gkgonzalez@conacyt.mx
3 ENCB, Instituto Politécnico Nacional (IPN), Av. Wilfrido Massieu, Unidad Adolfo López Mateos, 07738 Mexico City, Mexico; sergio.prc81@gmail.com
4 ITAV-CNRS, Université de Toulouse, CNRS, Toulouse, France; childerick.severac@itav.fr
5 LAAS-CNRS, Université de Toulouse, CNRS, Toulouse, France
* Correspondence: nanobiomex@hotmail.com or amartinezri@cic.ipn.mx (A.M.-R.); edague@laas.fr (E.D.); Tel.: +52-55-5729-6000 (ext. 56606) (A.M.-R.); +33-56-133-7841 (E.D.)

Received: 7 November 2017; Accepted: 28 November 2017; Published: 29 November 2017

Abstract: Micropatterning and manipulation of mammalian and bacterial cells are important in biomedical studies to perform in vitro assays and to evaluate biochemical processes accurately, establishing the basis for implementing biomedical microelectromechanical systems (bioMEMS), point-of-care (POC) devices, or organs-on-chips (OOC), which impact on neurological, oncological, dermatologic, or tissue engineering issues as part of personalized medicine. Cell patterning represents a crucial step in fundamental and applied biological studies in vitro, hence today there are a myriad of materials and techniques that allow one to immobilize and manipulate cells, imitating the 3D in vivo milieu. This review focuses on current physical cell patterning, plus chemical and a combination of them both that utilizes different materials and cutting-edge micro-nanofabrication methodologies.

Keywords: cell patterning and manipulation; mammalian and bacterial cells; micro-nanofabrication; microfluidics; organs-on-chips (OOC); biomedical microelectromechanical systems (bioMEMS); point-of-care (POC); soft lithography

1. Introduction

The objective of micropatterning and manipulating mammalian and bacterial cells is to have better controls, a deeper understanding, and to apply these in practical biomedical microelectromechanical systems (bioMEMS), point-of-care (POC) devices, and organs-on-chips (OOC) [1]. In this regard, (nano)biotechnologists have developed and implemented novel methodologies to fix cells on substrates, in a controlled manner, so-called micropatterning. It is a challenging task, however, new micro and nanofabrication methodologies have contributed to the achievement of satisfactory outcomes. Cell micropatterning and cell manipulation currently represent the basic steps to perform drug testing experiments [2,3], to understand biochemical processes [4,5], to design microfluidic devices for medical applications, and to conduct fundamental studies in biological areas [6,7]. In this context, in vitro assays have increased their efficiency because of the simplicity of cell micropatterning and manipulation, which permit the carrying out of 3D human cells assays, replacing animal in vivo models [8]. Additionally, because of the versatility of these cell micropatternings, they can be applied to biomolecules [9], bacteria [10], yeasts [11], and other bioparticles involved in therapies [12], diagnosis [13], or interaction with numerous biochemical processes [14].

Nanoscale Horizons

COMMUNICATION

View Article Online
View Journal | View Issue

Cite this: *Nanoscale Horiz.*, 2020, 5, 131

Received 3rd July 2019,
Accepted 14th August 2019

DOI: 10.1039/c9nh00438f

rsc.li/nanoscale-horizons

Beyond the paradigm of nanomechanical measurements on cells using AFM: an automated methodology to rapidly analyse thousands of cells†

S. Proa-Coronado, [abd] C. Séverac,[b] A. Martinez-Rivas‡*[ac] and E. Dague ‡*[d]

Nanomechanical properties of cells could be considered as cellular biomarkers. The main method used to access the mechanical properties is based on nanoindentation measurements, performed with an operator manipulated Atomic Force Microscope (AFM) which is time-consuming and expensive. This is one of the reasons that prevent the transfer of AFM technology into clinical laboratories. In this paper we report a methodology which includes an algorithm (transferred to a script, executed on a commercial AFM) able to automatically move the tip onto a single cell and through several cells to record force curves combined with a smart strategy of cell immobilization. Cells are placed into microwells of a microstructured polydimethylsiloxane (PDMS) stamp. Inside a classical 100 × 100 μm^2 AFM field, 100 cells can be immobilized. In an optimal configuration we were able to measure, within 4 h, a population of 900 *Candida albicans* cells both native and caspofungin treated, which represents an unprecedented performance. We discovered that the population is heterogeneous and can be divided, on the basis of nanomechanical properties, into 2 subgroups.

New concepts

The current concept in Bio-AFM is to perform manually hundreds or thousands of force curves on a few cells. In contrast, in our work, we went beyond this concept and performed automatically nanomechanical measurements on hundreds of cells. The paper reports and demonstrates nanoindentations on organized living cells, automatically, which represents a major step forward in the field of nanotechnology. The massive nanomechanical data, acquired on 900 cells, open the door to the heterogeneity of populations, inaccessible in the framework of measuring only a few cells. We discovered in a classical *C. albicans* culture, 2 subpopulations of cells that can be distinguished on the basis of their nanomechanical properties. This will lead to a better understanding and use of nanomechanical data because their statistical significance power is higher than that in previously reported studies. Awakening AFM to statistics will enhance its potential use to analyze bionanomechanical properties and maybe pave the way for mechanopathology.

Introduction

Medical doctors constantly have to face the issues of diagnosis, prognosis or evaluation of treatment efficiency. To tackle these issues there is a constant need to develop and adapt new, more accurate and sensitive biomarkers, able to help in differential diagnosis or predict as early as possible the disease evolution. In this aspect cell mechanical properties have the potential of being used as label free biomarkers for some pathologies.[1]

Indeed, cell mechanical properties have the potential to address the diagnosis of cancer[1–4] as it has been reported that cancerous cells change their mechanical phenotype, presenting a lower Young modulus[5–7] and adhesion[7–9] than normal cells. Other authors have reported that cell mechanical properties are modified during proliferation,[10] by comparing their elastic modulus to differentiate normal cells from cancerous cells[11] or normal cells from cells treated for example with H_2O_2, *N*-ethylmaleimide and chymotrypsin.[12] In the field of cardiology, it is also known that erythrocyte interactions with fibrinogen, as probed by AFM, are modified in ischemia and that the stiffness of red blood cells is altered.[13] Cardiomyocytes are difficult to handle, and then works have reported the characterization of 1 to 30 cardiomyocytes[14–20] in about 6–8 h, which is too small an amount of cells to provide statistically relevant information in the context of human diseases and therefore will never be reliable enough for clinicians. Mechanical properties have also helped in understanding the effects of antimicrobial molecules on bacteria or yeast cell's walls.[21] Another example in the bacteria field is the work of Francius *et al.*[22] They reported that *S. aureus* exposed to lysostaphin presented a decrease in elasticity and stiffness of its

[a] *ENCB-Instituto Politécnico Nacional (IPN), Av. Wilfrido Massieu, Unidad Adolfo López Mateos, 07738, Mexico City, Mexico. E-mail: nanobiomex@hotmail.com*
[b] *ITAV-CNRS, Université de Toulouse, CNRS, Toulouse, France*
[c] *CIC-Instituto Politécnico Nacional (IPN), Av. Juan de Dios Bátiz S/N, Nueva Industrial Vallejo, 07738, Mexico City, Mexico*
[d] *LAAS-CNRS, Université de Toulouse, CNRS, Toulouse, France. E-mail: edague@laas.fr*

† Electronic supplementary information (ESI) available. See DOI: 10.1039/c9nh00438f

‡ These authors contributed equally to this work.

jove

Automation of Bio-Atomic Force Microscope Measurements on Hundreds of *C. albicans* Cells

Childérick Severac[*,1], **Sergio Proa-Coronado**[*,1,2,3], **Cécile Formosa-Dague**[4], **Adrian Martinez-Rivas**[3,5], **Etienne Dague**[2]

[1] ITAV-CNRS, Université de Toulouse, CNRS, Toulouse, France [2] LAAS-CNRS, Université de Toulouse, CNRS, Toulouse, France [3] ENCB-Instituto Politécnico Nacional (IPN) [4] TBI, Université de Toulouse, CNRS, INRA, INSA, Toulouse, France [5] CIC-Instituto Politécnico Nacional (IPN)

[*] These authors contributed equally

Corresponding Author

Etienne Dague
edague@laas.fr

Citation

Severac, C., Proa-Coronado, S., Formosa-Dague, C., Martinez-Rivas, A., Dague, E. Automation of Bio-Atomic Force Microscope Measurements on Hundreds of *C. albicans* Cells. *J. Vis. Exp.* (), e61315, doi:10.3791/61315 (2020).

Date Published

June 16, 2020

DOI

10.3791/61315

URL

jove.com/video/61315

Abstract

The method presented in this paper aims to automate Bio-AFM experiments and the recording of force curves. Using this method, it is possible to record forces curves on 1000 cells in 4 hours automatically. To maintain a 4 hour analysis time, the number of force curves per cell is reduced to 9 or 16. The method combines a Jython based program and a strategy for assembling cells on defined patterns. The program, implemented on a commercial Bio-AFM, can center the tip on the first cell of the array and then move, automatically, from cell to cell while recording force curves on each cell. Using this methodology, it is possible to access the biophysical parameters of the cells such as their rigidity, their adhesive properties, etc. With the automation and the large number of cells analyzed, one can access the behavior of the cell population. This is a breakthrough in the Bio-AFM field where data have, so far, been recorded on only a few tens of cells.

Introduction

This work provides a methodology to perform automatic force measurements on hundreds of living cells using an atomic force microscope (AFM). It also provides a method to immobilize microbes on a PDMS microstructured stamp that is compatible with AFM experiments conducted in a liquid environment.

Bio-AFM is a highly specialized technology conceived for applications in biology and then used to study living cells. It requires a trained engineer who can analyze one cell at the time. In these conditions, the number of different cells that can be analyzed is rather small, typical 5 to 10 cells in 4-5 hours. However, the quantity of force measurements recorded on a single cell are usually very high and can easily reach 1000. Thus, the current paradigm of AFM force measurements on living cells is to record hundreds of force curves (FCs) but on a limited number of cells.

1. WO2019112414 - PROCESS USING ATOMIC FORCE MICROSCOPY FOR MASS PHYSICAL AND MECHANICAL ANALYSIS IN MATERIALS, BIOMATERIAL ARRANGEMENTS AND STRUCTURES

Publication Number
WO/2019/112414

Publication Date
13.06.2019

International Application No.
PCT/MX2018/050027

International Filing Date
04.12.2018

IPC
G01Q 60/24 (2010.01) G01Q 60/36 (2010.01) G01Q 10/00 G01Q 10/04 (2010.01) G01Q 30/20 (2010.01) G01Q 80/00 (2010.01)

Applicants
INSTITUTO POLITÉCNICO NACIONAL [MX/MX]; EDIFICIO DE LA DIRECCIÓN GENERAL, AV LUIS ENRIQUE ERRO S/N 07738 MEXICO, MX

Inventors
MARTÍNEZ RIVAS, Adrián; MX
DAGUE, Etienne; MX
PROA CORONADO, Sergio; MX
SÉVERAC, Childérick; MX
GONZÁLEZ QUIJANO, Génesis Karendash; MX

Agents
BROCA NUCAMENDI, Arturo; MX

Priority Data
MX/A/2017/015624 04.12.2017 MX

Publication Language
Spanish (ES)

Filing Language
Spanish (ES)

Designated States
View All

Title
(EN) PROCESS USING ATOMIC FORCE MICROSCOPY FOR MASS PHYSICAL AND MECHANICAL ANALYSIS IN MATERIALS, BIOMATERIAL ARRANGEMENTS AND STRUCTURES
(ES) PROCESO POR MEDIO DE MICROSCOPÍA DE FUERZA ATÓMICA PARA EL ANÁLISIS MASIVO FÍSICO Y MECÁNICO EN MATERIALES, ARREGLOS DE BIOMATERIALES Y ESTRUCTURAS
(FR) PROCÉDÉ PAR MICROSCOPIE À FORCE ATOMIQUE POUR L'ANALYSE MASSIVE PHYSIQUE ET MÉCANIQUE DE MATÉRIAUX, AGENCEMENTS DE BIOMATÉRIAUX ET STRUCTURES

Abstract
(EN)
The Present Invention Relates To A Process Implemented By A Computer Which Comprises Steps Of Precise Securing, Handling And Mass Measurement By Atomic Force Microscopy (AFM Or BioAFM), Automatically, Of The Physical And Mechanical Properties Of Various Types Of Samples Such As Cells Or Bacteria Alone Or Interacting With Nanoparticles, Biomolecules And Other Types Of Carbon-Based Nanostructures Such As Graphene Or Synthetic Particles. The Process Takes Multiple Measurements In A Single Sample That Is Arranged Precisely And Automatically Continues The Process With Other Samples. At The End, The Working Area Continues With Other Areas Making Thousands Of Nano-Indentations In A Very Short Time In A Reliable And Reproducible Manner In Order To Obtain Mass Data And Obtain Quantitative Data On The Physical-Mechanical Parameters, Making It Possible To Confirm The Measurement And Representativeness Of The Type Of Material Derived From The Extraction Of The Mass Physical And Mechanical Analysis Thereof That Is Obtained From The Statistical Analysis.
(ES)
La Presente Invención Se Refiere A Un Proceso Implementado Por Computadora Que Consiste En Etapas De Fijado Preciso, Manipulación Y Mediciones Masivas Por Microscopía De Fuerza Atómica (MFA, AFM O BioAFM) De Manera Automática De Las Propiedades Físicas Y Mecánicas De Diferentes Tipos De Muestras Como Células, Bacterias Solas O Con Interacción Con Nanopartículas, Biomoléculas Y Otro Tipo De Nanoestructuras Derivadas Del Carbono Como El Grafeno O Partículas Sintéticas. El Proceso Realiza Múltiples Mediciones En Una Sola Muestra Que Están Arregladas De Forma Precisa Y Continúa El Procedimiento De Forma Automática A Otras Muestras. Al Finalizar, El Área De Trabajo Continúa Con Otras Áreas Realizando Miles De Nanoindentaciones En Un Tiempo Muy Corto De Manera Confiable Y Reproducible Para La Obtención De Datos Masivos Y La Obtención Datos Cuantitativos De Los Parámetros Físico-Mecánicos, Permitiendo Dar Certeza A La Medición Y Representatividad Del Tipo De Material Derivado De La Extracción De Su Análisis Masivo Físico Y Mecánico Que Se Obtiene Del Análisis Estadístico.
(FR)
La Présente Invention Concerne Un Procédé Mis En Oeuvre Par Ordinateur Qui Consiste En Des Étapes De Fixation Précise, De Manipulation Et Des Mesures Massives Par Microscopie À Force Atomique (MFA, AFM Ou BioAFM) De Manière Automatique Des Propriétés Physiques Et Mécaniques De Différents Types D'échantillons Comme Des Cellules, Des Bactéries Seules Ou Interagissant Avec Des Nanoparticules, Des Biomolécules Et Un Autre Type De Nanostructures Dérivées Du Carbone Comme Le Graphène Ou Des Particules Synthétiques. Le Procédé Consiste À Effectuer De Multiples Mesures Dans Un Seul Échantillon, Lesquelles Sont Réglées De Manière Précise Et À Étendre Le Procédé De Manière Automatique À D'autres Échantillons. A La Fin, La Zone De Travail Est Étendue À D'autres Zones En Effectuant Des Milliers De Nano-Indentations Dans Un Temps Court De Manière Fiable Et Reproductible Pour L'obtention De Données Massives Et L'obtention De Données Quantitatives Des Paramètres Physico-Mécaniques, Permettant De Garantir La Mesure Et La Représentativité Du Type De Matériau Dérivé De L'extraction De Son Analyse Massive Physique Et Mécanique Qui Est Obtenue À Partir De L'analyse Statistique.

Latest bibliographic data on file with the International Bureau

Python script for yeast cells

```
# Programmer: Sergio Proa Coronado
# JPK Script
from __future__ import division
import math
import time
start_time=time.time()

#New data type declaration
class Point(object):
    def __init__(self, x = 0, y = 0):
        self.x = x
        self.y = y

# Function to calculate angle
def calculateAngle(A = [], B = []):
    """ Given two points (x,y) an angle is calculated
    """
    Time_angleS = time.time()
    if A[0] != B[0]:
             print 'angle calculated: ' + str(math.atan((B[1] -
A[1])/(B[0]-A[0])))
        Time_angleF = time.time()
           print'Time for calculate angle: ' + str(Time_angleF -
Time_angleS)
        return math.atan((B[1] - A[1])/(B[0]-A[0]))


    else:
        Time_angleF = time.time()
           print'Time for calculate angle: ' + str(Time_angleF -
Time_angleS)
        return 0

# Function to determine plane equations
def planeEq(Ph, Qh, Rh, P = [], Q = [],R = []):
      """Given three points (coordinates x, y) and its heights
calculates the plane equation
    """
    coef = []
    coef.append((R.y - P.y) * (Qh - Ph) - (Q.y - P.y) * (Rh - Ph))
    coef.append((Rh - Ph) * (Q.x - P.x) - (Qh - Ph) * (R.x - P.x))
```

```
     coef.append((R.x - P.x) * (Q.y - P.y) - (Q.x - P.x) * (R.y -
P.y))
    coef.append(-(coef[0] * P.x + coef[1] * P.y + coef[2] * Ph))
      #print 'Zero plane equation: ' + str(coef[0]) + ' X +' +
str(coef[1]) + ' Y +' + str(coef[2]) + ' Z +' + str(coef[3]) + ' =
0'
    return coef

#Function to recalculate points 1, 2 and 3.
def calculatePoints(ws, a, fN, P = []):
     """ Given the well size and a list variable which stores the
average central coordinates of a well,
    recalculates these coordinates to be at the center of the well
    """
    Time_centerS = time.time()
    dateTemp = time.asctime()
    #-------------Variables for global zero plane calculation
    global TP
    global TH
    global Tsd
    PC = []
    PH = []

    #-------------------------------------------------
    #Variables to determine weights
    zeroPlane = []
    tHeights = []
    weights = []
    distances = []
    #-----Variables for the grid
    FastLength = ws + 3e-06
    SlowLength = ws + 4e-06
    XGridCenter = P[0]
    YGridCenter = P[1]
    NumFastPoints = 5
    NumSlowPoints = 5
    #---------------------------
        #---------------Variables  for  local  zero  plane  points
determination
    temp = 0
    numX = 0
    numY = 0
    den = 0
    tempX = 0
    tempY = 0
```

```
    tempDen = 0
    invtempDen = 0
    #-------------------------------------------------------------
    if (P[0] + (FastLength / 2)) > 50e-6:
        extraDistance = ((P[0] + FastLength / 2) - 50e-6) + 1e-6
        P[0] += extraDistance
        print 'FastLength modified' + str(P[0])
    if (P[1] + (SlowLength / 2)) > 50e-6:
        extraDistance = ((P[1] + SlowLength / 2) - 50e-6) + 1e-6
        P[1] += extraDistance
        print 'SlowLength modified'
    ForceSpectroscopy.setPosition(P[0], P[1])
    #Saving an image of the initial position of the tip
                  Snapshooter.saveOpticalSnapshot(path+"initialP-"+
str(dateTemp) + ".png")
          ForceSpectroscopy.setGridPattern(FastLength,  SlowLength,
XGridCenter, YGridCenter, NumFastPoints, NumSlowPoints, a)
         #ForceSpectroscopy.setGridPattern(FastLength,  SlowLength,
XGridCenter, YGridCenter, NumFastPoints, NumSlowPoints, a)
    Scanner.approach()
    # Iterating through the grid
    for h in range(NumFastPoints * NumSlowPoints):
        Scanner.retractPiezo()
        ForceSpectroscopy.moveToForcePositionIndex(h)
        Scanner.approachPiezo()
        # Storing grid coordinates
         PC.append(Point(ForceSpectroscopy.getForcePosition(h).getX
(), ForceSpectroscopy.getForcePosition(h).getY()))
        # Storing grid coordinates heights
        PH.append(Scanner.getCurrentHeight())

        temp += Scanner.getCurrentHeight()

    #Calculating  average coordinate for the global zero plane
    for h in range(5):
        tempX += PH[h] * PC[h].x
        tempY += PH[h] * PC[h].y
        tempDen += PH[h]
    invtempDen = 1/tempDen
    TP = Point(tempX * invtempDen, tempY * invtempDen)


    # zero plane calculation
       zeroPlane  =  planeEq(PH[0],  PH[4],  PH[24],  PC[0],  PC[4],
PC[24])
```

```
    logFile = open(fN, "a")
    logFile.write("Distances to the zero plane:\n")
    logFile.close()
    # Storing the heigh for the global zero plane
    ForceSpectroscopy.setPosition(TP.x, TP.y)
    TH = Scanner.getCurrentHeight()
    #Assigning weights
    for h in range(len(PC)):
        invden = 1 / math.sqrt(zeroPlane[0] ** 2 + zeroPlane[1] **
2 + zeroPlane[2] ** 2)
            d=(zeroPlane[0] * PC[h].x + zeroPlane[1] * PC[h].y
+zeroPlane[2] * PH[h] + zeroPlane[3]) * invden
        distances.append(d)
        print str(h) + ': ' + str(d)
    # Storing the heights to calculate the zero distance
    tDistances = distances[:5]
    tDistances[6:6] = distances[20:25]
    # Determination of zero distance
    zDmax = max(tDistances)
    zDmin = min(tDistances)
    for h in range(len(PC)):
        if distances[h] >= (5 * zDmax):
            weights.append(Point(h, 5)) # Using class Point we
store index (x position) and weight (y position) for that
coordinate
        elif distances[h] >= (4 * zDmax):
            weights.append(Point(h, 4))
        elif distances[h] >= (3 * zDmax):
            weights.append(Point(h, 3))
        elif distances[h] >= (2 * zDmax):
            weights.append(Point(h, 2))
        elif distances[h] >= zDmax:
            weights.append(Point(h, 1))
        elif distances[h] <= (5 * zDmin):
            weights.append(Point(h, -5))
        elif distances[h] <= (4 * zDmin):
            weights.append(Point(h, -4))
        elif distances[h] <= (3 * zDmin):
            weights.append(Point(h, -3))
        elif distances[h] <= (2 * zDmin):
            weights.append(Point(h, -2))
        elif distances[h] < (zDmin):
            weights.append(Point(h, -1))
        else:
            weights.append(Point(h, 0))
```

```
    # Discarding points which weight = 0
    weights = [value for value in weights if value.y != 0]

    #Select the apropiate point to be the new center
    #minimum value
    mi = min([value.y for value in weights])

    #Obtaining the heightes weight
    ma = max([value.y for value in weights])
    #Only the maximum heights are considered
    weights = [value for value in weights if value.y == ma]
    for h in range(len(weights)):
        logFile = open(fN, "a")
         logFile.write(str(weights[h].x) + ', ' + str(weights[h].y)
+ "\n")
        logFile.close()
        print str(weights[h].x) + ', ' + str(weights[h].y)
    #Calculating new central point
    if len(weights) > 1:
        for h in range(len(weights)):
            numX += distances[weights[h].x] * PC[weights[h].x].x
            numY += distances[weights[h].x] * PC[weights[h].x].y
            den += distances[weights[h].x]
        invden = 1/den
        P[0] = numX * invden    # PX recalculated
        P[1] = numY * invden    # PY recalculated
    else:
        P[0] = PC[weights[0].x].x # PX recalculated
        P[1] = PC[weights[0].x].y # PY recalculated
    Scanner.retractPiezo()
    Time_centerF = time.time()
    logFile = open(fN, "a")
      logFile.write('Time for centering: ' + str(Time_centerF -
Time_centerS) + "\n")
    logFile.close()
    print'Time for centering: ' + str(Time_centerF - Time_centerS)

#************************Inputs
block*******************************

#--------------The working area is defined as 100 x 100
micrometers-----------------------------------
#Points 1 and 2, take this coordinates from the center of each
well, MANUAL INPUT
```

```
P1=[40.047e-6 , 41.382e-6]

P2=[40.964e-6 , -40.957e-6]


#-------------Pitch------------
pitch= 10.3e-6

#Well dimensions assuming square wells
Ws=4.5e-6

#Path for saving directory
path="~/jpkdata/Automatip/20190320/"

# Pattern area
totalArea = 300e-6

# ForceScan matrix for the wells
numScans=[3,3]

#**************************************************************
**

#Temporal variables for global zero plane
TP = Point(0,0)
#temporal piezo hight for the zero plane
TH = 0
#temporal zero plane error
Tsd = 0
# Creating the log file to store the messages displayed on screen
#You can find this log file in the Automatip folder
now = time.asctime(time.localtime(time.time()))
fileName = "Automatip_LogFile-" + str(now) + ".txt"
logFile = open(fileName, "w")
logFile.close()
#used for the calculation of motor stage coordinates
g = 0
# Temporal variable for timer
parcialTimeMS = 0
#Calculating the angle, two points distance equation
angle = math.fabs(calculateAngle(P1, P2))
logFile = open(fileName, "a")
logFile.write("angle calculated: " + str(angle) + "\n")
logFile.close()
print 'Angle calculated: ' + str(angle)
```

```
#Defining distance in order to know the number of wells
da = math.sqrt((P2[0]-P1[0])**2 + (P2[1]-P1[1])**2)
nFP = int(da/pitch+0.4)
nSP = int(da/pitch+0.4)
logFile = open(fileName, "a")
logFile.write(str(nFP) + ' x ' + str(nSP) + "\n")
logFile.close()
print str(nFP)+' x '+str(nSP)
if P1[0] > P2[0]:
    option = 0
else:
    option = 1
logFile = open(fileName, "a")
logFile.write('option = ' + str(option) + "\n")
logFile.close()
print'option = ' + str(option)
#variables needed for loop
i=0
j=-1
e=0

#path2 = "~/jpkdata/forceScans/20180725/"
#Redefining P1
calculatePoints(Ws,angle, fileName, P1)
P1First = P1
logFile = open(fileName, "a")
logFile.write('P1: ' + str(P1[0]) + ', ' + str(P1[1]) + "\n")
logFile.close()
print 'P1: ' + str(P1[0]) + ', ' + str(P1[1])
ForceSpectroscopy.setPosition(P1[0], P1[1])
Scanner.approachPiezo()
Snapshooter.saveOpticalSnapshot(path+"P1-Corrected.png")
Scanner.retractPiezo()
zP1 = TP
zH1 = TH
#Tsd1 = Tsd

#Redefining P2
calculatePoints(Ws,angle, fileName, P2)
logFile = open(fileName, "a")
logFile.write('P2: ' + str(P2[0]) + ', ' + str(P2[1]) + "\n")
logFile.close()
print 'P2: ' + str(P2[0]) + ', ' + str(P2[1])
ForceSpectroscopy.setPosition(P2[0], P2[1])
Scanner.approachPiezo()
```

```
Snapshooter.saveOpticalSnapshot(path+"Test1-25p-afterP2.png")
Scanner.retractPiezo()
zP2 = TP
zH2 = TH
#Tsd2 = Tsd

#Redefining P3
#calculatePoints(Ws,angle, P3)
#ForceSpectroscopy.setPosition(P3[0], P3[1])
#Scanner.approachPiezo()
#Snapshooter.saveOpticalSnapshot(path2+"Test1-25p-afterP3.png")
#Scanner.retractPiezo()
#zP3 = TP
#zH3 = TH
#Tsd3 = Tsd

#Global_zeroPlane = planeEq(zH1, zH2, zH3, zP1, zP2, zP3)
#time.sleep(10)

#Distance for the MotorStage
delta = pitch*nFP
logFile = open(fileName, "a")
logFile.write('Total distance to cover on X axis: ' + str(delta)+'
m' + "\n")
logFile.close()
print'Total distance to cover on X axis: ' + str(delta)+' m'

# MSstep is the number of motorstage steps
MSstep = int(totalArea / delta)
logFile = open(fileName, "a")
logFile.write('The pattern was divided into: ' + str(MSstep) + "
scanning areas\n")
logFile.close()
print 'MSstep = ' + str(MSstep)
#Variable WellPositions stores the coordinates for the WellGrid
WellPositions=[]

#Variable MSCoord stores MotorStage coordinates
MSCoord = []

# Create a MSCoord list full of zeros
for f in range(MSstep * MSstep):
    MSCoord.append(Point(0,0))

# Assign the first motor stage coordinate to the first position
```

```
MSCoord[0].x = MotorizedStage.getPosition().getX()
MSCoord[0].y = MotorizedStage.getPosition().getY()
#Scanner.approach()
if (MSCoord[0].x > 0):
    # Calculating MotorStage coordinates
    for f in range(1,MSstep):
        MSCoord[f].x = MSCoord[f-1].x - delta * math.cos(angle)
        MSCoord[f].y = MSCoord[f-1].y + delta * math.sin(angle)

    i = (MSstep*2) -1
    for f in range(0, len(MSCoord) - MSstep):
        if i < 1:
            i = (MSstep*2) -1
         MSCoord[f+i].x = MSCoord[f].x - delta * math.sin(angle) -
(Ws / 5)
        MSCoord[f+i].y = MSCoord[f].y - delta * math.cos(angle)
        i = i-2
else:
    # Calculating MotorStage coordinates
    for f in range(1,MSstep):
        MSCoord[f].x = MSCoord[f-1].x + delta * math.cos(angle)
        MSCoord[f].y = MSCoord[f-1].y + delta * math.sin(angle)

    i = (MSstep*2) -1
    for f in range(0, len(MSCoord) - MSstep):
        if i < 1:
            i = (MSstep*2) -1
         MSCoord[f+i].x = MSCoord[f].x - delta * math.sin(angle) -
(Ws / 5)
        MSCoord[f+i].y = MSCoord[f].y - delta * math.cos(angle)
        i = i-2
#Iterating through the MotorStage coordinates
logFile = open(fileName, "a")
logFile.write('Going to the motor stage initial coordinate: ' +
str(MSCoord[0].x) + ' , ' + str(MSCoord[0].y) + "\n")
logFile.close()
print 'Going to the motor stage initial coordinate:
'+str(MSCoord[0].x)+' , '+str(MSCoord[0].y)

while g < len(MSCoord):
    initialMStime=time.time()

    #Retract the scanner to avoid damages
    #Scanner.retract()
    Scanner.retractPiezo()
```

```
    P1 = P1First
    #Moving the scanner to the initial point
    ForceSpectroscopy.setPosition(P1[0], P1[1])

    if g > 0:
        #Engaging MotorStage
        MotorizedStage.engage()

        #Moving the MotorStage to a particular coordinate
               MotorizedStage.moveToAbsolutePosition(MSCoord[g].x,
MSCoord[g].y)
        logFile = open(fileName, "a")
         logFile.write('Motor stage current coordinate '+ str(g)+':
'+str(MSCoord[g].x)+str(MSCoord[g].y) + "\n")
        logFile.close()
             print 'Motor stage current coordinate '+ str(g)+':
'+str(MSCoord[g].x)+str(MSCoord[g].y)
        MotorizedStage.disengage()
        calculatePoints(Ws,angle,fileName, P1)
    logFile = open(fileName, "a")
    logFile.write('Calculating well coordinates...' + "\n")
    logFile.close()
    print 'Calculating well coordinates...'
    # Loops in order to store the coordinates;
    for i in range(nFP*nSP):
        WellPositions.append(Point(0,0))

    # Assign the first coordinate (P1) to the first position
    WellPositions[0].x = P1[0]
    WellPositions[0].y = P1[1]

    # Calculating Well positions
    if option == 0:
        for f in range(1, nFP):
               WellPositions[f].x = WellPositions[f-1].x - pitch *
math.cos(angle)
               WellPositions[f].y = WellPositions[f-1].y - pitch *
math.sin(angle)

        i = (nFP*2) -1
        for f in range(0, len(WellPositions) - nFP):
            if i < 1:
                i = (nFP*2) -1
               WellPositions[f+i].x = WellPositions[f].x - pitch *
math.sin(angle)
```

```
                WellPositions[f+i].y = WellPositions[f].y + pitch *
math.cos(angle)
            i = i-2
    else:
        for f in range(1, nFP):
                WellPositions[f].x = WellPositions[f-1].x + pitch *
math.cos(angle)
                WellPositions[f].y = WellPositions[f-1].y - pitch *
math.sin(angle)

        i = (nFP*2) -1
        for f in range(0, len(WellPositions) - nFP):
            if i < 1:
                i = (nFP*2) -1
                WellPositions[f+i].x = WellPositions[f].x - pitch *
math.sin(angle)
                WellPositions[f+i].y = WellPositions[f].y + pitch *
math.cos(angle)
            i = i-2
       # activate spectroscopy gui mode (show the force scan
oscilloscope)
    ForceSpectroscopy.activateGUIMode()

    # activate autosaving
    ForceSpectroscopy.setAutosave(1)

    # Variable for date
    date = time.asctime()

    #Path to store optical images
    pathR = path+"/Area"+str(g) + '--' + str(date)

    #Iterating through the Wellgrid
    for a in range(nSP):
        for b in range(nFP):
            #Timer
            initialParcialWtime=time.time()

             #Compute index position in WellGrid and use it to move
there
            index=a*nFP+b

            #Move to the center of each square
              ForceSpectroscopy.setPosition(WellPositions[index].x,
WellPositions[index].y)
```

```
            # Print the WellGrid current position
            logFile = open(fileName, "a")
            logFile.write('Current Well: '+ str(index) + "\n")
            logFile.close()
            print 'Current position on Wellgrid: '+ str(index)

              # set the directory where the force scans should be
stored  HAVE FUN
            date = time.asctime()
             ForceSpectroscopy.setOutputDirectory(pathR+"/WellGrid"
+str(index) + '--' + str(date))

            #Cleaning the position list
            ForceSpectroscopy.clearPositions()

            #Defining the measurement grid
            FastLength=Ws - 1.5e-6
            SlowLength=Ws - 1.5e-6
            XGridCenter=WellPositions[index].x
            YGridCenter=WellPositions[index].y
            NumFastPoints=numScans[0]
            NumSlowPoints=numScans[1]
            try:
                        ForceSpectroscopy.setGridPattern(FastLength,
SlowLength,      XGridCenter,      YGridCenter,      NumFastPoints,
NumSlowPoints, angle)
                Scanner.approachPiezo()
                #Iterating through the measurement grid
                ForceSpectroscopy.startScansPerPosition(1)
                Scanner.retractPiezo()
            except:
                     print 'This well has some points outside the
scanning area\nProceeding to the next one'
                logFile = open(fileName, "a")
                  logFile.write("This well has some points outside
the scanning area\nProceeding to the next one\n")
                logFile.close()
            #Timers to show the time consumed on 100x100 um area
            endingParcialWtime=time.time()
            partialTime=endingParcialWtime - initialParcialWtime
            logFile = open(fileName, "a")
             logFile.write('Time for one well: ' + str(partialTime)
+ "\n")
            logFile.close()
```

```
            print'Time for one well: ' + str(partialTime)
                timeLeft = (partialTime * (len(WellPositions))) -
( partialTime * (index + 1))
            logFile = open(fileName, "a")
                    logFile.write('Time left for this area: ' +
str(timeLeft/60) + "\n")
            logFile.close()
             print 'Time left for this area: ' + str(timeLeft/60) +
' min'

    # Returning the scanner to the first well position
    #Scanner.retractPiezo()
                  ForceSpectroscopy.setPosition(WellPositions[0].x,
WellPositions[0].y)

    #Saving optical images
          Snapshooter.saveOpticalSnapshot(path+"image"+   str(date)
+str(g))
    g += 1
      # This gives info about how much time will take for the
remaining areas
    endingMStime = time.time()
    parcialTimeMS = endingMStime-initialMStime

#Retract the piezo after finish
Scanner.retract()
MotorizedStage.moveToAbsolutePosition(MSCoord[0].x, MSCoord[0].y)
end_time=time.time()
print 'Elapsed time: '+ str((end_time-start_time)/60)+' min'
```

Python script for mammalian cells

```
#Programmer: Ms.C. Sergio Proa Coronado
#Test of centering algorithm on bigger cells
# JPK Script
from __future__ import division
checkVersion('SPM', 5, 0, 135);
import math
import time
import os

#New data type declaration
class Point(object):
    def __init__(self, x = 0, y = 0):
        self.x = x
        self.y = y

# Function to calculate angle
def calculateAngle(A = [], B = []):
    """ Given two points (x,y) an angle is calculated
    """
    Time_angleS = time.time()
    if A[0] != B[0]:
             print 'angle calculated: ' + str(math.atan((B[1] -
A[1])/(B[0]-A[0])))
        Time_angleF = time.time()
           print'Time for calculate angle: ' + str(Time_angleF -
Time_angleS)
        return math.atan((B[1] - A[1])/(B[0]-A[0]))


    else:
        Time_angleF = time.time()
           print'Time for calculate angle: ' + str(Time_angleF -
Time_angleS)
        return 0


#*************************Inputs
block*****************************

#--------------The scanning area is defined as 100 x 100
micrometers-----------------------------------
```

```
#Points 1 and 2, take this coordinates from the approximate center
of each cell, MANUAL INPUT

P1=[3.6149e-3 , -0.5099e-3]

P2=[3.6409e-3 , -1.5967e-3]


#Well dimensions assuming square wells
Ws=30e-6

#Path for saving directory
path="~/jpkdata/Automatip/20190716"


#If you want force maps from the cells set value to 0 if you want
to indent set value to 1
choice = 1

# ForceScan matrix for the wells
numScans=[3,3]

#****************************************************************
*****************************************
startTime = time.time()
Scanner.retract()
#Angle calculation
angle = math.fabs(calculateAngle(P1, P2))
print 'Angle calculated: ' + str(angle)

#Pitch calculation
#pitch = math.sqrt((P2[0]-P1[0])**2 + (P2[1]-P1[1])**2)
da = math.sqrt((P2[0]-P1[0])**2 + (P2[1]-P1[1])**2)
pitch = da/9
print "Pitch: " + str(pitch)



#Point to indent, this coordinate is inside the scanning area
P = [0,0]
#calculatePoints(Ws,angle, P)
ForceSpectroscopy.setPosition(P[0], P[1])

#Checking for a positive or negative slope in the tilt
if abs(P1[0]) > abs(P2[0]):
```

```
    option = 0
else:
    option = 1
if option == 0:
    msg = "negative"
else:
    msg = "positive"
print'Slope = ' + msg

#Calculating Z slope
Heights = []

#MotorizedStage.moveToAbsolutePosition(P1[0],P1[1])
#ForceSpectroscopy.moveToForcePositionIndex(0)
MotorizedStage.moveToAbsolutePosition(P1[0],P1[1], 500e-6)
Scanner.approach()
Heights.append(Scanner.getCurrentHeight())
Scanner.retract()
MotorizedStage.moveToAbsolutePosition(P2[0],P2[1], 500e-6)
ForceSpectroscopy.moveToForcePositionIndex(0)
Scanner.approach()
Heights.append(Scanner.getCurrentHeight())
Scanner.retractPiezo()
MotorizedStage.moveToAbsolutePosition(P1[0],P1[1])
print "P1 and P2 heights: "
for ele in Heights:
    print ele
#Variable MSCoord stores MotorStage coordinates
MSCoord = []


nFP = int(da/pitch+0.4) + 1
print "Number of cels to visit: " + str(nFP)
# Create a MSCoord list full of zeros
for f in range(nFP * nFP):
    MSCoord.append(Point(0,0))

# Assign the first motor stage coordinate to the first position
MSCoord[0].x = MotorizedStage.getPosition().getX()
MSCoord[0].y = MotorizedStage.getPosition().getY()

rowFlag = 0
corrX = 1.7e-6
corrY = 9e-6
```

```
#Scanner.approach()
if option == 0:
    for f in range(1, nFP):
        MSCoord[f].x = MSCoord[f-1].x - pitch * math.cos(angle)
        MSCoord[f].y = MSCoord[f-1].y - pitch * math.sin(angle)
    i = (nFP*2) -1
    for f in range(0, len(MSCoord) - nFP):
        if i < 1:
            i = (nFP*2) -1
         #MSCoord[f+i].x = MSCoord[f].x - pitch * math.sin(angle) +
(Ws / 5)
         MSCoord[f+i].x = MSCoord[f].x - pitch * math.sin(angle) +
corrX
         MSCoord[f+i].y = MSCoord[f].y + pitch * math.cos(angle) -
corrY
        #if MSCoord[f].y < 0:
               #       MSCoord[f+i].y  =  MSCoord[f].y  +  pitch  *
math.cos(angle) + corrY
        #else:
               #       MSCoord[f+i].y  =  MSCoord[f].y  +  pitch  *
math.cos(angle) - corrY
        i = i-2
else:
    for f in range(1, nFP):
        MSCoord[f].x = MSCoord[f-1].x + pitch * math.cos(angle)
        MSCoord[f].y = MSCoord[f-1].y - pitch * math.sin(angle)
    i = (nFP*2) -1
    for f in range(0, len(MSCoord) - nFP):
        if i < 1:
            i = (nFP*2) -1
            rowFlag += 1
            if rowFlag > 5:
                corrY += 2e-6
                rowFlag = 0
         MSCoord[f+i].x = MSCoord[f].x - pitch * math.sin(angle) -
corrX
        if MSCoord[f].y < 0:
                        MSCoord[f+i].y  =  MSCoord[f].y  +  pitch  *
math.cos(angle) - corrY
        else:
                        MSCoord[f+i].y  =  MSCoord[f].y  +  pitch  *
math.cos(angle) - corrY
        i = i-2

for ele in MSCoord:
```

```
    print str(ele.x) + ", " + str(ele.y)
#Iterating through the MotorStage coordinates
g = 0
while g < len(MSCoord):
    #initialMStime=time.time()
    #Retract the scanner to avoid damages
    #Scanner.retract()

    ForceSpectroscopy.setPosition(P[0], P[1])

    if g > 0:
        #Engaging MotorStage
        MotorizedStage.engage()

        #Moving the MotorStage to a particular coordinate
               MotorizedStage.moveToAbsolutePosition(MSCoord[g].x,
MSCoord[g].y, 500e-6)
        #logFile = open(fileName, "a")
          #logFile.write('Motor stage current coordinate '+ str(g)
+': '+str(MSCoord[g].x)+str(MSCoord[g].y) + "\n")
        #logFile.close()
        MotorizedStage.disengage()
             print 'Motor stage current coordinate '+ str(g)+':
'+str(MotorizedStage.getPosition().getX())
+str(MotorizedStage.getPosition().getY())
        #MotorizedStage.disengage()
        #calculatePoints(Ws,angle,fileName, fineCoord)
    Scanner.approachPiezo()
    if choice == 0:
        ForceMapping.activateGUIMode()
        ForceMapping.Autosave.on()
         ForceMapping.setOutputDirectory(path+"/Cell"+str(g) + '--'
+ str(time.asctime()))
        ForceMapping.setScanSize(50e-6, 50e-6)
        ForceMapping.setScanPixels(16, 16)
           ForceMapping.setScanOffset(0, 0) #coordinates where the
force map is going to be obtained
        ForceMapping.setScanAngle(angle)
          ForceMapping.startScanning(1) #Number of force maps you
want from this region
    else:
        FastLength=5e-6
        SlowLength=5e-6
        XGridCenter=P[0]
        YGridCenter=P[1]
```

```
        NumFastPoints=numScans[0]
        NumSlowPoints=numScans[1]
        ForceSpectroscopy.activateGUIMode()
        ForceSpectroscopy.setAutosave(1)
         ForceSpectroscopy.setOutputDirectory(path+"/Cell"+str(g) +
'--' + str(time.asctime()))
           ForceSpectroscopy.setGridPattern(FastLength, SlowLength,
XGridCenter, YGridCenter, NumFastPoints, NumSlowPoints, angle)
        Scanner.approachPiezo()
        #Iterating through the measurement grid
        ForceSpectroscopy.startScansPerPosition(1)
        Scanner.retractPiezo()
    #print "Indenting point: " + str(P[0]) + ", " + str(P[1])
    Scanner.retractPiezo()
    g += 1
endTime = time.time()
print "Total time = " + str((endTime - startTime) / 60) + "
minutes"
```

Python script to copy files

```
# Program to extract files from a directory tree to a single
folder
# Programmer: Sergio Proa Coronado

import os
import shutil
# path where the files are stored
path = '/Documentos/pruebas/Resultados/mammalian_cells/'
Fullpath = os.environ['HOME'] + path
# path to the single folder where the files are going to be copied
dst_dir = '/Documentos/pruebas/Resultados/mammalian_cells/'
dst_path = os.environ["HOME"] + dst_dir
#variables to store folder names, and file names
lFiles = []
lRFiles = []
TWells = 0
con = 0
# lDir stores the complete directory tree
lDir = os.walk(Fullpath)
# root is a string, is the path to the directory.
# dirs is a list with all the names of the subdirectories.
# files is the list of all non-directories files
for root,dirs,files in lDir:
     for directory in files:
          (nameDirectory, extention) = os.path.splitext(directory)
          # This line guarantees that only the files with a
specific extention are located
          # inside the directory tree
          if extention == ".jpk-force":
               #This line generates a list with the path to the
files, including file
               #names and extentions
               lFiles.append(root + '/' + nameDirectory +
extention)

# Every force curve has an identifier (for example Well01) which
helps knowing from which part of
# the cell has been taken. However this identifier repeats itself
every time the area is changed.
# To prevent overwritten files the name must change according to
the total number of force curves
```

```
# These variables store the part of the string inside the list
lFiles that contains the identifier
# and preserve the directory strucutre
iniS = lFiles[0].find('Cell')
finS = lFiles[0].find('-', iniS) + 1
direc = lFiles[0][iniS:finS]

# Generates a new list that will contain the directory tree path
and the filename. However, the
#  identifier  in  the  filename  will  be  changed  and  enumerated
accordingly to the total number of
# force curves files
for ele in lFiles:
     iniFn = ele.find('force-save')
     Fname = ele[iniFn:]

     if direc != ele[iniS:finS]:
          iniS = ele.find('Cell')
          finS = ele.find('-', iniS) + 1
          direc = ele[iniS:finS]
          TWells += 1
     sufix = 'Cell' + str(TWells)
     lRFiles.append(dst_path + sufix + '-' + Fname)

# copy the files from its original source (lFiles) to a new path
(lRFiles). The files are renamed
# at the same time they are copied
for ele in range(len(lFiles)):
     shutil.copy( lFiles[ele], lRFiles[ele])
print ('Done')
```

R script for data analysis

```
#Ph.D. Student Sergio Proa Coronado
# The images will be stored on a folder name Images, this folder should be created where the R script is
# By default this script saves images in SVG format but PNG can be used too.
# This script analyze two experiments (untreated and treated per experiment) at the same time.
#Libraries imported
library(tidyverse)
library(stringi)
library(reticulate)
library(ggsignif)
#Loading the sets. Treated and untreated cells sets
#Here you can select all columns from the file or just a few. The ones presented here
#are enough for the analysis
Exp1Unt <- subset(Exp1, select =  c("UFNR30", "UCPR30", "USlR30", "UWells"))
Exp1Tre <- subset(Exp1, select =  c("TFNR30", "TCPR30", "TSlR30", "TWells"))

Exp2Unt <- subset(Exp1, select =  c("UFNR30", "UCPR30", "USlR30", "UWells"))
Exp2Tre <- subset(Exp1, select =  c("TFNR30", "TCPR30", "TSlR30", "TWells"))

#Eliminating NAs
Exp1Unt <- na.omit(Exp1Unt)
Exp1Tre <- na.omit(Exp1Tre)
Exp2Unt <- na.omit(Exp1Unt)
Exp2Tre <- na.omit(Exp1Tre)

#Converting to pN/nm (slope) and um (contact point)
Exp1Unt$USlR30 <- Exp1Unt$USlR30 * 1e3
Exp1Tre$TSlR30 <- Exp1Tre$TSlR30 * 1e3
Exp1Unt$UCPR30 <- Exp1Unt$UCPR30 * 1e6
Exp1Tre$TCPR30 <- Exp1Tre$TCPR30 * 1e6
Exp2Unt$USlR30 <- Exp2Unt$USlR30 * 1e3
Exp2Tre$TSlR30 <- Exp2Tre$TSlR30 * 1e3
Exp2Unt$UCPR30 <- Exp2Unt$UCPR30 * 1e6
Exp2Tre$TCPR30 <- Exp2Tre$TCPR30 * 1e6
```

```
#For convenience we separate the number of the wells from the
filename and added to a new column
fileName = Exp1Unt[["UFNR30"]]
TempPyNames = r_to_py(fileName, convert = FALSE)
i = 0
vectorWells = c()
while(i < length(TempPyNames)){
  finS = TempPyNames[i]$find('-')
  NumberWells = substr(TempPyNames[i], 0, py_to_r(finS))
          vectorWells     =     append(vectorWells,     NumberWells,
length(vectorWells))
  i = i + 1
}
#Adding Wells column to the data frames
Exp1Unt$UWells <- vectorWells

fileName = Exp1Tre[["TFNR30"]]
TempPyNames = r_to_py(fileName, convert = FALSE)
i = 0
vectorWells = c()
while(i < length(TempPyNames)){
  finS = TempPyNames[i]$find('-')
  NumberWells = substr(TempPyNames[i], 0, py_to_r(finS))
          vectorWells     =     append(vectorWells,     NumberWells,
length(vectorWells))
  i = i + 1
}
#Adding Wells column to the data frames
Exp1Tre$TWells <- vectorWells

fileName = Exp2Unt[["UFNR30"]]
TempPyNames = r_to_py(fileName, convert = FALSE)
i = 0
vectorWells = c()
while(i < length(TempPyNames)){
  finS = TempPyNames[i]$find('-')
  NumberWells = substr(TempPyNames[i], 0, py_to_r(finS))
          vectorWells     =     append(vectorWells,     NumberWells,
length(vectorWells))
  i = i + 1
}
#Adding Wells column to the data frames
Exp2Unt$UWells <- vectorWells
```

```
fileName = Exp2Tre[["TFNR30"]]
TempPyNames = r_to_py(fileName, convert = FALSE)
i = 0
vectorWells = c()
while(i < length(TempPyNames)){
  finS = TempPyNames[i]$find('-')
  NumberWells = substr(TempPyNames[i], 0, py_to_r(finS))
        vectorWells    =    append(vectorWells,    NumberWells,
length(vectorWells))
  i = i + 1
}
#Adding Wells column to the data frames
Exp2Tre$TWells <- vectorWells

#Filtering by height (contact point)
filterU1.byCP <- na.omit(filter(Exp1Unt, UCPR30 > 4.15))
filterT1.byCP <- na.omit(filter(Exp1Tre, TCPR30 > 4.15))
filterU2.byCP <- na.omit(filter(Exp2Unt, UCPR30 > 4.15))
filterT2.byCP <- na.omit(filter(Exp2Tre, TCPR30 > 4.15))

#Filtering negative values (slope)
filterU1.byNV <- na.omit(filter(filterU1.byCP, USlR30 > 0))
filterT1.byNV <- filter(filterT1.byCP, TSlR30 > 0)
filterU2.byNV <- na.omit(filter(filterU2.byCP, USlR30 > 0))
filterT2.byNV <- filter(filterT2.byCP, TSlR30 > 0)

#Filtering by slope values (discarding PDMS)
filterU1.Cells          <-          na.omit(filter(filterU1.byNV,
filterU1.byNV$USlR30 < 150))
filterT1.Cells  <-  filter(filterT1.byNV,  filterT1.byNV$TSlR30  <
150)
filterU2.Cells          <-          na.omit(filter(filterU2.byNV,
filterU2.byNV$USlR30 < 150))
filterT2.Cells  <-  filter(filterT2.byNV,  filterT2.byNV$TSlR30  <
150)

#Dividing the data into clusters, the number of clusters depends
on the number of peaks
kmU1 <- filterU1.Cells %>%
  subset(select = c("UCPR30", "USlR30")) %>%
  kmeans(centers = 3)
filterU1.Cells$Clust <-as.factor(kmU1$cluster)
kmT1 <- filterT1.Cells %>%
  subset(select= c("TCPR30", "TSlR30")) %>%
  kmeans(centers = 3)
```

```
filterT1.Cells$Clust <- as.factor(kmT1$cluster)
kmU2 <- filterU2.Cells %>%
  subset(select = c("UCPR30", "USlR30")) %>%
  kmeans(centers = 2)
filterU2.Cells$Clust <-as.factor(kmU2$cluster)
kmT2 <- filterT2.Cells %>%
  subset(select= c("TCPR30", "TSlR30")) %>%
  kmeans(centers = 2)
filterT2.Cells$Clust <- as.factor(kmT2$cluster)

#Histogram         of         the         untreated         cells
%-------------------------------------------------------
#Determining the binwidth Freddman-Diaconis rule.
bw     <-     (2     *     IQR(filterU1.Cells[["USlR30"]])     /
length(filterU1.Cells[["USlR30"]]) ^ (1 / 3))
CellSlopeU1_FR <- ggplot(filterU1.Cells, aes(x = USlR30)) +
    geom_histogram(aes(y  =  ((..count..)/sum(..count..)  *  100)),
binwidth = bw, color = "#FF9999", fill = "#FF6666") +
   stat_density(aes(y = ((..count..)/sum(..count..)) * 1500), geom
= "line", color = "red", size = 1) +
  theme(text = element_text(size = 22)) +
  ylab("Relative frequency [%]") +
  xlab("Spring constant [pN/nm]")

ggsave("Images/CellSlope_U1_FR.svg", CellSlopeU1_FR, width = 7.5,
height = 5, dpi = 300)

bw     <-     (2     *     IQR(filterU2.Cells[["USlR30"]])     /
length(filterU2.Cells[["USlR30"]]) ^ (1 / 3))
CellSlopeU2_FR <- ggplot(filterU2.Cells, aes(x = USlR30)) +
    geom_histogram(aes(y  =  ((..count..)/sum(..count..)  *  100)),
binwidth = bw, color = "#FF9999", fill = "#FF6666") +
   stat_density(aes(y = ((..count..)/sum(..count..)) * 1400), geom
= "line", color = "red", size = 1) +
  theme(text = element_text(size = 22)) +
  ylab("Relative frequency [%]") +
  xlab("Spring constant [pN/nm]")

ggsave("Images/CellSlope_U2_FR.svg", CellSlopeU2_FR, width = 7.5,
height = 5, dpi = 300)

#Histogram         of         the         treated         cells
%-------------------------------------------------------
bw     <-     (2     *     IQR(filterT1.Cells[["TSlR30"]])     /
length(filterT1.Cells[["TSlR30"]]) ^ (1 / 3))
```

```
CellSlopeT1_FR <- ggplot(filterT1.Cells, aes(x = TSlR30)) +
    geom_histogram(aes( y = ((..count..)/sum(..count..) * 100)),
binwidth = bw, color = "#66CCFF", fill = "#0099FF") +
   stat_density(aes(y = ((..count..)/sum(..count..)) * 1500), geom
= "line", color = "red", size = 1) +
  theme(text = element_text(size = 22)) +
  ylab("Relative frequency [%]") +
  xlab("Spring constant [pN/nm]")

ggsave("Images/CellSlope_T1_FR.svg", CellSlopeT1_FR, width = 7.5,
height = 5, dpi = 300)

bw <- (2 * IQR(filterT2.Cells[["TSlR30"]]) /
length(filterT2.Cells[["TSlR30"]]) ^ (1 / 3))
CellSlopeT2_FR <- ggplot(filterT2.Cells, aes(x = TSlR30)) +
    geom_histogram(aes(y = ((..count..)/sum(..count..) * 100)),
binwidth = bw, color = "#66CCFF", fill = "#0099FF") +
   stat_density(aes(y = ((..count..)/sum(..count..)) * 1500), geom
= "line", color = "red", size = 1) +
  theme(text = element_text(size = 22)) +
  ylab("Relative frequency [%]") +
  xlab("Spring constant [pN/nm]")

ggsave("Images/CellSlope_T2_FR.svg", CellSlopeT2_FR, width = 7.5,
height = 5, dpi = 300)

#Obtaining statistics of each peak inside the
plots-----------------------------------
#Assign a variable to each cluster number, the number of clusters
is related to the number
# of center used in the kmeans function

#Exp 1
StatasU1.1 <- filterU1.Cells %>%
  filter(filterU1.Cells$Clust == 1)
StatasU1.2 <- filterU1.Cells %>%
  filter(filterU1.Cells$Clust == 2)
StatasU1.3 <- filterU1.Cells %>%
  filter(filterU1.Cells$Clust == 3)

StatasT1.1 <- filterT1.Cells %>%
  filter(filterT1.Cells$Clust == 1)
StatasT1.2 <- filterT1.Cells %>%
  filter(filterT1.Cells$Clust == 2)
StatasT1.3 <- filterT1.Cells %>%
```

```
  filter(filterT1.Cells$Clust == 3)
#Exp2
StatasU2.2 <- filterU2.Cells %>%
  filter(filterU2.Cells$Clust == 1)
StatasU2.2 <- filterU2.Cells %>%
  filter(filterU2.Cells$Clust == 2)

StatasT2.1 <- filterT2.Cells %>%
  filter(filterT2.Cells$Clust == 1)
StatasT2.2 <- filterT2.Cells %>%
  filter(filterT2.Cells$Clust == 2)

#ANOVA                                                          test
Slope-------------------------------------------------------------
----------------------
# Data frames must contain the same number of data in order to
transform it in large data format
Temp <- head(filterU1.Cells, nrow(filterT1.Cells))
Set1.Sl <- cbind(filterT1.Cells,Temp)
Temp <- head(filterU2.Cells, nrow(filterT2.Cells))
Set2.Sl <- cbind(filterT2.Cells,Temp)

Oneway1.info <- Set1.Sl %>%
  subset(select = c("USlR30","TSlR30")) %>%
  gather(SlopeType, SlopeVal, USlR30, TSlR30)
Oneway2.info <- Set2.Sl %>%
  subset(select = c("USlR30","TSlR30")) %>%
  gather(SlopeType, SlopeVal, USlR30, TSlR30)

aov1.out = aov(SlopeVal ~ SlopeType, data = Oneway1.info)
aov2.out = aov(SlopeVal ~ SlopeType, data = Oneway2.info)

summary(aov1.out)
summary(aov2.out)

# Renaming values for SlopeType
Oneway1.info$SlopeType  <-  plyr::revalue(Oneway1.info$SlopeType  ,
c("USlR30" = "Native", "TSlR30" = "Treated"))
Oneway2.info$SlopeType  <-  plyr::revalue(Oneway2.info$SlopeType  ,
c("USlR30" = "Native", "TSlR30" = "Treated"))

Anova1 <- ggplot(Oneway1.info, aes(x = SlopeType, y = SlopeVal,
fill = SlopeType)) +
  geom_boxplot(colour = "blue", fill = c("#FF6666", "#0099FF")) +
```

```
  scale_x_discrete() + xlab("C. albicans") + ylab("Spring constant
[pN/nm]") +
  scale_fill_discrete(breaks = c("Native", "Treated")) +
      geom_signif(comparisons   =   list(c("Native",   "Treated")),
map_signif_level = TRUE) +
  theme(legend.title = element_blank(), text = element_text(size =
20))

ggsave("Images/ANOVA1.svg", Anova1, width = 6, height = 4, dpi =
200)

Anova2 <- ggplot(Oneway2.info, aes(x = SlopeType, y = SlopeVal,
fill = SlopeType)) +
  geom_boxplot(colour = "blue", fill = c("#FF6666", "#0099FF")) +
  scale_x_discrete() + xlab("C. albicans") + ylab("Spring constant
[pN/nm]") +
  scale_fill_discrete(breaks = c("Native", "Treated")) +
   theme(text = element_text(size = 20), legend.position = "none")
+
      geom_signif(comparisons   =   list(c("Native",   "Treated")),
map_signif_level = TRUE)

ggsave("Images/ANOVA2.svg", Anova2, width = 6, height = 4, dpi =
200)


#Obtaining                          median                          per
cell-------------------------------------------------------------
----
#Obtaining the number of cells per treatment (Unt or Treat)
UstringNumber                                                      <-
r_to_py(filterU1.Cells$UWells[nrow(filterU1.Cells)],   convert   =
FALSE)
UtotWells1        <-        strtoi(substr(UstringNumber,        5,
stri_length(UstringNumber)))
TstringNumber                                                      <-
r_to_py(filterT1.Cells$TWells[nrow(filterT1.Cells)],   convert   =
FALSE)
TtotWells1        <-        strtoi(substr(TstringNumber,        5,
stri_length(TstringNumber)))

j = 0
filterU1.AMxCell <- data.frame(Well = character(),
                               averagUAdh = numeric(),
                               medianUAdh = numeric(),
```

```
                              stringsAsFactors = FALSE)

while(j <= UtotWells1){
  compstr <- paste("Well", toString(j), sep = "")
     SelectedWell   =   na.omit(filter(filterU1.Cells,   UWells   ==
compstr))
  averageUA = mean(as.numeric(SelectedWell$USlR30))
  medianUA = median(as.numeric(SelectedWell$USlR30))
   filterU1.AMxCell[nrow(filterU1.AMxCell) + 1,] <- list(compstr,
averageUA, medianUA)
  j = j + 1
}
filterU1.AMxCell <- na.omit(filterU1.AMxCell)
j = 0
filterT1.AMxCell <- data.frame(Well = character(),
                               averagTAdh = numeric(),
                               medianTAdh = numeric(),
                               stringsAsFactors = FALSE)

while(j <= TtotWells1){
  compstr <- paste("Well", toString(j), sep = "")
     SelectedWell   =   na.omit(filter(filterT1.Cells,   TWells   ==
compstr))
  averageTA = mean(as.numeric(SelectedWell$TSlR30))
  medianTA = median(as.numeric(SelectedWell$TSlR30))
   filterT1.AMxCell[nrow(filterT1.AMxCell) + 1,] <- list(compstr,
averageTA, medianTA)
  j = j + 1
}
filterT1.AMxCell <- na.omit(filterT1.AMxCell)

#Plots median per cell
bw    <-    (2    *    IQR(filterU1.AMxCell[["medianUAdh"]])    /
length(filterU1.AMxCell[["medianUAdh"]]) ^ (1 / 3))
MedianSlopeU1_FR <- ggplot(filterU1.AMxCell, aes(x = medianUAdh))
+
    geom_histogram(aes(y  =  ((..count..)/sum(..count..)  *  100)),
binwidth = bw, color = "#FF9999", fill = "#FF6666") +
   stat_density(aes(y = ((..count..)/sum(..count..)) * 2800), geom
= "line", color = "red", size = 1) +
  theme(text = element_text(size = 20)) +
  ylab("Relative frequency [%]") +
  xlab("Spring constant [pN/nm]")
ggsave("Images/MedianSlope_U1_FR.svg",  MedianSlopeU1_FR,  width  =
7.5, height = 5, dpi = 300)
```

```
bw <- (2 * IQR(filterT1.AMxCell[["medianTAdh"]]) /
length(filterT1.AMxCell[["medianTAdh"]]) ^ (1 / 3))
MedianSlopeT1_FR <- ggplot(filterT1.AMxCell, aes(x = medianTAdh))
+
    geom_histogram(aes(y = ((..count..)/sum(..count..) * 100)),
binwidth = bw, color = "#66CCFF", fill = "#0099FF") +
   stat_density(aes(y = ((..count..)/sum(..count..)) * 2500), geom
= "line", color = "red", size = 1) +
  theme(text = element_text(size = 20)) +
  ylab("Relative frequency [%]") +
  xlab("Spring constant [pN/nm]")
ggsave("Images/MedianSlope_T1_FR.svg", MedianSlopeT1_FR, width =
7.5, height = 5, dpi = 300)


#Time                                                    dependance
analysis-----------------------------------------------------------
--------
#Adding a column which will contain the hour of the experiment,
the format will NOT be datetime type
fileHour = filterU1.Cells[["UFNR30"]]
TempPyHours = r_to_py(fileHour, convert = FALSE)
i = 0
vectorHours = c()
while(i < length(TempPyHours)){
  iniS = TempPyHours[i]$find('.')
   ini = as.numeric(py_to_r(iniS)) + 8 #+8 is because the object
changes to r, in r the index starts at 1 and after 8 positions you
will be in the first number of the hour
  finS = ini + 4
  WellsHours = substr(TempPyHours[i], ini, finS)
          vectorHours     =     append(vectorHours,     WellsHours,
length(vectorHours))
  i = i + 1
}
filterU1.Cells$Time <- as.numeric(vectorHours)

fileHour = filterU2.Cells[["UFN"]]
TempPyHours = r_to_py(fileHour, convert = FALSE)
i = 0
vectorHours = c()
while(i < length(TempPyHours)){
  iniS = TempPyHours[i]$find('.')
  ini = as.numeric(py_to_r(iniS)) + 8
```

```
  finS = ini + 4
  WellsHours = substr(TempPyHours[i], ini, finS)
          vectorHours     =     append(vectorHours,     WellsHours,
length(vectorHours))
  i = i + 1
}
filterU2.Cells$Time <- as.numeric(vectorHours)

fileHour = filterT1.Cells[["TFNR30"]]
TempPyHours = r_to_py(fileHour, convert = FALSE)
i = 0
vectorHours = c()
while(i < length(TempPyHours)){
  iniS = TempPyHours[i]$find('.')
   ini  =  as.numeric(py_to_r(iniS))  +  8  #+8 is because the object
changes to r, in r the index starts at 1 and after 8 positions you
will be in the first number of the hour
  finS = ini + 4
  WellsHours = substr(TempPyHours[i], ini, finS)
          vectorHours     =     append(vectorHours,     WellsHours,
length(vectorHours))
  i = i + 1
}
filterT1.Cells$Time <- as.numeric(vectorHours)

fileHour = filterT2.Cells[["TFN"]]
TempPyHours = r_to_py(fileHour, convert = FALSE)
i = 0
vectorHours = c()
while(i < length(TempPyHours)){
  iniS = TempPyHours[i]$find('.')
   ini  =  as.numeric(py_to_r(iniS))  +  8  #+8 is because the object
changes to r, in r the index starts at 1 and after 8 positions you
will be in the first number of the hour
  finS = ini + 4
  WellsHours = substr(TempPyHours[i], ini, finS)
          vectorHours     =     append(vectorHours,     WellsHours,
length(vectorHours))
  i = i + 1
}
filterT2.Cells$Time <- as.numeric(vectorHours)

#Plots        showing        if        there        is        time
dependance-------------------------------------------------------
----
```

```
filterU1.Cells$Time <- filterU1.Cells$Time - 7
filterU2.Cells$Time <- filterU2.Cells$Time - 9
#Adding a variable for grouping the data on each hour
filterU1.Cells$Hour <- ifelse(filterU1.Cells$Time <= 1.37, 1,
                              ifelse(filterU1.Cells$Time <= 2.38,
2,
                                     ifelse(filterU1.Cells$Time <=
3.39, 3,
                                            ifelse(filterU1.Cells$
Time <= 4.4, 4, 5))))
filterU2.Cells$Hour <- ifelse(filterU2.Cells$Time <= 1.29, 1,
                              ifelse(filterU2.Cells$Time <= 2.30,
2,
                                     ifelse(filterU2.Cells$Time <=
3.31, 3, 4)))
#Histograms ploted by hour, the result should show the two
populations

tPlot <- ggplot(filterU1.Cells, aes(x = filterU1.Cells$USlR30, y =
filterU1.Cells$UCPR30, color = Clust)) +
  geom_point() +
       theme(axis.text.y   =   element_blank(),   axis.ticks.y   =
element_blank(),
                 axis.title.y  =  element_blank(),  axis.line.y  =
element_blank(),
    text = element_text(size = 18), legend.position = "none") +
  scale_color_manual(values = c("#33FF00","#33CCCC", "#33FF00")) +
  scale_y_continuous() +
  xlab("Spring constant [pN/nm]") +
  ylab("Counts")

hours.labs <- c("1 hr","2 hrs","3 hrs","4 hrs", "5 hrs")
names(hours.labs) <- c("1","2","3","4","5")
timePlotU1  <-  tPlot  +  facet_wrap(~  Hour,  ncol  =  1,  labeller  =
labeller(Hour = hours.labs))

ggsave("Images/timePlotU1.svg",  timePlotU1,  width  =  5,  height  =
10, dpi = 600)

tPlot  <-  ggplot(filterU2.Cells,  aes(x  =  filterU2.Cells$Usl,  y  =
filterU2.Cells$UCP, color = Clust)) +
  geom_point() +
       theme(axis.text.y   =   element_blank(),   axis.ticks.y   =
element_blank(),
```

```
                axis.title.y  =  element_blank(),  axis.line.y  =
element_blank(),
    text = element_text(size = 18), legend.position = "none") +
  scale_color_manual(values = c("#33CCCC", "#33FF00")) +
  scale_y_continuous() +
  xlab("Spring constant [pN/nm]") +
  ylab("Counts")

hours.labs <- c("1 hr","2 hrs","3 hrs","4 hrs")
names(hours.labs) <- c("1","2","3","4")
timePlotU2 <- tPlot + facet_wrap(~ Hour, ncol = 1, labeller =
labeller(Hour = hours.labs))
ggsave("Images/timePlotU2.svg", timePlotU2, width = 5, height =
10, dpi = 600)

#Dot plots per position, we assume the same as above
pPlot <- ggplot(centralUVals, aes(x = centralUVals$USlR30, y =
centralUVals$UCPR30, color = centralUVals$Clust)) +
  geom_point() +
      theme(axis.text.y   =   element_blank(),   axis.ticks.y   =
element_blank(),
                axis.title.y  =  element_blank(),  axis.line.y  =
element_blank(),
    text = element_text(size = 18), legend.position = "none") +
  scale_color_manual(values = c("#33FF00","#33CCCC", "#33FF00")) +
  scale_y_continuous() +
  xlab("Spring constant [pN/nm]") +
  ylab("Counts")

posit.labs <- c("Position 1","Position 2","Position 3","Position
4")
names(posit.labs) <- c("5","6","9","10")
posPlotU1 <- pPlot + facet_wrap(~ Index, ncol = 2, labeller =
labeller(Index = posit.labs))
ggsave("Images/posPlotU1.svg", posPlotU1, width = 7.5, height = 5,
dpi = 600)

pPlotU2 <- ggplot(filterU2.Cells, aes(x = filterU2.Cells$Usl, y =
filterU2.Cells$UCP, color = Clust)) +
  geom_point() +
      theme(axis.text.y   =   element_blank(),   axis.ticks.y   =
element_blank(),
                axis.title.y  =  element_blank(),  axis.line.y  =
element_blank(),
    text = element_text(size = 18), legend.position = "none") +
```

```
  scale_color_manual(values = c("#33CCCC", "#33FF00")) +
  scale_y_continuous() +
  xlab("Spring constant [pN/nm]") +
  ylab("Counts")

posit.labs <- c("Position 1","Position 2","Position 3","Position
4", "Position 5",
                       "Position 6", "Position 7", "Position 8",
"Position 9")
names(posit.labs) <- c("0","1","2","3", "4", "5", "6", "7", "8")
posPlotU2 <- pPlotU2 + facet_wrap(~ UPI, ncol = 3, labeller =
labeller(UPI = posit.labs))
ggsave("Images/posPlotU2.svg", posPlotU2, width = 7.5, height = 5,
dpi = 600)

#Histograms separated by cluster
CellSlopeU1_FR <- ggplot(filterU1.Cells, aes(x = USlR30)) + #,
fill = filterU1.Cells$Clust )) +
    geom_histogram(aes(y = ((..count..)/sum(..count..) * 100)),
binwidth = bw, color = "#FF9999", fill = "#FF6666") +
  #stat_density(aes(y = ((..count..)/sum(..count..)) * 1500), geom
= "line", color = "red", size = 1) +
  theme(text = element_text(size = 22)) +
  ylab("Relative frequency [%]") +
  xlab("Spring constant [pN/nm]")

groupPlotU1 <- CellSlopeU1_FR +
    annotate("rect", xmin = c(0,33), xmax = c(33,155), ymin =
c(0,0), ymax = c(20,12), alpha = 0.2, color = c("#33CCCC",
"#33FF00"), fill = c("#33CCCC", "#33FF00"))
ggsave("Images/U1GroupedClust.svg", groupPlotU1, width = 7.5,
height = 5, dpi = 600)

groupPlotU2 <- CellSlopeU2_FR +
   annotate("rect", xmin = c(0,56.5), xmax = c(56.5,155), ymin =
c(0,0), ymax = c(10,5), alpha = 0.2, color = c("#33CCCC",
"#33FF00"), fill = c("#33CCCC", "#33FF00"))
ggsave("Images/U2GroupedClust.svg", groupPlotU2, width = 7.5,
height = 5, dpi = 600)

#Adhesion
analysis-----------------------------------------------------------
--------
#Untreated
```

```
#Because Adhesion and Slope analysis were made separately, we need
to merge them by the filename
#slope results
CellsU1Cp <- filterU1.Cells
CellsU2Cp <- filterU2.Cells
#adhesion results
colnames(CellsU1Cp)[1] <- "UFN"
colnames(AdhUnt1)[1] <- "UFN"

fileName = CellsU1Cp[["UFN"]]
TempPyNames = r_to_py(fileName, convert = FALSE)
i = 0
vectorNames = c()
while(i < length(TempPyNames)){
  starS = TempPyNames[i]$find('-')
  endS = stri_length(TempPyNames[i]) - 10
  FilesNam = substr(TempPyNames[i], py_to_r(starS) + 2, endS)
  vectorNames = append(vectorNames, FilesNam, length(vectorNames))
  i = i + 1
}
CellsU1Cp$FileNames <- vectorNames

fileName = AdhUnt1[["UFN"]]
TempPyNames = r_to_py(fileName, convert = FALSE)
i = 0
vectorNames = c()
while(i < length(TempPyNames)){
  starS = TempPyNames[i]$find('-')
  endS = stri_length(TempPyNames[i]) - 4
  FilesNam = substr(TempPyNames[i], py_to_r(starS) + 2, endS)
  vectorNames = append(vectorNames, FilesNam, length(vectorNames))
  i = i + 1
}
AdhUnt1$FileNames <- vectorNames

fileName = CellsU2Cp[["UFN"]]
TempPyNames = r_to_py(fileName, convert = FALSE)
i = 0
vectorNames = c()
while(i < length(TempPyNames)){
  starS = TempPyNames[i]$find('-')
  endS = stri_length(TempPyNames[i]) - 10
  FilesNam = substr(TempPyNames[i], py_to_r(starS) + 2, endS)
  vectorNames = append(vectorNames, FilesNam, length(vectorNames))
  i = i + 1
```

```
}
CellsU2Cp$FileNames <- vectorNames

fileName = AdhUnt2[["FileName"]]
TempPyNames = r_to_py(fileName, convert = FALSE)
i = 0
vectorNames = c()
while(i < length(TempPyNames)){
  starS = TempPyNames[i]$find('-')
  endS = stri_length(TempPyNames[i]) - 4
  FilesNam = substr(TempPyNames[i], py_to_r(starS) + 2, endS)
  vectorNames = append(vectorNames, FilesNam, length(vectorNames))
  i = i + 1
}
AdhUnt2$FileNames <- vectorNames

AdhUn1.Cells <- left_join(CellsU1Cp, AdhUnt1, by = "FileNames")
AdhUn2.Cells <-left_join(CellsU2Cp, AdhUnt2, by = "FileNames")
AdhUn1Filtered.Cells <- na.omit(AdhUn1.Cells)
AdhUn2Filtered.Cells <- na.omit(AdhUn2.Cells)
#Treated
fileName = AdhTre1[["FileName"]]
TempPyNames = r_to_py(fileName, convert = FALSE)
i = 0
vectorNames = c()
while(i < length(TempPyNames)){
  starS = TempPyNames[i]$find('-')
  endS = stri_length(TempPyNames[i]) - 4
  FilesNam = substr(TempPyNames[i], py_to_r(starS) + 2, endS)
  vectorNames = append(vectorNames, FilesNam, length(vectorNames))
  i = i + 1
}
AdhTre1$FileNames <- vectorNames

fileName = filterT1.Cells[["TFNR30"]]
TempPyNames = r_to_py(fileName, convert = FALSE)
i = 0
vectorNames = c()
while(i < length(TempPyNames)){
  starS = TempPyNames[i]$find('-')
  endS = stri_length(TempPyNames[i]) - 10
  FilesNam = substr(TempPyNames[i], py_to_r(starS) + 2, endS)
  vectorNames = append(vectorNames, FilesNam, length(vectorNames))
  i = i + 1
}
```

```
filterT1.Cells$FileNames <- vectorNames


fileName = filterT2.Cells[["TFN"]]
TempPyNames = r_to_py(fileName, convert = FALSE)
i = 0
vectorNames = c()
while(i < length(TempPyNames)){
  starS = TempPyNames[i]$find('-')
  endS = stri_length(TempPyNames[i]) - 10
  FilesNam = substr(TempPyNames[i], py_to_r(starS) + 2, endS)
  vectorNames = append(vectorNames, FilesNam, length(vectorNames))
  i = i + 1
}
filterT2.Cells$FileNames <- vectorNames

fileName = AdhTre2[["FileName"]]
TempPyNames = r_to_py(fileName, convert = FALSE)
i = 0
vectorNames = c()
while(i < length(TempPyNames)){
  starS = TempPyNames[i]$find('-')
  endS = stri_length(TempPyNames[i]) - 4
  FilesNam = substr(TempPyNames[i], py_to_r(starS) + 2, endS)
  vectorNames = append(vectorNames, FilesNam, length(vectorNames))
  i = i + 1
}
AdhTre2$FileNames <- vectorNames

AdhT1.Cells   <-   left_join(filterT1.Cells,   AdhTre1,   by   =
"FileNames")
AdhT2.Cells <-left_join(filterT2.Cells, AdhTre2, by = "FileNames")
AdhT1Filtered.Cells <- na.omit(AdhT1.Cells) # This dataF contains
the values of adhesion corresponding to treated cells
AdhT2Filtered.Cells <- na.omit(AdhT2.Cells)
#Extracting the number of the well to filter the data
UtemStr                                                          <-
r_to_py(AdhUn1Filtered.Cells$UWells[nrow(AdhUn1Filtered.Cells)],
convert = FALSE)
UtotWells <- strtoi(substr(UtemStr, 5, stri_length(UtemStr)))
TtemStr                                                          <-
r_to_py(AdhT1Filtered.Cells$TWells[nrow(AdhT1Filtered.Cells)],
convert = FALSE)
TtotWells <- strtoi(substr(TtemStr, 5, stri_length(TtemStr)))
#Obtaining the 4 central points of untreated cells
```

```
centralUVals = AdhUn1Filtered.Cells[FALSE,]
j = 0
while(j <= UtotWells){
  compstr <- paste("Well", toString(j), sep = "")
   SelectedWell  =  na.omit(filter(AdhUn1Filtered.Cells,  UWells  ==
compstr))
  i = 1
  while( i <= 4){
     h = - (4 * (i - 1) * (i - 2) * (i - 3)) / 6 + (i - 1) * (i -
2) + (i - 1) + 5
    selected <- filter(SelectedWell, Index == h)
    centralUVals <- rbind(centralUVals, selected[1,] )
    i = i + 1
  }
  j = j + 1
}
#Obtaining the 4 central points of treated cells
centralTVals = AdhT1Filtered.Cells[FALSE,]
j = 0
while(j <= TtotWells){
  compstr <- paste("Well", toString(j), sep = "")
   SelectedWell  =  na.omit(filter(AdhT1Filtered.Cells,  TWells  ==
compstr))
  i = 1
  while( i <= 4){
      h = - (4 * (i - 1) * (i - 2) * (i - 3)) / 6 + (i - 1) * (i -
2) + (i - 1) + 5
      selected <- filter(SelectedWell, Index == h)
      centralTVals <- rbind(centralTVals, SelectedWell[1,] )
      i = i + 1
  }
  j = j + 1
}
#cleaning the central values data frames
centralUVals <- na.omit(centralUVals)
centralTVals <- na.omit(centralTVals)
colnames(centralUVals)[14] <- "Adhesion"
colnames(centralTVals)[13] <- "Adhesion"
colnames(AdhT2Filtered.Cells)[14] <- "Adhesion"
#Converting adhesion values to nN
centralUVals$Adhesion <- centralUVals$Adhesion * 1e9
centralTVals$Adhesion <- centralTVals$Adhesion * 1e9
AdhUn2Filtered.Cells$Uadhesion <- AdhUn2Filtered.Cells$Uadhesion *
1e9
AdhT2Filtered.Cells$Adhesion <- AdhT2Filtered.Cells$Adhesion * 1e9
```

```
#Ploting adhesion histograms %

bw <- (2 * IQR(centralUVals[["Adhesion"]]) /
length(centralUVals[["Adhesion"]]) ^ (1 / 3))
CellSlUnAdh1.p <- ggplot(centralUVals, aes(x = Adhesion)) +
    geom_histogram(aes(y = ((..count..)/sum(..count..) * 100)),
binwidth = 0.17, color = "#CCCCCC", fill = "#FFFF00") +
   stat_density(aes(y = ((..count..)/sum(..count..)) * 1500), geom
= "line", color = "red", size = 1) +
  xlim(0,6) +
  scale_y_continuous() +
  theme(text = element_text(size = 22)) +
  ylab("Relative frequency [%]") +
  xlab("Adhesion [nN]") #+
  #labs(title = "Histogram of the cells adhesion",
  #     subtitle = "Untreated  c. albicans cells")
ggsave("Images/CellSlAdh%_Unt1.svg", CellSlUnAdh1.p, width = 7.5,
height = 5, dpi = 300)

bw <- (2 * IQR(centralTVals[["Adhesion"]]) /
length(centralTVals[["Adhesion"]]) ^ (1 / 3))
CellSlTrAdh1.p <- ggplot(centralTVals, aes(x = Adhesion)) +
    geom_histogram(aes(y = ((..count..)/sum(..count..) * 100)),
binwidth = 0.17, color = "#FFFFCC", fill = "#CCCC00") +
   stat_density(aes(y = ((..count..)/sum(..count..)) * 1400), geom
= "line", color = "red", size = 1) +
  scale_x_continuous(breaks = c(0,2, 4, 6)) +
  scale_y_continuous() +
  theme(text = element_text(size = 22)) +
  ylab("Relative frequency [%]") +
  xlab("Adhesion [nN]") #+
  #labs(title = "Histogram of the cells adhesion",
  #     subtitle = "C. albicans cells + caspofungin (4xMIC)")
ggsave("Images/CellSlAdh%_Tre1.svg", CellSlTrAdh1.p, width = 7.5,
height = 5, dpi = 300)

bw <- (2 * IQR(AdhUn2Filtered.Cells[["Uadhesion"]]) /
length(AdhUn2Filtered.Cells[["Uadhesion"]]) ^ (1 / 3))
CellSlUnAdh2.p <- ggplot(AdhUn2Filtered.Cells, aes(x = Uadhesion))
+
    geom_histogram(aes(y = ((..count..)/sum(..count..) * 100)),
binwidth = 0.17, color = "#CCCCCC", fill = "#FFFF00") +
   stat_density(aes(y = ((..count..)/sum(..count..)) * 1700), geom
= "line", color = "red", size = 1) +
  scale_x_continuous(breaks = c(0,2, 4, 6)) +
```

```
  scale_y_continuous() +
  theme(text = element_text(size = 22)) +
  ylab("Relative frequency [%]") +
  xlab("Adhesion [nN]") #+
  #labs(title = "Histogram of the cells adhesion",
  #     subtitle = "Untreated  c. albicans cells")
ggsave("Images/CellSlAdh%_Unt2.svg", CellSlUnAdh2.p, width = 7.5,
height = 5, dpi = 300)

bw    <-    (2    *    IQR(AdhT2Filtered.Cells[["Adhesion"]])    /
length(AdhT2Filtered.Cells[["Adhesion"]]) ^ (1 / 3))
CellSlTrAdh2.p <- ggplot(AdhT2Filtered.Cells, aes(x = Adhesion)) +
    geom_histogram(aes(y  =  ((..count..)/sum(..count..)  *  100)),
binwidth = 0.17, color = "#FFFFCC", fill = "#CCCC00") +
   stat_density(aes(y = ((..count..)/sum(..count..)) * 1400), geom
= "line", color = "red", size = 1) +
  scale_x_continuous(breaks = c(0,2, 4, 6)) +
  scale_y_continuous() +
  theme(text = element_text(size = 22)) +
  ylab("Relative frequency [%]") +
  xlab("Adhesion [nN]") #+
  #labs(title = "Histogram of the cells adhesion",
  #     subtitle = "C. albicans cells + caspofungin (4xMIC)")
ggsave("Images/CellSlAdh%_Tre2.svg", CellSlTrAdh2.p, width = 7.5,
height = 5, dpi = 300)

#Grouping the data
kmU1 <- centralUVals %>%
  subset(select = c("Adhesion")) %>%
  kmeans(centers = 2)
centralUVals$AClust <-as.factor(kmU1$cluster)

kmT1 <- centralTVals %>%
  subset(select = c("Adhesion")) %>%
  kmeans(centers = 2)
centralTVals$AClust <-as.factor(kmT1$cluster)

kmU2 <- AdhUn2Filtered.Cells %>%
  subset(select = c("Uadhesion")) %>%
  kmeans(centers = 2)
AdhUn2Filtered.Cells$AClust <-as.factor(kmU2$cluster)

kmT2 <- AdhT2Filtered.Cells %>%
  subset(select = c("Adhesion")) %>%
  kmeans(centers = 3)
```

```
AdhT2Filtered.Cells$AClust <-as.factor(kmT2$cluster)

#Obtaining Adhesion statistics of each peak inside the
plots-----------------------------------
#Change the variable and number of peak and use sd() function
Statas <- centralTVals %>%
  filter(centralTVals$Clust == 2)
#Plots of the subgroups of adhesion
bw     <-     (2     *     IQR(centralUVals[["Adhesion"]])     /
length(centralUVals[["Adhesion"]]) ^ (1 / 3))
CellAdhU1_Clst <- ggplot(centralUVals, aes(x = Adhesion, fill =
centralUVals$AClust )) +
    geom_histogram(aes(y  =  ((..count..)/sum(..count..)  *  100)),
binwidth = 0.17, color = "#FF9999") +
  xlim(0,6) +
  theme(text = element_text(size = 18)) +
  ylab("Relative frequency [%]") +
  xlab("Adhesion [nN]")
bw     <-     (2     *     IQR(centralTVals[["Adhesion"]])     /
length(centralTVals[["Adhesion"]]) ^ (1 / 3))
CellAdhU1_Clst <- ggplot(centralTVals, aes(x = Adhesion, fill =
centralTVals$AClust )) +
    geom_histogram(aes(y  =  ((..count..)/sum(..count..)  *  100)),
binwidth = 0.17, color = "#FF9999") +
  xlim(0,6) +
  theme(text = element_text(size = 18)) +
  ylab("Relative frequency [%]") +
  xlab("Adhesion [nN]")
bw    <-    (2    *    IQR(AdhUn2Filtered.Cells[["Uadhesion"]])    /
length(AdhUn2Filtered.Cells[["Uadhesion"]]) ^ (1 / 3))
CellAdhU1_Clst <- ggplot(AdhUn2Filtered.Cells, aes(x = Uadhesion,
fill = AdhUn2Filtered.Cells$AClust )) +
    geom_histogram(aes(y  =  ((..count..)/sum(..count..)  *  100)),
binwidth = 0.17, color = "#FF9999") +
  xlim(0,6) +
  theme(text = element_text(size = 18)) +
  ylab("Relative frequency [%]") +
  xlab("Adhesion [nN]")
bw    <-    (2    *    IQR(AdhT2Filtered.Cells[["Adhesion"]])    /
length(AdhT2Filtered.Cells[["Adhesion"]]) ^ (1 / 3))
CellAdhU1_Clst <- ggplot(AdhT2Filtered.Cells, aes(x = Adhesion,
fill = AdhT2Filtered.Cells$AClust )) +
    geom_histogram(aes(y  =  ((..count..)/sum(..count..)  *  100)),
binwidth = 0.17, color = "#FF9999") +
  xlim(0,6) +
```

```
  theme(text = element_text(size = 18)) +
  ylab("Relative frequency [%]") +
  xlab("Adhesion [nN]")

#Anova
adhesion-------------------------------------------------------------
--------------------------
#Fisrt merging U+T into one dataFrame
colnames(centralUVals)[14] <- "UAdhesion"
colnames(centralTVals)[13] <- "TAdhesion"
colnames(centralTVals)[14] <- "AClust"

Temp <- head(centralTVals, nrow(centralUVals))
Set1.Ad <- cbind(centralUVals,Temp)
Temp2 <- head(AdhT2Filtered.Cells, nrow(AdhUn2Filtered.Cells))
Set2.Ad <- cbind(AdhUn2Filtered.Cells,Temp2)
colnames(Set2.Ad)[14] <- "TAdhesion"
colnames(Set2.Ad)[7] <- "Wells"

#Re-arranging the variables
Set1.AnovaAdh1 <- Set1.Ad %>%
  subset(select = c("UAdhesion", "TAdhesion")) %>%
  gather(AdhGroup, AdhesionVal, UAdhesion, TAdhesion)
Set2.AnovaAdh2 <- Set2.Ad %>%
  subset(select = c("Wells", "Uadhesion", "Adhesion")) %>%
  gather(AdhGroup, AdhesionVal, Uadhesion, Adhesion)
#Renaming AdhesionGroup
Set1.AnovaAdh1$AdhGroup  <-  plyr::revalue(Set1.AnovaAdh1$AdhGroup,
c("UAdhesion" = "Native", "TAdhesion" = "Treated"))
Set2.AnovaAdh2$AdhGroup  <-  plyr::revalue(Set2.AnovaAdh2$AdhGroup,
c("Uadhesion" = "Native", "Adhesion" = "Treated"))

AnovaAdh1  <-  ggplot(Set1.AnovaAdh1,  aes(x  =  AdhGroup,  y  =
AdhesionVal)) +
  geom_boxplot(colour = "blue", fill = c("#FFFF33", "#CC9900")) +
   scale_x_discrete() + xlab("C. albicans") + ylab("Adhesion [N]")
+
  scale_fill_discrete(breaks = c("Native", "Treated")) +
      geom_signif(comparisons   =   list(c("Native",   "Treated")),
map_signif_level = TRUE) +
  theme(legend.title = element_blank(), text = element_text(size =
18))

ggsave("Images/ANOVA-Adh1.svg", AnovaAdh1, width = 6, height = 4,
dpi = 200)
```

```
AnovaAdh2 <- ggplot(Set2.AnovaAdh2, aes(x = AdhGroup, y =
AdhesionVal)) +
  geom_boxplot(colour = "blue", fill = c("#FFFF33", "#CC9900")) +
   scale_x_discrete() + xlab("C. albicans") + ylab("Adhesion [N]")
+
  scale_fill_discrete(breaks = c("Native", "Treated")) +
  theme(legend.title = element_blank(), text = element_text(size =
18)) +
      geom_signif(comparisons = list(c("Native", "Treated")),
map_signif_level = TRUE)

ggsave("Images/ANOVA-Adh2.svg", AnovaAdh2, width = 6, height = 4,
dpi = 200)


#Obtaining the number of cells contributing to
adhesion-----------------------------------
UstringNumber <- r_to_py(centralUVals$UWells[nrow(centralUVals)],
convert = FALSE)
UtotWells1 <- strtoi(substr(UstringNumber, 5,
stri_length(UstringNumber)))
TstringNumber <- r_to_py(centralTVals$TWells[nrow(centralTVals)],
convert = FALSE)
TtotWells1 <- strtoi(substr(TstringNumber, 5,
stri_length(TstringNumber)))
UstringNumber <-
r_to_py(AdhUn2Filtered.Cells$UWells[nrow(AdhUn2Filtered.Cells)],
convert = FALSE)
UtotWells2 <- strtoi(substr(UstringNumber, 5,
stri_length(UstringNumber)))
TstringNumber <-
r_to_py(AdhT2Filtered.Cells$TWells[nrow(AdhT2Filtered.Cells)],
convert = FALSE)
TtotWells2 <- strtoi(substr(TstringNumber, 5,
stri_length(TstringNumber)))
j = 0
AveMedianUAdh1 <- data.frame(Well = character(),
                             averagUAdh = numeric(),
                             medianUAdh = numeric(),
                             stringsAsFactors = FALSE)

while(j <= UtotWells1){
  compstr <- paste("Well", toString(j), sep = "")
  SelectedWell = na.omit(filter(centralUVals, UWells == compstr))
```

```
  averageUA = mean(as.numeric(SelectedWell$Adhesion))
  medianUA = median(as.numeric(SelectedWell$Adhesion))
    AveMedianUAdh1[nrow(AveMedianUAdh1)  +  1,]  <-  list(compstr,
averageUA, medianUA)
  j = j + 1
}
j = 0
AveMedianTAdh1 <- data.frame(Well = character(),
                             averagTAdh = numeric(),
                             medianTAdh = numeric(),
                             stringsAsFactors = FALSE)

while(j <= TtotWells1){
  compstr <- paste("Well", toString(j), sep = "")
  SelectedWell = na.omit(filter(centralTVals, TWells == compstr))
  averageTA = mean(as.numeric(SelectedWell$Adhesion))
  medianTA = median(as.numeric(SelectedWell$Adhesion))
    AveMedianTAdh1[nrow(AveMedianTAdh1)  +  1,]  <-  list(compstr,
averageTA, medianTA)
  j = j + 1
}

j = 0
AveMedianUAdh2 <- data.frame(Well = character(),
                             averagUAdh = numeric(),
                             medianUAdh = numeric(),
                             stringsAsFactors = FALSE)

while(j <= UtotWells2){
  compstr <- paste("Well", toString(j), sep = "")
   SelectedWell  =  na.omit(filter(AdhUn2Filtered.Cells,  UWells  ==
compstr))
  averageUA = mean(as.numeric(SelectedWell$Uadhesion))
  medianUA = median(as.numeric(SelectedWell$Uadhesion))
    AveMedianUAdh2[nrow(AveMedianUAdh2)  +  1,]  <-  list(compstr,
averageUA, medianUA)
  j = j + 1
}
AveMedianTAdh2 <- data.frame(Well = character(),
                             averagTAdh = numeric(),
                             medianTAdh = numeric(),
                             stringsAsFactors = FALSE)

j = 0
while(j <= TtotWells2){
```

```
  compstr <- paste("Well", toString(j), sep = "")
    SelectedWell = na.omit(filter(AdhT2Filtered.Cells, TWells ==
compstr))
  averageTA = mean(as.numeric(SelectedWell$Adhesion))
  medianTA = median(as.numeric(SelectedWell$Adhesion))
    AveMedianTAdh2[nrow(AveMedianTAdh2) + 1,] <- list(compstr,
averageTA, medianTA)
  j = j + 1
}
#Eliminating NA values
AveMedianUAdh1 <- na.omit(AveMedianUAdh1)
AveMedianTAdh1 <- na.omit(AveMedianTAdh1)
AveMedianUAdh2 <- na.omit(AveMedianUAdh2)
AveMedianTAdh2 <- na.omit(AveMedianTAdh2)

#Ploting median values for adhesion
bw <- (2 * IQR(AveMedianUAdh2[["averagUAdh"]]) /
length(AveMedianUAdh2[["averagUAdh"]]) ^ (1 / 3))
CellSlAverageUA2 <- ggplot(AveMedianUAdh2, aes(x = averagUAdh)) +
   geom_bar(aes(y = (..count..)/sum(..count..) * 100), binwidth =
bw, color = "#FF3333", fill = "#993300") +
  theme(text = element_text(size = 16)) +
  ylab("Frequency %") +
  xlab("Adhesion [N]") +
   labs(title = "Histogram of the average adhesion values per
cell",
       subtitle = "Native C. albicans cells")
ggsave("Images/CellSlAverage_UA2.png", CellSlAverageUA2, width =
7.5, height = 5, dpi = 300)

bw <- (2 * IQR(AveMedianUAdh2[["medianUAdh"]]) /
length(AveMedianUAdh2[["medianUAdh"]]) ^ (1 / 3))
CellSlMedianUA2 <- ggplot(AveMedianUAdh2, aes(x = medianUAdh)) +
   geom_bar(aes(y = (..count..)/sum(..count..) * 100), binwidth =
bw, color = "#99CCFF", fill = "#3333FF") +
  theme(text = element_text(size = 16)) +
  ylab("Frequency %") +
  xlab("Adhesion [N]") +
  labs(title = "Histogram of the median adhesion values per cell",
       subtitle = "Native C. albicans cells")
ggsave("Images/CellSlMedian_UA2.png", CellSlMedianUA2, width =
7.5, height = 5, dpi = 300)

bw <- (2 * IQR(AveMedianTAdh2[["averagTAdh"]]) /
length(AveMedianTAdh2[["averagTAdh"]]) ^ (1 / 3))
```

```
CellSlAverageTA2 <- ggplot(AveMedianTAdh2, aes(x = averagTAdh)) +
   geom_bar(aes(y = (..count..)/sum(..count..) * 100), binwidth =
bw, color = "#FF3333", fill = "#993300") +
  theme(text = element_text(size = 16)) +
  ylab("Frequency %") +
  xlab("Adhesion [N]") +
   labs(title = "Histogram of the average adhesion values per
cell",
       subtitle = "C. albicans cells + caspofungin (4xMIC)")
ggsave("Images/CellSlAverage_TA2.png", CellSlAverageTA2, width =
7.5, height = 5, dpi = 300)

bw <- (2 * IQR(AveMedianTAdh2[["medianTAdh"]]) /
length(AveMedianTAdh2[["medianTAdh"]]) ^ (1 / 3))
CellSlMedianTA2 <- ggplot(AveMedianTAdh2, aes(x = medianTAdh)) +
   geom_bar(aes(y = (..count..)/sum(..count..) * 100), binwidth =
bw, color = "#99CCFF", fill = "#3333FF") +
  theme(text = element_text(size = 16)) +
  ylab("Frequency %") +
  xlab("Adhesion [N]") +
  labs(title = "Histogram of the median adhesion values per cell",
       subtitle = "C. albicans cells + caspofungin (4xMIC)")
ggsave("Images/CellSlMedian_TA2.png", CellSlMedianTA2, width =
7.5, height = 5, dpi = 300)
```